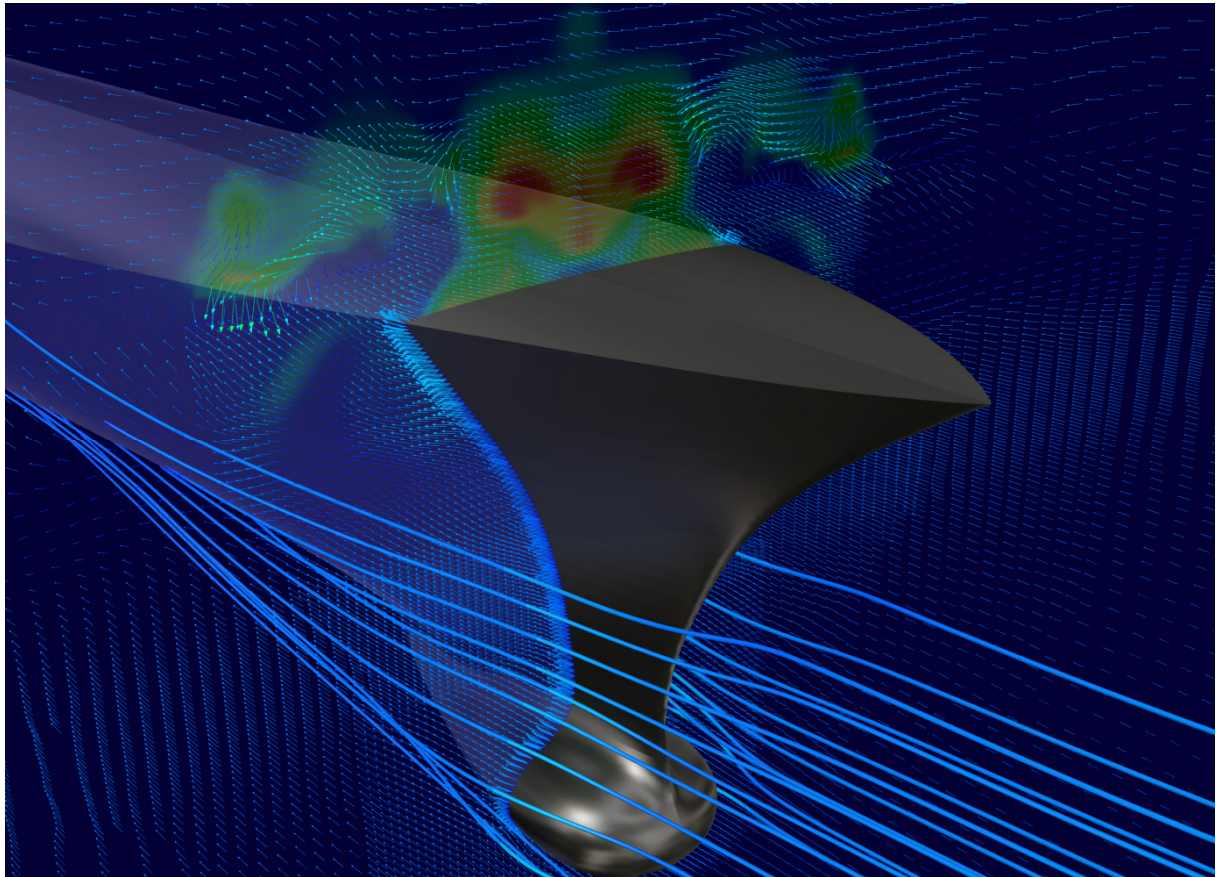# 16th Numerical Towing Tank Symposium

2-4 September 2013

Mülheim/Germany

Volker Bertram (Ed.)

Sponsored by

CD-Adapco
www.cd-adapco.com

Numeca
www.numeca.be

Germanischer Lloyd / FutureShip
www.gl-group.com

Table of Contents

Development and validation of a hybrid RANS-LES method for ship hydromechanics applications

Nawar Abbas*, Ivan Shevchuk and Nikolai Kornev

Chair for Modelling and Simulation,
University of Rostock, 18059 Rostock, Germany
nawar.abbas@uni-rostock.de

Introduction

Ship structure vibrations are caused by a complex combination of different hydrodynamical and mechanical effects. The main source of the hydrodynamically-excited vibrations is the propeller. Determination of loads on marine propeller is one of the important and challenging problems for the prediction of hull structure and propulsion shafting vibration.

The main source of the propeller excited vibrations is the unsteady loading, which results from the rotation of the propeller through nonstationary and nonuniform wake. The nonuniformness of the wake is the dominant effect for the vast majority of ships. Classical engineering methods of the marine propeller forces calculations are based on this effect, approximately assuming the velocity field to be stationary, the so-called "frozen field". These methods allow one to predict the propeller forces fluctuations with dominating blade frequencies proportional to nZ, where Z is the number of blades and n is the frequency of the propeller.

If the wake is steady the variations of forces and moments are strictly periodical. In mechanics, such processes are referred to periodic rather than unsteady. In this paper the unsteady non-periodic loadings are considered that correspond to non-periodic flow within the wake, which is the usual case for turbulent flows. The nonstationarity of the wake plays a more important role for ships with large block coefficients (the full-bottomed ships) but is far less studied. The wake of full-bottomed ships contains complicated vortex structures which amplify the unsteady effects in wakes. The existing engineering methods do not take the nonstationarity of the wake into account due to the difficulties connected with its determination. From the measurement point of view, it is a big challenge to measure the unsteady velocities in the wake using traditional techniques like the Pitot tube or the modern non-intrusive methods like LDV or PIV.

From the computational point of view, it is difficult to resolve vortex structures responsible for the velocity field fluctuations. The URANS (Unsteady Reynolds Averaged Navies Stokes) method, which is widely used in shipbuilding community, is not capable of modeling unsteady vortices arising in the ship stern area flow. The modern numerical methods like LES (Large Eddy Simulations) require large computational resources for accurate prediction of flows with large Reynolds numbers which are typical for shipbuilding applications. The grid resolution necessary for a pure LES is so huge that it makes the direct application of LES impossible. A practical solution of this problem is the use of a hybrid URANS-LES approach, in which the near body flow region is treated using URANS and far flow regions are treated with LES.

Hybrid CFD model

The hybrid CFD model developed in our previous work [1] is based on the observation that the basic transport equations have the same form in LES and URANS

$$\frac{\partial \overline{u}_i}{\partial t} + \frac{\partial (\overline{u}_i \overline{u}_j)}{\partial x_j} = -\frac{\partial \overline{p}^*}{\partial x_i} + \frac{\partial (\tau_{ij}^l + \tau_{ij}^t)}{\partial x_j}, \tag{1}$$

but the interpretation of the overline symbol is different. In LES it means filtering, and in URANS it stands for the Reynolds averaging (the term "ensemble averaging" is also used in this context). Here we use the standard notation of p^* for the pseudo-pressure, and τ_{ij}^l and τ_{ij}^t for the laminar and turbulent stresses respectively. Note that the turbulent stresses are calculated in different ways in LES and URANS regions.

1

The computational domain in our model is dynamically (i.e. at each time step) divided into the LES and URANS regions. The key quantities of this decomposition are the integral length scale L and the extended LES filter Δ which are computed for each cell of the mesh. The former is determined by the formula of Kolmogorov and Prandtl

$$L = Ck^{3/2}/\varepsilon \tag{2}$$

where k is the turbulent kinetic energy, ε is the dissipation rate and C is a certain empiric constant. The latter is computed as $\Delta = \sqrt{0.5(d_{\max}^2 + \delta^2)}$, where $d_{\max}$ is the maximal length of the cell edges $d_{\max} = \max(d_x, d_y, d_z)$ and $\delta = \sqrt[3]{\text{(the cell volume)}}$ is the common filter width used in LES. A cell of the mesh belongs to one area or the other depending on the value of L relative to Δ, if

$$L > \Delta \tag{3}$$

then the cell is in LES area, in the other case it is in URANS region. The extended LES filter Δ depends only on the geometry of the mesh and is computed only once, but the integral length scale L varies from one time step to another, which results in dynamic decomposition of the computational domain into the LES and URANS regions.

The turbulent stresses τ_{ij}^t are calculated from the Boussinesq approximation using the concept of the turbulent viscosity which is considered as the subgrid viscosity. These stresses are computed according to the dynamic model of Smagorinsky in the LES region and according to the k-ω SST turbulent model in the URANS region with the following smoothing the turbulent kinematic viscosity between the regions:

$$\nu(L) = \frac{\nu_t - \nu_{SGS}}{\pi} \arctan\big(100(\frac{L}{\Delta} - 1)\big) + \frac{1}{2}(\nu_t + \nu_{SGS}) \tag{4}$$

where ν_t is the RANS turbulent kinematic viscosity and ν_{SGS} is the subgrid viscosity. The factor 100 in the arctangent function is chosen such that $\nu \approx \nu_{SGS}$ when $L/\Delta > 1.05$ (LES region) and $\nu \approx \nu_t$ when $L/\Delta < 0.95$ (RANS region) and for $0.95 < L/\Delta < 1.05$ this expression gives a smooth interpolation of ν between the two regions. The CFD calculations using both URANS and hybrid models were carried out with the OpenFOAM code.

Present hybrid model versus *DES models

The typical question arising during the presentations of the model [1] is: what is the principal difference between this model and the *DES family models like DES, IDDES, DDES etc.? Based on the same general idea of the decomposition of flow area into URANS and LES parts, the methods differ in the way of the determination of the interface between URANS and LES. In both methods the interface is not prescribed and determinated dynamically. An important parameter in DES is the distance from the wall d. It is shown that if d is getting large the URANS models implemented in DES are transformed smoothly into the Smagorinsky model. Between URANS and LES, there is the grey zone in which LES and URANS models are mixed. Within our method the transition between LES and URANS happens according to the rule (3). There is also a grey zone between URANS and LES determined by the smoothing formula (4). Various computations shows that the hybrid method [1] reproduces the fluctuations in the propeller disc in the wake of the KVLCC2 tanker whereas the *DES models do not. This result is valid at least for moderate resolutions of a few millions of cells. The reason is that the URANS region in *DES calculations is much wider than in the hybrid method [1]. The propeller area is proved to be fully submerged into the URANS region where the fluctuations are not resolved. In our method the URANS region is much thinner and the propeller is located fully or partially in the LES region. The interface between URANS and LES lies closer to the ship hull. As a result, the method [1] indicates a resolved turbulence whereas it is absent in *DES calculations. Thus two following questions arise: Is this correct? Which method is more suitable for prediction of unsteady loadings on propellers? Unfortunately, there are almost no measurements which can be helpful to answer these questions. Certainly, substantial turbulent fluctuations are present in the propeller disc as shown in classical KRISO measurements behind the KVLCC2 tanker model. In our model, they are partly resolved in LES region, whereas they are represented only statistically in URANS submodels of *DES family. To predict the propeller loadings we need the temporally and spatially resolved fluctuations. Their statistical moments are not usable. This is a clear indication that the method [1] has advantage over the *DES methods at least at moderate resolutions since it is able to resolve flow field fluctuations which are necessary for propeller unsteady loading predictions. However, the accuracy of this prediction remains an open question. The computations presented in [2] shows that the thrust fluctuations are predicted quite reasonably and agree with predictions by well-tried empiric engineering approaches. However, a more detailed validation of the method is still necessary and is the aim of the present paper.

Validation of the Prandt Kolmogorov formula (2)

The reason why the thickness of the URANS area is larger in *DES models than in the hybrid one could be the overestimation of the integral length predicted by the Parndtl Kolmogorov formula (2) which, strictly speaking, is valid for high local Reynolds numbers far from the wall. To prove the accuracy of the prediction (2), we performed a series of calculations of zero gradient turbulent boundary layer (TBL) on a plate using 1420×40×40 knots, whereas the mean value of y^+ in the first node from the wall is equal to 3.18. The lower surface of our computational domain is a wall and the domain is a box with sizes of $4m \times 0.1m \times 0.1m$. Calculations were conducted using k-ω-SST-model and OpenFOAM code. This case has been studied as a very important step for the development of our hybrid RANS/LES method in order to calculate the fluctuations in the stern area of ships using OpenFOAM code. The maximum Re number at the end of the computational domain was $Re_x = 15 \times 10^5$ for the maximum length of the plate $4m$ and with velocity of incoming flow $3.75m/s$. The integral length L is calculated from k-ω-SST-model using following estimations:

$$L = C\frac{k^{3/2}}{\varepsilon}, \varepsilon = \frac{9}{100}\omega k \Rightarrow L = C\frac{100}{9}\frac{k^{0.5}}{\omega} \tag{5}$$

In order to ensure that the fields of k and ω (and hence the integral length scale) are predicted properly in OpenFOAM, the comparison with NASA benchmark for 2D turbulent flat plate has been performed. The results showed a pritty good agreement with distributions obtained by NASA, see Figure 1 . After validation using NASA benchmark the further methodical investigations were focused on the integral length computations at different distances from the plate leading edge. The integral lengths L at $x = 0.5, 1, 1.5, ...4m$ were compared with the experimental approximation obtained by Tomas et al. [4]:

$$\frac{L}{\delta} = \frac{0.3\left(\frac{z}{\delta} - 0.03\right)}{0.31 + \left(\frac{z}{\delta} - 0.03\right)^2} \tag{6}$$

where δ is the boundary layer thickness and y is the distance from the wall. The integral length in formula (6) was calculated as the average of four integral lengths obtained from autocorrelation functions for the axial and vertical velocities ρ_{uu} and ρ_{ww} as well for the cross correlations of these velocities ρ_{uw} and ρ_{wu}. As noted by Rodi [7], the coefficient C in (2) is not constant across the boundary layer. According to [3] $C = 0.168$. Analysis of data from [4] shows that this value is correct in close proximity to the wall at $0 < y/\delta < 0.2$. In the layer $0.2 < y/\delta < 0.8$ this constant is around 0.35. Fig. 2 shows the comparison of the numerical results obtained using the constant $C = 0.35$ with experimental data (6). As seen, when the absciss x increases the agreement between the experimental and numerical results is getting better, since the Reynolds number Re_x grows. This confirms, that within the boundary layer at $0.2 < y/\delta < 0.8$ the formula (2) can be used and the value of constant C is around 0.35. Within the area $y/\delta > 0.8$ C is not fixed and changes between 0.35 and 1.00 in the region $0.8 < y/\delta < 1$. The comparison between the experimental and numerical results (Fig. 3) shows that, the proper agreeement is attained with $C = 0.5$ within the region $0.8 < y/\delta < 1$ and $C \approx 1.0$ for $y/\delta > \sim 1.3$. Additionally to integral length L we present the estimation of the maximal vortex size $L_v = 0.227\delta$ (blue curve in Fig. 3) at the outer boundary of TBL $y > 0.4\delta$ obtained in [8] and presented in more convinient form in [6]. The vortex size can be used as a rough estimation for the integral length L. As seen from Fig. 3 pure numerical results and two experimental estimations are in a proper agreement. It leads to two following conclusions: a) the formula of Prandtl Kolmogorov can be used if the coefficient C is properly chosen depending on y/δ, b) the integral length scale prediction (2) is in a good agreement with measurements in the outer part of the TBL if the constant C is chosen from the conditions $C \approx 1.0$ at $y/\delta > 1.3$. Since the switch between LES and URANS happens in the outer region of the TBL, it is assumed that the formation of the turbulent boundary layer along the ship and generation of unsteady bilge vortices can be predicted accurately by hybrid method with the constant $C = 1.0$ in formula (2). The propeller is located in the wake. Thomas et al. [5] has shown that the value $C \approx 1$ is also valid for wake flows. Thus, the classic formula (2) with the coefficient $C = 1.0$ can be accepted as quite accurate for estimation of the integral length both along the ship boundary layer and in the wake.

Calculation of the unsteady wake of the KVLCC2 tanker at straight course and at manoeuvering conditions

DDES (Delayed Detached Eddy Simulation), IDDES (Improved DDES) and hybrid URANS-LES methods are applied for calculation of the KVLCC2 tanker hull without propeller at straight course and at
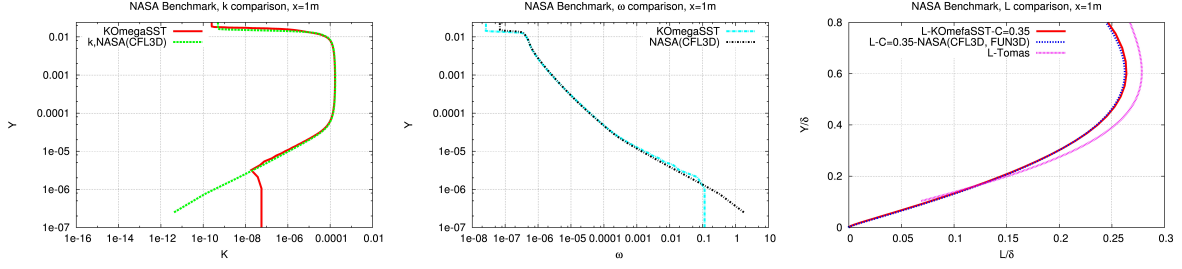
Figure 1: Validation of k-ω-SSTmodel implemented in OpenFOAM using NASA benchmark test
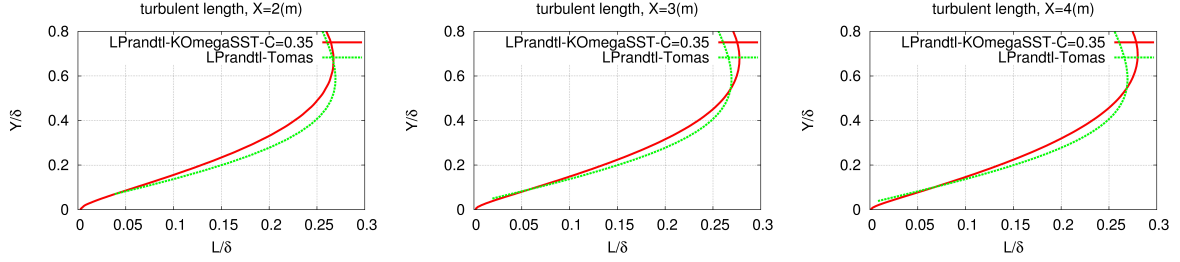
Figure 2: Comparison of turbulent length scales L obtained from k-ω-SST-model and Tomas's empirical formula [4] for the inner part of the boundary layer
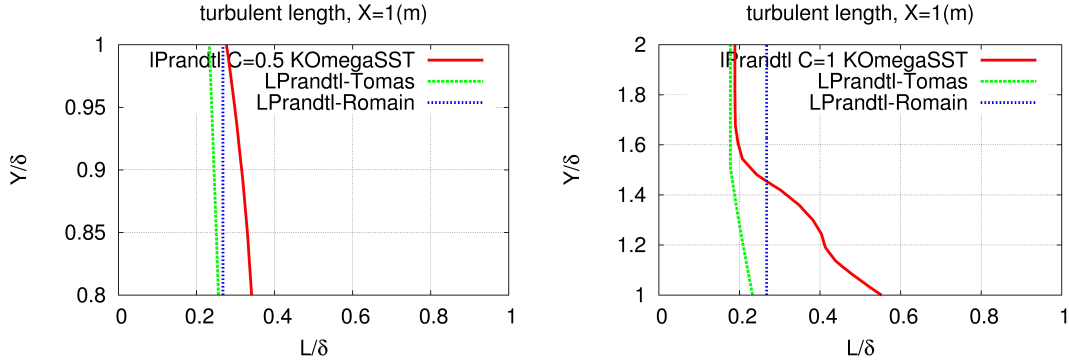
Figure 3: Comparison of turbulent length scales L obtained from k-ω-SST-model and empirical estimations for outer part of the boundary layer $y/\delta > 0.8$

manoeuvering conditions. Ship resistance, resistance components and unsteady velocities in the propeller disk are calculated and compared with each other and with measurements. The ship model has the following parameters $L \times B \times T = 5.5172(m) \times 1(m) \times 0.3586(m)$. Computational domain is a box of $25.4567(m) \times 15.92(m) \times 8.3(m)$. Numerical simulations were carried out using three grids, the first layer of the first grid (Grid 1=7-mln cells) was at $y^+ = 6$ from the wall with a sufficient refinement in the propeller disc. In the second grid (Grid 2=11 mln cells) the cells in the boundary layer and in the propeller disc were finer and the first layer was at $y^+ = 2.6$ from the wall. The latest grid (Grid 3=13 mln cells) is the finest among all both in the boundary layer and in propeller disc. The first layer in the boundary layer has the thickness ($y^+ = 1.6$). The resistance and resistance components obtained using grid-1, grid-2 and grid-3 and DDES, IDDES and hybrid model are presented in the table 1. For hybrid model the agreement with measurement for the resistance components and the resistance coefficient becomes better when the grid resolution increases. The opposite tendency was stated for *DES approaches. In hybrid calculations the pressure resistance is always slightly overestimated than this from KRISO estimations. However, the total resistance coefficient agrees well with measurements.

The most important discovery in hybrid model calculations is the observation of the velocity field fluctuations in the wake of the KVLCC2 tanker at straight course which have not been taken into account in modern engineering methods yet. These fluctuations are presented in the history of the axial

Table 1: Results of the resistance prediction using different methods. C_R is the nondimensional resistance coefficients, C_P is the pressure resistance and C_F is the friction resistance in Newton.

	Total resistance coefficient C_R	Pressure resistance(N)	Friction resistance(N)
Grid-1-KVLCC2 tanker at straight course			
KRISO EXP.	4.11×10^{-3}	2.92 (ITTC estimation)	15.28 (ITTC estimation)
DDES	4.44×10^{-3}	2.72	16.92
IDDES	4.52×10^{-3}	2.74	17.22
Hybrid	3.71×10^{-3}	3.21	13.16
Grid-2-KVLCC2 tanker at straight course			
DDES	4.64×10^{-3}	2.89	17.65
IDDES	4.73×10^{-3}	2.95	17.98
Hybrid	4.23×10^{-3}	5.00	13.73
Grid-3-KVLCC2 tanker at straight course			
DDES	4.83×10^{-3}	3.19	18.73
IDDES	4.93×10^{-3}	3.30	19.11
Hybrid	4.14×10^{-3}	4.20	14.63
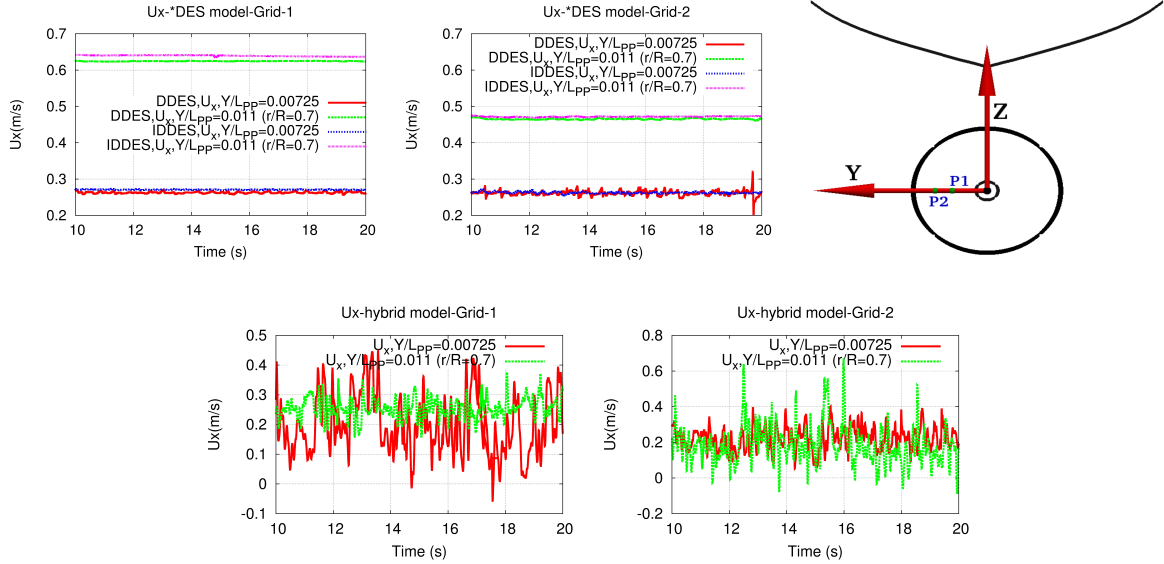
Figure 4: History of U_x at points 1 and 2 in the unsteady wake of KVLCC2 tanker at straight course

velocity at points (P1) ($Y/L_{PP} = 0.00725, r/R = 0.5$) and (P2) ($Y/L_{PP} = 0.011, r/R = 0.7$) (see Fig.4). Particalirly, the velocity at the point (P2) oscillates from 0.15 to 0.35 m/s in grid 1 computations and from -0.1 to 0.65 m/s in grid 2 computations. Fig. 4 illustrates that the results of *DES calculations do not have any fluctuations at these points, and this certainly contradicts to reality. For comparison, the time averaged velocity gained from KRISO measurements was 0.25 at the point (P1) and 0.39 at the point (P2). The influence of the grid resolution on the velocity fluctuations is now being studied further. Fig. 5 shows the history of the axial velocity at manoeuvering conditions (drift angle is 16°, and yaw rate $\Omega = 0.275$). As seen from this Figure the DDES model produces small fluctuations at the point (P1), whereas there is no fluctuations at the point (P2). On the contrary, the hybrid model produces fluctuations at both point.

Through the above, it can be noted that in contrast to other methods the hybrid method [1] reproduces the strong unsteadiness of the wake. *DES family failed to predict the unsteadiness of the wake in particular for the ship at straight course.
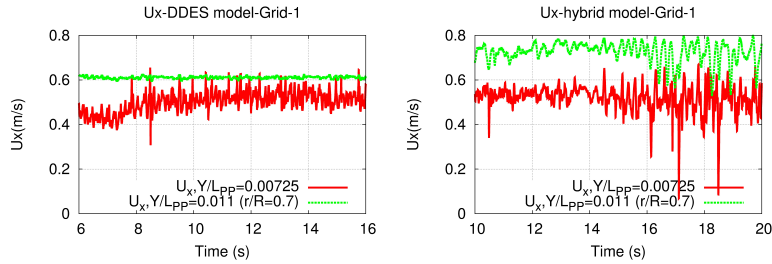
Figure 5: History of U_x at points (P1) and (P2) in the unsteady wake of KVLCC2 tanker at manoeuvering conditions

Conclusion

In this paper we presented some new validation results for the hybrid method [1] based on the combination of the LES dynamic Smagorinsky SGS model (DSM) with k-ω SST-URANS approach. Switching between LES and URANS regions is performed automatically depending on the ratio of the integral length scale L and the grid cell size Δ. For the zero gradient turbulent boundary layer it was shown that the formula of Kolmogorov Prandtl for the integral length scale L, which is applied for the determination of LES-URANS interface in the hybrid model, is valid if the coefficient C is chosen depending on the distance from the wall. It is recommended to use the value $C = 1.0$ for the outer part of the boundary layer and wake flow. The method is applied to the calculation of the resistance components, resistance coefficient and the unsteady wake flow of the tanker KVLCC2. The hybrid model provides good results for the resistance in particular with fine grid and predicts the fluctuations of the wake flow which cannot be captured using other modern hybrid *DES methods at least at grid resolutions used in this paper. Simulations show that the instantaneous velocities in the wake can deviate sufficiently from the mean values which usually are used for hull-propeller interaction. Neglecting this fact can negatively influence the accuracy of the propulsion and unsteady loads prediction, which are now being studied for KVLCC2 tanker at straight course and at manoevering conditions.

References

[1] Kornev, N., Taranov, A., Shchukin, E., & Kleinsorge, L. (2011). "Development of hybrid URANS-LES methods for flow simulation in the ship stern area." Ocean Engineering, 38(16), 1831-1838.

[2] Kornev, N., Taranov, A., Shchukin, E., Springer, J., Palm, M. and Batrak, Y. (2012) "Development, application and validation of hybrid URANS-LES methods for flow simulation in the ship stern area." 29th Symposium on Naval Hydrodynamics, Gothenburg, Sweden, 26 - 31 August 2012.

[3] Schlichting, H., and Gersten, K. (2000). "Boundary-layer theory." Springer Verlag.

[4] Tomas, S., Eiff, O., and Masson, V. (2009). "Experimental study of the turbulent structure of a boundary layer developing over a rough surface." 19éme Congrés Francais de Mécanique.

[5] Thomas, Russell, H., Joesph, A., Schetz, and Dominique, H., Pelletier. (1991). "Three-dimensional finite element method analysis of turbulent flow over self-propelled slender bodies." Journal of Propulsion and Power 7.2, 281-287.

[6] Laraufie, R.,and Deck, S. (2013). "Assessment of Reynolds stresses tensor reconstruction methods for synthetic turbulent inflow conditions. Application to hybrid RANS/LES methods." International Journal of Heat and Fluid Flow 42, 68-78.

[7] Rodi, W. (1975). "A note on the empirical constant in the Kolmogorov-Prandtl eddy-viscosity expression." ASME Transactions Journal of Fluids Engineering 97, 386-389.

[8] Pamiès, M., Weiss, P.-E., Garnier, E., Deck, S., Sagaut, P. (2009). "Generation of synthetic turbulent inflow data for large eddy simulation of spatially evolving wall-bounded flows." Physics of Fluids 21, 045103.

Wave Height Measurement and Numerical Analysis of Flow around Rounded Wedges by the Moving Particle Simulation Method

Jun Arai, Naval Systems Research Center, Ministry of Defense, araijun@cs.trdi.mod.go.jp

1. Background

Prediction of free-surface waves around a ship bow is quite important to reduce the noise generated by bow wave breaking. However, it is a very difficult phenomenon because of its nonlinearity or unsteadiness. Theoretical studies on bow wave were done by Ogilvie [1], Standing [2] or Miyata et al [3]. Miyata suggested free-surface shockwave (FSSW) and surveyed non-linearity of bow wave. They pointed out that non-linear CFD calculations were necessary to analyze breaking waves resulting from FSSW in detail. Recently, Waniewski et al. [4] measured overturning waves around wedges, and Noblesse et al [5] suggested empirical formula for the maximum wave height and the crest position based on the past experimental results including Waniewski's. There are some studies about CFD analysis of breaking waves around ships. Sato et al [6] estimated resistance force of a model ship involving bow wave breaking by the Finite Volume solver. Splashes were not predicted because of the insufficient grid resolution in their calculations. A study on numerical analysis of spray around a high speed ship was done by Akimoto et al [7]. Spray from a simple column model was calculated by the gridless MPS (Moving Particle Simulation or Moving Particle Semi-implicit) method. In this study, basic validation of the MPS method for overturning waves around rounded wedges is conducted. We compared calculation results with the wave height measurement results from towing tank experiments.
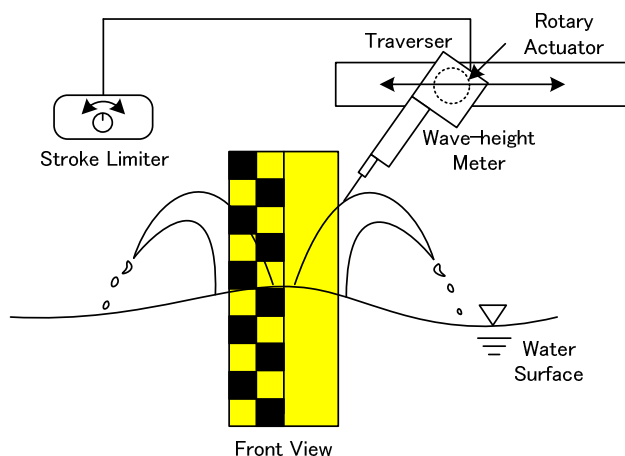
Fig.1 Wave-height measurement equipment   Fig.2 Influence of the stroke limiter
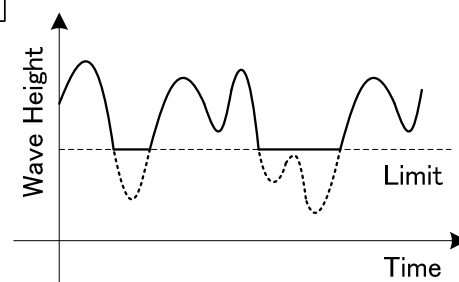
2. Experimental Apparatus

Fig.1 shows the measurement equipment. The angle and span-wise position of a wave-height meter are controlled by rotary and linear actuators to measure the wave-height near the model body. The

range of the wave-height meter is limited by a stroke limiter to prevent the probe from penetrating over turning wave and colliding with the model. Note that each measured data takes only lager values than the arbitrary threshold set by the limiter as shown in Fig.2. Therefore, the median value is used as a substitute for the mean value. The standard deviation is also estimated by using the median value and measured values lager than the median.

3. Calculation Condition

In this study, we use the Moving Particle Simulation (MPS) method [8] which is one of particle methods. This method can easily treat large surface deformation including the breakup or coalescence of fluid without numerical diffusion, since no numerical grid is necessary in the particle methods. In addition to the original MPS method, the polygon wall model [9], the surface tension model [10] and the pressure stabilization similar to Kondo's method [11] are incorporated. Fig.3 shows the rounded wedge we calculated and measured. The model has length L_{pp}=1006 mm, L_{pa},=337 mm, width B_m=320 mm, height D_m=600 mm, entrance angle α_E=20°, tip diameter 100 mm and draft T = 250 mm.
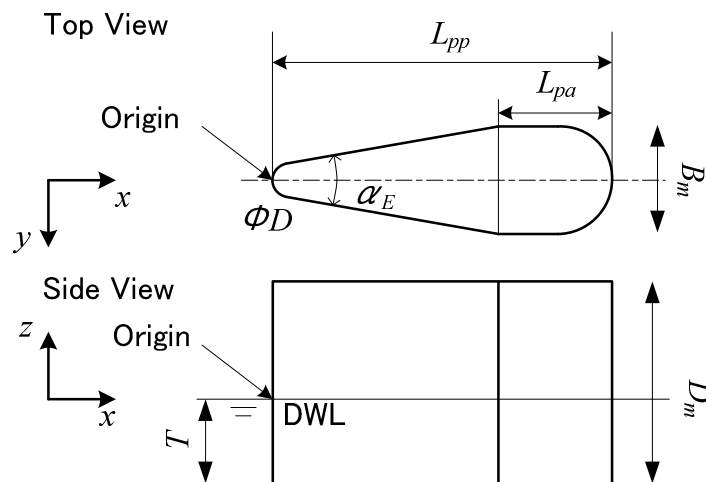
Fig.3 Rounded wedge model
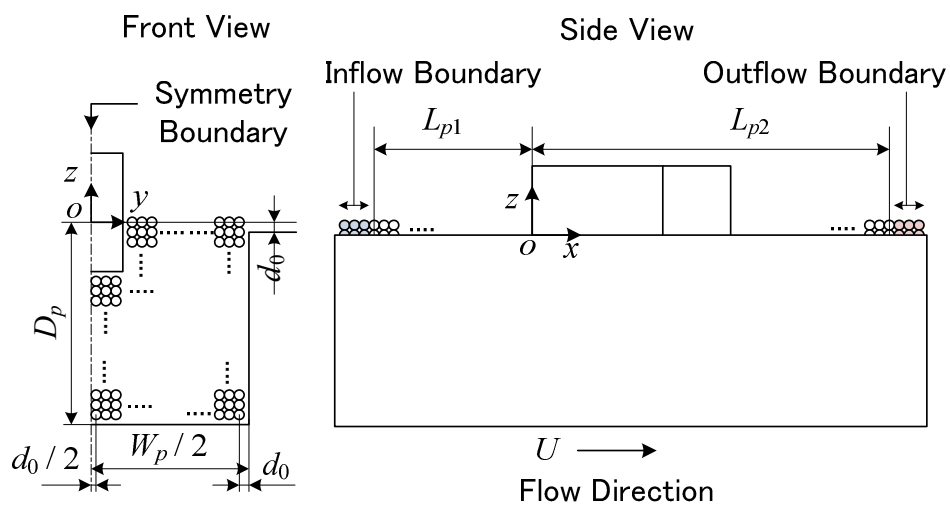
Fig.4 Calculation region

Fig.4 shows the computational domain. The distance from inflow boundary to model is L_{p1}=2000 mm, distance to outflow boundary L_{p2}=3000 mm, depth D_p=1000 mm, width W_p=2012.5 mm. The average particle distance or particle size is 12.5 mm and the number of particles is about 2.6 millions. The blockage effect to the wave height is about 4.1% at velocity U = 2.5 m/s, estimating by Tamura's method [12].

4. Experimental Results

A time series of wave height at a fixed point is shown in Fig.5. It shows quasi-steady state behavior and its standard deviation is 4.2 mm.
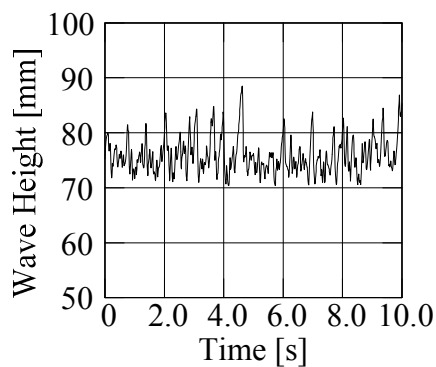
(a) Wave height
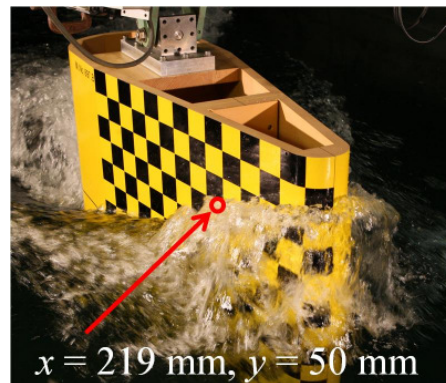
(b) Measurement location

Fig.5 Time series of wave height at x = 219 mm, y = 50 mm, U = 2.5 m/s

Figs.6 to 8 present wave height distributions at U = 2.0, 2.2, 2.5 m/s, respectively. Error bars in these figures indicate the standard deviation in 10 s measurement. Horizontal error bars appear because of the rotation angle of the wave height meter.
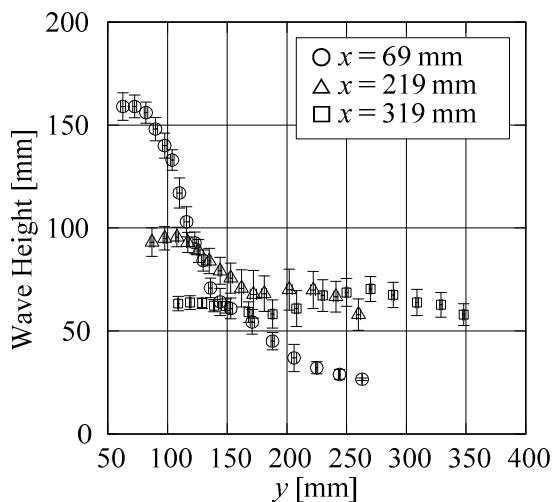
Fig.6 Wave height distribution: U = 2.0 m/s
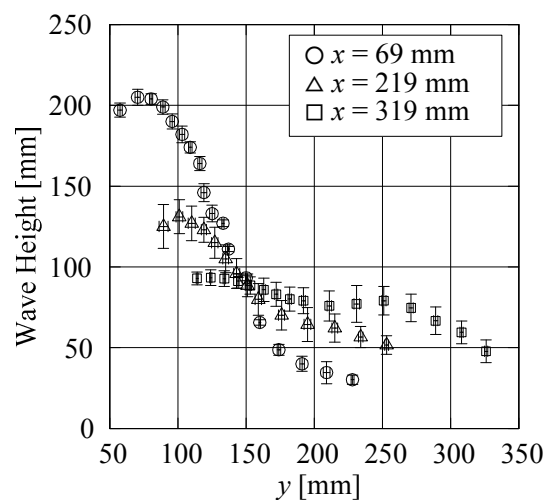
Fig.7 Wave height distribution: U = 2.2 m/s
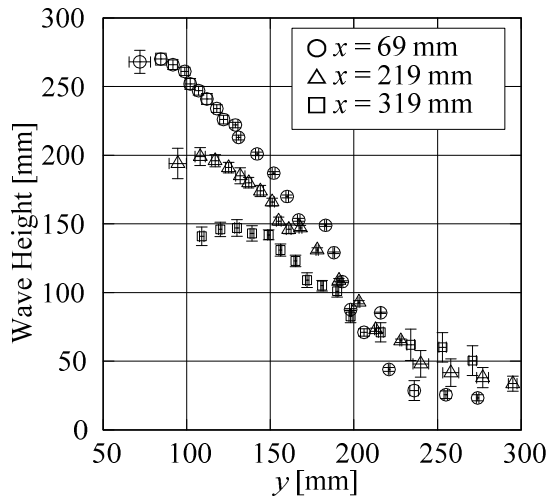
Fig.8 Wave height distribution: U = 2.5 m/s

5. Calculation Results

Breaking waves occur at model tip and water surface goes down after the model in Fig.9. In the section views, overturning waves moving on to the front and side are calculated qualitatively.
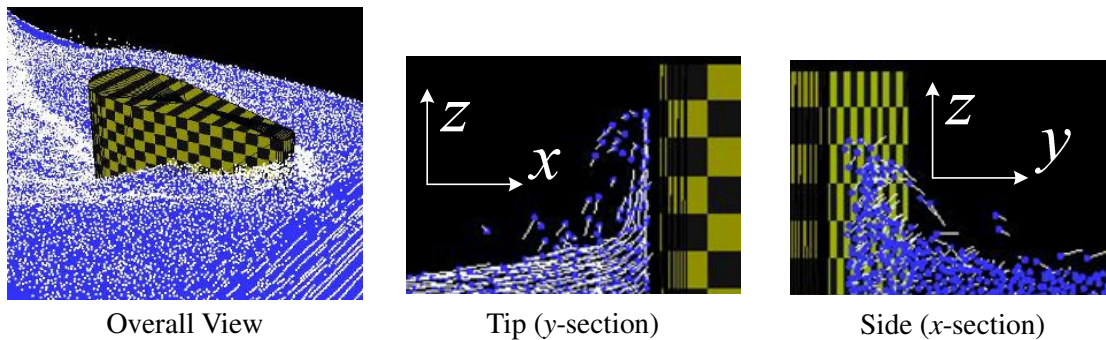
Overall View   Tip (*y*-section)   Side (*x*-section)

Fig.9 Calculation result at 4.2 s
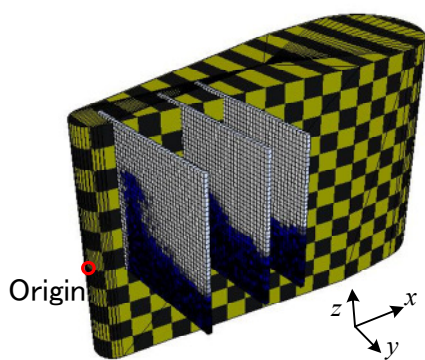
Fig.10 Grids for calculating particle's probability
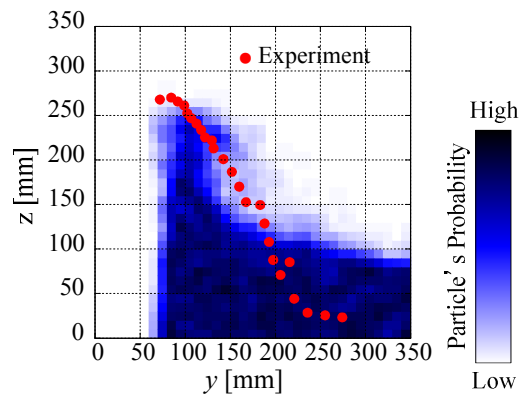
Fig.11 Probability distribution at x = 69 mm
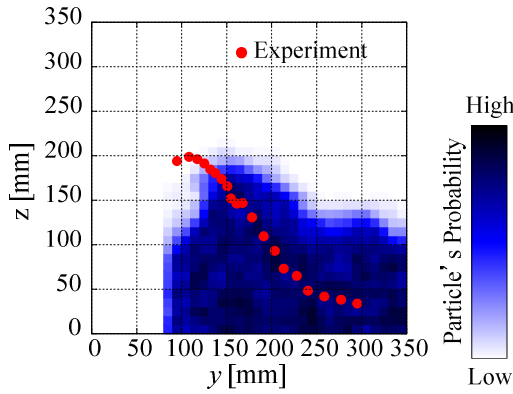
Fig.12 Probability distribution at $x = 219$ mm
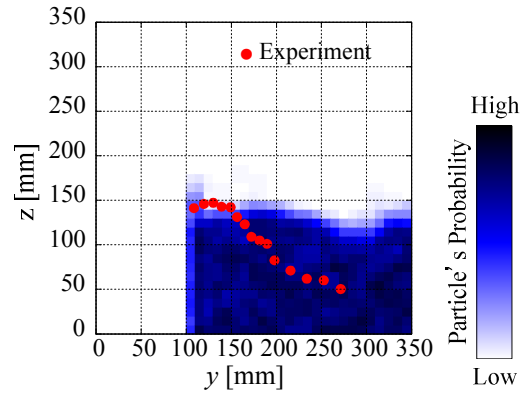
Fig.13 Probability distribution at $x = 319$ mm

Numerical and experimental results are compared quantitatively by calculating particle's probability distributions at each section in Figs.10 to 13. Each section is partitioned by 10 mm square grids and particles in each grid are counted and averaged to get probability distributions as shown in Fig.10. For the wave height distribution near the model, the calculation result moderately agrees with the experimental result in Fig.11. In Figs.12 and 13, calculated wave distributions are not so steep as the experimental results and separate earlier. In addition, water surface elevates more than experimental results in the distant regions for all sections. Further consideration is needed for the size of the calculation region or calculation resolution.

6. Conclusions

Wave height measurements and the MPS calculation of rounded wedges were conducted in this study. Wave height distributions of overturning waves at the model tip were successfully measured by the raked wave height meter. The MPS could simulate the over turning wave qualitatively and wave height distributions near the model moderately agreed with experimental result. However, water surface elevates more than experimental results in the distant regions. As a future study, we will conduct larger scale calculations for higher resolution and larger region by using the variable resolution model, the overset particle method [13] and so on.

References

[1] Ogilvie, T. F., "The Wave Generated by a Fine Ship Bow", 9th Symp. on Naval Hydrodynamics, 1972, pp.1483-1525.

[2] Standing, R. G., "Phase and Amplitude Discrepancies in the Surface Wave due to a Wedge-ended Hull Form", J. Fluid Mechanics, Vol.62, 1974, pp.625-642.

[3] Miyata, H., Inui, T. and Kajitani, H., "Free Surface Shock Waves around Ships and Their Effects on Ship Resistance", J. Society of Naval Architects of Japan, Vol.147, 1980, pp.324-325.

[4] Waniewski, T. A., Brennen, C. E. and Raichlen, F., "Bow Wave Dynamics", J. Ship Research, Vol.46, 2002, pp.1-15.

[5] Noblesse, F., Delhommeau, G., Guilbaud, M., Hendrix, D. and Yang, C., "Simple Analytical

Relations for Ship Bow Waves", J. Fluid Mechanics, Vol.600, 2008, pp.105-132.

[6] Sato, Y., Hino, T. and Hinatsu, M., "Estimation of Ship Resistance with Wave-breaking at the Bow by CFD", Preprints 4th Annual Meeting of NMRI, 2004, pp.163-166. (in Japanese)

[7] Akimoto, H., Iida, K. and Kub, S., "Numerical Simulation of the Flow around a Planing Wedged Cylinder by a Particle Method", J. Society of Naval Architects of Japan, Vol.196, 2004, pp.81-89. (in Japanese)

[8] Koshizuka, S. and Oka, Y., "Moving-Particle Semi Implicit Method for Fragmentation of Incompressible Fluid", Nuclear Science and Engineering, Vol.123, 1996, pp.421-434.

[9] Harada, T., Koshizuka, S. and Shimazaki, K., "Improvement of Wall Boundary Calculation Model for MPS Method", Trans. JSCES, Paper No.20080006, 2008. (in Japanese)

[10] Kondo, M., Koshizuka, S. and Takimoto, M., "Surface Tension Model using Inter-particle Potential Force in Moving Particle Semi-implicit Method", Trans. JSCES, Paper No.20070021, 2007. (in Japanese)

[11] Kondo, M. and Koshizuka, S., "Suppressing the Numerical Oscillations in Moving Particle Semi-implicit method", Trans. JSCES, Paper No.20080015, 2008. (in Japanese)

[12] Tamura, K. , "Study on the Blockage Correction", J. Society of Naval Architects of Japan, Vol.131, 1972, pp.17-28.

[13] Shibata, K., Koshizuka, S., Tamai, T. and Murozono, K., "Overlapping Particle Technique and Application to Green Water on Deck", 2nd Int. Conf. Violent Flows, 2012, pp.106-111

Effect of Turbulence Closure on the Simulation of the Cavitating Flow on the Delft Twist11 Foil.

Abolfazl Asnaghi, Andreas Feymark, Rickard E Bensow

Department of Shipping and Marine Technology, Chalmers University of Technology, Gothenburg, Sweden
abolfazl.asnaghi@chalmers.se, andreas.feymark@chalmers.se, rickard.bensow@chalmers.se

In this paper, we test and evaluate different approaches of turbulence closures for the simulation of unsteady sheet cavitation. At the workshop on cavitating flows in connection with the 2nd international symposium on cavitation, Bensow (2011) showed results for RANS, DES, and implicit LES, and some peculiarities regarding the behaviour of the RANS and DES models were detected, especially in combination with the *ad hoc* correction by Reboud (3rd International Symposium on Cavitation, 1998) which is frequently used in connection with RANS modelling of cavitating flows. These effects will be further explored in the final abstract. As part of this, another set of turbulence closure will be tested, as the Spalart-Almaras RANS model used for the RANS simulation in (Bensow, 2011) has also in other papers, e.g. Eskilsson and Bensow (29th Symposium on Naval Hydrodynamics, 2012), not giving as good results as has been published using other models.

Fluid Structure Interaction Analyses
of Tidal Turbines

Joseph Banks, Kutalmis Bercin, Thomas P. Lloyd, Stephen R. Turnock

Faculty of Engineering and the Environment, University of Southampton, Southampton, SO17 1BJ. UK.

E-mail: {J.Banks; K.Bercin; T.P.Lloyd; S.R.Turnock}@soton.ac.uk

I. INTRODUCTION

Horizontal axis tidal turbines (HATTs) must provide reliable electrical energy production in a subsea environment with minimal maintenance. Failures related to turbine blades will have a significant impact on their overall cost-effectiveness. The use of composite blades for such devices offers mass and cost savings [1], [2], however to fully utilise this benefit blades have to be designed to be more flexible than traditional blades. Hence it is important that the fluid structure interaction (FSI) of the blades is well understood. In its simplest form this allows the performance of a turbine blade to be assessed in it deformed state. Composite materials also create the possibility of blades that deform into different optimised shapes for different load conditions [2]. This could maximise the turbine efficiency over a broader range of the tidal cycle. To achieve this the interaction between the fluid loading and the structural response needs to be considered within the design process.

HATTs operate in a highly unsteady environment due to large fluctuating velocities caused by the oceanic turbulent boundary layer. This results in a dynamic interaction of the hydrodynamic blade loading and its structural response with implications for the assessment of device efficiency and through-life fatigue loading. The coupling of a stochastic flow regime with flapwise and twist deformations of the blade requires fully coupled hydrodynamic and structural simulation of the blade to deal with the inherent non-linearities.

Turbine blade modelling methods are essentially made of three components: hydrodynamics of the flow regime around and through the machine; structural dynamics of the blades and the interaction of these two mechanisms [3]. Hydrodynamic loading applied to the blade can be assessed using a number of methods, such as BEM, actuator line and CFD methods. Similarly, a number of approaches can be used to assess the structural response of the blades. These include bean modal decomposition (beam theory), multi-body and finite element methods. Coupling the hydrodynamic and structural solutions can be achieved in an iterative manner (two-way), where the fluid and structural convergence simultaneously, or quasi-steady (one-way), where the converged fluid loadings are applied to the structural model.

Computational cost increases for higher fidelity simulations. Hence the size of the problem in terms of number of grid cells and time steps required influences the choice of simulation approach. For example, BEM theory can be used to represent turbine arrays inside a CFD simulation [4]. More recently a beam theory structural solver has been included into this method allowing both static and dynamic structural deformations to gust loading to be analysed [3]. This approach allows dynamic simulations of fluid structure interactions of devices in an efficient way; however as only the blade twist in included in the assessment of the deformed blades' performance this will come at the expense of physics fidelity. In contrast detailed simulations of the hydrodynamic loading on a tidal turbine in a turbulent flow have been performed using large eddy simulation (LES) [5]. This comes at a considerable computational cost ($\sim 10^4$ CPU hours). If this type of simulation was directly coupled with a finite element analysis of the dynamic structural response the computational cost would likely triple based on the fully coupled analysis of a flapping foil presented in [6]. High fidelity simulations provide the opportunity to assess the limitations and accuracy of simpler, more efficient methods.

This paper aims to take the high fidelity fluid loading obtained in [5] and apply a static structural response using the beam theory adopted by [3]. The same test case is also simulated using the coupled BEM-beam theory approach. This allows the impact of flapwise deflections and fluid solver fidelity to be assessed on the fluid structure analysis of the thrust and power produced by a flexible bladed device.

II. FSI METHODOLOGY

In this section we outline the computational methodology adopted. Figure 1 shows a flowchart depicting procedure, which involves three computational models: a finite volume fluid dynamics code; a BEM theory code; and an analytical beam theory model. These components are described individually next. A key consideration is that we only consider quasi-static blade deflection in both the LES and BEM approaches. Note that the BEM approach can also be used to assess dynamic FSI [3], although this is not included here.

A. Finite volume method

Simulations were carried out using the OpenFOAM® 2.1.0 libraries, augmented by custom solvers and boundary conditions. Full details of the solver settings are
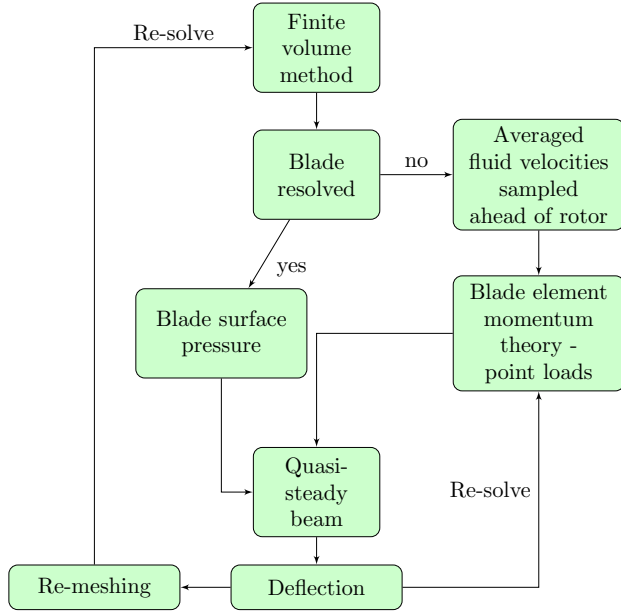
Fig. 1. Flowchart describing fluid structure interaction assessment procedure.

provided by [3] and [5]. When the turbine blades are resolved, the simulation is fully unsteady; that is, rotation is included using a dynamic mesh procedure, with a cylinder surrounding the turbine. Fluxes are interpolated between the grid regions using an *arbitrary mesh interface*. Where OpenFOAM is used to provide velocity data to the BEM code, no explicit rotation is included. Both the filtered (LES) and unsteady Reynolds-averaged (URANS) governing equations are solved, depending on the simulation. LES is used to resolve turbulence. This allows spectra of turbine performance to be derived, based on stochastic fluid loading. The URANS equations can represent low wavenumber unsteady effects, such as low frequency gust, but model the turbulence spectrum.

B. BEM theory code

The modified BEM code was *Cwind*, developed by [7]. The code has been written into C++ for easier integration with OpenFOAM. Improvements to the original code are detailed in [3]. BEM theory is used to estimate the forces exerted on a specified blade geometry. The theory combines momentum theory (i.e. the actuator disk theory) and blade element analysis. The former represents the blade swept area as an infinitely thin disc which alters the axial and tangential momentum of fluid particles passing through. The latter divides the blade into a number of non-interacting sections and estimates forces generated by using its aerodynamic force coefficients for its relative velocity inflow.

Such methods have been used by [8] to investigate the possible differences between the loading prediction capabilities of a sectional BEMT model and a finite element model that maps pressure distribution over an identical

wind turbine blade, showing negligible difference with respect to the deflection results.

C. Structural modelling

It is Baumgart's [9] assertion that slender solid body modelling, such as for a tidal turbine blade, with a beam model captures the essential features in comparison to a more complex solid or shell - finite element model. In addition, as is claimed in [10], as far as the mechanical features of a three-dimensional blade can be extracted, a one-dimensional beam model can cope with most structural examinations in a prompt way.

BEM theory and LES provides hydrodynamic loading at discrete locations along the blade span that are located at the centre of each segment. A linear structure is considered for simplicity; therefore, each deflection is computed separately and then summed using superposition. Flapwise and edgewise static deformations are computed as

$$v(x) = -Fx^2(3s - x)/6EI \qquad 0 \le x \le s \qquad \text{(1a)}$$

and

$$v(x) = -Fs^2(3x - s)/6EI \qquad s < x \le x_{tip} \qquad \text{(1b)}$$

where x is the location where the deflection is monitored on the beam neutral axis $[m]$, s is the location where point loads is applied $[m]$, $v(x)$ is the deflection $[m]$, F is the force in the direction of deflection [N], E is Young's modulus of the blade element material $[Nm^{-2}]$, I is the area moment of inertia of the blade element's cross section $[m^4]$.

Torsional deflections are computed as

$$\gamma(x) = Mx/GJ \qquad 0 \le x \le s \qquad \text{(2a)}$$

and

$$\gamma(x) = \gamma(s) \qquad s < x \le x_{tip} \qquad \text{(2b)}$$

where $\gamma(x)$ is the angle of twist relative to the undeformed configuration $[rad]$, M is the twisting moment [Nm], G is the shear modulus of the material $[Nm^{-2}]$ and J is the polar moment of inertia of the relevant section $[m^4]$. The structural properties of the blade were based on a uniform rectangular beam section, matching the blade thickness and 50 % of the blade chord (at a span location of 70 % of the rotor radius). The blade material was chosen as aluminium, with a Young's Modulus of 70 GPa.

D. Re-meshing

When the blades are resolved in the fluid computation, the corrected turbine performance based on the deflected blade shape is desired. To achieve this, the sectional flapwise, edgewise and torsional deflections are applied to morph the blade geometry file. Morphing is achieved using the in-house *adaptFlexi* tool. The new blade shape is then used to re-mesh the fluid domain. This is relatively simple when using the *snappyHexMesh* utility. The fluid problem is then re-solved to derive adjusted thrust and power coefficients.

III. TEST CASE DESCRIPTION

A. Experimental data

The simulated turbine is a model scale device that has been previously tested by [11]. Key parameters are given in Table I.

TABLE I
TEST CASE PARTICULARS.

Symbol	Meaning	Value
R	Rotor radius	$0.4\ m$
B	Number of blades	3
U_0	Mean freestream velocity	$1.4\ ms^{-1}$
Ω	Rotational velocity	$20.68\ rads^{-1}$
TSR	Tip speed ratio	5.96
θ_{hub}	Hub twist angle	$15°$

The tip speed ratio is defined as $TSR = \Omega R/U_0$. For this case, the turbine thrust and power coefficients are $C_T = 2T/\rho AU_0^2 = 1$ and $C_P = 2\Omega Q/\rho AU_0^3 = 0.36$. Here, T is thrust [$kgms^{-2}$], Q torque [kgm^2s^{-2}], ρ_0 the fluid density [$1000\ kgm^{-3}$] and A [m^2] the rotor projected area. The turbine was tested in low turbulence facilities, and hence the results reported here are not directly comparable. The experimental C_T and C_P are used primarily to assess the quality of the simulation grid. It should be noted that introducing inflow turbulence in the numerical simulation has little effect ($< 1\%$) on the mean thrust and power coefficients [12]. A larger effect is observed for the root mean square of these quantities.

B. Domain design

Since the experimental data have been corrected for tunnel blockage effects, an unbounded domain is used for the simulations. The domain has overall dimensions $L_x \times L_y \times L_z = 10D \times 6D \times 6D$, where x,y and z are the streamwise, vertical and horizontal directions (see Figure 2). The inlet is located $3D$ upstream of the turbine rotor plane, which is centred at the domain origin. A cylindrical rotating region of dimensions $L_x \times R = 0.5\ m \times 0.5\ m$ centred at the domain origin encompasses the turbine rotor. Full details of the LES simulations and grid are provided in [5].

Since the grid is not wall-resolved ($y_1^+ \approx 30$), a wall function is used for the subgrid viscosity. y_1^+ is the non-dimensional first cell height based on the friction velocity and kinematic viscosity, and is a measure of how well the viscous sublayer is resolved. Although we were able to generate a wall-resolved ($y_1^+ = 1$) grid, the smaller time step required proved prohibitive in achieving a converged solution within a reasonable computational time. The implication of this modelling assumption will be assessed in the following Sections.

IV. RIGID BLADE RESULTS

Mean performance measures for the two numerical approaches are compared to the experimental values in
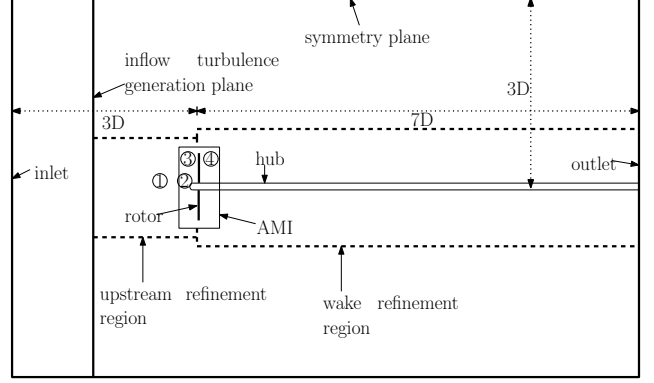
Fig. 2. Schematic representation of simulated case domain.

Table II. Due to the computational efficiency advantage of the BEM code, this method has been used to assess the turbine performance for a range of tip speeds. This data is presented in Figures 3 and 4. Table II reveals some differences between the LES and BEM methods. The thrust coefficient derived from LES is closer to the experimental value than the BEM. However, the power coefficient predicted by BEM is in very good agreement with the experiment. The LES value is $\sim 19\%$ over-predicted. This effect has been attributed to the wall function approach used in the LES, which does not capture separation well; the BEM is based on aerofoil lift and drag data, and therefore includes separation, despite the lower fidelity of this approach.

TABLE II
MEAN EXPERIMENTAL AND NUMERICAL INTEGRAL PERFORMANCE
MEASURES.

Coeff.	Exp.	BEM	LES (rigid)	LES (deformed)
$\overline{C}_T$	1.0	0.86	0.98	0.73
$\overline{C}_P$	0.36	0.37	0.43	0.22

Whilst the LES is not suited to providing every data point in Figure 3, it can be used to analyse the time-dependent behaviour of the turbine performance. Samples of the thrust and power coefficients are provided in Figure 6. Large fluctuations in the time traces are evident; these effects cannot be captured by the BEM code.

V. DEFORMED BLADE RESULTS

The deformed blade shape was calculated using the method outlined in Figure 1, using the mean surface pressure derived from the rigid LES case. Figure 5 shows the deformed shape, where the tip deflection is $\sim 0.035\ m$, or $\sim 9\ \%$ of the turbine radius. Both the edgewise and twist deformations were negligible.

Figures 3 and 4 depict the thrust and power using the quasi-steady beam theory model, coupled with BEM for the full scale turbine presented in [3]. It is evident that FSI effects become more prominent at higher TSRs. The BEM approach allows a rapid assessment of static and dynamic FSI effects (see [3]), however as only the effects of twist
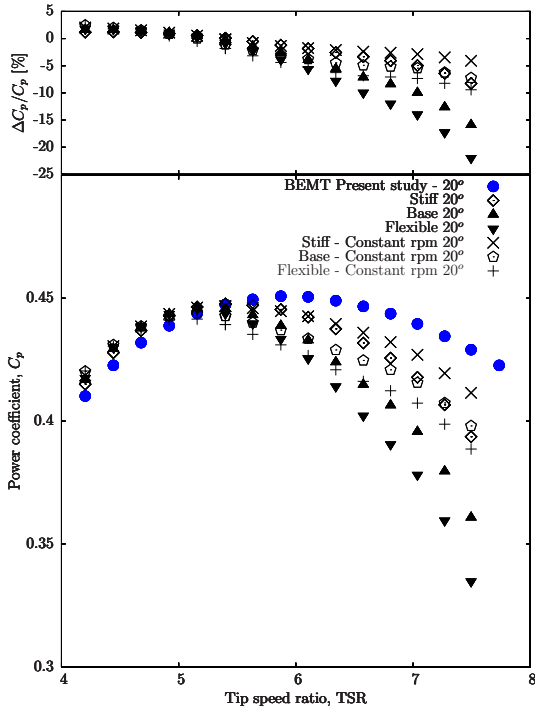
Fig. 3. Power coefficient against tip speed ratio using BEM code. Results shown for both rigid and flexible blades.
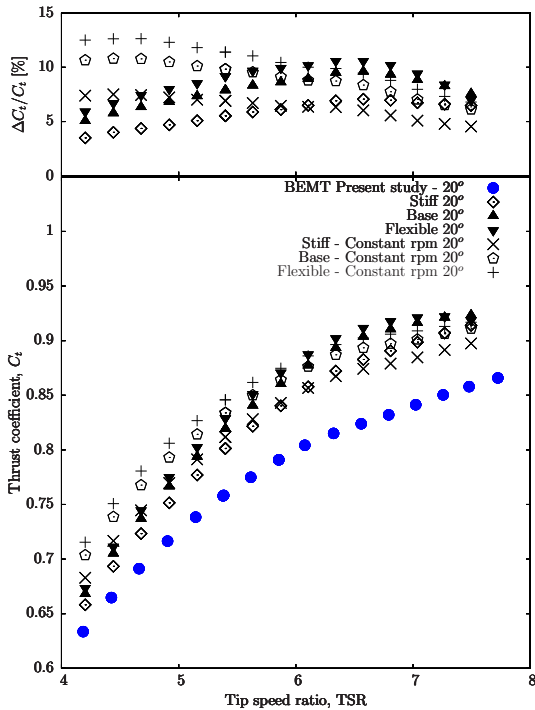
Fig. 4. Thrust coefficient against tip speed ratio using BEM code. Results shown for both rigid and flexible blades.

(a) side   (b) end
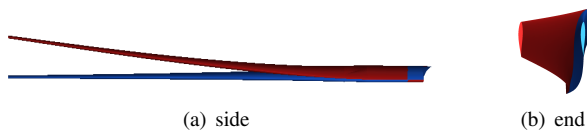
Fig. 5. Deformed blade shape: rigid (blue); deformed (red).

are currently included in the BEM analysis the significant flap-wise deformation observed in Figure 5 could not be assessed.

rigid (A) ———   deformed (B) ------
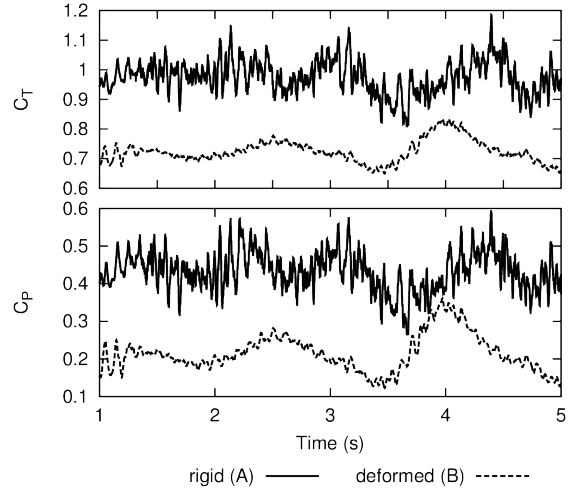
Fig. 6. Time history of turbine thrust and power coefficients derived using LES.

A reduction in power coefficient for a deformed wind turbine blade was also seen by [13]. The authors predicted flapwise deflections similar to those used here. The effect on turbine power was seen to be dependent on TSR, an indication that flow separation is an important effect. For a full scale device ($R = 64\ m$), a reduction in power of $\sim 14\%$ is seen for a TSR of 6, but not at TSR = 5.

The LES of the deformed blade geometry revealed a significant decrease in both the thrust and Torque (see Table II). This reduction in the mean values can also be seen in the time history trace in Figure 6. Both the rigid and deformed blade simulations display a similar low frequency fluctuation caused by the turbulent eddies passing through the rotor. However there is a noticeable difference in the high frequency fluctuations; this may be due to an increased amount of upwinding introduced in the deformed case, in order to ensure stability. The reduction in power and thrust for the deformed blade can be seen in the pressure distribution at key blade sections down the blade presented in Figure 7. The pressure coefficient is defined as

$$\overline{C}_{pr} = \frac{2\overline{p}}{\rho_0(U_0^2 + \Omega^2 r^2)}. \tag{3}$$

The reduced magnitude of the pressure difference over the deformed blade reveals a reduction in the blade's performance. Reduced lift would contribute to a reduction in thrust, while increased drag serves to lower the power. This indicates that the operating condition of the blade has been altered by the significant flapwise deformation. The main cause of the performance reduction can be identified as a significant increase in separation along the blade, depicted in Figure 8. The difference between the rigid and deformed cases is easily observed on the blade suction side. There is some separation in the rigid case, but this is restricted to the root area, where the blade geometry has
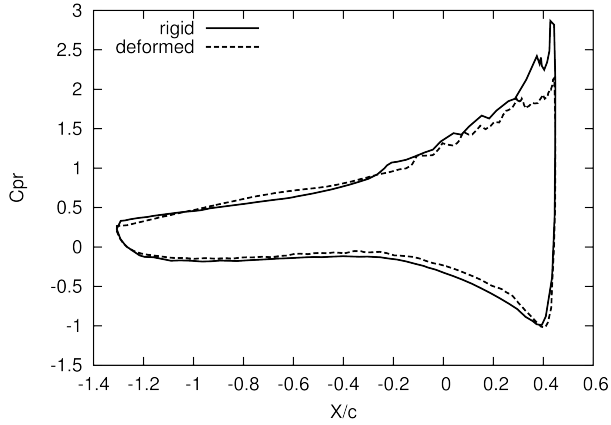
(a) $r/R = 0.35$
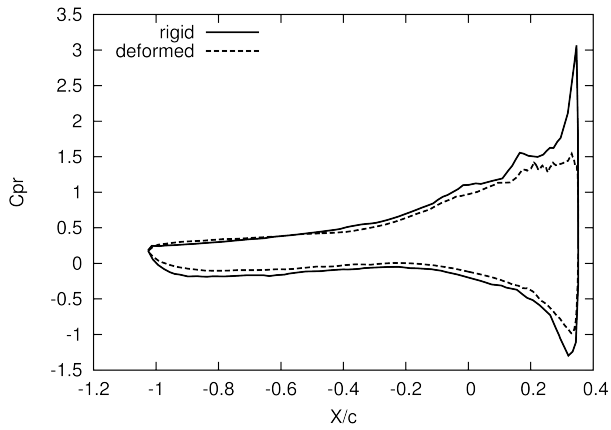
(b) $r/R = 0.6$
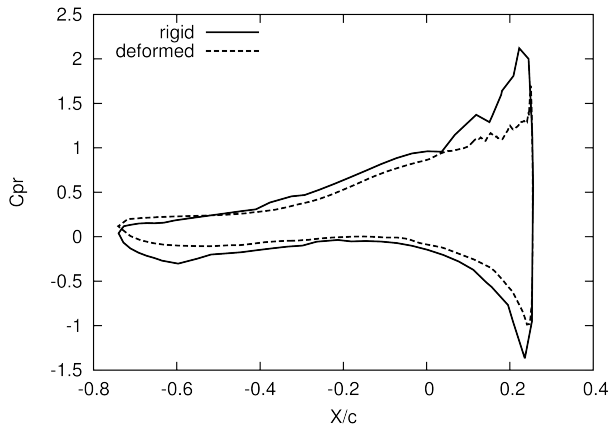
(c) $r/R = 0.85$

Fig. 7. Surface pressure coefficient at three spanwise locations.

(a) Rigid   (b) deformed

(c) Rigid   (d) deformed

Fig. 8. Limiting surface streamlines for rigid and deformed blades: pressure side (top); suction side (bottom).

been simplified. Hence this is not expected to contribute significantly to the turbine power. For the deformed case, the separated region extends along the span almost up to the tip.

The flow pattern revealed in Figure 8 is elucidated by examining the radial velocity. In Figure 9, the blade is aligned with the z axis. It is evident that flow in the separated region is towards the blade tip. This phenomenon is expected to directly contribute to the large reduction

in mean power between the rigid and deformed cases, as well as the change in mean thrust.

VI. CONCLUSIONS

A comparison between two computational approaches for FSI of tidal turbines has been made: one based on LES; the other on BEM. The results presented concern a quasi-static methodology, where a deformed blade ge-
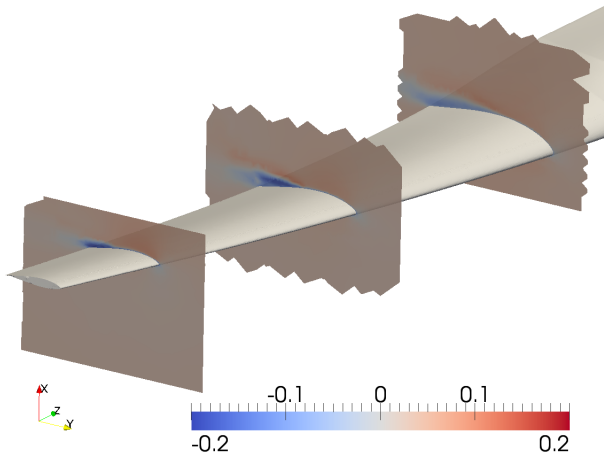
Fig. 9. Slices of mean radial velocity at $r/R = 0.35$, 0.6 and 0.85.

ometry is derived using mean blade loads and a beam theory structural model. This new geometry is then re-meshed and updated performance assessments made using LES. For the chosen case, the hydrodynamic loads are seen to induce minimal twist and edgewise deflection, but large flapwise deflection. The effects of flapwise deflection on performance are not included in BEM. The LES approach offers the ability to investigate this effect, which has not been widely addressed in the literature. A large reduction in power coefficient was observed for the deformed case. This has been linked to increased separation on the deformed blade, which extends over the majority of the blade span. Therefore it is concluded that flapwise deflections can significantly alter the operating condition of a turbine blade and should be included into a FSI BEM analysis.

VII. ACKNOWLEDGEMENTS

REFERENCES

[1] R. F. Nicholls-Lee and S. R. Turnock, "Enhancing performance of a horizontal axis tidal turbine using adaptive blades," in *OCEANS 2007 - Europe*, USA, 2007, pp. 1–6.

[2] R. F. Nicholls-Lee, S. R. Turnock, and S. W. Boyd, "Application of bend-twist coupled blades for horizontal axis tidal turbines," *Renewable Energy*, vol. 50, pp. 541 – 550, 2013.

[3] K. Bercin, T. Lloyd, Z.-T. Xie, and S. R. Turnock, "Efficient method for analysing fluid-structure interaction of horizontal axis tidal turbine blades," in *Proceedings of the 10th European Wave and Tidal Energy Conference*, 2nd-5th September, Aalborg (to appear), 2013.

[4] S. R. Turnock, A. B. Phillips, J. Banks, and R. Nicholls-Lee, "Modelling tidal current turbine wakes using a coupled rans-bemt approach as a tool for analysing power capture of arrays of turbines," *Ocean Engineering*, vol. 38, no. 11-12, pp. 1300 – 1307, 2011.

[5] T. Lloyd, S. R. Turnock, and V. Humphrey, "Computation of inflow turbulence noise of a tidal turbine," in *Proceedings of the 10th European Wave and Tidal Energy Conference*, 2nd-5th September, Aalborg (to appear), 2013.

[6] A. Feymark, "A large eddy simulation based fluid-structure interaction methodology with application in hydroelasticity," Ph.D. thesis, Chalmers University of Technology, 2013.

[7] M. Barnsley and J. Wellicome, "Dynamic models of wind turbines aerodynamic model development," the Commission of the European Communities Directorate, Tech. Rep. JOUR 0110, 1993.

[8] T. J. Knill, "The application of aeroelastic analysis output load distributions to finite element models of wind," *Wind Engineering*, vol. 29, no. 2, pp. 153–168, 2005.

[9] A. Baumgart, "A mathematical model for wind turbine blades," *Journal of Sound and Vibration*, vol. 251, no. 1, pp. 1 – 12, 2002.

[10] D. J. Malcolm and D. L. Laird, "Modeling of blades as equivalent beams for aeroelastic analysis," in *2003 ASME Wind Energy Symposium AIAA/ASME*, Reno, USA, 2003, pp. 293–303.

[11] A. S. Bahaj, A. F. Molland, J. R. Chaplin, and W. Batten, "Power and thrust measurements of marine current turbines under various hydrodynamic flow conditions in a cavitation tunnel and a towing tank," *Renewable Energy*, vol. 32, no. 3, pp. 407–426, Mar. 2007.

[12] I. Afgan, J. Mcnaughton, D. Apsley, S. Rolfo, and T. Stallard, "Large-eddy simulation of a 3-bladed horizontal axis tidal stream turbine: comparisons to RANS and experiments," in *Proceedings of the 7th International Symposium on Turbulence, Heat and Mass Transfer*, 24th-27th September, Palermo, 2012, pp. 1–13.

[13] D.-h. Kim and Y.-h. Kim, "Performance Prediction of a 5MW Wind Turbine Blade Considering Aeroelastic Effect," *World Academy of Science, Engineering and Technology*, vol. 57, pp. 771–775, 2011.

Wave impact with air entrapped in shallow water sloshing flow.

Andrea Bardazzi[(1,3)]**, Claudio Lugni**[(1),(2)]**, Giorgio Graziani**[(3)]
(1) CNR-INSEAN, Rome/Italy (2) AMOS-NTNU, Trondheim/Norway
(3) DIMA-Univ. Roma 'Sapienza, Roma
bardazzi.andrea@gmail.com, claudio.lugni@cnr.it

INTRODUCTION

LNG carriers with prismatic membrane tanks are more exposed than other carriers to violent sloshing phenomena resulting large impact loads [1]. Because of the large and clean tanks used in LNG ship, low filling depth conditions are of concern for the maximum loads occurring on the walls.
Further, the tank size causes natural sloshing periods in the same range of those due to large ship motions. Then violent impacts may happen, for example in low filling conditions, when a travelling bore or an incipient breaking wave approaching the wall may characterize the sloshing flow inside the tank [2], [3], [4]. Here an experimental investigation is presented to study the role of the hydroelasticity during the evolution of a slamming event with air-entrapment. Will be evaluated the stress distribution along a deformable aluminium plate inserted in a rigid vertical wall of a two-dimensional sloshing tank, to characterize the features of the local loads. The shape and the structural properties of the deformable plate, have been fixed in order to reproduce the lowest wet natural frequency of a prototype panel typically used in a Mark III containment system [1]. The geometric and Froude scaling have been satisfied. Because of the influence of the Euler's and Cavitation's number on the maximum impact pressure the ullage pressure P_u, inside the tank, is moved from the atmospheric value to one close at water's vapour pressure at atmospheric temperature.

THE EXPERIMENTAL SET-UP

The experimental set-up is the same used in [5], [6] for the hydroelastic tests during the evolution of a flip-through event. A 2D Plexiglas tank (LxHxB = 1 m x 1 m x 0.1 m) reinforced with steel and aluminium structures allows to perform tests in depressurized conditions(see fig. 1) The filling depth considered is $h/L = 0.122$. The aluminium elastic plate has been inserted in an extremely rigid stainless steel wall, its lowest end is located 13 cm above the bottom of the tank. Two extrema of the plate are clamped to the steel frame, while the other two are free. In this way, assuming a two-dimensional evolution of the hydrodynamics load, a double-clamped beam behaviour is realized. A small steel's box (see fig. 1), directly linked to the main tank, ensures the same air pressure on the two face of the elastic plate for any ullage pressure. The box has been designed to avoid the influence of the acoustic waves on the structural load along the elastic beam. The ullage pressure is regulated by a vacuum pump. For the measurement of the strain of the structure, 5 strain gauges have been mounted along the vertical centreline of the aluminium plate (see fig. 1). To verify the dynamic behaviour of the strain gauges, their signals have been compared with the ones of two miniaturized accelerometers, temporarily mounted, close to a pair of strain gauges. Two differential pressure probes along the rigid vertical wall, below the elastic plate, were also applied. A second set-up has been developed to reproduce the same case studied in the hydroelastic test on a rigid wall, measuring the pressure distribution along the wall. The thin "hydroelastic plate" has been replaced with a rigid, 20 mm tick, aluminium plate. At the same position of the strain gauges, 5 pressure transducer have been installed on the new plate. An accelerometer has been used to check the rigidity of the plate as

well as the global motion of the tank. Accelerometer, strain gauges and pressure probes have been recorded with a sample rate of 50 kHz. One digital high-speed camera (5 kHz), pointed toward the impact position, provides the view of the formation and evolution of the air-cavity. The global sloshing flow was recorded by 2 digital camera (100 Hz). A common reference signal allowed for the synchronism between flow images and analog signals of the transducers. An absolute pressure transducer measured the ullage pressure inside the tank.

Finally, the hexapod system 'MISTRAL' (made by Symetrie) forced a pure sinusoidal sway motion of the tank with a period of T_m =1.6 s.

PHYSICAL INVESTIGATION

Based on the results of the previous investigation [7], the different volume of the air-entrapped during the impact causes a different oscillation frequency of the bubble which decrease with the size of the cavity. To obtain cavity with different size, at the same ullage pressure, the amplitude of the tank motion has been varied, in particular, three different conditions have been considered: *large* Amp=65mm, *medium* Amp=63mm and *small* Amp=615mm. The natural frequency of the air-cavity depends also by the ullage pressure [8], [7]: a decrease of the ullage pressure in the tank implies an increase of the air-cavity size and, as consequence, a decreasing of the natural frequencies. Hydroelasticity matters when the lowest natural frequencies of the air-cavity are comparable with the lowest wet frequencies of the structure. Because the impulsive behaviour of the load at the beginning of the event, also the time scale of the local rise up of the pressure during the first peak have to be monitored [1]. When this time scale is smaller than the highest natural period of the structure, hydroelasticity is excited. Here, we define the time rise as twice the time interval necessary to reach the maximum load value, starting from one half this value. In the following, the observation of these parameters will guide the discussion of the occurrence of the hydroelastic phenomena by varying the ullage pressure of the tank. (**Note** for the figures from (2) to (4). All the figures show: **top left**: image from the fastcam at impact time t=0, **top right**: beam deflection at impact time, **middle right**: time history of normalized stress in the middle of the beam, **left-right bottom**: time history of pressure probe on rigid wall at 35mm from bottom in rigid and hydroelastic test. The blue line refers to a single case
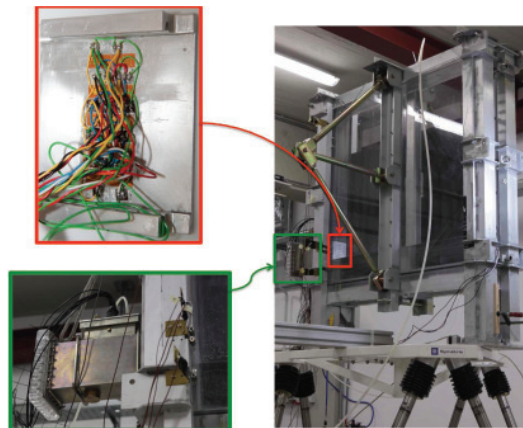
Figure 1: Experimental set-up for the sloshing-tank experiments. Top-left panel: enlarged view of the rear part of the elastic plate with the strain gauges (top panel). Bottom-left panel: enlarged view of the small tank used to ensure the depressurized conditions on the external part of the elastic plate.

shown in the image, the red one refers to the mean value calculated on five repetition of the same run. Error bar representing the corresponding standard deviation). For each cases (A-B-C) are shown the results at P_u= 1000 and 100 mbar).

A: Large air-cavity ($A = 65$ mm)-Fig.(2). By comparing the maximum deformation
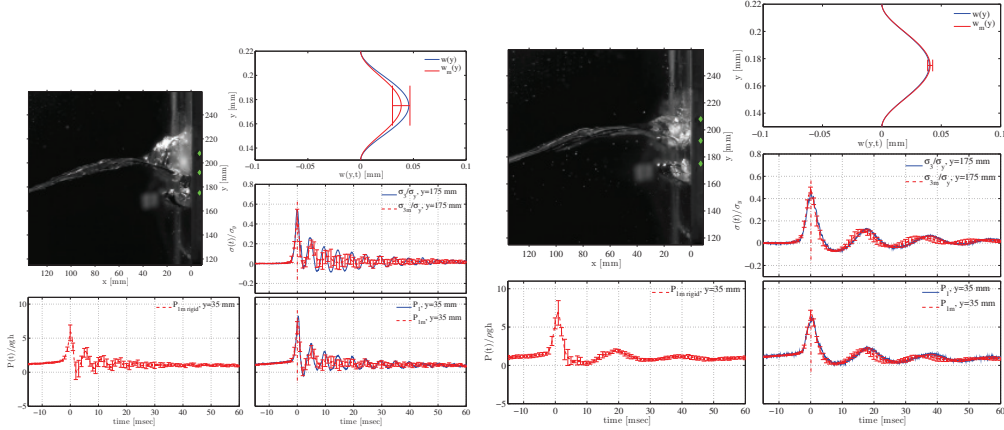
Figure 2: Left: $P_u = 800$ mbar. Right: $P_u = 100$ mbar. See **.

measured at the centre of the elastic plate (see top panel on right), we can observe that this value is almost independent on the ullage pressure. Just at the largest ullage pressure we observed a larger value of the maximum deformation. As expected, this is also confirmed when looking at the maximum stress recorded in the centre of the beam (see middle panel on right). To check the existence of the hydroelastic behaviour, we must look at the rise time characterizing the first load peak. From the stress time history, the time scale of the first peak ranging between approximately 1.5 and 3.5 ms at P_u=800 and 100 mbar, respectively. Note that, at the impact time, for each ullage pressure, the wetted length is approximately the same and equal to $h/L = 0.18$. As a consequence, from [6] the lowest natural frequency of the beam is expected to be approximately equal to 0.55 - 0.65 f_{dry} = 900 - 1000 Hz, with f_{dry} =1580Hz. Previous observation suggest that hydroelasticity is not present during the first load peak at least at the lower ullage pressure. This behaviour is confirmed also by comparing the pressure measured on the elastic and rigid cases: the maximum values are practically the same, even smaller for the elastic case at Pu = 100 mbar. Then, we can conclude that no hydroelasticity occurs during the first load peak at the ullage pressure 100 mbar. At the largest ullage pressure, although a larger value of the peak pressure and of the maximum stress occur, it is difficult to assess a clear hydroelastic behaviour. The successive evolution of the phenomenon is driven by the air-cavity dynamic. In fact, the lowest natural frequency, during the impact evolution, moves from 1000 Hz at impact time to 600 Hz in a fully wet condition, while the oscillation frequency of the bubble is about 200 Hz at P_u=800 mbar. Because the distance between the two frequencies, no hydroelasticity is excited by the air-cavity oscillation. The elastic response is the typical driven response where the structure's motion is characterized by the forcing frequency.

B: Medium air-cavity ($A = 63$ mm)- Fig.(3). In this case, a different behaviour of the first peak of the structural load is observed. As for the case **A**, the rise time is almost constant with the ullage pressure but has a lower value, 1ms and also the natural frequency of the beam at the impact time is always 1000 Hz ($h/L = 0.18$); in this case the two characteristic times are really close each other and the forcing is able to excite the hydroelastic behaviour of the elastic plate, as highlighted by the vibration (around 1kHz) occurring during the first 6 ms and properly emphasized on the time history of the stress at the lowest ullage pressure. As
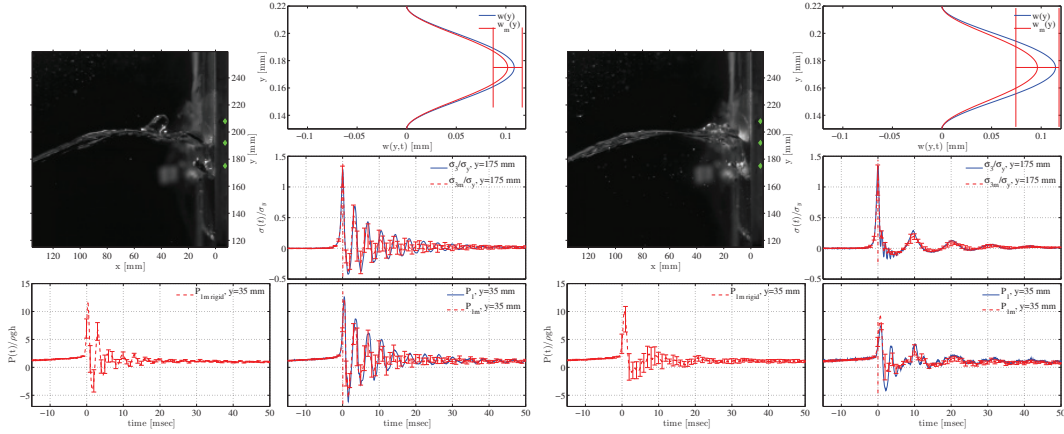
Figure 3: Left: $P_u = 800$ mbar. Right: $P_u = 100$ mbar. See **.

for the rise time, also the maximum peak of the structural load on the beam is ullage pressure (Euler) independent. When hydroelasticity is triggered during the first peak, the pressure signal recorded below the elastic beam did not reach its maximum value at the impact time t=0 s. It is present a slightly shift due to the elastic reaction of the plate which moves against the fluid. This causes an increase of the first (though it is a small increase) and second peak pressure measured in the elastic case relative to the rigid case (bottom panels). A quite evident increase of the absolute value of the first minimum is also observed. This means that, for lower pressure than P_u=100 mbar, cavitation phenomenon may occur. The successive evolution preceded as for the case **A**, the beam's evolution is driven by the bubble's dynamic; this because the bubble frequency (300 Hz at P_u=800 mbar) is still lower then the structural fully wet lowest one (600 Hz).

C: Small air-cavity($A = 615$ mm)-Fig.(4) This case is similar to **B**. The rise time is
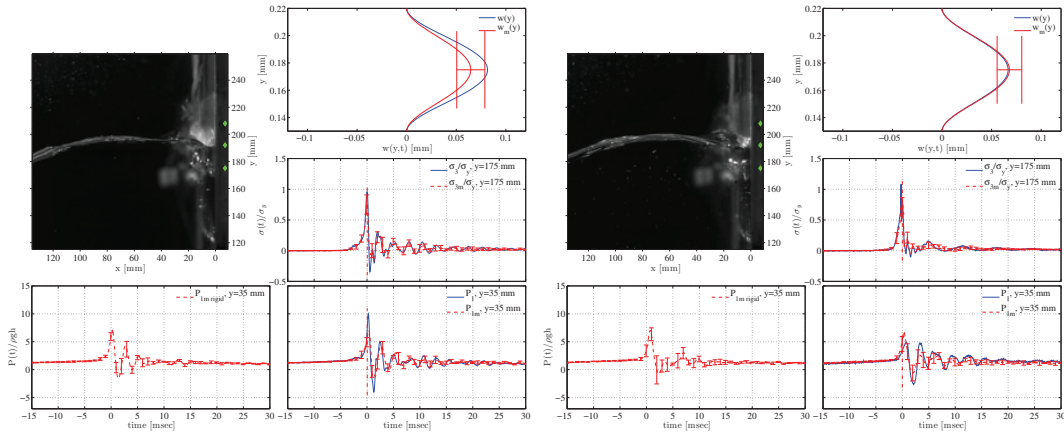
Figure 4: Left: $P_u = 800$ mbar. Right: $P_u = 100$ mbar. See **.

about 1 ms, really close to the first natural period of the structure: hydroelasticity may occur. This observation is further confirmed by the high frequency oscillations occurring just after the maximum load peak (see for example the time history of the stress in figure 11) and by the time shift between the maximum stress on the plate and the maximum pressure below it, as already discussed for the case B. Because the small size of the bubble a higher frequency oscillations,

induced by the compressibility of the air, are expected: this means that hydroelasticity may occur when the beam is fully wet. At P_u=800 mbar, the excitation of the hydroelasticity occurs in the period 6.5ms< t < 13ms. An increase of the instantaneous structural peaks is visible in the right middle panel. This behaviour is further confirmed by the pressure time history below the elastic plate (see bottom-right panel in the same figure). Because the frequency of the oscillating bubble decreases with the ullage pressure, this phenomenon is not triggered at Pu = 100 mbar.

Simplified Structural Model

Usually, in the design stage, two different strategies are used to take in account the liquid-structure interaction: the (a) Direct Dynamic Finite Analysis and the (b) Indirect Dynamic Analysis. The approach (a) solves the unsteady structural problem with the external forcing coming from the rigid pressure distribution measured in the sloshing model tests, while (b) solves the steady structural problem whit the forcing given by the maximum rigid pressure loads measured in the tests. In this last case, a suitable dynamic amplification factor (DAF) has to be taken in account to quantify the dynamic effect. A proper modelling of the added mass term associated with the vibration of the structure is also necessary. Here, following the approach (a), we implemented a dynamic model where the forcing and the instantaneous wetted length of the beam have been measured during the rigid test. The measure of the instantaneous wetted length is fundamental to calculate a more accurate added mass contribution, which changes during the impact evolution. By the eigenfunctions method and modelling the added mass as in [1] (considering only the first natural mode):

$$(M + M_{add}(t))\ddot{W}_1(t) + C\dot{W}_1(t) + KW_1(t) = P_{rig.}(t) \tag{1}$$

where $M_{add}(t)$ and $P_{rig.}(t)$ are known, the damping coefficient has been estimated from the results of the experimental test. The time evolution of (1) is performed with a fourth order Runge-Kutta scheme. The figure (5)) shows the comparison between the numerical and experimental results for the time history of the strain #3 (middle of the beam). The figures show two single cases relative respectively, to the maximum pressure (forcing for numerical test) and strain disribution. The results highlight how the added mass model predicts quite good the wet vibration frequency of the beam and also for the strain, there is a quite satisfactory agreement. However some under/over-estimations are present in the time history. These can be ascribed to: further hydoelastic effects not included in the present model, a damping model not completely adequate and/or, to a forcing term for the numerical scheme that is slightly different from the elastic one. To better estimate the capability of the numerical model, it would be interesting to use a sloshing tank that allows wave impacts on rigid and elastic wall simultaneously. A "numerical" future development will involve the integration of the structural model with an hydrodynamic one for the liquid phase, and with an air model for the gaseous-phase (air-cavity).

CONCLUSIONS

Present research investigation is a preliminary study about the hydroelastic effect in a LNG tank when wave impact events with air entrapment occur. The design of a suitable experimental setup allowed the Froude scaling of the lowest natural frequency of a MarkIII structural panel (in fully wetted condition). The analysis emphasized that hydroelasticity can be triggered in two cases:

   1) during the occurrence of the first structural peak load, when the rise time is smaller than

lcr
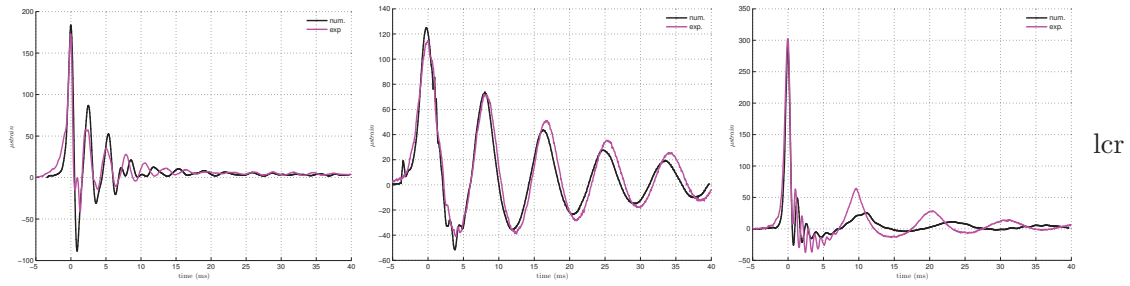
Figure 5: Left: case **C**, $P_u = 800$ mbar; Center:case **A**, $P_u = 400$ mbar; Right: case **B**, $P_u = 100$ mbar.

the lowest wet natural period of the structure;

2) after the complete closure of the air-cavity, during its free-oscillation stage, when the oscillation frequency of the bubble is close to the natural frequency of the structure.

References

[1] Faltinsen, O. M., and Timokha, A. N., 2010. *Sloshing*. Cambridge University Press, Cambridge, UK.

[2] Antuono, M., Bouscasse, B., Colagrossi, A., and C.Lugni, 2012. "Two-dimensional modal method for shallow-water sloshing in rectangular basins". *J. Fluid Mech.,* **700**, pp. 419–440.

[3] Chan, E. S., and Melville, W. K., 1988. "Deep-water plunging wave pressures on a vertical plane wall". *Proc. of the R. Soc. of Lond. A,* **417**, pp. 95–131.

[4] Lugni, C., Brocchini, M., and Faltinsen, O. M., 2006. "Wave impact loads: The role of flip-through". *Physics of Fluids*(18), p. 19.

[5] Bardazzi, A., Lugni, C., Faltinsen, O., Greco, M., Colicchio, G., and Graziani, G., 2012. "Wave-impact in a sloshing tank: hydroelastic challenges". *Proc. IWWWFB, Denmark.*

[6] Bardazzi, A., Lugni, C., Faltinsen, O., and Graziani, G., 2012. "Hydroelastic study of the impact phenomena in sloshing flow". *Hydroelasticity in Marine Technology, Tokyo.*

[7] C.Lugni, M.Brocchini, and Faltinsen, O., 2010. "Evolution of the air cavity during a depressurized wave impact.ii. the dynamic field". *Physics of Fluids*(22), p. 13.

[8] Lugni, C., Miozzi, M., Brocchini, M., and Faltinsen, O. M., 2010. "Evolution of the air cavity during a depressurized wave impact.i. the kinematic flow field". *Physics of Fluids*(22), p. 16.

Simulation of Unsteady Propeller Blade Loads Using OpenFOAM

Rickard E Bensow

Department of Shipping and Marine Technology, Chalmers University of Technology, Gothenburg, Sweden
rickard.bensow@chalmers.se

Unsteady propeller blade loads are important to consider in the design of the propulsion system in order to avoid problems with noise and vibrations. This is normally done through an analysis of the average wake field flowing into the propulsor in order to correctly match the different components of the propulsion system. As computational resources increase, it now starts to become possible to better study the impact on the natural wake flow unsteadiness and how this influences the behaviour of the propeller. This work is a feasibility study to investigate different computational aspects regarding the flow around a propeller operating in a ship wake. The simulations are performed in OpenFOAM 2.2.x using LES, Large Eddy Simulation.The interest concerns both how the sliding mesh implementation in OpenFOAM performs and how large variation in the propeller flow that the resolved transient wake field incurs.

The case studied is a 7000 DWT chemical tanker in model scale with $Lpp = 5.86m$ at the scale factor of $1 : 16.5$. The model is used as a base line vessel in the EU project STREAMLINE and has been designed by CNR-INSEAN, and an extensive experimental and computational database is currently being collected by the partners in STREAMLINE; results have already been presented in e.g. [5, 6]. The simulated conditions presented in this work is for model ship speed of $1.773 \, m/s$, corresponding to $Fn = 0.23$ and $14 \, kn$ in full scale, and with a propeller revolution rate of $8.92 \, rps$. Computations are made for a double body model so the effect of the wavy free surface is neglected; judging from available experimental data this is however a minor approximation at this speed. The simulations are performed with a rudder.

The simulations have been run using an implicit LES approach, where no sub grid model is used for the energy dissipation and instead we rely on numerical diffusion to be a sufficiently good emulation of this process. The reason for choosing implicit LES for these simulations is that we also run the case with a cavitating propeller, and for these flows we have normally used this technique. We have good experiences using this modeling technique for both wetted and cavitating flows, see [2, 1, 4] and the references therein.

The computational domain is a half cylinder of radius 1.5 Lpp which extends one Lpp fore of the bow and two Lpp aft of the transom, see Figure 1. The mesh has been generated using Pointwise® and consists of in total 19.6 M cells split into one cylindrical (rotating) region around the propeller and one region for the rest of the domain, see Table 1 for more information. Around the propeller, a structured boundary layer mesh with hexahedral cells has been created and the propeller cylinder was then filled with tetrahedral elements (interfaced with pyramids). The hull surface is triangulated and cell layers of prisms are then grown into the fluid domain with a smooth transition to tetrahedrals in the interior using the T-rex feature of Pointwise. The mesh is refined in the propeller wake and around the rudder and its wake, see Figure 2. The mesh resolution is decent for a model scale LES, with typical cell sizes in the aft body boundary layer and on the propeller of $(\Delta x^+, \Delta y^+) = (100, 5)$, where Δx^+ represents the longest surface cell edge and Δy^+ the wall normal cell size.

Table 1: Mesh sizes

No cells	All	Hex	Tets	Prisms	Pyramids
Propeller	7,422,464	1,251,760	6,067,816	40300	62,588
Hull	12,203,976	-	6,340,556	5,784,515	78,905
Total	19,626,440	1,251,760	12,408,372	5,824,815	141,493
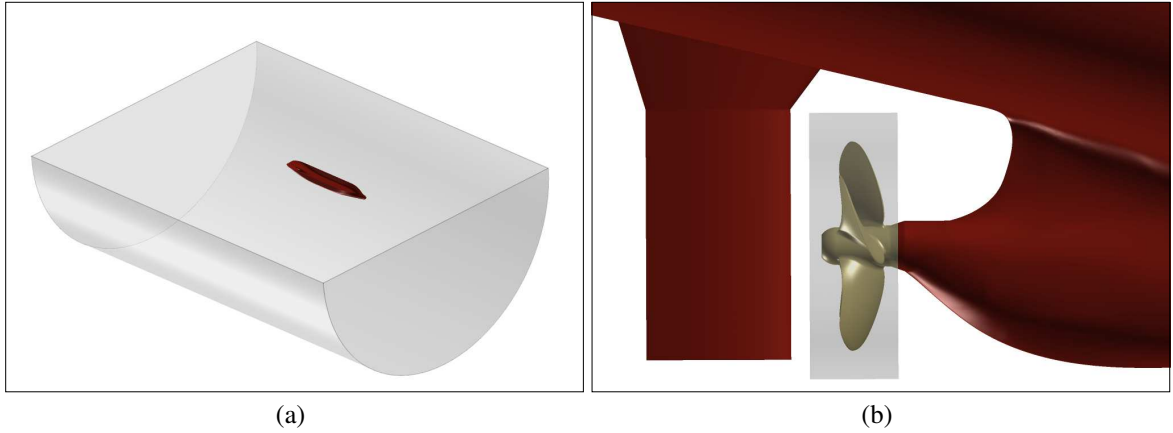
Figure 1: The computational domain in (a) and the location of the sliding grid interfaces in (b).
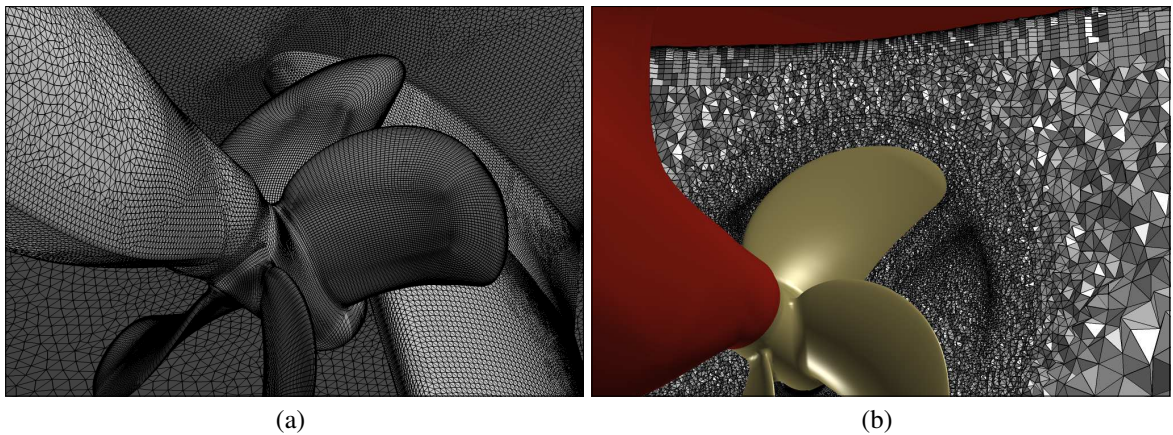
Figure 2: (a) Surface mesh of propeller and aft body, and (b) cut through the refined propeller wake.

The experiences of using the OpenFOAM 2.2.x implementation of sliding grids, based on AMI (Arbitrary Mesh Interface), are in general quite good. No detailed check on continuity or interpolation errors has been performed but in 'eye' norm the primary variables are continuous although some minor disturbance can from time to time be noted, examples can be seen in Figure 4; note that these might also result from post-processing issues across the interface. The speed performance has been measured in two ways, both through a weak scalability study of the open water propeller, using a slightly less dense mesh than in the final simulations summing up to around 3.5 M cells. The case was then run using AMI on 16, 32, and 64 cores, as well as on a single mesh without a sliding interface but where the whole domain was rotated. The results are presented in Table 2, and the conclusion is that the parallel performance is decent and will not cause a major problem thus allowing for large complex problems as reported here.

Table 2: AMI Scalability

Cases	Time ratio
32 cores / 16 cores	1.84
64 cores / 32 cores	1.55
AMI / no AMI	1.1

A general overview visualization of the flow is presented in Figure 3 through an iso-surface of $||\nabla \times \mathbf{v}|| - ||\nabla \mathbf{v}||$; this structure function is a simple to compute approximation to the Q-function. We can here see that substantial flow structures are entering the propeller. Furthermore, the simulation nicely captures the smaller scale vortices in the blade wake that later merges with the tip vortex. In this condition we observe flow separation along the trailing edge of the propeller blades, although not obvious in this particular visualization. We also remark that the tip vortex interaction with the

rudder is well captured and agrees qualitatively with published results on open water propeller/rudder interaction [3], although this will not be further discussed here.
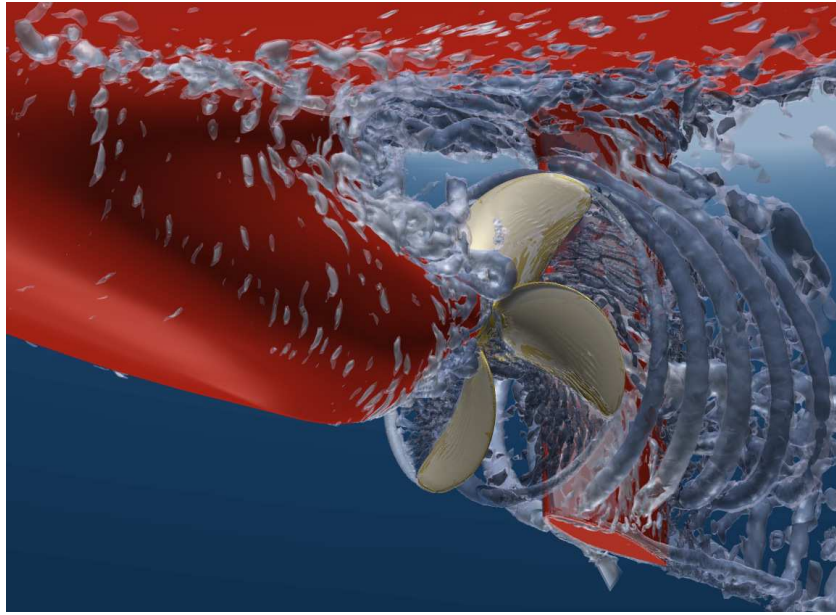
Figure 3: Flow visualisation based on an iso-surface of $||\nabla \times \mathbf{v}|| - ||\nabla \mathbf{v}||$.

| (a) | (b) |
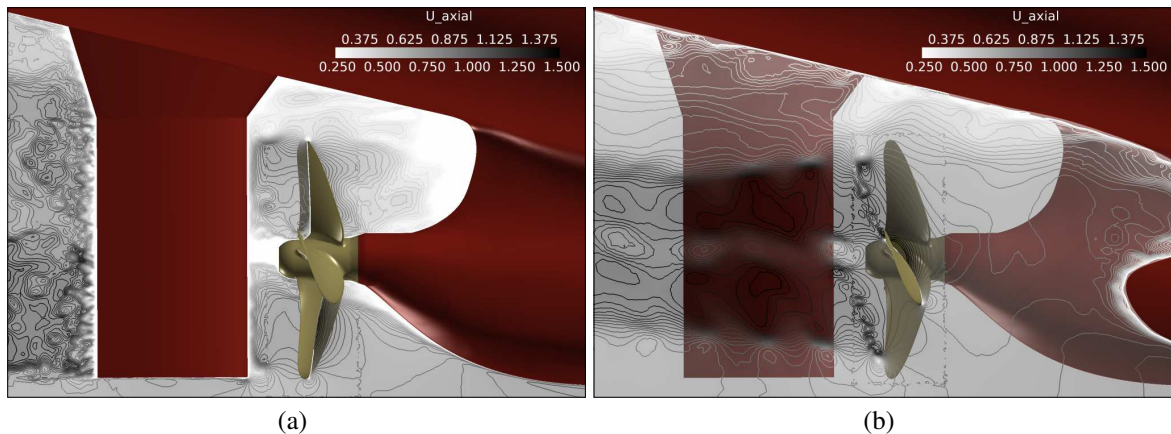
Figure 4: Contours of instantaneous axial velocity in (a) the centre plane and in (b) offset by $R_P/2$, where R_P is the propeller radius.

Wake unsteadiness is visualized in Figure 5, where contours of the instantaneous axial velocity component just upstream of the propeller are shown. Unfortunately, the still snapshots are not sufficient to see the wake behaviour clearly, but from an animation of the full sequence, it's clear that an instantaneous sharp wake peak is always present but moves slowly from side to side of the centre line. This implies that for propeller design with respect to noise and vibrations, a sharp wake velocity deficit should always be considered, and the wider average wake is clearly not relevant. It would be highly interesting to investigate this behaviour in full scale, where the average wake is much thinner.

In Figure 6, the transient propeller thrust is plotted, both for the individual blades (colored lines), the total thrust (divided by four; black line in (a)), and the phase average taken over the plotted revolutions (black line in (b)). Looking at the total thrust, the blade passing frequency is obvious in the thrust variation, but we also clearly see a slower variation that presumably is related to the wake unsteadiness. The deviation from the average is overall quite modest, but a few peaks are noted, as well as occurrences of a phase shift between different revolutions.

The forces presented here are based on a simulation time of six to seven propeller revolutions which is not sufficient to give reliable frequency content information. The simulation is still running in order sample longer times and deepen the analysis. Furthermore, we are also performing simulations on the

same hull with pre-swirl stators mounted in order to get information on how the unsteady blade loads are influenced by such an energy saving device. Finally, also cavitation behaviour simulations are in progress. Unfortunately for this research, however, it has turned out that at relevant conditions this vessel is almost cavitation free, and new conditions need to be identified in order for us to learn more about the feasibility and accuracy of a cavitation simulation in this complex configuration.
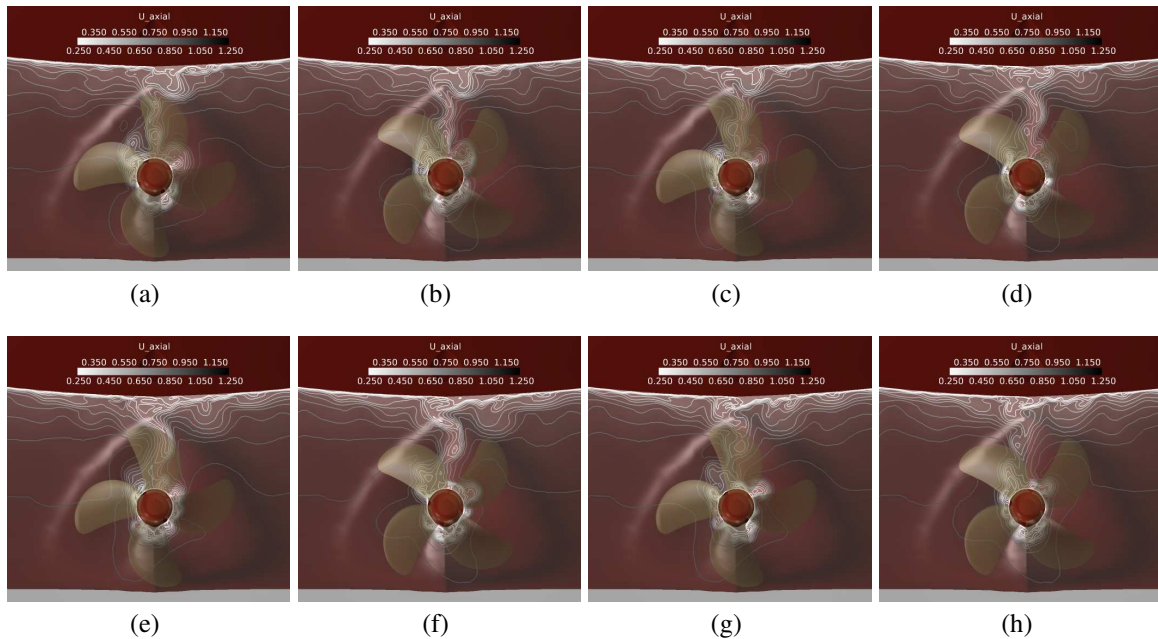
Figure 5: Velocity contours upstream the propeller during one revolution; the time sequence runs row wise from left to right.
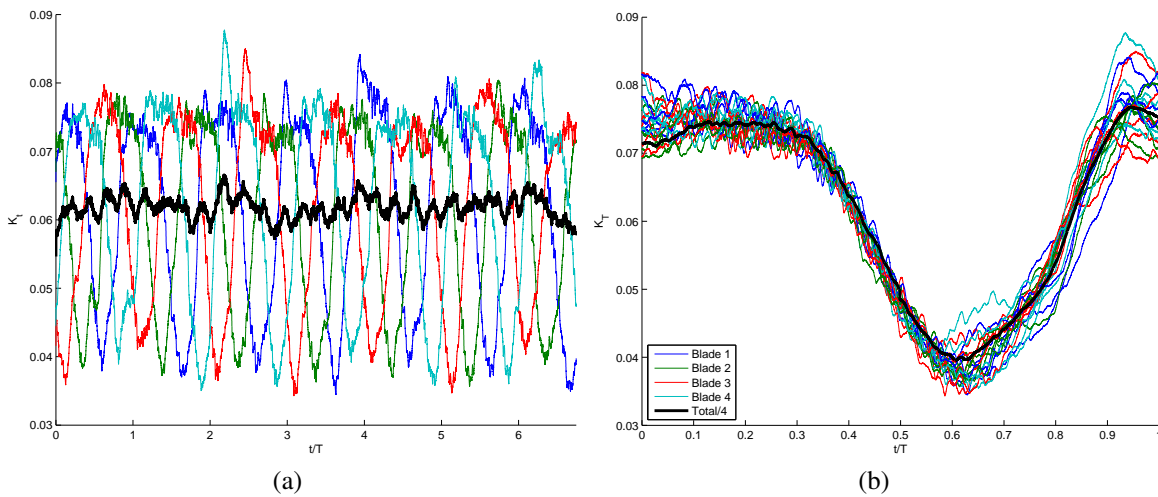
Figure 6: (a) Time series of individual blade thrust and the total thrust (divided by four), and (b) individual blade passages and phase average over one revolution of the previous data.

Acknowledgements

References

[1] R.E. Bensow and G. Bark. Implicit LES prediction of the cavitating flow on a propeller. *J. Fluids Eng.*, 2010.

[2] R.E. Bensow and M. Liefvendahl. Implicit and explicit subgrid modeling in LES applied to a marine propeller. Number AIAA-2008-4144, 2008.

[3] M. Felli and M. Falchi. Propeller tip and hub vortex dynamics in the interaction with a rudder. *Exp Fluids*, 51(5):1385, 2011.

[4] A. Feymark, N. Alin, R.E. Bensow, and C. Fureby. Numerical simulation of an oscillating cylinder using large eddy simulation and implicit large eddy simulation. *J. Fluids Eng. of Fluids Engineering*, 134(3), 2012.

[5] A. Pecoraro, F. Di Felice, M. Felli, F. Salvatore, and M. Viviani. Propeller-hull interaction in a single-screw vessel. Third International Symposium on Marine Propulsors smp'13, Launceston, Tasmania, Australia, May 2013.

[6] A. Van der Ploeg and E.J. Foeth. Optimization of a chemical tanker and propeller with CFD. V International Conference on Computational Methods in Marine Engineering - MARINE2013, Hamburg, May.

Performance of Darrieus Tidal Turbine with and without Transition Model

Pierre-Luc Delafin, François Deniset, Jacques-André Astolfi

IRENav, Ecole navale, Lanveoc, CC 600, 29240 Brest cedex 9, France

pierre-luc.delafin@ecole-navale.fr

Nomenclature

$\lambda = \omega R / U_\infty$ tip speed ratio

$\omega = \mathrm{d}\theta/\mathrm{d}t$ turbine angular velocity [rad/s]

σ=N c/R turbine solidity

θ azimuth angle [°]

AoA_{rel} relative Angle of Attack [°]

c   foil chord [m]

$\mathrm{CP} = \frac{T\omega}{\rho R H U_\infty^3}$ power coefficient

H   turbine height [m]

N   number of blades

R   turbine radius [m]

Re_W relative Reynolds number

T   turbine torque [N.m]

1   Introduction

Marine current turbines currently arouse great enthusiasm since they represent a large market and offer a solution for European governments to reach the renewable energy targets. A lot of technologies exist, most of them being horizontal axis turbines but vertical axis turbines are also developing and are the subject of many papers. Vertical axis turbines have the advantage of being indifferent to the stream direction which is of interest for tidal turbines. Lots of papers dealing with Darrieus turbines study the optimal foil shape, the optimal blade pitch angle, the optimal solidity, etc... with either RANS or LES methods. However, the turbines considered in these studies generally operate at relatively low Reynolds numbers (10^5 - 10^6) while the numerical methods employed are fully turbulent (e.g. k-ω SST turbulence model). The present study, then, aims at evaluating the effect of laminar to turbulent transition on the Darrieus turbine performance.

The turbine studied in this paper was designed at the French naval academy research institute (IRENav) and is part of the SHIVA project which aim is to develop a variable-pitch vertical axis tidal turbine. Momentum streamtube model and CFD calculations have already been performed on other turbines to show the improvement of variable pitch without successfully considering laminar to turbulent transition [8, 9].

First, the geometry, mesh and numerical method are presented, followed by a verification procedure. Then, the $\gamma - \mathrm{Re}_\theta$ transition model of Menter [5] coupled to the k-ω SST turbulence model, already validated for fixed and pitching foils [2], is compared to the fully turbulent k-ω SST turbulence model [7] on three cases: Tip Speed Ratio (λ) = 3 & U_∞=2 m/s, λ=2 & U_∞=2 m/s and λ=3 & U_∞=1 m/s to show the influence of transition for different λ and upstream velocities.

2   Model and numerical methods

2.1   Geometry and mesh

The turbine studied in this paper is a 3-blade vertical axis tidal turbine. A 150 mm chord NACA 0018 fixed at its quarter chord is used for each blade and the turbine diameter is set to 1.6 m. These characteristics correspond to the scale model designed at the IRENav that will soon be tested. The solidity, as defined by Paraschivoiu [10], is N × c / R = 0.56, with N the number of blades, c the chord and R the turbine radius.

The 2D computational domain is divided in three parts: a rotational ring and two stator domains. Figure 1 shows a zoom of the rotational ring surrounded by the stators. The domain extends 3 turbine diameters upstream, 10 diameters downstream and 10 diameters for the total width.

The mesh is created with ICEM CFD so that the y_{max}^+ stays of the order of 1 during the calculations. An O-mesh is created around the foils and expansion ratios are kept below 1.2 in the direction normal to the walls. Each foil is discretized by 350 nodes for calculations with the transition model and 256 nodes for calculations with the fully turbulent model. Figure 2 shows the near foil mesh. The computational domain contains 253,000 (transition model) or 225,000 (fully turbulent model) hexahedral elements.

2.2   Model

The physical model is based on the mass and momentum conservation equations. The fluid is consid-
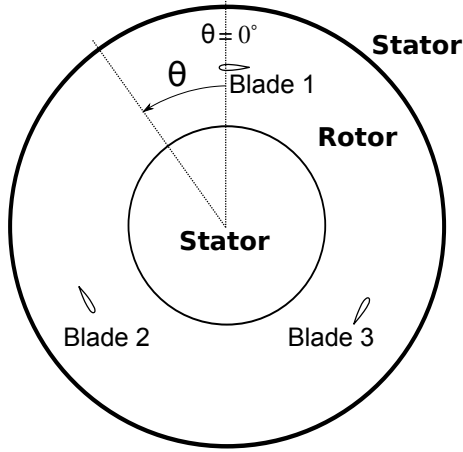
Figure 1: Computational domain showing rotor and stator
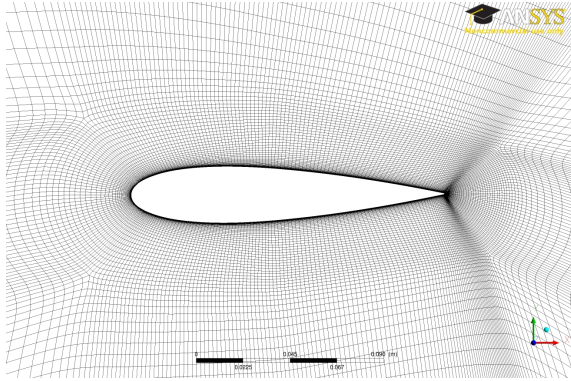
Figure 2: Near foil mesh

ered viscous and incompressible. The $k - \omega\ SST$ closure turbulence model used is known to predict better boundary layers submitted to adverse pressure gradients than other two-equation RANS turbulence models [6]. The turbulence model is coupled with a two transport equations ($\gamma - Re_\theta$) transition model based on experimental correlations [5]. One equation is dedicated to intermittency (γ) which is used to turn on the production term of the turbulent kinetic energy downstream of the transition point.

$$\frac{\partial(\rho\gamma)}{\partial t} + \frac{\partial(\rho U_j \gamma)}{\partial x_j} = P_\gamma - E_\gamma + \frac{\partial}{\partial x_j}[(\mu + \frac{\mu_t}{\sigma_f})\frac{\partial\gamma}{\partial x_j}]$$
(1)

The second transport equation is for transition momentum thickness Reynolds number ($Re_{\theta t}$). This equation transforms non local empirical correlations into local quantities and allows the calculation of the transition length and the critical Reynolds number that are useful for the intermittency calculation.

$$\frac{\partial(\rho\overline{Re_{\theta t}})}{\partial t} + \frac{\partial(\rho U_j \overline{Re_{\theta t}})}{\partial x_j} = P_{\theta t}$$

$$+ \frac{\partial}{\partial x_j}[\sigma_{\theta t}(\mu + \mu_t)\frac{\partial\overline{Re_{\theta t}}}{\partial x_j}] \quad (2)$$

In the paper, calculations carried out with the fully turbulent $k - \omega\ SST$ model will be referred as SST while those carried out with the $k - \omega\ SST$ model coupled with the $\gamma - Re_\theta$ transition model will be referred as SST-TM.

2.3 Boundary conditions

Calculations are carried out in water (density ρ = 997 kg.m^{-3}, kinematic viscosity ν = 0.89 10^{-6} m^2.s^{-1}). Inlet velocity is set to 2 m.s^{-1} which corresponds to a typical towing tank velocity. An *outlet* boundary condition is set on the downstream boundary with a 0 Pa static pressure. Lateral, top and bottom boundaries are set as *symmetry* and blades are set as *wall*. An angular velocity ω, function of the Tip Speed Ratio, is imposed for the rotating ring. Finally interfaces between rotor and stator areas use the General Grid Interface (GGI) method.

2.4 Numerical method

The problem is solved by the finite volumes method [3], using the CFD RANS based code CFX [1]. Continuity and momentum equations transient schemes are *Second order backward Euler* while the turbulent kinetic energy (k) and the turbulent eddy frequency (ω) transient schemes and all advection schemes are taken as *High Resolution*. *High Resolution* is a hybrid scheme between the first and the second order. A blending coefficient ensures a first order where convergence is difficult to provide robustness and a second order where convergence is easier to provide accuracy.

3 Numerical convergence

Grid and time step convergence are discussed on the case λ = 3 & U$_\infty$ = 2 m/s.

3.1 Grid resolution

Grid was designed according to the following rules:

- According to Maître et al. [4], y_{max}^+ values are kept low, very close to one to ensure a y^+ independent solution.
- Foils are discretized by 256 nodes in fully turbulent calculations which is a common discretization, and 350 nodes in transition model calculations to provide an accurate prediction of the transition location.

- Cells sizes in the inner stator range from c/75 to c/30 which is small compared to the foil chords and the vortex diameters.

Calculations have been run for both foils discretizations with the fully turbulent model and showed a difference of only 0.2% on the $\overline{CP}$. Grid can therefore be considered converged.

3.2 Time step

Three time steps, corresponding to $\Delta\theta$=1°, 4° and 8°, are compared to assess convergence in time. Table 1 shows the average power coefficient $\overline{CP}$ obtained after 30 turbine revolutions. $\Delta\theta$=4° leads to a very small decrease of the $\overline{CP}$ (-0.59%) compared to $\Delta\theta$=1° while $\Delta\theta$=8° leads to a slightly higher difference (-1.80%). It should be noted that residual convergence of the case $\Delta\theta$=8° was more difficult than the two others. Results are then converged for a time step lower than $\Delta\theta$=4°. All calculations are run with $\Delta\theta$=1° to ensure converged results despite λ or U_∞ modifications.

$\Delta\theta$ (°)	$\overline{CP}$	Deviation (%)
1	0.557	ref
4	0.554	-0.59
8	0.547	-1.80

Table 1: Average $\overline{CP}$ as a function of $\Delta\theta$, λ=3

4 Results and discussion

Hydrodynamics of a Darrieus turbine is complicated since relative angle of attack (AoA_{rel}) and relative velocity modulus (W) change during a revolution. Velocity triangle applied on one blade gives, in the upstream half of the turbine:

$$W = U_\infty \sqrt{1 + 2\lambda\cos\theta + \lambda^2} \qquad (3)$$

$$AoA_{rel} = \arctan\frac{\sin\theta}{\lambda + \cos\theta} \qquad (4)$$

Equation 3 is used to calculate the relative Reynolds number seen by the blade :

$$Re_W = \frac{W \times c}{\nu} \qquad (5)$$

Equations 4 and 5 are plotted on figures 3 and 4 respectively, for 3 sets of parameters corresponding to the cases studied in this paper:

1. $\lambda = 3$, $U_\infty = 2$ m.s^{-1}
2. $\lambda = 2$, $U_\infty = 2$ m.s^{-1}
3. $\lambda = 3$, $U_\infty = 1$ m.s^{-1}

Case 1 is considered as a reference case with relatively high Reynolds numbers (Fig. 4) and low angles of attack (Fig. 3). Case 2 aims at showing the difference of power output predictions when decreasing λ. Relative angles of attack are higher at $\lambda = 2$ (Fig. 3) and a difference of the stall prediction is expected with SST-TM. Case 3 aims at showing the influence of the Reynolds number, which plays a key role for the transition model. Figure 4 shows that the relative Reynolds numbers are most of the time below 10^6 and the laminar to turbulent transition may then influence the power coefficient.
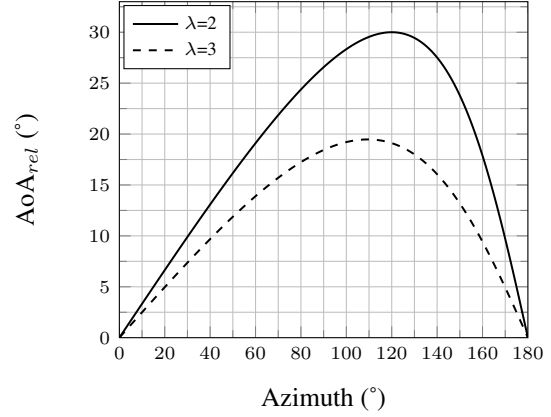
Figure 3: Relative angle of attack in the upstream half of the turbine
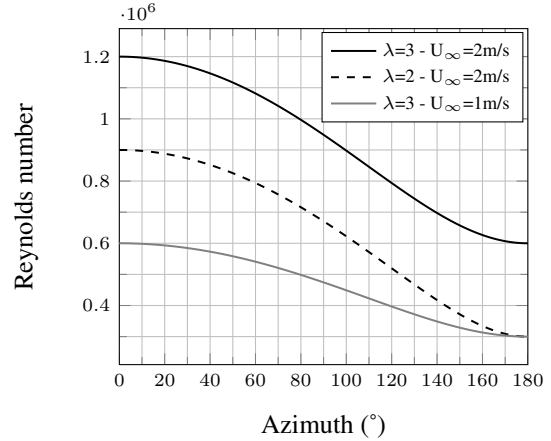
Figure 4: Instantaneous relative Reynolds number in the upstream half of the turbine

4.1 Case 1: λ = 3 & U_∞ = 2 m.s^{-1}

Considering λ and the solidity of the turbine, this case should generate a high power coefficient ($\overline{CP}$), according to Paraschivoiu [10]. The upstream velocity of 2 m.s^{-1} leads to relative Reynolds numbers (Fig. 4) between 6×10^5 (foil at θ=180°) and 1.2×10^6 (foil at θ=0°). $Re_W = 6\times10^5$ is a transitional Re and results obtained with the transition model may then differ from

those obtained with the fully turbulent model. Figure 5 shows the instantaneous power coefficient (CP) as a function of the azimuth. The three lobes represent the maximum efficiency of blades 1, 2 and 3 successively as they pass through θ=110° which corresponds to the maximum relative angle of attack (Fig. 3). The smooth and symmetrical shape of the lobes indicate that blades do not experience stall at this operating condition. Calculation with the transition model predicts a higher CP than the fully turbulent calculation whatever the azimuth. This results in the following average power coefficients : $\overline{CP}_{SST-TM}$=0.605 and $\overline{CP}_{SST}$=0.557. $\overline{CP}_{SST-TM}$ is close to the Betz limit and $\overline{CP}_{SST}$ is slightly lower. These power coefficients are high and must be taken carefully because of the 2D assumption. Such values are commonly found in academic papers [4].
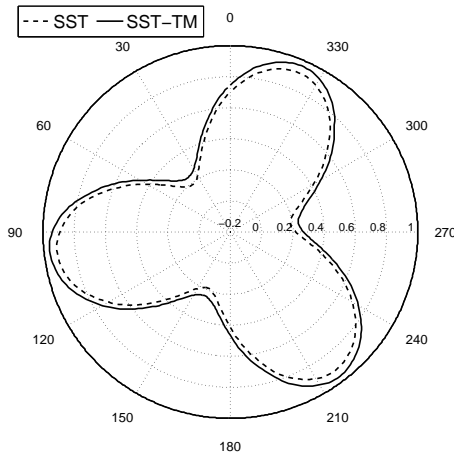
Figure 5: Instantaneous power coefficient CP, case 1

Figure 6 shows the azimuth variations of blade one's CP. SST-TM calculation leads to higher CP than SST calculation in the upstream half of the turbine. Both SST-TM and SST predictions are very close in the downstream half. CP_{max} occurs at θ=98° for both SST and SST-TM calculations, which is about 10° (azimuth) before the theoretical maximum relative angle of attack. Figure 6 also shows that, under this operating condition, the major part of the energy is harvested in the upstream half of the turbine while the downstream half produces near 0 or even negative contributions to CP.

Figure 7 shows the Z-vorticity field in the turbine. The wake of each blade can be clearly seen on the picture but no vortex is generated.

4.2 Case 2: λ = 2 & U_∞ = 2 m.s^{-1}

Reducing λ leads to a higher maximum relative angle of attack (AoA$_{rel\ max}$=30°) and relative Reynolds numbers are lower (Fig. 4): Re$_W$ = 3×10^5 (foil at θ=180°) and Re$_W$ = 9×10^5 (foil at θ=0°). Figure 8 shows that lobes are no longer symmetric in this case.
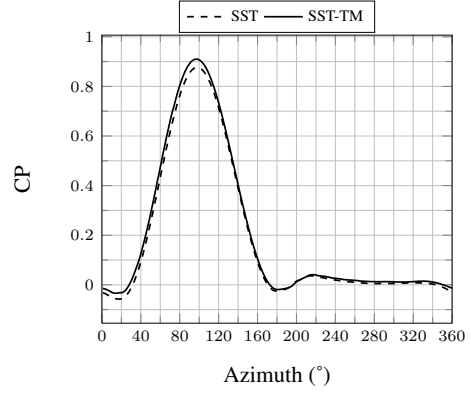
Figure 6: CP of blade 1, case 1
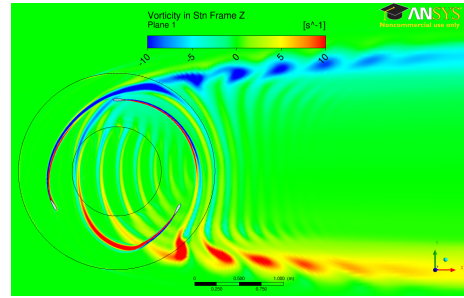
Figure 7: Z-vorticity field, case 1

The side corresponding to the increasing relative angle of attack is rounded while the other side is almost straight due to the dynamic stall of the blades at high angle of attack. Similar behaviors are observed with SST and SST-TM models and in this case, CP_{min} is negative which means that driving and braking torques successively apply on the main shaft. However, SST-TM predicts higher CP_{max} and lower CP_{min}. This results in the following average power coefficients: $\overline{CP}_{SST-TM}$=0.359 and $\overline{CP}_{SST}$=0.338.
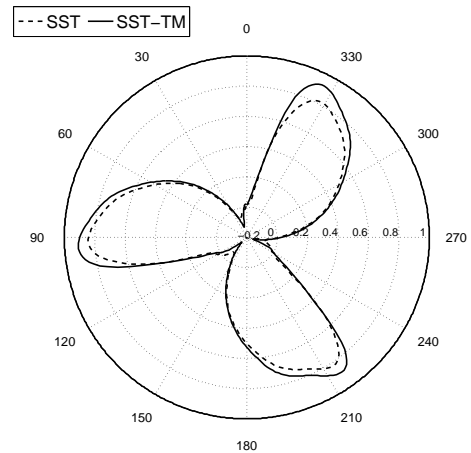
Figure 8: Instantaneous power coefficient CP, case 2

CP calculated on blade 1 is plotted on figure 9 for cases 1 (red) and 2. Predictions of SST and SST-TM models are very close excepted around $\theta=110°$ and $\theta=220°$. These azimuths correspond respectively to the vortex shedding in the upstream half of the turbine and the interaction between the blade and the vortex shed by the previous blade in the downstream half of the turbine, as can be seen on figure 10. SST-TM predicts a lower CP_{min} at $\theta=110°$ and a higher CP_{max} at $\theta=220°$ which explains the differences observed on figure 8: when blade 1 is at $\theta=90°$, blade 2 is at $\theta=210°$ and blade 3 is at $\theta=330°$. The sum of each blade CP is then higher with SST-TM than with SST. The comparison with case 1 ($\lambda=3$) shows that less power is harvested in the upstream half and more in the downstream half for $\lambda=2$. The average turbine power coefficient is however decreased by 39% (SST) or 41% (SST-TM) from $\lambda=3$ to $\lambda=2$.
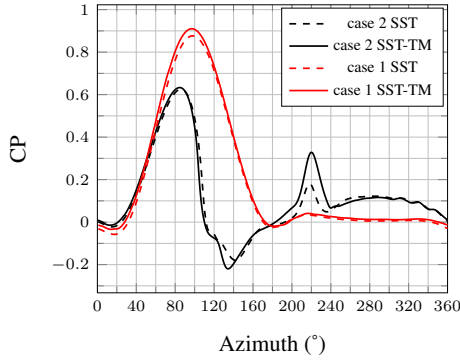
Figure 9: CP of blade 1, comparison between cases 1 (red) and 2 (black)
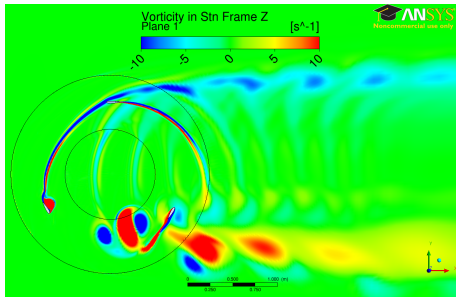
Figure 10: Z-vorticity field, case 2

Figure 11 shows a close view of the Z-vorticity field around blade 2 at $\theta=120°$. SST (left) and SST-TM (right) results are compared, showing the difference of vortex structure between the two models. SST-TM predicts a more intense leading edge vortex which is being shed at $\theta=120°$. Two secondary counter rotating vortices can be seen with SST-TM while they are just developing with SST. The higher intensity of the vortices predicted by SST-TM explain the difference observed on figure 9.
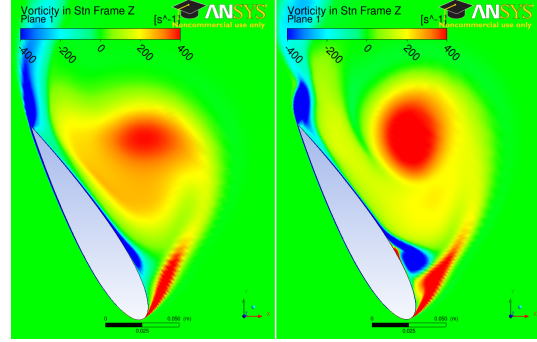
Figure 11: Comparison between SST (left) and SST-TM (right) Z-vorticity fields of blade 2 at $\theta=120°$, case 2

4.3 Case 3: $\lambda = 3$ & $U_\infty = 1$ m.s^{-1}

Relative angles of attack are the same as in the first case ($\lambda=3$ & $U_\infty=2$ m.s^{-1}) but relative Reynolds number is lower (Fig. 4). The flow field may then be modified, especially when considering transition. Figure 12 shows that CP predicted by SST-TM are higher or equal to those predicted by SST for all azimuths. The difference is significant for $\theta \in [30°,100°]$, $\theta \in [150°,220°]$ and $\theta \in [270°,340°]$. These three parts correspond to the three foils going through the first quarter of the turbine revolution where the relative angle of attack is increasing. Elsewhere, models predictions are very close one from another.
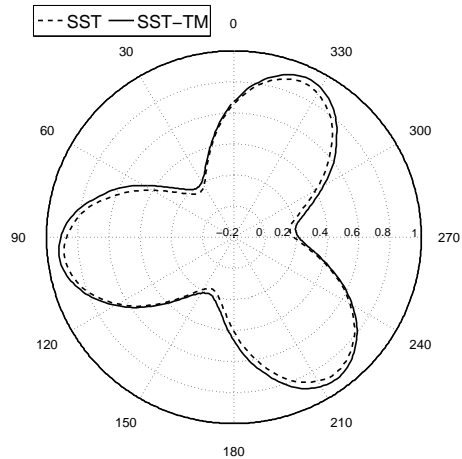
Figure 12: Instantaneous power coefficient CP, case 3

CP calculated on blade 1 is displayed on Figure 13 and confirms the observations made on figure 12: transition model leads to higher CP from $\theta=0°$ to $\theta=100°$, then both predictions are very close from $\theta=100°$ to $\theta=170°$ and transition model predicts a slightly higher CP from $\theta=170°$ to $\theta=360°$. Corresponding curves of case 1 are also plotted on figure 13 (red) and show that the increase of relative Reynolds number does not change anything from $\theta=0°$ to $\theta=80°$. From $\theta=80°$ to

$\theta=180°$ CP is higher for case 1 since the higher Re leads to higher maximum lift and lower drag. From $\theta=180°$ to $\theta=360°$, both case 1 and case 3 predictions are very close.

The average power coefficient predicted by SST ($\overline{CP}_{SST} = 0.530$) is 6.1% lower than the prediction of the transition model $\overline{CP}_{SST-TM} = 0.565$. Decreasing the upstream velocity leads to a decrease of the average power coefficient for both SST and SST-TM models (respectively -4.9% and -6.7%). The decrease is bigger with the transition model because of its higher sensitivity to the Reynolds number.

The Z-vorticity field, though not presented, shows similar flow patterns as case 1 (e.g. no vortex shedding) with lower vorticity values.
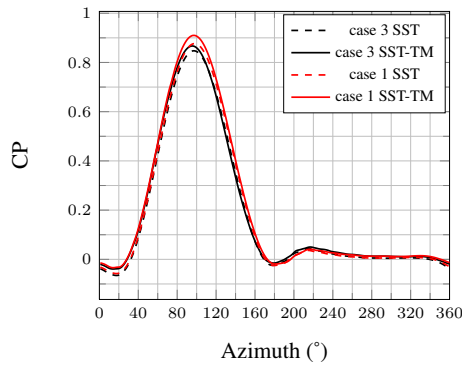
Figure 13: CP of blade 1, comparison between cases 1 (red) and 3 (black)

Table 2 sums up all average power coefficients and gives the deviation of $\overline{CP}_{SST-TM}$ from $\overline{CP}_{SST}$ expressed in percents.

	$\overline{CP}_{SST}$	$\overline{CP}_{SST-TM}$
$\lambda=3$, $U_\infty=2$ m.s^{-1}	0.557	0.605 (+8.6%)
$\lambda=2$, $U_\infty=2$ m.s^{-1}	0.338	0.360 (+6.5%)
$\lambda=3$, $U_\infty=1$ m.s^{-1}	0.530	0.564 (+6.4%)

Table 2: Power coefficients summary

5   Conclusion

2D U-RANS calculations of the SHIVA cross flow turbine have been performed with both k-ω SST turbulence model and $\gamma - Re_\theta$ transition model (coupled with k-ω SST). Three cases have been studied: $\lambda = 3$ & $U_\infty = 2$ m/s, $\lambda = 2$ & $U_\infty = 2$ m/s and $\lambda = 3$ & $U_\infty = 1$ m/s. Considering the laminar to turbulent transition led in all cases to an increase of the power coefficient from 6 to 9%. $\overline{CP}$ predictions were not deeply modified but some flow structures as vortices were slightly changed depending on the model. Modeling the transition led to a stronger decrease of $\overline{CP}$ when decreasing U_∞ (-6.7%

instead of -4.9%) because the Reynolds sensitivity is more important with SST-TM. Experimental data will soon be available to validate these results.

References

[1] Ansys. *Ansys CFX Solver Modeling Guide V14.0*. Ansys, 2011.

[2] P.L. Delafin, F. Deniset, J.A. Astolfi, and J.M. Laurens. Prediction of hydrodynamic forces with and without transition model. In *Proceedings of the 15th Numerical Towing Tank Symposium*, 2012.

[3] J. Ferziger and M. Peric. *Computational methods for fluid dynamics*. Springer New York, 2002.

[4] T. Maître, E. Amet, and C. Pellone. Modeling of the flow in a darrieus water turbine: Wall grid refinement analysis and comparison with experiments. *Renewable Energy*, 51(0):497–512, 2013.

[5] F. Menter, R. Langtry, and S. Volker. Transition modelling for general purpose cfd codes. *Flow, Turbulence and Combustion*, 77:277–303, 2006.

[6] F. R. Menter, M. Kuntz, and R. Langtry. Ten years of industrial experience with the SST turbulence model. In K. Nagano Y Hankjalic and M. Tummers, editors, *Turbulence, Heat and Mass Transfer 4*, 2003.

[7] F.R. Menter. Two-equation eddy-viscosity turbulence models for engineering applications. *AIAA Journal*, 32(8):1598–1605, 1994.

[8] B. Paillard, J.A. Astolfi, and F. Hauville. Cfd simulation and experimental validation of a vertical axis turbine: Toward variable pitch cross-flow marine turbine for maximizing hydropower extraction—the shiva project. In *30th International Conference on Ocean Offshore and Arctic Engineering - OMAE2011*, 2011.

[9] B. Paillard, F. Hauville, and J.A. Astolfi. Simulating variable pitch crossflow water turbines: A coupled unsteady onera-edlin model and streamtube model. *Renewable Energy*, 52(0):209–217, 2013.

[10] Ion Paraschivoiu. *Wind Turbine Design With Emphasis on Darrieus Concept*. Presses Internationales Polytechnique, 2009.

Waterjet Propelled Hull Transom Clearance

Arash Eslamdoost, Lars Larsson, Rickard Bensow

Department of Shipping and Marine Technology,
Chalmers University of Technology, 412 96 Gothenburg, Sweden

arash.eslamdoost@chalmers.se

Parameters which are playing role in waterjet/hull interaction can be split into two major categories of global and local flow changes. The former is caused by the sinkage and trim variations and the later is due to the missing surface of the intake opening along with the changes in the boundary layer profile ahead of the intake, wave pattern in the aft-part of the hull and also the transom clearance. According to published measurement of a series of waterjet-propelled hulls, a sudden change in the trust deduction fraction can be seen close to the critical Froude number, when the transom starts to become dry. This might be related to the effect of the global and local flow changes which both together result in two different critical Froude numbers for the bare hull and the self-propelled one. Employing a RANS solver, the aim of the current study is first to investigate the possibility of predicting and validating the critical Froude number for the towed and self-propelled hulls and then studying the dependency of the hull resistance on the transom clearance for both of the cases.

Wave Impact Simulations using Smoothed Particle Hydrodynamics

Paul H L Groenenboom, ESI Group Netherlands, Delft/NL, paul.groenenboom@esi-group.com

1. Introduction

This paper presents a Virtual prototyping (VP) tool which is built around an explicit Finite Element (FE) software package with an embedded and fully coupled Smoothed Particle Hydrodynamics (SPH) solver that enables numerical simulation of large hydrodynamic loads on structures. Since SPH is a Lagrangian method that does not require a mesh it offers as significant advantage that it can very well describe violent free-surface flows in domains or around (partially) submerged bodies of arbitrary complex shape without loss of accuracy due to transport of volume fractions along interfaces as in most Eulerian numerical methods. The SPH method is therefore very well suited for simulation of overturning waves, water entry, slamming and green water phenomena.

A brief review of the basic SPH method and the coupling to the FE part of the solver will be presented below. Selected applications involving fluid-structure interaction will also be presented.

2. Overview of Smoothed Particle Hydrodynamics

An overview of the 'standard' (Weakly Compressible) Smoothed Particle Hydrodynamics (WC-SPH) method and the optional coupling with Finite Elements will be presented in this section. The special features that have recently been introduced into SPH to provide more accurate pressure results and that allow for reduction of the computational efforts are discussed in the following section. Additional information may be found in *Groenenboom et al (2013)* and *Groenenboom and Cartwright (2013).*

2.1. The standard SPH method

The SPH method is an interpolation method in which each "particle" describes a fixed amount of material in a Lagrangian reference frame. Despite its appearance as a collection of points, the SPH is a solution method of the continuum mechanics equations of fluids and solid materials. Since the method requires no mesh, SPH facilitates the simple handling of the motion and topology changes of material surfaces. As shown in figure 1, the evaluation of relevant field variables such as density and velocity, at the location of a selected particle is conducted by interpolation over all neighbor particles in a region of influence. The size of the sphere (or circle in 2D) of this region is defined by a smoothing length, h. Importantly, spatial derivatives of unknown field variables may be evaluated using the known derivative of the smoothing kernel.
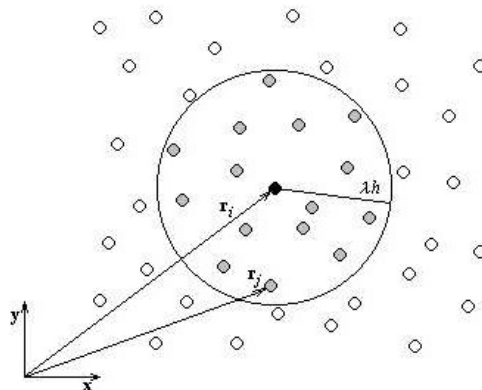
Fig.1: Two-dimensional representation of the region of influences of particle 'i'

The continuity equation provides the derivative of the density for particle i:

$$\frac{\mathrm{d}\rho_i}{\mathrm{d}t} = \sum_j m_j (\vec{v}_i - \vec{v}_j) \cdot \nabla_i W_{ij} \qquad (1)$$

where the sum extends over all neighbor particles j, each with a mass of m_j. $\vec{v}_i$ and $\vec{v}_j$ are the velocities of the ith and j^{th} particles, respectively, and W is the smoothing kernel evaluated at the distance between the ith and j^{th} particles. The updated velocity may be obtained from the momentum equation:

$$\frac{d\vec{v}_i}{dt} = -\sum_j m_j \left(\frac{p_i}{\rho_i^2} + \frac{p_j}{\rho_j^2} + \prod_{ij} \right) \cdot \nabla_i W_{ij} \tag{2}$$

where p_i and p_j represent the particle pressures. The artificial viscosity is defined as:

$$\prod_{ij} = \frac{2}{\rho_i + \rho_j} \left(-\alpha \frac{c_i + c_j}{2} \mu_{ij} + \beta \mu_{ij}^2 \right), \tag{3}$$

with c_i and c_j being the local sound speed, and with

$$\mu_{ij} = \tfrac{1}{2}(h_i + h_j) \frac{(\vec{v}_i - \vec{v}_j) \cdot (\vec{r}_i - \vec{r}_j)}{\left| \vec{r}_i - \vec{r}_j \right|^2 + \varepsilon^2 h^2} \quad \text{when } (\vec{v}_i - \vec{v}_j) \cdot (\vec{r}_i - \vec{r}_j) < 0 \tag{4}$$

And zero otherwise; h_i and h_j are the smoothing lengths. The $\varepsilon^2 h^2$ term in the denominator is included to avoid divergence in case particles collide. The parameters α and β determine the strength of the artificial viscosity required to suppress numerical shocks. These artificial viscosity parameters should be set as low as possible to avoid the flow becoming too viscous. To mitigate the effect of particle clumping together during flow simulations, the anti-crossing option (XSPH), *Monaghan (1994)*, may be employed as follows:

$$\frac{d\vec{r}_i}{dt} = \vec{v}_i + \eta \sum_j m_j \frac{(\vec{v}_i - \vec{v}_j)}{\tfrac{1}{2}(\rho_i + \rho_j)} W_{ij} \tag{5}$$

For a non-zero η parameter, equation (5) is used to update the particle positions, whereas the strains remain based on the uncorrected displacements. The smoothing kernel W is a bell-shaped function of the distance between particles for which in most simulations the cubic spline will be used.

The flow is assumed to be nearly incompressible implying that the pressure field is obtained from an equation of state (EOS) model. A polynomial EOS may be used for water, but it is convenient to use an alternative, the Murnaghan (also known as the Tait) model, whose EOS is given by:

$$p = {}^0p \left[\left(\frac{\rho}{{}^0\rho} \right)^\gamma - 1 \right] \tag{6}$$

where ${}^0p$ is the reference pressure, ${}^0\rho$ the reference density and γ is a user-defined parameter, which is commonly 7.0. A cut-off pressure may be included as a simple approximation to cavitation.

Particles are assumed to interact mutually only if they are sufficiently close to each other. This is established by a nearest neighbor (NN) search. Second-order accurate leap-frog time stepping is used for the explicit time integration of the above rate equations. The numerical time step is set at a fraction (usually about 0.8) of the well-known Courant (or CFL) criterion based on the current size and sound speed of all particles and finite elements present in the model.

Despite obvious advantages of SPH to simulate fluid flow involving free surfaces or interaction with a structure or other fluids, the method has not gained general acceptance in the maritime industry. Some reasons for this are the generation of irregular particle distributions ('clumping'), the occurrence of scatter in computed pressures, and limitations in spatially varying SPH solutions. These limitations have been largely overcome by correction terms in the SPH formulations as discussed in *Groenenboom et al (2013)* and *Groenenboom and Cartwright (2013)*.

2.2. Moving Domains and Periodic Boundaries

In many cases, particles located outside a region of interest are not expected to be relevant for at least part of the simulation time. To take advantage of this, an 'active moving box' has been developed. None of the particles outside of the box are processed during the particle interaction computation and hence do not contribute to the CPU load.

Another method of reducing the CPU load for flow simulations is that of 'periodic boundaries'. This feature allows particles leaving a user-defined rectangular domain to be entered at the other end with the same velocity and is useful for a variety of flow studies. It has recently been extended to allow opposing boundaries to be translated according to the motion of a user-defined node. With this extension, the particle domain can follow the motion of a moving structure such as a ship or a ditching aircraft, without needing to introduce additional velocities for the particles themselves.

2.3. Hydrostatic initialization and pressure gauges

Another feature that helps to reduce the CPU effort when chasing more accurate results is that of a 'hydrostatic equilibrium condition'. Adding the hydrostatic pressure to the material pressure from the start of the simulation avoids the need to conduct an initialization-simulation to obtain hydrostatic pressure equilibrium dynamically.

A 'gauge' feature provides a mechanism to monitor the pressures and, in relevant situations, the free surface level. A 'pressure gauge' may be considered as the computational equivalent to physical pressure gauge in an experiment, *Siemann and Groenenboom (2013)*. They may be positioned anywhere within an SPH domain without influencing the results. Due to the averaging conducted over nearby particles, the pressures obtained suffer less from the oscillations observed for individual particles. A 'level gauge' is used to monitor the free surface location.

3. Coupling with structures

Interaction between particles, representing a fluid, and finite elements, representing moving or deformable structures, may be modeled by one of the sliding interface contact algorithms available in VPS (of which the explicit part dedicated to crashworthiness is also known as PAM-CRASH) . Such algorithms prevent penetration between selected structures, with sliding allowed in most cases. The sliding interfaces employed are based on the well-known penalty formulation, where geometrical interpenetrations between so-called slave nodes and matching master faces are penalized by counteracting forces that are essentially proportional to the penetration depth. The contact algorithm automatically detects when a particle (slave) penetrates any segments (master) representing the outer surface of the finite element model of the structure. The contact thickness indicates the distance away from a contact face where physical contact is established. For SPH particles as slaves, the contact thickness should be representative of the particle spacing. This type of contact has been validated by simulating the vertical motion of floating bodies. It has been found that the neutrally buoyant position and buoyancy forces are accurately predicted when the thickness defined for the contact is one half the particle spacing and the artificial viscosity coefficients are taken significantly smaller than the values normally applied for shocks. The contact thickness and the relative strength of the repulsive forces are defined by the user.

4. Wave generation

In physical wave tanks waves are generated by the prescribed motion of wave makers. Since SPH is a Lagrangian method, wave creation for numerical simulation can be done completely analogously. Moreover, there is no restriction to let the computational wave maker model deform such that analytical wave profiles are generated exactly. The limitation that instantaneous application of the full amplitude of the wave maker would lead to numerical instabilities can be circumvented by imposing appropriate initial velocities to the particles, *Groenenboom et al (2009)*.

The most interesting waves are deep water waves for which the water motion at a depth beyond the

limit of about half a wavelength has become small enough to be neglected. To reduce the size of the computational the domain, the depth will be chosen to be less than this limit. In that case, the domain floor can no longer be assumed to remain at rest but will be assigned the displacement field corresponding to the analytical approximation for the undisturbed waves. Second-order Stokes' waves are assumed. Another reason to assign the undisturbed wave motion to the floor is to counteract any losses in the wave amplitude usually observed when a wave series traverses an extended domain represented by a computationally acceptable number of particles. With this 'moving floor' approach, excellent wave propagation results have been obtained, *Cartwright at al. (2004).* Similar displacement conditions are assigned to all other walls enclosing the domain. In case the waves are disturbed by floating or dropped objects, the location of the boundaries needs to be chosen sufficiently far away from the objects that the reflection of any wave disturbance can safely be ignored. A similar approach has recently been applied to create irregular waves, *Aristodemo and Groenenboom (2012)*.

Before trying to simulate ships moving in waves, it had to be proven that undisturbed waves could be simulated employing the moving floor concept. As discussed by *Groenenboom and Cartwright (2009)*, this has been tested for second-order deep water waves in a two-dimensional section in which both the wave length and domain length was set to 294 m. The model had a depth of 24 m, filled with particles on an initial spacing of 0.5 m. Contours of the pressure for 16m high waves are shown in Fig.2. Also shown in this figure are a few particle paths that display the combination of circular motion with the Stokes' drift in the direction of wave propagation. Although not shown, the velocity distribution within the wave correlates well with the theoretical distribution.
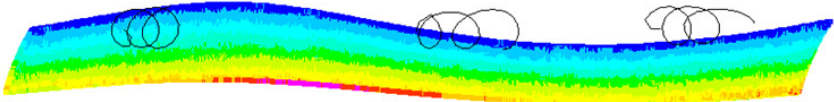
Fig. 2: Pressure contour and selected particle trajectories for the 16 m high 294 m long wave

For a similar test case of a regular wave of 4.0 m height and 73.5 m length, the computed vertical velocities of a selected particle in the domain are compared to the analytical result in Fig.3. Even for this case with higher wave steepness, there is excellent agreement with the analytical solution.
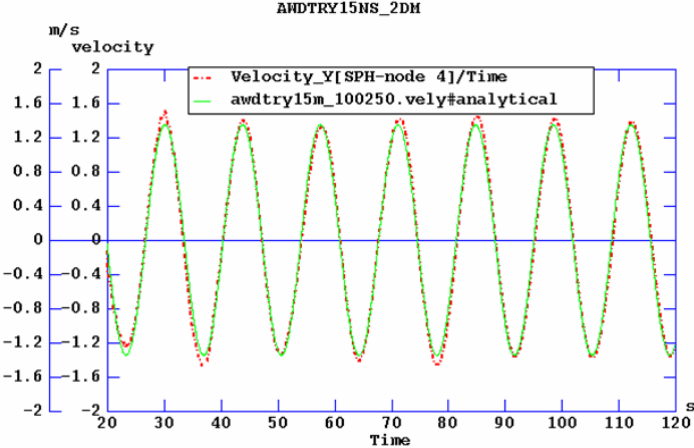
Fig. 3: Time histories of the vertical velocity of a selected particle compared to the second-order analytical solution. For clarity the initialization phase is deleted in this figure.

These results demonstrate that the wave dynamics generated using the moving floor technique is correct and hence suitable for the study of the response of floating objects.

Simulation of free surface waves and the interaction with floating objects in open seas requires definition of artificial boundaries. The option of a 'damping zone' has recently been introduced to eliminate the problems arising from reflections at the boundaries. Using this feature, the user may define regions in space having a smooth transition from no damping to full damping. If the transition is smooth enough, the size of the reflected waves is negligible.

5. Ships Moving In Waves

Having generated a non-diminishing regular wave as discussed in the previous section, it was then possible to drive a ship through the waves to observe the ship response. Fig.4 illustrates the response of a generic frigate in seas of 3 m high waves with a 110 m wavelength.
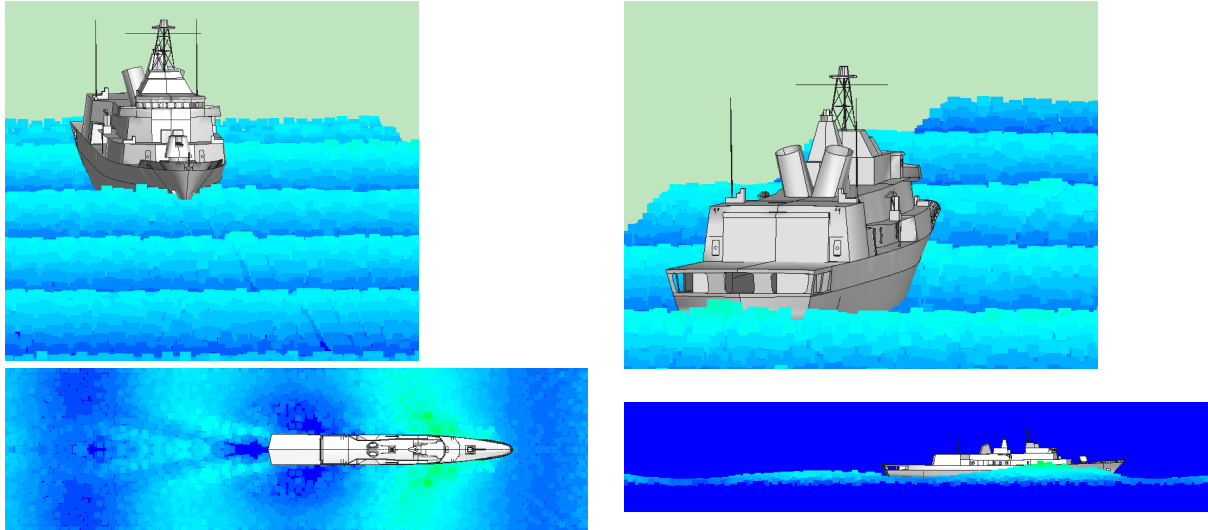
Fig. 4: Generic frigate with typical responses and wave-making tendencies when traversing waves generated by the moving floor boundary conditions. Upper images show the vessel beginning to move; lower images show top and side views for vessel at 30+ knots.

Most numerical studies of ships in waves are conducted assuming the hull to be rigid. However, *Groenenboom et al. (2010)* demonstrated that it is possible to simulate the motion of the flexible hull of a generic frigate in waves using the coupled FE-SPH approach. This study demonstrated that the flexibility of the frigate model does influence the kinematics of the vessel response.

6. Waves on Off-shore Structures

The dynamic response of a floating (moored) offshore platform subject to strong wave action has been investigated, Fig.5. The platform was modeled using finite elements and was 105 m long, 65 m wide, and had draft of 16.5 m with a mass of 27.7 t. The water domain was 1460 m x 244 m x 55 m and employed approximately 2.4 million SPH particles. The main body of the platform was modeled as a rigid body with appropriate mass, centre of gravity and moments of inertia defined. The anchor cables were modeled using flexible 1-dimensional (1D) finite elements. The use of periodic boundary conditions applied to the SPH particles allowed the computational domain to be limited to 4 wavelengths in the direction of wave travel. The waves were generated by applying the moving floor technique.
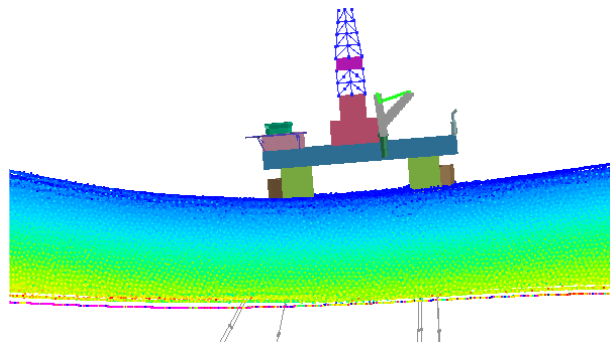
Fig. 5: Offshore platform responds to waves (with mooring lines beneath the moving floor)
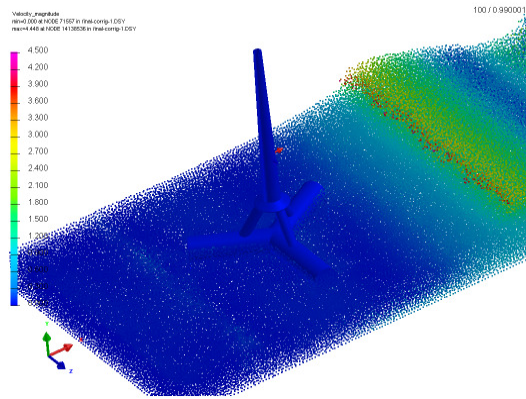
Fig. 6: Particle distribution and velocities for a wave approaching a TLP support of a wind turbine

The dynamic response of the above platform was presented by *Croaker et al. (2011)* for the case of the platform operating at a depth of 310 m under the influence of waves with a wavelength of 365 m and wave height of 20 m. An extension of this approach also considered the motion-induced stresses in the structural members of the cranes located on the operations deck of the platform.

As the stable time step for these 1D elements was much smaller than for the SPH particles, employing MMC (Section 4) greatly reduced the computation time of this simulation. This reduction exceeded 25 when MMC was used in the model containing both flexible anchor cables and flexible cranes.

A recent study assesses the hydrodynamic forces due to extreme waves acting on the Tension-Leg Platform (TLP) support for a floating wind turbine, *Adam et al. (2012)*. Fig.6 shows a preliminary result of the velocities in the approaching wave. The resulting accelerations of the wind turbine may be used to determine the forces and kinematics of the structure.

Additional examples may be found in *Groenenboom et al (2013)* and references contained therein.

References

Adam, F.; Dahlhaus, F.; Grossmann J. (2012), *Schwimmende Fundamente für Offshore WEA,* Presentation at the ESI Energy Seminar, Hamburg, Germany

Aristodemo, F.; Groenenboom, P. (2012), *SPH modelling of irregular waves occurring in ocean sea states,* XIX Convegno Italiano di Meccanica Computazionale, Rossano, Italy

Cartwright, B.; Groenenboom, P.; McGuckin, D. (2004), *A novel technique to predict non-steady loads in vessels in severe seas*, ISOPE Conf., Toulon, France

Croaker, P.J.; El-Khaldi, F.; Groenenboom, P.H.L.; Cartwright, B.K.; Kamoulakos, A. (2011), *Structural performance and dynamic response of semi-submersible offshore platforms using a fully coupled FE-SPH approach,* Int. Conf. Comp. Methods in Marine Engineering (MARINE), Lisbon

Groenenboom, P.; Cartwright, B. , McGuckin, D. (2009), *numerical simulation of ships in high seas using a coupled FE-SPH Approach*, RINA Int. Conf. on Innovation in High Speed Marine Vessels, Fremantle, Australia

Groenenboom, P.; Cartwright, B. (2009), *Hydrodynamics and fluid-structure interaction by coupled SPH-FE method*, J. Hydraulic Research 47, pp.1–13

Groenenboom, P.; Cartwright, B. (2013), *Pressure-corrected SPH with innovative particle regularization algorithms and non-uniform, initial particle distributions*, 8th SPHERIC Workshop, Trondheim, Norway

Groenenboom, P.; Croaker, P.; Kamoulakos, A. ; El-Khaldi, F.; McGuckin, D. (2013), *Innovative Smoothed Particle Hydrodynamics for Wave Impact Simulation on Ships and Platforms,* 12th Int. Conf. on Computer Applications and Information Technology in the Maritime Industries (COMPIT'13), Cortona, Italy

Siemann, M.; Groenenboom, P.H.L. (2013), *Pressure evaluation at arbitrary locations in SPH water impact simulations*, accepted for the PARTICLES-2013 Conference, Stuttgart, Germany

Reynolds effect on Propulsive Performance of Marine Propeller operating in wake flow

Nobuhiro Hasuike*, Akinori Okazaki*, Shosaburo Yamasaki* and Jun Ando[†]
*Nakashima Propeller Co., Ltd.
688-1, Joto-Kitagata, Higashi-ku, Okayama 709-0625, Japan
E-mail: nobuhiro@nakashima.co.jp, web page: http://www.nakashima.co.jp/
[†] Faculty of Engineering, Kyushu University
744 Motooka Nishi-ku Fukuoka 819-0395, Japan
E-mail: ando@nams.kyushu-u.ac.jp, Web page: http://www.eng.kyushu-u.ac.jp/e/index.html

Abstract

This paper focuses on the Reynolds effect on the propulsive performance of marine propellers in wake flow. 3 equations turbulence model was adopted for the prediction of the propulsive performance in the wide range of Reynolds number.

Background

The demand for improvement in propulsive performance of a vessel is increasing drastically against the background of the jump of fuel fee and EEDI target. In order to realize an efficient propeller design, it becomes an important issue to establish the reliable powering method to estimate total propulsive performance improvement by propeller design improvement.

Propeller open water characteristics for self propulsion analysis

In an usual propeller design chain by EFD, such as self propulsion test(SPT in short) and a propeller open water test(POT in short) are performed for evaluation of propulsive performance as practical use. POT result is used for extrapolation to the full scale propeller open characteristics(POC in short) and the analysis of a self-propulsion factor. For removing laminar separation effect and minimizing extrapolation range to full scale, full scale propeller characteristic are extrapolated from the POT result at as higher Reynolds number as possible range by towing tank.

On the other hand, POC used for self-propulsion analysis is derived from high Reynolds POT by consideration of difference of Reynolds number between POT and SPT. For simple use, typical scale correction of propeller characteristics is based on the simple correction of friction coefficient which is an analogy of flat plate friction.

In generally, flow character around a propeller blade is complicatedly changed against Reynolds number. Flow in model scale is mainly laminar and partially turbulent which includes partial laminar separation. In basically, distribution of laminar and turbulent flow and flow separation much depend on pressure distribution on the blade which is decided by attack angle and detail blade section shape. For propeller scale correction, simple formulae based on correction of friction coefficient by limited propeller geometry is useful for 'daily test', but it is too simple and there is much room for improvement of estimation accuracy.

Other way for deriving POC for self propulsion analysis is to conduct second POT which Reynolds number is corresponding to SPT[1]. Higher POT result is used for full scale propeller characteristics. This '2POT method' is widely used at many Japanese towing tanks and recommended also by ITTC[2]. As this method is experimental, detail propeller geometry effects are all included. The advantage of '2POT method' is not only to include friction component but also pressure component of propeller characteristics. Laminar flow separation effects are also taken account. These features are quite important for recent smaller blade area propellers.

Turbulence intensity of propeller inflow at self propulsion test condition

By ship wake flow, inflow to the propeller at SPT condition is more turbulent than POT condition. Lee et al.[3] (2003) investigated wake flow of KVLCC by wind tunnel (Fig.1). Turbulence intensity $T_{uin}(\%)$ is defined as dV/Vs. Maximum turbulence intensity T_{uin} was abt.10%. Minimum turbulence intensity T_{uin} was abt.3%. Averaged value in propeller plane is abt.5-7.5% . Recently, Streckwall et al.[4] proposed new 'Strip method' for improving scale correction by considering whole blade profile. In this proposal, the difference of turbulence intensity between POT and SPT condition is taken account. The assumption of different transitional Reynolds numbers for POT and SPT condition are independently applied. This idea highlights the importance of turbulence intensity for discussion about POC for self propulsion analysis. Tsuda et al.[5](1978) investigated the flow pattern of MAU propellers at POT and SPT condition. Flow character at SPT condition was still mainly laminar flow even though the turbulence intensity at SPT condition was higher than POT condition.

Target of this research

As mentioned above, 2POT method has lots of advantage to estimate propulsive performance in higher accuracy. However, it is difficult to conduct POT at the same turbulence intensity as propeller inflow at SPT. CFD approach may easily adjust turbulence intensity to SPT condition. Further, CFD may easily treat detail propeller geometry effects on scale effect as well as 2POT method. Therefore, numerical SPT is highly expected for reliable estimation of propulsive performance. In this research, CFD calculation of POC from

model scale to full scale is carried out. The effects of a turbulent model and turbulence intensity on the POC were investigated. Next, laminar and turbulent flow distribution at POT and SPT condition were compared at model and full scale. Finally, POC for self propulsion analysis was discussed.
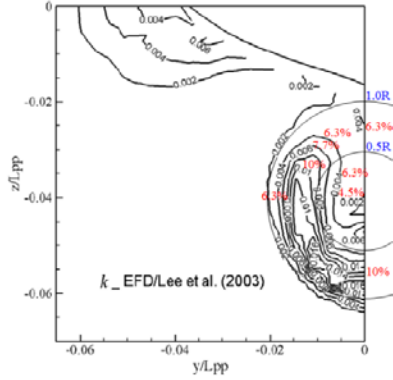

Figure 1: Turbulence intensity in wake flow of KVLCC at Re=4.6×10[6](Lee, 2003)[3]

Face   Back   Face   Back
POT   SPT(behind hull)
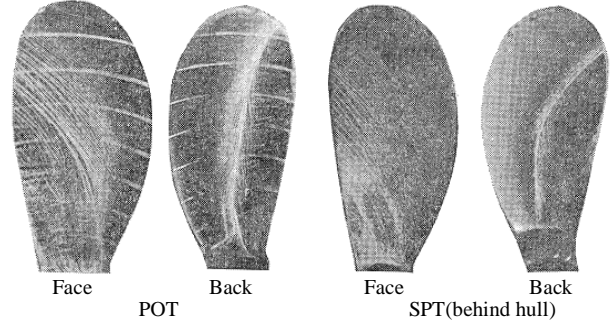
Figure 2: Comparison of flow pattern; in open-water and behind hull(MPNo.0011R: R_{ND}=3×10^{5}, J=0.35)(Tsuda et al. ,1978)[5]

2 NUMERICAL MODEL

In this research, transitional flow around propeller was simulated using SOFTWARE CRADLE SCRYU/Tetra V10 software, which was based on a finite volume method with an unstructured grid. The k-ε model, the Shear-Stress Transport k-ω model were applied to the transitional flow. In addition to these widely used turbulence models, newly developed 3-equations k-k_L-ω model was also applied.

2.1 Transitional flow simulation

It is important to predict the transition point of a flow around a propeller in operating in low-Reynolds-number. LKE (Laminar Kinetic Energy) model (Walters & Leylek 2004) was developed to simulate the transitional flow. In the LKE model, the disturbance energy in a pre-transitional region of a boundary layer is represented as Laminar Kinetic Energy (k_L), while the turbulence energy is as k. The transport equation of k_L is solved by using two equations of fully turbulent model. SC/Tetra introduces the following k-k_L-ω model (Walters & Cokljat 2008) which was developed based on the k-ω model:

$$\frac{\partial \rho k_T}{\partial t} + \frac{\partial \rho u_i k_T}{\partial x_i} = \rho\left(P_{k_T} + R_{BP} + R_{NAT} - \omega k_T - D_T\right) + \frac{\partial}{\partial x_i}\left(\left(\mu + \frac{\rho \alpha_T}{\sigma_k}\right)\frac{\partial k_T}{\partial x_i}\right) \tag{1}$$

$$\frac{\partial \rho k_L}{\partial t} + \frac{\partial \rho u_i k_L}{\partial x_i} = \rho\left(P_{k_L} - R_{BP} - R_{NAT} - D_L\right) + \frac{\partial}{\partial x_i}\left(\mu \frac{\partial k_L}{\partial x_i}\right) \tag{2}$$

$$\frac{\partial \rho \omega}{\partial t} + \frac{\partial \rho u_i \omega}{\partial x_i} = \rho\left[C_{\omega 1}\frac{\omega}{k_T}P_{k_T} + \left(\frac{C_{\omega R}}{f_w}-1\right)\frac{\omega}{k_T}(R_{BP}+R_{NAT}) - C_{\omega 2}f_W^{\frac{4}{3}}\omega^2 + f_\omega \alpha_T f_W^2 \frac{\sqrt{k_T}}{Y^3}\right] + \frac{\partial}{\partial x_i}\left(\left(\mu + \frac{\rho \alpha_T}{\sigma_\omega}\right)\frac{\partial \omega}{\partial x_i}\right) \tag{3}$$

The parameter P_{kT} and P_{kL} are both production terms of k_T and k_L.

The parameter $\nu_{T,s}$ and $\nu_{T,l}$ are the eddy viscosities of small scale and large scale, respectively.

2.3 Numerical grids

The computational domain was composed of the inner rotational part including the propeller and the outer stationary part(Fig.3). The numerical mesh was an unstructured grid, and basic cells were tetrahedral and prismatic cells were applied to near the blade surface for resolving the boundary layer (Fig. 4). The first layer thickness of the prism layer was set to a non-dimensional wall distance for a wall-bounded flow (y^+ in short) =50 in the case of the k-ε model. y^+=1 was set in the case of the SST k-ω model and the k-k_L-ω model.

3 NUMERICAL SIMULATION OF PROPELLER OPEN CHARACTERISTICS
3.1 Propeller open characteristics

Figure 3: Computational domain(POT)

Figure 4: Prism mesh arrangement near blade surface

POC at model scale gratefully depends on mixture ratio of laminar and turbulent flow. DTMB P4119 propeller[6,7] was selected for the benchmark. Table 1 shows the principal particulars. The k-ε model, the SST k-ω model with low Reynolds correction(SST k-ω (Low) in short), the SST k-ω model without low Reynolds

correction(SST k-ω(w/o corr.) in short) and the k-k$_L$-ω model were applied.

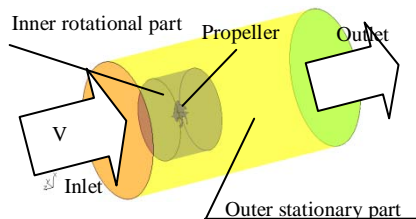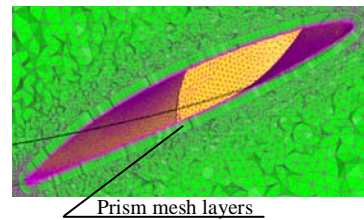First of all, POC in a different operation point is compared in Fig. 5. In the case of the k-ε model, thrust coefficient K$_T$ was overall small compared with the experiment, and torque constant K$_Q$ was large excluding advancement ratio J=1.1. The SST k-ω (Low) predicted higher K$_T$ and corresponding K$_Q$ value compared with experiment. Predicted open efficiency η$_o$ was overestimated at design point J=0.833. On the other hand, The k-k$_L$-ω model gave corresponding K$_T$ and little smaller K$_Q$ value. Propeller open efficiency η$_o$ was more corresponding well than the other turbulence models at design point J=0.833.

Next, the velocity distributions in boundary layer are compared in Fig. 6. Y/C and V_B/V_R denote non-dimensional distance from wall and velocity in the boundary layer divided by outer flow respectively. The k-ε model shows good agreement with the experimental measurement results shown in figure as "Tripped" which means the state of with roughness on the leading edge of the propeller. The estimated boundary layer thickness by the SST k-ω (Low) model is thinner than the experimental measurement results shown in figure as "Smooth" which means the state of without roughness on the leading edge of the propeller. The k-k$_L$-ω model gave better result than the SST k-ω(Low) in case of "Smooth".

Turbulence kinetic energy distributions around the blade section at 70% radius are compared in Figs. 7(a)-(d). The k-ε and the SST k-ω(w/o corr.) predicted the fully turbulent flow. Underestimation of η$_o$ was mainly due to overestimation of viscous component of K$_Q$. On the other hand, the flow field simulated by the SST k-ω(Low) was fully laminar and which causes underestimation of viscous component of K$_Q$. In the case of the k-k$_L$-ω model, flow field was mainly composed by laminar flow and partially composed by turbulent flow. In POT, leading edge roughness was not applied. Therefore, the k-k$_L$-ω model gave more corresponding η$_o$ for the POC prediction at model scale.

Table 1 Principal particulars of DTMB P4119 [6,7]

	DTMB P4119
Number of blades	3
Diameter	0.3048m
Pitch ratio(0.7R)	1.084
Skew angle	0°
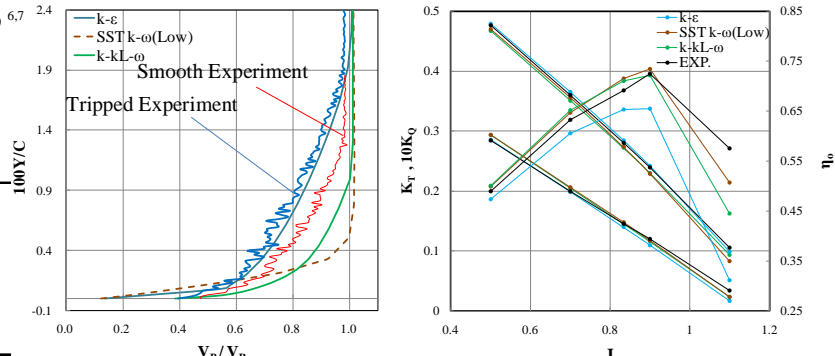
Figure 5 : Boundary layer profiles at r/R=0.7, back side, x/C=0.9

Figure 6: Propeller open characteristics

(a) k-ε   (b) SST k-ω Low   (c) SST k-ω w/o.corr   (d) k-k$_L$-ω
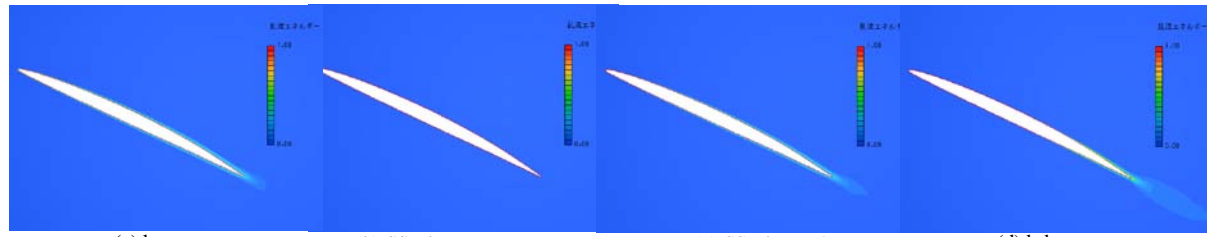
Figure 7: Turbulent kinetic energy at r/R=0.7

3.2 Transitional flow simulation

Prediction accuracy of the transitional position by using the k-k$_L$-ω model was validated with experimental results. MP2293R propeller has 'MAU' blade section which was traditionally used in past decades. MP0193R has laminar flow type of blade section. Principal particulars of propellers are shown in Table 2. Experimental and simulated results are shown in Fig. 8. Back side transitional line was located at about 60% chord length from leading edge in case of MP2293 and located at about 70% in case of MP0193. Further, simulated results of both MP2293R and MP0193 show good agreement with experimental results. It was confirmed that the k-k$_L$-ω model predicted the effects of blade section on transitional region.

3.3 Investigation of turbulence model and turbulence intensity for scale effects on POC

Seiun-Maru conventional MAU propeller(CP) [8] was selected(Table 3) for the calculation. Calculation results are compared with experimental results in Figs. 9-11. Subscripts p and v denote pressure component and viscous component respectively. Fig.12 shows flow patterns.

1) SST k-ω (w/o corr.) , SST k-ω(Low), T$_{uin}$=5%

Simulated flow field was fully turbulent. Pressure component of K$_T$ increased and frictional component of

K_T decreased when Reynolds number increased. Pressure component of K_Q increased and frictional component of K_Q decreased when Reynolds number increased. K_Q much depended on frictional component and decreased totally. As a result, η_o simply increased, however η_o was lower than experimental results at lower range of Reynolds number because of the overestimation of the frictional component. .

   2) SST k-ω(Low), T_{uin}=1%

Simulated flow field was mixture of laminar and turbulent flow and its critical radius was fixed in the range of $R_n(K)=2.5\times10^5\sim3.7\times10^5$. In this range of Reynolds number, η_o increased by decrease of boundary layer thickness. In the range of $R_n(K)=3.7\times10^5\sim1\times10^6$, critical radius moved toward inner radius and turbulent area increased when Reynolds number increased. η_o decreased by increasing wall shear stress of turbulent flow part. Over the range of $R_n(K)= 1\times10^6$, flow field was fully turbulent. By decreasing of turbulent boundary layer thickness, η_o increased at this range of Reynolds number.

   3) k-k_L-ω model, T_{uin}=1%, 5%

Simulated flow field was mixture of laminar and turbulent flow and its critical radius was fixed in the range of $R_n(K)=2.5\times10^5\sim1\times10^6$. In this range of Reynolds number, η_o increased by decrease of boundary layer thickness. This tendency was corresponding to POT. In the range of $R_n(K)=1\times10^6\sim3\times10^6$, critical radius moved toward inner radius and turbulent area increased when Reynolds number increased. η_o decreased by increasing wall shear stress of turbulent flow part. Over the range of $R_n(K)= 3\times10^6$, flow field was fully turbulent.

   4) k-k_L-ω model, T_{uin}=7.5%

Simulated flow field was mixture of laminar and turbulent flow and its critical radius was fixed in the range of $R_n(K)=2.5\times10^5\sim6.2\times10^5$. In this range of Reynolds number, η_o increased by decrease of boundary layer thickness. This tendency was corresponding to POT. In the range of $R_n(K)=6.2\times10^6\sim3\times10^6$, critical radius moved toward inner radius and turbulent area increased when Reynolds number increased. η_o decreased by increasing wall shear stress of turbulent flow part. Over the range of $R_n(K)= 3\times10^6$, flow field was fully turbulent.

In the case of Tuin=5%, SST k-ω(Low) result showed fully turbulent. This tendency was not corresponding to oil flow measurement result at SPT which flow characteristics was still mainly laminar(Fig.2). SST k-ω(Low) showed too early transition at lower Reynolds number. Normally, propeller open efficiency is increasing at $2.5\times10^5\sim8\times10^5$. k-$k_L$-ω model showed same tendency. The propeller open efficiency at turbulence intensity Tuin=1%, 5% and 7.5% were almost same and didn't depend on turbulence intensity at the normal SPT Reynolds number($R_n(K)=1.5\times10^5\sim4\times10^5$), This result supports the validity of 2POT methods.

On the other hand, propeller open efficiency in full scale depended on turbulence intensity. When energy saving devise such as duct or fin contributes to reduce the turbulence intensity of propeller inflow, there is some possibility to increase propeller efficiency by itself. However, it seems that the reduction effects of turbulence intensity may be difficult to be estimated at model scale SPT Reynolds number.

4   Numerical Self Propoulsion test
4.1 Wake simulation

The wake flow of 749GT Chemical tanker was simulated in model scale and full scale. Principal hull and MP21-5 propeller dimension are shown in Table 4 and Table 5. Turbulence intensity of inflow to the ship was set to 1%. Fig.13 shows numerical grids of wake flow simulation and numerical self propulsion simulation. For wake simulation, dummy boss was included. Fig. 14 shows comparison result of axial velocity and turbulence intensity in model and full scale. Averaged turbulence intensity in propeller plane was 5% at model scale and 3.4% at full scale.

Table 2 Principal particulars of model propellers

	MP2293R	MP0193R
Number of blades	5	5
Diameter	250 mm	250 mm
Pitch ratio(0.7R)	0.703	0.7506
Expanded area ratio	0.4	0.4
Skew angle	20°	20°

Table 3 Principal particulars of CP[12]

Number of blades	5
Diameter	400(950)mm
Pitch ratio	0.95
Expanded area ratio	0.65
Skew angle	10.5°
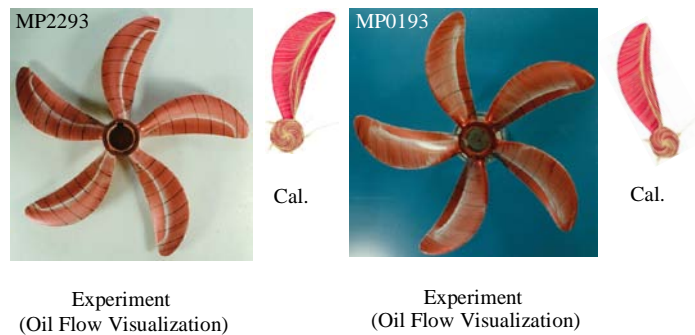
Figure 8: Surface streamlines of MP2293 & MP0193
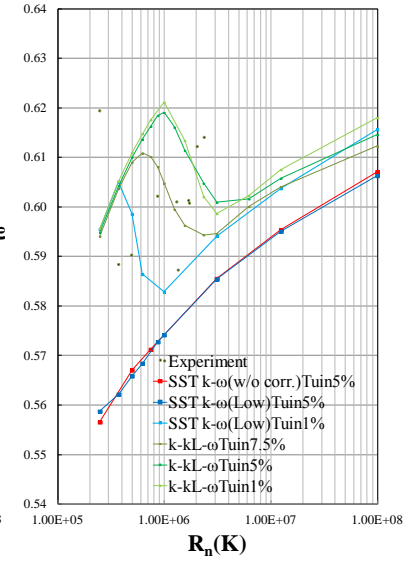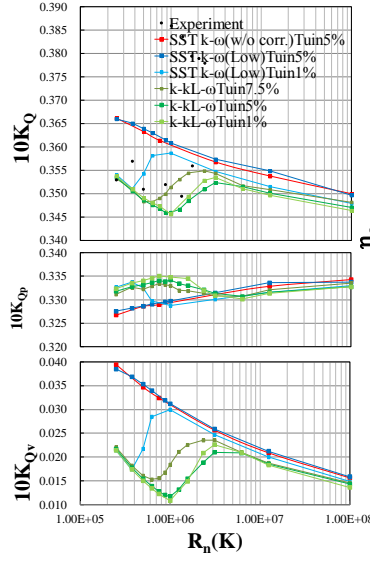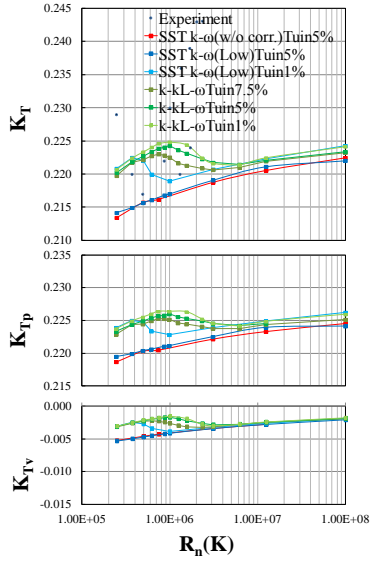
Figure 9: Effect of Reynolds number on K_T Figure 10: Effect of Reynolds number on K_Q Figure 11: Effect of Reynolds number on η_o

(a) $R_n(K)=2.5\times10^5$ (a) $R_n(K)=2.5\times10^5$ (a) $R_n(K)=2.5\times10^5$

(b) $R_n(K)=3.7\times10^5$ (b) $R_n(K)=1\times10^6$ (b) $R_n(K)=6.2\times10^5$

(c) $R_n(K)=5\times10^5$ (c) $R_n(K)=1.5\times10^6$ (c) $R_n(K)=1\times10^6$

(a) $R_n(K)=2.5\times10^5$ (d) $R_n(K)=6.2\times10^5$ (d) $R_n(K)=2.3\times10^6$ (d) $R_n(K)=1.5\times10^6$

(b) $R_n(K)=1\times10^6$ (e) $R_n(K)=1\times10^6$ (e) $R_n(K)=3.1\times10^6$ (e) $R_n(K)=3.1\times10^6$

(c) $R_n(K)=1\times10^7$ (f) $R_n(K)=3.1\times10^6$ (f) $R_n(K)=1.2\times10^7$ (f) $R_n(K)=1.2\times10^7$

SST k-ω (w/o corr.), T_{uin} 5%   SST k-w (Low), T_{uin} 1%   k-k_L-ω, T_{uin} 5%   k-k_L-ω, T_{uin} 7.5%
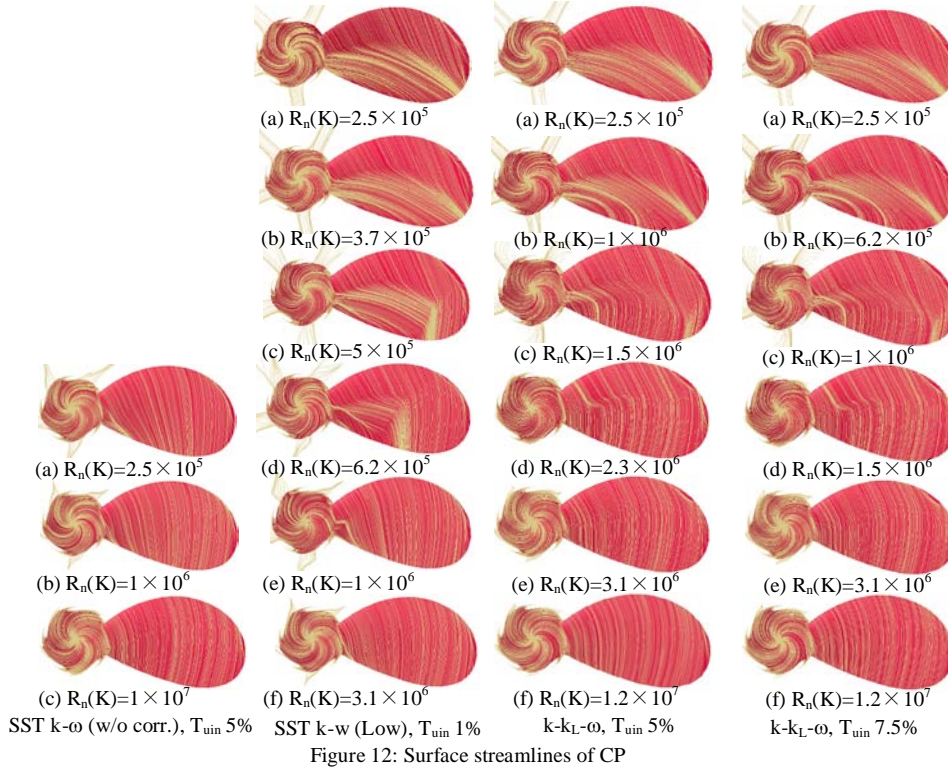
Figure 12: Surface streamlines of CP

4.2 Comparison of flow characteristics between POT and SPT condition

From the wake simulation of 749GT Chemical tanker, turbulence intensity for the propeller seemed to be abt.5% in model scale. In this research, flow characteristics around blade of MP21-5 propeller were investigated. POC is shown in Fig. 15. For also this case, POC at 1% and 5% were close value at model scale($R_n(K)=3.5\times10^5$). Flow patterns at 1% and 5% are compared in Fig.16(a) and (b). Both results showed similar laminar and turbulent flow at POT condition. Flow pattern at SPT condition is shown in Fig. 17(a). Propeller flow pattern was still laminar and similar to POT condition. This result supports the validity of 2POT methods, although the turbulence intensity of propeller inflow at POT is less than SPT. On the other hand, full scale flow pattern were fully turbulent at POT and SPT condition(Fig.16(c) and Fig.17(b)).

4.2 Numerical self propulsion analysis

For deriving self propulsion factors, propeller shaft speed was changed to adjust propeller thrust to hull resistance just as same as experimental SPT. Wave resistance was not derived from numerical calculation but referred from experimental result. Self propulsion factors were derived by using propeller open water characteristics at turbulence intensity $T_{uin}=1\%$ and 5% in model scale. Full scale condition was also analyzed

by using the propeller open efficiency at turbulence intensity T_{uin}=3.4%. Table 6 shows derived self propulsion factors. Numerical results showed comparatively good agreement except thrust deduction factor and rotative efficiency. Derived self propulsion factors are almost same value at turbulence intensity T_{uin}=1% and 5% at model scale($Rn(K)$=3.5×10^5) . Full scale result shows well known decrease of wake fraction factor.

Table 4: Pricipal particualrs of hull dimension

Ship	67m
LBP	11.3m
Depth	5.5m
Draught	4.75m

Table 5: Pricipal particualrs of MP21-5

	MP21-5
Number of blades	4
Diameter	3.0m
Pitch ratio(0.7R)	0.8
Expanded Area ratio	0.48
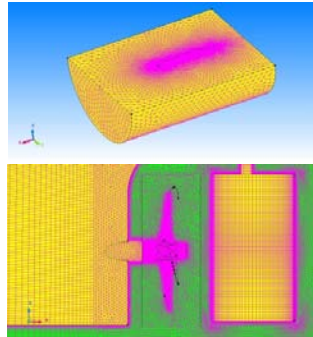
Figure 13:Numerical grids
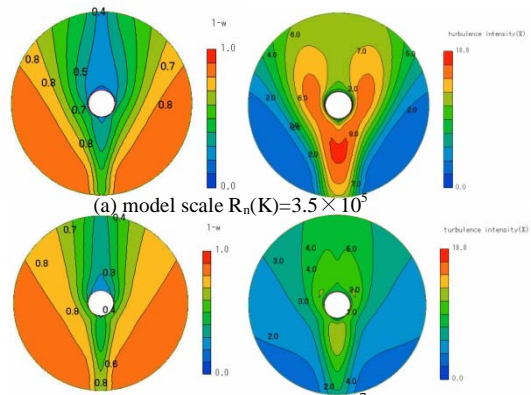
(a) model scale $R_n(K)$=3.5×10^5

(b) full scale $R_n(K)$=1.5×10^7

Axial velocity   turbulence intensity Tuin(%) in wake flow

Figure 14:Axial velocity and turbulence intensity in wake

T_{uin} 1%(POT) T_{uin} 5%(POT)   SPT

(a) $R_n(K)$=3.5×10^5

T_{uin} 3.4%(POT)   SPT

(b) $R_n(K)$=1.5×10^7
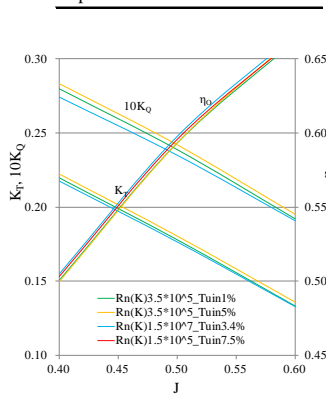
Figure 16: Surface streamlines (MP21-5)

Figure 15: POC of MP21-5

Table 6: Numerical self propulsion analysis result

	Exp.	Numerical		
Rn(K)		3.5*10^5		1.5*10^7
POT_T_{uin}(%)	-	1.0	5.0	3.4
J_{POT}	0.531	0.523	0.529	0.535
K_T	0.171	0.168	0.168	0.162
$10K_{Q\ POT}$	0.233	0.228	0.229	0.220
η_o	0.620	0.612	0.617	0.625
1-w	0.700	0.687	0.694	0.744
1-t	0.832	0.811	0.811	0.826
η_r	1.034	1.019	1.022	1.037
η_d	0.762	0.737	0.737	0.720

5   CONCLUSIONS

- The k-k_L-ω model predicted boundary layer thickness and POC in comparatively good accuracy in the range of transitional Reynolds number.
- Flow pattern of POT condition at turbulence intensity T_{uin}=1% and 5% were still mainly laminar and almost same at model scale. Flow pattern at SPT was also still mainly laminar and similar to POT condition. This result supports the validity of 2POT methods, although the turbulence intensity of propeller inflow at POT is less than SPT.
- Numerical self propulsion analysis results showed comparatively good agreement with experimental result except thrust deduction factor and rotative efficiency. Further improvement is necessary.

REFERENCES

[1] Tamura, K. and Sasajima, T.,"Some Investigation on Propeller Open-Water Characteristics for Analysis of Self-Propulsion Factors", Mitsibishi Technical Bulletin, No.119, pp.1-12 (1977).

[2] ITTC-Recommended Procedures and Guidelines, Testing and Extrapolation Methods Propulsion, Propulsor Open Water Test, 7.5-02-03-02.1, Revision 02, (2008).

[3] Lee, S.-J., Kim, H.-R., Kim, W.-J., Van, S.-H., 2003. Wind tunnel tests on flow characteristics of the KRISO 3,600 TEU containership and 300K VLCC double- deck ship models. J. Ship Res. 47 (1), 24–38.

[4] Streckwall, H., Greitsch, L. and Scharf, M.," An advanced Scaling Procedure for Marine Propellers", Proc. of The 3rd International Symposium on Marine Propulsors smp'13, Launceston, Australia, (2013).

[5] Tsuda, T., Konishi, S., Asano, S., Ogawa, K. and Hayasaki, K.,"Effect of Propeller Reynolds Number on Self-Propulsion Performance", The Japan Society of Naval Architects and Ocean Engineers, 169, (1978).

[6] Gindroz, B., Hoshino, T. and Pylkkanen, V.,"Propeller RANS/Panel Method Workshop", 22nd ITTC Propulsion Committee Propeller RANS/Panel Method Workshop, Grenoble, Apr., (1998).

[7] Jessup, S.D.,"Experimental Data For RANS Calculations and Comparisons(DTMB P4119)", 22nd ITTC Propulsion Committee Propeller RANS/Panel Method Workshop, Grenoble, Apr., (1998).

[8] Funeno, I.,"On Viscous Flow around Marine Propellers - Hub Vortex and Scale Effect –", J. of Kansai SNA, Vol.238, pp.17-27, (2002).

Reflections on the Importance of Full-Scale Computations for Ship Flows

Karsten Hochkirch, FutureShip, Potsdam/Germany, karsten.hochkirch@GL-group.com
Volker Bertram, FutureShip, Hamburg/Germany, volker.bertram@GL-group.com
Benoit Mallol, Numeca, Brussels/Belgium, benoit.mallol@numeca.be

CFD for resistance and propulsion analyses is sometimes referred to as the "numerical towing tank". The term "numerical sea trials" would be more appropriate, as CFD nowadays often simulates the flow around ships at full-scale Reynolds numbers. High-fidelity CFD refers to RANSE (Reynolds-averaged Navier-Stokes equations) solvers which employ fine grids and advanced turbulence models. We will discuss here the justification for using high-fidelity, full-scale CFD for ship flows. We refer to *Hochkirch and Mallol (2013)* for a much more extensive discussion and description of the employed CFD software suite FINE^{TM}/Marine.

Scale effects do not only concern the boundary layer, but also flow separation and wave breaking, which interact. *Visonneau et al. (2006)* come to the conclusion that a "[…] complete analysis of the scale effects on free-surface and of the structure of the viscous stern flow reveals that these scale effects are not negligible and depend strongly on the stern geometries."

The main choices for hydrodynamic assessment of hull, trim and appendages are:

- Rankine panel methods (fully non-linear wave resistance codes). Pros and cons are:
  - ☺ The codes capture global wave patterns and predict dynamic trim and sinkage well in most cases.
  - ☺ The codes are very fast. Processes for grid generation and computation have been fully automated and computational times may be less than a minute for one speed and one geometry on a regular single-processor computer.
  - ☹ The codes reach limits of applicability for flows with breaking waves, semi-planing or planing boats, and extreme non-linearity. Typical critical cases are emerging bulbous bows and immersing transom sterns with the associated complex wave breaking.
  - ☹ Viscous effects (such as a recirculation zone at the stern or wave-boundary layer interaction) cannot be modelled correctly.

  The automation and the short computational times have fostered wide-spread acceptance in ship design and with some time delay also in ship hull optimization.

- Free-surface RANSE methods (in our case, FINE^{TM}/Marine). Pros and Cons are:
  - ☺ The codes capture global and local wave patterns including complex breaking waves.
  - ☺ The codes can capture viscous effects at full scale.
  - ☹ Computational times are significant, even on parallel processor architectures.
  - ☹ Quality of results differs significantly between various CFD service suppliers. It is difficult for the general public to identify competent and less competent suppliers.

  Free-surface RANSE codes are the standard choice in designing propulsion improving devices and ship aftbodies, i.e. cases where viscosity effects dominate. Application in ship design are much more widespread than in optimization where the high computational effort requires a combination of massive computing power and smart optimization strategies.

- Model basin tests. Pros and cons are:
  - ☺ Widely known in the industry and de facto standard for power predictions.
  - ☺ Industry standards exist for most procedures through ITTC (International Towing Tank Conference) as international expert body. Therefore all larger model basins listed by ITTC offer comparable quality in services.
  - ☹ Scaling laws are violated by necessity.
  - ☹ Model tests are time-consuming and expensive.
  - ☹ Parallel operation is not possible.

In summary, model tests suffer from scale effects like panel methods and are slow and expensive as RANSE simulations, albeit without the hope of parallel operation which makes RANSE simulations increasingly feasible also for wide-spread design investigations and optimization projects. Model tests are hardly suitable for appendages such as propulsion improving devices due to scale effects. For trim optimization, model tests are also hardly suitable. Trim optimization for most ship types require sufficiently fine coverage of a range of speeds, drafts and trim angles to be accurate. Certain intermediate draft and trim conditions will feature discontinuities, when bulbous bows emerge and transom stern immerse. The associated breaking wave patterns show larger scale effects than "benevolent" loading conditions such as the design draft and trim.

In the following, we look at some case studies illustrating our point:

- Trim optimization

  For the Military Sealift Command (MSC), FutureShip evaluated trim dependence by traditional model testing and CFD simulations for one vessel. The model tests were performed at the Hamburg Ship Model Basin (HSVA). The analyses focused on calm-water powering performance, specifically on changes of the delivered power (P_D) requirement. CFD simulations were performed both for full scale and for model scale (1:25.67). The study showed that generally full-scale measurements, model tests, and CFD agreed well with each other concerning the trends in power requirement with respect to trim. As full-scale data were available only for a few sailing conditions, most comparisons focused on CFD and model test results. The ranking derived from CFD simulation at model scale agreed very well with model tests, Fig.1 (left). However, for certain conditions, the model basin extrapolations to full scale deviated significantly from the CFD prediction, Fig.1 (right).
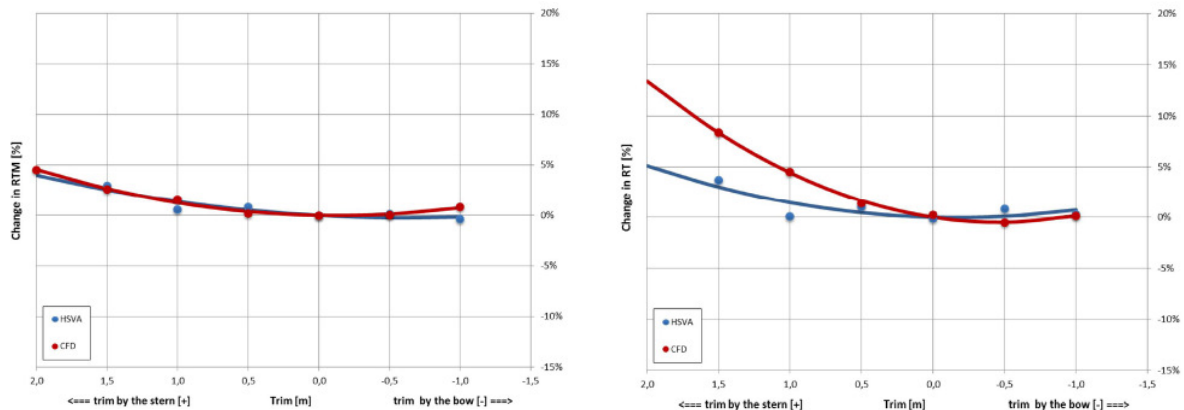
Fig.1: Change in total resistance R_T with trim for one speed and draft;
model scale (left) and full scale (right);
HSVA = model tests / model test extrapolation; CFD = computations with FINE^{TM}/Marine

- Hull optimization

  For a new build project of a 2300 TEU container ship, a ship owner and a ship yard agreed on a formal hull optimization to improve fuel efficiency of the new design across an operational profile of service conditions. The parametric design for the optimization had 65 free form parameters. The ship owner specified nine operational conditions (combinations of draft and speed), with an associated weight reflecting the estimated time the vessel would sail in each condition. Constraints were imposed on displacement, stability, and several hard points (deck for container stowage, aftbody for engine, forebody for bow thruster, etc.). First, a concept exploration model was set up based on a wave resistance calculation. Displacement constraints were relaxed allowing 4% deviation for wider design exploration. More than 6000 variants were thus investigated covering the design space with a quasi random sequence

(SOBOL algorithm). This concept exploration served as discussion basis for the next stage with more constrained specifications. The pre-optimization study revealed already significant potential for hull improvement, Fig.2. The most promising design candidate from the pre-study was selected for an optimization restart focusing on the aft body flow and the wake characteristics, using a RANSE solver and performing numerical propulsion tests. This proper optimization loop considered more than 3000 aftbody variants, considering resistance and wake as indicators for least power and fuel consumption, however, it must considered, that the full scale wake significantly differs from the model scale prediction. The wave pattern shows significant improvement, Fig.3. The optimized hull design had approximately 8% lower required power P_D compared to the baseline design. In addition, the stability was improved adding 14 cm to the KM value at scantling draft.
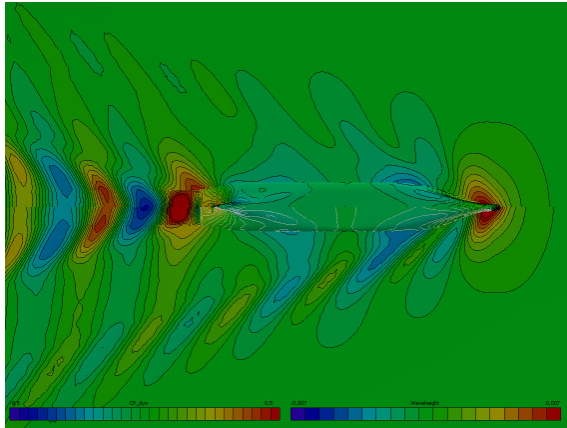
Fig.2: Wave pattern and hull pressures by potential-flow based pre-study; baseline design (bottom) and best design of pre-study (top)
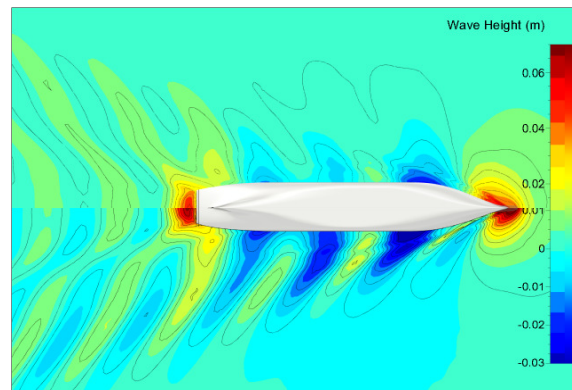
Fig.3: Wave pattern by RANSE; baseline design (bottom) and optimized design (top)

- Appendage improvement

Appendages contribute above proportion to fuel consumption of ships. The rise in fuel costs has lead to a renaissance in interest in propulsion improving devices (PIDs). These are generally appendages in the aftbody of the ship, in the (upstream or downstream) vicinity of the propeller. As such, PIDs are strongly affected by scale effects. An OCIMF (Oil Companies International Marine Forum) report on energy efficiency measures for large tankers sums up, *NN (2011)*: "Opinions on propulsion improving devices scatter widely, from negative effects (increasing fuel consumption) to more than 10% improvement. Full scale CFD simulation [during design] [...] may reduce the present uncertainty." *Zorn et al. (2010)* compare the effect of a propulsion improving device both in model and in full scale, and both on resistance and propulsion, Fig.4. The investigation is typical for the lowest level of hydrodynamic design involving PIDs, namely just the comparison of two variants (with and without a given nozzle geometry and arrangement). Such an investigation should always be performed at full scale and including the propeller in the computational model. Similar analyses have been used to improve "negative" appendages, i.e. recesses in ship hulls, such as bow thrusters, Fig.5.
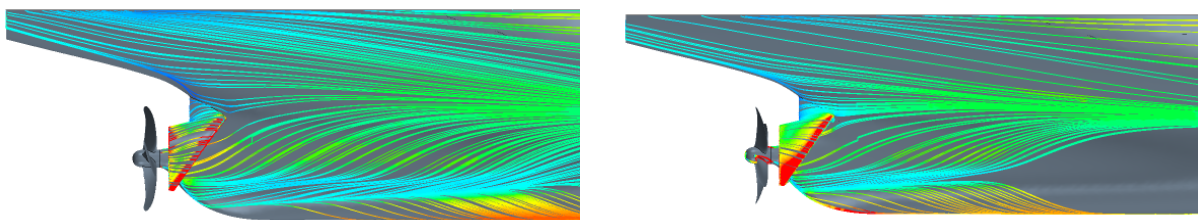
Fig.4: Numerical propulsion test for tanker with nozzle; streaklines (wall shear stress streamlines) for model scale (left) and full scale (right); *Zorn et al. (2010)*
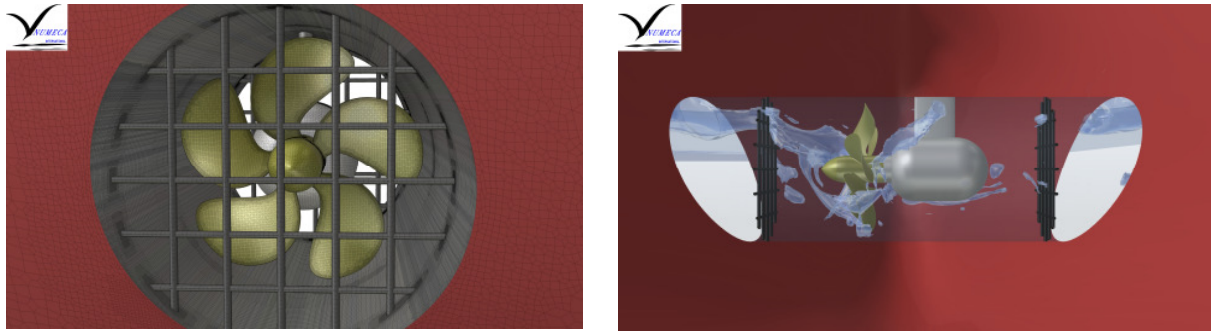
Fig.5: Bow thruster analyses using full-scale RANSE

Yu (2011) investigates a twisted rudder. After the classical investigation of two geometries (twisted and not twisted), he couples the FRIENDSHIP Framework to the CFD solver to reduce the rudder drag by 12% (for given rudder lift force) which corresponds roughly to 1% fuel savings. Fig.6 shows an application for an optimization of headbox and twisted rudder for a twin-skeg vessel. As the rudders of twin-skeg vessels are much closer to the free surface, their impact on the wave pattern is not negligible and fine tuned optimization is required to achieve best fuel efficiency. Such formal optimization studies reflect the current state of the art in industry. However, only few projects provide sufficient time and budget to spend similar attention and resources on appendages as on the main hull. We expect this to changes, as response time for such analyses will decrease with time and attention to appendages is likely to increase with fuel prices.
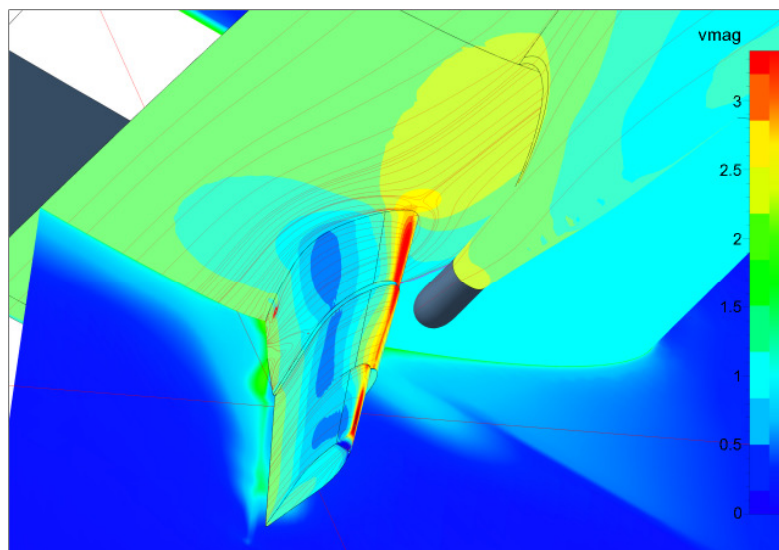
Fig.6: Twisted rudder behind propeller in CFD optimization study

In conclusion, simpler methods such as panel methods or model-scale investigations have their usefulness, as demonstrated in many projects. However, our experience confirms the observation of *Duvigneau et al. (2002,2003)*: "[…] the information given by the model scale computations is useful for the full-scale problem, but only in terms of trend. When the fitness of the shape optimized at model scale is evaluated at full scale, it can be seen that about three-quarters of the improvement is obtained compared with the optimization at full scale." Thus we get trends, we get even significant improvement, when using model-scale analyses, but we may also miss out on significant further improvement.

Advances in available brute-force computing power, parallel computing, re-use of knowledge from other computations (restart and meta-modelling) will eventually open to path to wide-spread application of full-scale computations. This is a natural evolution which has started already and we expect that full-scale CFD analyses also for optimization projects will become standard within the next decade.

References

DUVIGNEAU, R.; VISONNEAU, M.; DENG, G.B. (2002), *On the role played by turbulence closures in hull shape optimization at model and full scale,* 24th ONR Symp. Naval Hydrodynamics, Fukuoka
http://www-sop.inria.fr/members/Regis.Duvigneau/Publis/article_ONR_2002.pdf

DUVIGNEAU, R.; VISONNEAU, M.; DENG, G.B. (2003), *On the role played by turbulence closures in hull shape optimization at model and full scale,* J. Marine Science Technology 8, pp.11-25

HOCHKIRCH, K.; MALLOL, B. (2013), *On the importance of full-scale CFD simulations for ships*, 12th Conf. Computer and IT Applications in the Maritime Industries (COMPIT), Cortona, pp.85-95
http://www.ssi.tu-harburg.de/doc/webseiten_dokumente/compit/dokumente/compit2013_cortona.pdf

MIZINE, I.; KARAFIATH, G.; QUEUTEY, P.; VISONNEAU, M. (2009), *Interference phenomenon in design of trimaran ship,* 10th Int. Conf. on Fast Sea Transportation (FAST), Athens
http://www.numeca.be/fileadmin/newsite/Papers/2009_-
_Interference_Phenomenon_in_Design_of_Trimaran_Ship_-_FAST_09_-_Misine_et_al.__1_.pdf

NN (2011), *GHG emission-mitigating measures for oil tankers*, Oil Companies International Marine Forum (OCIMF), London
http://www.ocimf.com/mf.ashx?ID=e6b71174-bd2f-4248-b88d-f4977955c0f2

VISONNEAU, M.; QUEUTEY, P.; DENG, G.B. (2006), *Model and full-scale free-surface viscous flows around fully-appended ships,* ECCOMAS CFD 2006, Egmond aan Zee

YU, H.Z. (2011), *Twisted rudder in viscous flow,* Master Thesis, TU Berlin

ZORN, T.; HEIMANN, J.; BERTRAM, V. (2010), *CFD analysis of a duct's effectiveness for model scale and full scale*, 13th Numerical Towing Tank Symp. (NuTTS), Duisburg
http://www.uni-due.de/imperia/md/content/ist/nutts_01_2010_duisburg.pdf

Appendix: FINE^{TM}/Marine Software

Our high-fidelity CFD applications shown here are based on FINE^{TM}/Marine, which can be seen as representative of leading-edge CFD marine software. FINE^{TM}/Marine is a CFD product of NUMECA International. This software suite is dedicated to marine applications and integrates:

- Full-hexahedral unstructured mesh generator HEXPRESS^{TM}, Fig.7

- Free-surface RANSE solver ISIS-CFD: Turbulent flow is simulated by solving the incompressible unsteady Reynolds-averaged Navier-Stokes equations (RANSE). The solver is based on the finite volume method to build the spatial discretization of the transport equations. The face-based method is generalized to two-dimensional, rotationally symmetric, or three-dimensional unstructured meshes for which non-overlapping control volumes are bounded by an arbitrary number of constitutive faces. The velocity field is obtained from the momentum conservation equations and the pressure field is extracted from the mass conservation constraint, or continuity equation, transformed into a pressure equation. In the case of turbulent flows, additional transport equations for modelled variables are discretized and solved using the same principles. Several turbulence models ranging from one-equation model to Reynolds stress transport model are implemented in ISIS-CFD. Free-surface flow is simulated with an interface capturing approach. Both non-miscible flow phases (air and water) are modelled through the use of a conservation equation for a volume fraction of phase. The free-surface location corresponds to the isosurface with volume fraction a = 0.5. To avoid any smearing of the interface, the volume fraction transport equations are discretized with a specific discretization scheme which ensures the accuracy and sharpness of the interface.

- Dedicated flow visualizer CFView, Fig.8

FINE^{TM}/Marine has been validated against model tests for a variety of test cases, e.g. *Mizine et al. (2009)*. The performance of the code has been also demonstrated in computations at model and full scale for a fully appended hull configuration including free-surface, ducted propeller, brackets and rudder, *Visonneau et al. (2006)*. The computations agree well with full-scale measurements (within the EU project EFFORT). This indicates that CFD tools may be used with confidence to predict full-scale conditions in ship design. Various CFD codes can capture full-scale viscous flows with free surfaces. However, good quantitative predictions require advanced techniques as offered by FINE™/Marine and sufficient grid resolution.
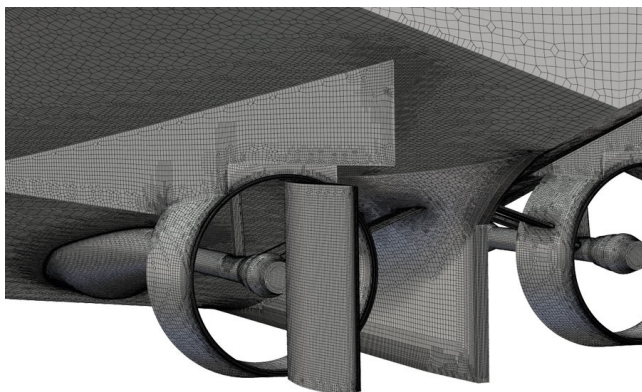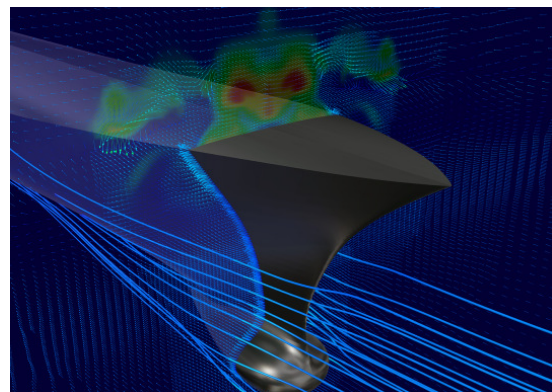

Fig.7: Mesh generation with HEXPRESS^{TM}

Fig.8: Flow visualization with CFView

Flow past a sphere at the free-surface using URANS

Marion C. James[*], **Stephen R. Turnock, Dominic A. Hudson**

Fluid-Structure Interactions Research Group; University of Southampton, Southampton, UK. SO17 1BJ

1 Introduction

A better understanding of the fluid-structure interactions of a sphere located at the free-surface would benefit many engineering fields such as the offshore oil and gas sector with storage tanks, the marine transportation industry with bulbous bows and submarines, as well as any swimming body. Most of these fields are within the Reynolds number range $4x10^4$ - $6x10^6$. Achenbach (1972) studied this Reynolds number range in a wind tunnel environment, and classified the different flow types observed into: sub-critical (Re $\leq 2x10^5$), critical ($2x10^5 \leq$ Re $\leq 4x10^5$), super-critical ($4x10^5 \leq$ Re $\leq 10^6$) and transcritical (Re $\geq 10^6$). Hoerner (1965) gathered several experimental data, and identified that the drag coefficient has a fairly constant value of 0.47 at sub-critical Reynolds numbers, but it drops drastically to a value of 0.1 between $2x10^5$ and $4x10^5$. This phenomenon is well known under the name of 'drag crisis'. As the flow speed increases, mixing of the turbulences becomes more chaotic in the boundary layer region increasing the fluid momentum. Consequently, the boundary layer flow separation is delayed resulting in a decrease in the pressure differential between the front and the rear of the sphere.

The critical Reynolds number range was further studied experimentally by Taneda (1978), Jeon et al. (2004), Bakic and Peric (2005), Ozgoren et al. (2011). Taneda (1978) identified separation points using an oil-flow visualisation technique. On average, the flow separates at an angle of 80°from the front stagnation point for $10^4 \leq$ Re $\leq 3x10^5$. Furthermore, Taneda (1978) observed a radical change in the boundary layer characteristics around Re = $3.5x10^5$ with three speration lines at 100°, 117°and 135°. These lines may be identified as the laminar separation line, the reattachment line and the turbulent separation line respectively. At the rear of the sphere, an Ω -shaped line was observed due to the reattachment of all the streamlines. Hair-pin vortices are shed at the rear of the sphere in an asymmetric manner (Kiya et al., 2000). Bakic et al. (2006) underlined the complexity of the wake structure behind the sphere and identified the existence of a sub-harmonic of the vortex shedding frequency.

Only a few numerical investigations of the flow past a sphere have been performed to-date. Large-Eddy Simulations (LES) and Detached-Eddy Simulations (DES) were undertaken at sub-critical (Constantinescu, 2000) and supercritical (Jindal et al., 2004) Reynolds numbers. Good agreements with experimental data gathered by Achenbach (1972) were found for the drag coefficient and the pressure distribution.

The influence of the free-surface on a submerged sphere travelling at a speed equivalent to Reynolds number 5000 was studied both experimentally and numerically ((Hassanzadeh et al., 2012), (Ozgoren et al., 2012), (Ozgoren et al., 2013)). For small immersion depths, Hassanzadeh et al. (2012) showed that the recirculating region in the half-lower side of the wake region is larger compared to the half-upper side. Furthermore, a strong interaction between the fluctuated streamwise and transverse velocities in the half-lower side of the wake region was observed leading to a higher mixing flow rate. A strong interference between the sphere wake and the free-surface was noticed by Ozgoren et al. (2013) at an immersed depth to diameter ratio of 0.25 (from the top side of the sphere). However, no literature on the fluid-structure interactions of a sphere located at the free-surface is known by the author, as previously mentioned by Ozgoren et al. (2012).

Consequently, this paper will investigate the influence of the free-surface on the flow past a sphere located half-way between the air and water phases using Unsteady Reynolds-Averaged Navier-Stokes (URANS) simulations, and validated with experimental data obtained in a towing tank environment.

2 Towing Tank Experiment

The flow past a sphere located at the free-surface, was studied over the critical Reynolds number range: $2x10^5 \leq$ Re $\leq 4x10^5$. Experiments were carried out in the Lamont tank at the University of Southampton. The tank dimensions are: 30 x 2.4 x 1.2 $[m^3]$. The equivalent depth-based Froude number for the tested speeds is between 0.3 and 0.7 (ie. within the sub-critical flow range).

Due to time and cost constraints, a first sphere prototype was manually constructed based on a youth-size basketball covered with an epoxy resin. The resulting sphere diameter is 225mm and was

---

[*]*corresponding author's e-mail*: M.James@soton.ac.uk

ballasted in order to attain neutral buoyancy. Drag measurements were taken at speeds between 1.0 and 2.2 $m.s^{-1}$ with a 0.2 $m.s^{-1}$ step, and further data points were obtained around the transitional point. The water temperature was recorded as 10 degrees Celsius, thus the kinematic viscosity value was taken as $1.31x10^{-6}m^2.s^{-1}$ (Newman, 1977).

An above-water camera was placed on the carriage in order to identify the separation angle. Drag and side forces were both recorded. Digital signal processing of the side force trace was performed to determine the shedding frequency of the vortex street formed at the rear of the sphere at high Reynolds numbers. The power spectral distribution was evaluated using the 'PWELCH' function in Matlab for each speed and for a sampling frequency of 100 Hz. This function is based on the Goertzel algorithm which efficiently solves the coefficients from the discrete Fourier transform in order to get the sampling data from the time domain into the frequency domain (Roth, 2008).

The vortex shedding frequency was identified from the power spectral distribution. This frequency represents the number of vortices formed at one side of the 'street' in the unit of time (Hoerner, 1965). The non-dimensionalised form is commonly called Strouhal number and may be expressed as $St = \frac{F_S D}{V}$.

Furthermore, an array of two wave probes was positioned on the side of the tank to obtain the wave resistance created by the sphere. A labelled picture of the experimental set-up is provided in Figure 1.
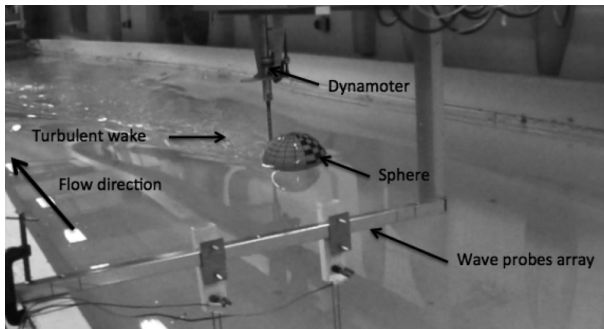
Figure 1: Overview of experiment set-up in the Lamont tank (University of Southampton)

3 Numerical Investigation

Due to time constraints, the experimental study only covered the case of a sphere located at the free-surface. The influence of the sphere's immersion depth on wave resistance was first analysed using a linear potential flow theory, before solving the Navier-Stokes equations.

3.1 Potential flow

Early linear potential flow method was pioneered by Michell (1898) and Eggers (1955), and further developed by Insel (1990) in order to determine the wave pattern of slender bodies and their associated wave resistance through a homogeneous, inviscid, incompressible and irrotational flow. The disturbance velocity potential of the discretised body is assumed to be generated by a distribution of Havelock sources over the centreline of the body (y = 0). According to Michell (1898), these sources have a strength of magnitude 2*U*Y(x,z), where U is the free stream velocity and Y(x,y) the offset at point (x,z). Couser et al. (1998) improved the results obtained from Insel (1990) method with the addition of a virtual appendage to the hull transom. The separated flow at low speeds and the air cavity at high speeds were then accounted for.

The wave resistance of the sphere tested in the Lamont tank was evaluated using an in-house potential flow code. The domain was defined by the Lamont tank width and depth dimensions (2.4 x 1.2 $[m^2]$). The sphere was discretised with 4900 triangular panels (50 vertical faces and 50 around faces). A virtual cylinder was then added at the rear of the sphere in order to simulate the separated wake at the lower speeds and the air gap at the higher speeds. Only the front half of the sphere was kept with the same level of discretisation and a cylinder of base D and height 2.5D (where D is the sphere diameter) was added (Figure 2).
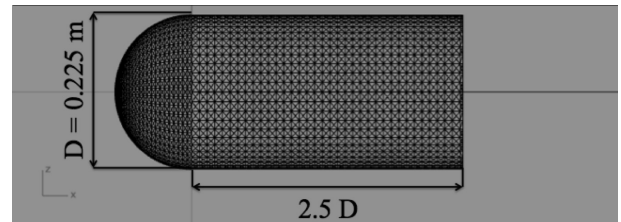
Figure 2: Discretised sphere and virtual appendage added to model the separated flow at low speeds

The effect of the virtual appendage on the total resistance was studied for the sphere located at the free-surface and compared with the experimental data. Based on these findings (Section 4.2), the influence of immersion depth on the wave resistance was tested across the critical Reynolds number range. The immersion depth of the sphere may be compared to the draught of a ship (i.e. the distance between the bottom of the sphere and the free-surface). It will be expressed as a percentage of the sphere diameter throughout this report.

3.2 URANS simulations

3.2.1 Pre-processing

The domain size is matched to the Lamont tank with both water and air phases separated by a free-surface. The cross-sectional area is based on the Lamont tank width and depth (2.4×1.2 $[m^2]$) in order to replicate the same blockage. An air draught of four sphere diameters above the free-surface was chosen. The air draught is thought to not have much influence on the results since the air resistance is considered as negligible. The domain total length is 3.2m, allowing 3D upstream and 10D downstream of the sphere.

Boundary conditions were chosen to closely represent the experimental conditions. The velocity and pressure fields inlet and outlet boundary conditions are fixedValue/outletInlet and zeroGradient/fixedValue respectively. The turbulence model entry fields (k, omega, nut) have fixed inlet values and zero gradient outlet boundary conditions. The sphere is modelled as a non-slip wall and the sides are considered as slip to reduce the computational time.
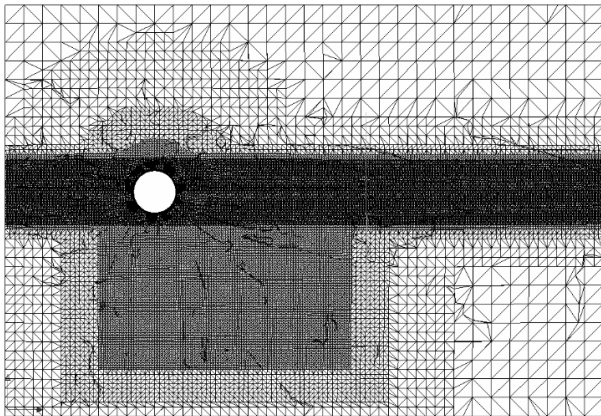
Figure 3: Hybrid mesh in the x-z plane

The OpenFOAM meshing tool snappyHexMesh (2.1.1) was used to design a hybrid mesh. A structured boundary layer was built on the sphere with a y^+ value of 30, based on the turbulent boundary layer thickness defined by Newman (1977). A non-structured mesh surrounds the sphere across the entire domain. The refined mesh at the free-surface was constructed to accommodate twice the wave elevation recorded during the experiment. The free-surface mesh was further refined vertically to effectively capture the wave pattern. Furthermore a refinement box was added around the sphere (1D upstream, 4D downstream) in order to define the stagnation point correctly and take into account the high pressure gradients just upstream of the sphere and in the wake. Using a smooth growth rate throughout the domain, a numerical beach was

added at the outlet to damp any waves which may be reflected. This mesh design totals 3.4 million cells and is shown in Figure 3.

3.2.2 Simulation

Due to the inclusion of a free-surface, the solver interFoam (version OF-2.2.0) was used to simulate the flow past the sphere with a Courant number of 1.2 to allow the simulations to run faster without compensating on the results' accuracy. The turbulence model $k\omega - SST$ was applied since it accurately models boundary layers under strong adverse pressure gradients, separation and recirculation. The turbulent energy, dissipation rate and viscosity were respectively defined as follows: $k = \frac{3}{2}(UI)^2$, $\omega = C_\mu^{-\frac{1}{4}}$, $\nu_T = \sqrt{\frac{3}{2}}(UIL)$.

A turbulence intensity of 1% was selected, although an investigation on the influence of the turbulence intensity level on the results should be performed. The turbulent length scale was based on 0.07D and the usual turbulent constant of 0.09 was used.

The sphere was first located three diameters below the free-surface and progressively brought up to the free-surface. The internal fields of the case with the sphere at the free-surface were mapped with a case where the sphere had one diameter of immersion depth to allow smooth formation of the wave pattern.

4 Results and Discussion

4.1 Qualitative results

From the above-water camera positioned above the sphere, screenshots were taken at each speed. A matrix of these screenshots is presented in Figure 4. It may be noticed that the flow stays laminar up to a speed of 1.7 $m.s^{-1}$ (Re = 2.9 x 10^5), and then transitions to turbulent at 1.75 $m.s^{-1}$ (Re = 3.0 x 10^5). After transition, the sphere wetted surface area is maximal, and as speed increases the flow stays attached to the sphere for longer reducing the pressure differential between the front and the rear of the sphere and hence decreasing the pressure drag. The transition from laminar to turbulent flow is strongly influenced by the free-surface with the creation of a bow wave at the lower speeds. The resulting flow characteristics should be further investigated with the use of dye paint and pressure sensors.
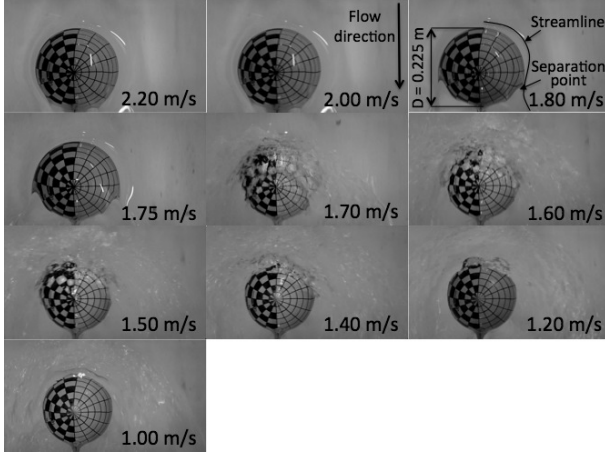
Figure 4: Above water screenshots emphasising transition from laminar to turbulent flow

Figure 6: Comparison of resistance curves obtained from the experiment, potential flow and CFD

Figure 5: Separation angle versus speed measured from above camera (+/- 5 degrees error margin)

From Figure 4, the separation angle was measured to study the variation with speed (Figure 5). At the lowest speed, a separation angle of 35°was found although this is suspected to be an observation of the bow wave characteristic. The separation angle increased up to about 70°just before the transitional speeds and reached 142°at $4x10^5$.

4.2   Drag force

Figure 6 provides a comparison of the total resistance coefficient obtained experimentally, with potential flow and from CFD simulations for a sphere advancing at the free-surface with speeds ranging between 1.0 $m.s^{-1}$ and 2.2 $m.s^{-1}$.

During the towing tank tests, the drag force was recorded using a sampling frequency of 100 Hz. The drag force was averaged over the steady portion of the drag force trace and non-dimensionalised with $0.5\rho A_p V^2$. Three repeats for each speed were performed in order to obtain an accurate mean drag curve as shown in Figure 6. The repeatability of the results proved to be very good, with a maximum error of 6.5% at the lowest speed and on average only a 0.5% discrepancy was recorded. At the lower speeds (below Re = 2.6 x 10^5), a constant drag coefficient of 0.8 was measured. The drag crisis follows between 1.5 $m.s^{-1}$ and 2.0 $m.s^{-1}$, and the drag coefficient drops down to 0.17 at 2.2 $m.s^{-1}$ (Re = 3.8 x 10^5).

Potential flow applied to the sphere only underpredicts the wave resistance and thus the total drag. The drag curve for the sphere including the virtual cylinder appendage is also displayed in Figure 6. At low speeds, there appears to be a better match with the experimental data for the sphere with the virtual appendage. Indeed, the flow separates early on after the stagnation point as emphasised in Figure 4. However, at higher speeds, there is a better agreement on the drag coefficient between experimental data and potential flow for the sphere without the virtual cylinder attached. Figure 7 exhibits a flow which stays attached to the sphere over a long portion of the sphere at the maximum speed tested. This translates in a very narrow (or absent) air cavity at the rear of the sphere, cancelling the need for a virtual appendage.

CFD simulations largely underestimate the drag coefficient at the laminar speeds. It is important to note that, due to time constraints, the mesh designed for a speed of 2.0 $m.s^{-1}$ was used for all tested speeds and may therefore not be adapted to the laminar speeds. Furthermore, all laminar speeds were run with the $k\omega - SST$ turbulence models. It would be preferable to re-run these sim-

ulations with the laminar RASmodel, acting as a dummy turbulence model.
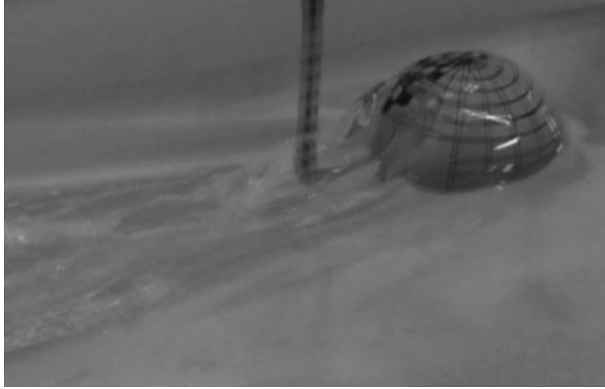
Figure 7: Turbulent wake at Re = 3.8 x 10^5

4.3 Shedding frequency analysis

Strouhal number obtained from the experiment is plotted in Figure 8 and compared with Hoerner (1965) empirical formula ($St = \frac{0.21}{(C_d)^{\frac{3}{4}}}$) for fully submerged bluff bodies. Before transition, there is a large discrepancy between Strouhal number from the experiment and from Hoerner (1965). A bow wave is indeed created at the lower speed and early separation occurs as previously observed in Figure 4. The wetted surface area of the sphere is thus less than when fully submerged. However, after transition, the wetted surface area is maximal and the sphere may now be considered to be in a similar condition as a fully submerged sphere since it sits just under the bow wave. Indeed, Strouhal number at the highest speed (2.2 $m.s^{-1}$) tends towards the empirical formula defined by Hoerner (1965) (Figure 8).
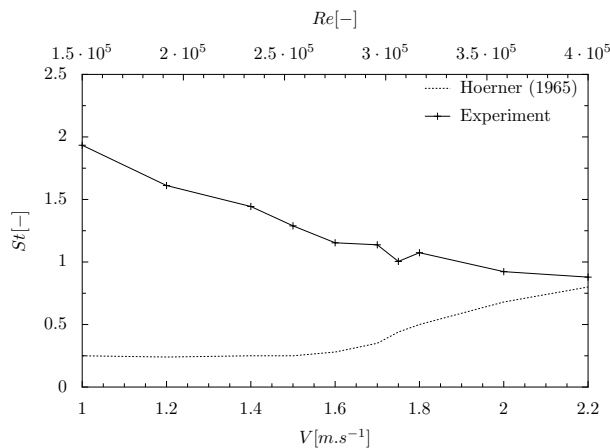
Figure 8: Strouhal number versus speed

4.4 Influence of immersion depth and speed

Due to time constraints, the experimental study only covered the case of a sphere located at the free-surface. The influence of the sphere's immersion depth on wave resistance was therefore first analysed using a linear potential flow theory. Based on previous findings (Figure 6), at speeds between 1.0 $m.s^{-1}$ and 1.7 $m.s^{-1}$, the virtual cylinder was added; and, above 1.7 $m.s^{-1}$, only the sphere was modelled.
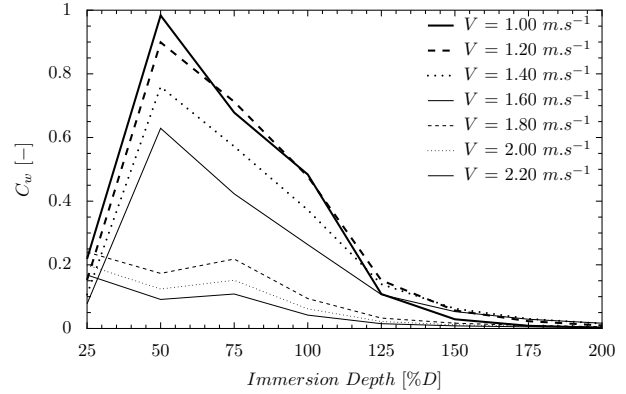
Figure 9: Influence of the sphere's immersion depth on the wave resistance across a range of Re (1.7x10^5 to 3.8x10^5) using potential flow theory

Figure 9 illustrates that maximum wave resistance occurs when the sphere is half-submerged as a consequence of the maximum cross-sectional area being at the free-surface. Wave resistance decreases sharply when the sphere has an immersion depth equal to 125% D, and becomes negligible as the sphere reaches an immersion of 175% D. As speed increases, the wave resistance coefficient decreases due to delayed separation and reaches a peak value at immersion depth 25% D and 75% D. Further data points would be needed when the sphere is partially submerged.

5 Conclusions and Further Work

In this paper, it was confirmed that the free-surface has a strong influence on the flow past a sphere at critical Reynolds numbers. Indeed, the drag coefficient doubles at low speeds compared to single phase problems due to the energy dissipation through the distortion of the free-surface. The drag crisis was observed for 2.5x10^5 ≤ Re ≤ 3.4x10^5.

The use of a virtual appendage at laminar speeds proved to be effective when using a potential flow method.

Initial results from URANS simulations agree with the experiment at turbulent Reynolds num-

bers; however an investigation of different turbulence models should be undertaken at speeds before the drag crisis. Furthermore, Large-Eddy Simulations (LES) should be performed in order to better capture the unsteadiness of the vortex shedding.

Maximum wave resistance occurs when the sphere is half-submerged due the maximum cross-sectional area of the sphere. The wave resistance component becomes negligible at an immersion depth greater than 175%D.

References

Achenbach, E. (1972), 'Experiments on the flow past spheres at very high Reynolds numbers', *Journal of Fluid Mechanics* **54**(03), 565.

Bakic, V. and Peric, M. (2005), 'Visualisation of flow around sphere for Reynolds numbers between 22000 and 400000', *Thermophysics ad Aeromechanics* **12**(3), 307–315.

Bakic, V., Schmid, M. and Stankovi, B. (2006), 'Experimental investigations of turbulent structures', pp. 97–112.

Constantinescu, G. S. (2000), 'LES and DES investigations of turbulent flow over a sphere', *AIAA Journal* **0540**, 1–11.

Couser, P. R., Wellicome, J. F. and Molland, A. F. (1998), 'An improved method for the theoretical prediction of the wave resistance of transom-stern hulls using a slender body approach', *International Shipbuilding Progress* **45**(444), 1–18.

Eggers, K. (1955), 'Resistance components of two-body ships', *Jahrbuch der Schiffbautechnischen Gesellschaft,* **49**.

Hassanzadeh, R., Sahin, B. and Ozgoren, M. (2012), 'Large eddy simulation of free-surface effects on the wake structures downstream of a spherical body', *Ocean Engineering* **54**, 213–222.

Hoerner, S. F. (1965), *Fluid-dynamic drag*, Hoerner Fluid Dynamics.

Insel, M. (1990), An investigation into the resistance components of high speed displacement catamarans, PhD thesis, University of Southampton.

Jeon, S., Choi, J., Jeon, W.-P., Choi, H. and Park, J. (2004), 'Active control of flow over a sphere for drag reduction at a subcritical Reynolds number', *Journal of Fluid Mechanics* **517**, 113–129.

Jindal, S., Long, L. N. and Plassmann, P. E. (2004), Large eddy simulations around a sphere using unstructured grids, *in* '34th AIAA Fluid Dynamics', Vol. 7, pp. 1–16.

Kiya, M., Mochizuki, O. and Ishikawa, H. (2000), Challenging issues in separated and complex turbulent flows, *in* '10th International Symposium on Applications of Laser Techniques to Fluid Mechanics', Lisbon, Portugal, pp. 1–13.

Michell, J. H. (1898), 'The wave-resistance of a ship', *Phil. Mag.* **45**(5), 106–123.

Newman, J. N. (1977), *Marine Hydrodynamics*, The Massachussets Institute of Technology.

Ozgoren, M., Dogan, S., Okbaz, A., Aksoy, M. H., Sahin, B. and Akilli, H. (2013), 'Comparison of flow characteristics of different sphere geometries under the free surface effect', *EPJ* **45**.

Ozgoren, M., Dogan, S., Okbaz, A., Sahin, B. and Akilli, H. (2012), 'Passive control of flow structure interaction between a sphere and free-surface', *EPJ* **25**.

Ozgoren, M., Okbaz, A., Kahraman, A., Hassanzadeh, R., Sahin, B., Akilli, H. and Dogan, S. (2011), Experimental investigation of the flow structure around a sphere and its control with jet flow via PIV, *in* '6th IATS', number 5, pp. 16–18.

Roth, E. H. (2008), Artic Ocean long-term acoustic monitoring: ambient noise, environmental correlates, and transients North of Barrow, PhD thesis, University of California, San Diego.

Taneda, S. (1978), 'Visual observations of the flow past a sphere at Reynolds numbers between 10^4 and 10^6', *Journal of Fluid Mechanics* **85**(1), 187 – 192.

Hull, Rudder and Propeller Investigation on a Vessel in Free Run Condition

Aitor Juandó, Marcos Meis[1], Adrián Sarasquete

[1]m.meis@vicusdt.com

Vicus Desarrollos Tecnológicos S.L. (VICUSdt), Vigo, Spain

1. Introduction

The rudder normally operates in the wake of the propeller in the stern of the ship. This is needed in order to create enough lift for its main role, maneuvering, with the high speed flow leaving the propeller. When the ship is in free sailing condition, the rudder is only responsible for doing minor course corrections, normally carried out by the autopilot. Due to the pressure distribution over the rudder, different forces appear, mainly a longitudinal force that could be drag or push force and a transverse force affecting the ship's course.

The wake adapted rudder is normally designed so as to improve the propulsive and maneuvering performance of the propeller – rudder unit. The amount of energy which is recovered will depend on the form and thickness of the profile of the propeller, the aspect ratio, Rn, the spatial distribution of the velocity upstream and the turbulence of the flow [1]. It is expected that a wake adapted rudder has less transverse force than a conventional one at 0º angle when a vessel sails in free run operation, therefore reducing the need for autopilot corrections.

In single screw vessels there are also a force unbalance due to the asymmetry of the propulsion system which modifies the flow differently on port and starboard side depending on how the propeller rotation is.

The flow is not stationary, mainly due to the rotation energy supplied by the propeller; also the presence of the rudder modifies the performance of the propeller compared to the open water case, partially blocking the water flow downstream the propeller. Analyzing this system by CFD means that the behaviour of the flow would imply the solution of an evolutionary problem on a moving mesh. These problems have high computational costs and are not suitable to be solved on a routine basis. A lot of articles consulted in the literature demonstrate that they can be dealt with in a quite precise way by means of Reynolds Averaged Numerical Stationary simulations so as to obtain integral values on the different regions of interest, among other can be cited Caldas et al. [2]

Numerical simulations of a conventional and a twisted rudder with the same area are performed behind the running propeller of a vessel in order to determine how large the transverse forces at 0º angle are. A parametric study was done analyzing small variations of angle in order to search the optimum angle that minimizes net transverse. The simulations carried out included an analysis of the forces from each part of the ship i.e. rudder, propeller and hull. All the calculations are carried out using commercial CFD code STAR-CCM+.

2. General Description

The aim of this study is to investigate, by means of CFD, the interaction between rudder, propeller and hull on a sailing ship at different angles of drift, especially at 0º angle and also, the manoeuvring performance of the twisted rudder fitted compared to a conventional one. To achieve this objective it is necessary to consider two conditions: static rudder and pure drift cases. The static rudder cases are used to compute the hydrodynamic forces and moments varying the rudder angle δ to determine the manoeuvre of the ship. During these cases, an appended model is modelled at constant speed and straight-head course, while the rudder angle is varied systematically, between 0º and 10º. The pure drift cases are used to determine the influence of oblique flow on the forces and moments in the sea course of the ship. In order to simulate these cases, the appended model is modelled at constant speed for a fixed angle rudder of 0º varying the drift angle (β) between -10º and 10º. The drift angle is defined as $\beta = \tan^{-1}(v/-u)$, where u and v are the sway and surge velocities, respectively. The Figure 1 illustrates these conditions.
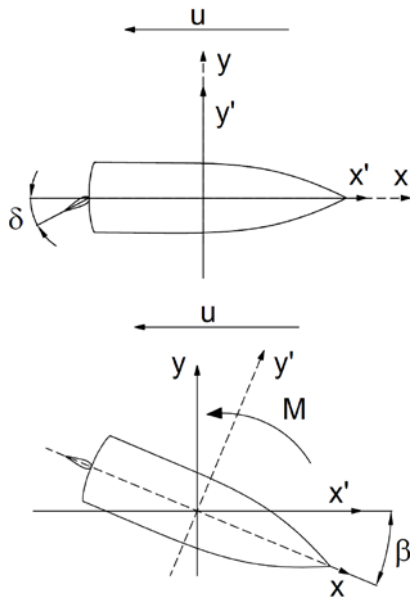
Figure 1. Sketches of the cases: static rudder (up) and pure drift (down).

In this study, several double-body self-propulsion simulations on both configurations at free run condition were carried out, which is defined by a speed of 10 knots and a propeller rotation rate of 205 rpm.

2.1. Geometry

The ship considered in this study is 46.7 m long equipped with a fixed pitch propeller and a central twisted rudder with bulb adapted to the flow. The main particulars of the ship are shown in Table 1.

Lpp	45.9	m
B	10.4	m
T	3.9	m
Propeller Diameter	2.95	m
Number of blades	5	-
Rudder Chord	1.9	m
Rudder Height	3.3	m
Lateral Area	6.27	m^2
Thickness	0.2*Chord	-

Table 1. Main geometric dimensions

The rudders to be analyzed are shown in Figure 2. Both rudders have the same dimensions in terms of chord and span being the only difference given by the lateral displacement on the leading edge for the twisted one. The bulb is the same in both geometries.

Despite the geometry has longitudinal symmetry, this symmetry cannot be applied in the domain as the rudders presence leads to

instabilities by means of the introduction of physical asymmetry in the problem (i.e., it produces a flow block at the exit of the propeller).
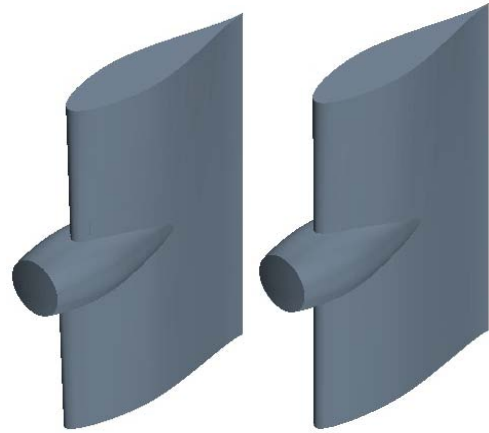
Figure 2. Geometry CAD of simulated rudders: wake adapted rudder (left) and straight rudder (right)

It has to be noted that propeller rotates clockwise, when is viewed from astern facing forward, since it is important to follow the argumentation.

2.2. Numerical model

The mathematical model used for the calculation of the numerical simulations is described by Reynolds Averaged Navier Stokes Equations (RANSE). The Reynolds stress tensor was modelled to close the governing equations by means of a two-equation model, named Two Layer K-Epsilon, with a Two Layers All y+ Wall Treatment for the wall modelling. The problem is closed establishing the initial and boundary conditions on the physical and computational boundaries.

Commercial code StarCCM+ has been used for the numerical solutions of the equations. StarCCM+ solves RANSE equations in their integral form, by means of Finite Volumes methods. The spatial discretization of the convective terms is done with a second order upwind based scheme, whereas the diffusive terms are discretized with second order centered scheme. Velocities and pressures are solved in a segregated manner, and then coupled by means of the SIMPLE algorithm. The rotation of the propeller is modelled used a moving reference frame system, i.e., the velocity is set on propeller blades and centripetal effects are included in additional source terms in the momentum equations. Further details about the

code can be found in [3] and about numerical aspects in [4]

The physical domain is discretized by means of non-structured mesh of polyhedral cells [5]. Several refinement zones or volume shapes were located at different parts of the domain, particularly in the wake region, in order to increase the density of cells and improve to the resolution of flow features. The whole mesh consists of a total of about 3 millions of cells, where the rotation region (propeller) has about 800.000 cells and the fixed region 2.100.000.

For all cases, the y+ values were in a range between $y+=30$ and $y+=150$ with an average of 50. A typical stern surface mesh can be seen in Figure 3.

Figure 3. Typical computational mesh

2.3. Figure of merit

The transverse forces and the yaw moment of rudder, hull and propeller were measured for both conditions. The transverse forces were measured locally for each part whereas the yaw moment was measured globally on the model respect to Lpp/2, as functions of rudder angle for the static rudder condition and function of drift angle for the pure drift condition. The positive directions are defined in the Figure 1, where the X-component acts in the longitudinal direction of the ship whereas the Y- component acts perpendicular to this direction. The transverse forces and the moment are non-dimensionalized by means of lateral underwater area of each part separately, the speed U_∞ and the water density. The Lpp is used as characteristic arm for the yaw moment.

$$L' = \frac{F}{0.5\rho U_\infty^2 A_0} \quad (1) \quad M' = \frac{M_Z}{0.5\rho U_\infty^2 A_0 L_{pp}} \quad (2)$$

3. Results and Discussions

Pressure distribution around a NACA profile is an important parameter from the hydrodynamic point of view because it determines the lift and drag forces. The pressure distributions are plotted on the rudder surface by means of local pressure coefficient, C_P

$$C_P = \frac{p - p_\infty}{0.5\rho U_\infty^2}$$

where $p - p_\infty$ is the local pressure, ρ is the density and U_∞ is the free stream velocity. This figure of merit is used along with the previous ones to have a deeper knowledge on the manoeuvre of the rudder and the performance of the ship in free run condition.

3.1. Static Rudder

As it was mentioned in the previous section, in the static rudder condition the rudder angle is varied between 0 and 10 degrees (to produce a turn to the starboard side) while the ship sails in straight-head course at constant speed. The non-dimensional transverse force and yaw moment are shown in the Figure 4 and Figure 5.

As it is expected (Figure 4), the higher rudder angle the larger transverse force is (at these low angles) for the rudder whereas for the propeller and the hull are kept constant with the variation of the angle. This is due to the fact that the incoming water into the hull and propeller is not modified during the change in the rudder angle. Indeed, due to the symmetrical geometry of hull, the transverse force for straight-head course is negligible. Special attention is paid to 0° rudder angle, where the transverse forces of rudder and propeller have opposite signs. The clockwise rotation of the propeller, along with the wake of the ship produces a positive side force of the propeller. The swirl and acceleration induced by the propeller alters the speed and incidence of the flow arriving to the rudder, giving rise to negative side force in this case, due to the lateral displacement of the rudders profiles.
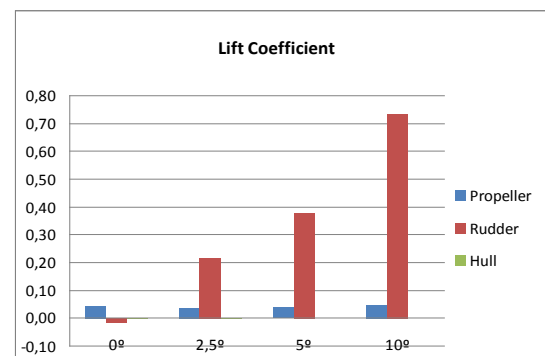
Figure 4. Lift coefficient of propeller, rudder and hull for each rudder angle configuration

The sum of transverse forces at 0º rudder angle leads to negative yaw moment (Figure 5), and hence, a small turn of the ship to the starboard are expected to occur. The pure drift result (above) allows appreciating the influence of this turn on the ship behaviour. As the rudder angle increase, the yaw moment of the rudder has the same sign as the propeller and the values are higher. The values of yaw moment for the rest of rudder angles are large if they are compared to the values of conventional rudders from ships with the same characteristics as the studied one. Therefore, the adapted rudder is able to perform manoeuvres in less time than others.
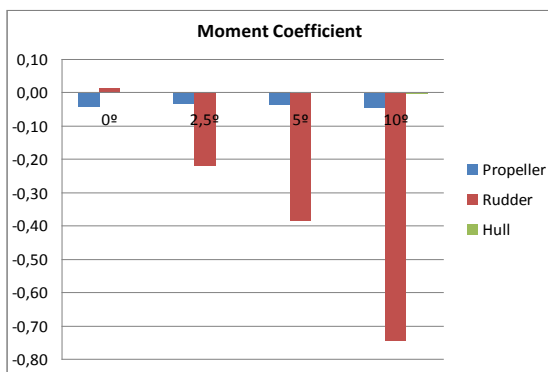
Figure 5. Moment coefficient of propeller, rudder and hull for each rudder angle configuration
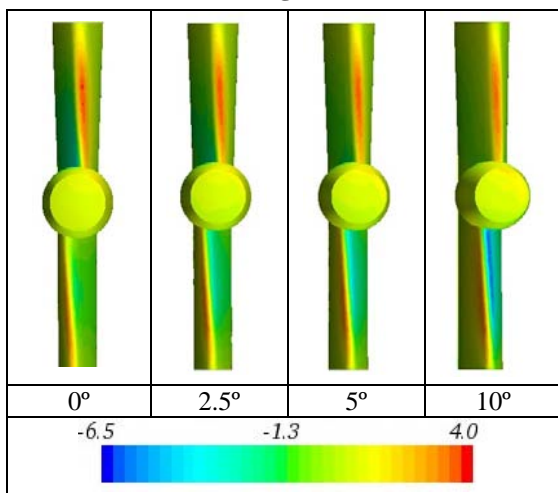
Figure 6. Pressure coefficient for rudder angle

The introduction of the propeller generates high pressure peaks both positive and negative on rudder which causes an increase in transverse forces. The rudder angle modifies the axial and tangential velocities coming from the propeller, leading to lower pressures and high velocities on the port side and higher pressure and lower velocities on the starboard side of the lower part of the rudder.

The opposite is produced in upper part of the rudder (Figure 6). As the angle increase from 0º to 10º, gradient pressures in the lower leading edge becomes higher (positive direction) whereas in the upper part becomes lower (negative direction), hence the transverse forces increase (Figure 4).

3.2. Pure Drift

For these cases, the rudder angle is kept fixed at 0º and the drift angle is varied between -10º and 10º whereas the ship is sailing at constant speed, as it was define in previous section. It has to be mentioned that case of drift angle with 0º coincides with studied case of rudder angle with 0º.

Figure 7 shows the transverse forces as a function of drift angle for propeller, twisted rudder and hull. The symmetry of the hull leads to symmetrical values respect to 0º, increasing with drift angle. At drift angle of 0º, the sign of transverse force is negative since the propeller has the higher load between 12 and 3 o'clock (looking from aster) leading an increase of suction on upper left side of stern, which induces a negative transverse force on the hull. Although this physical phenomena has no so much influence as the absolute drift angle increases.
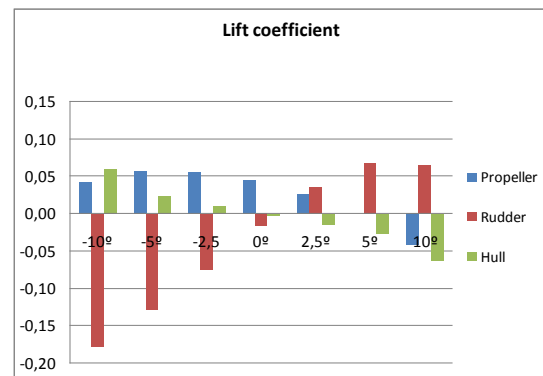
Figure 7. Lift coefficient of propeller, rudder and hull for each adapted rudder angle configuration for pure drift

The presence of the hull in the oblique flow (drift angle different than 0º) modifies the wake, and hence the local angle of attack on the propeller blades leading to a modification of propeller load. Negative drift angle implies higher velocity in the starboard side of the propeller and therefore higher port side propeller loading. This unbalance of loading leads to positive propeller transverse force. Whereas for positive drift angle the starboard side propeller has higher loading and negative

propeller transverse force is produced. The propeller rotation along with the wake due to the hull does not allow get a symmetrical results respect to 0º drift angle and the null transverse force is achieved approximately at 5º.

Finally, the rudder performance depends strongly on modification of tangential velocities produced by propeller and hull. The influence of drift angle on rudder performance is explained analysing the pressure coefficient as shown in Figure 9.
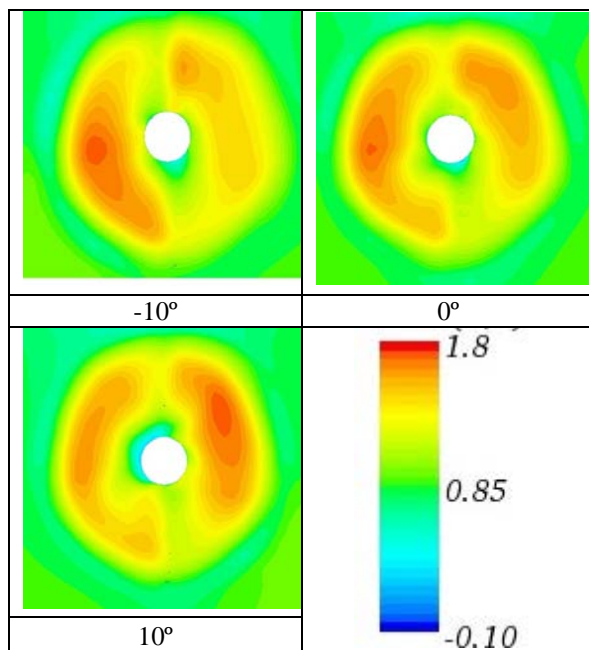
Figure 8. Non dimensional axial velocity on a normal plane to the ship between propeller and rudder (viewed from astern facing forward)

For a drift angle of -10º, the upper leading edge has the largest pressure gradient, given by lower pressures and high velocities on the starboard side and higher pressure and lower velocities on the port side. As the drift angle increases from -10º to 10º, the distribution of pressure and velocities are kept constant but the upper pressure gradient decreases whereas the lower one increases and becomes the largest pressure gradient on rudder. Then, the transverse force goes from negative to positive as the drift angle varies from -10º to 10º (Figure 7).

3.1. Comparison between rudders

The lateral displacement of twisted rudder allows to move the transverse force curve to the left, i.e. the transverse force for negative drift are higher for twisted rudder than straight rudder and vice versa for positive drift angle

(Figure 10). The rudder shape has a slight influence on propeller transverse force but the values for the hull are independent of rudder shape.
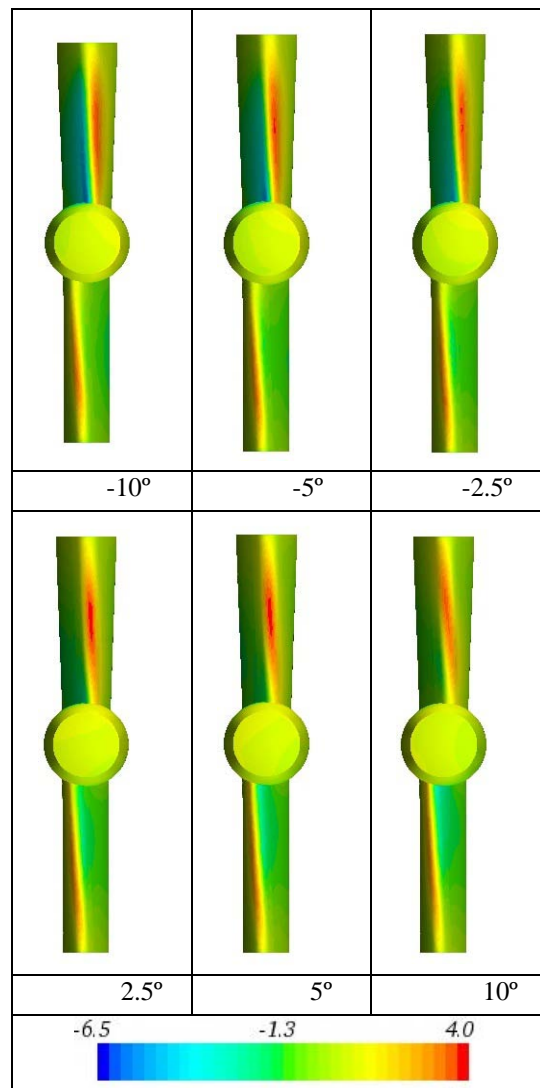
Figure 9. Effect of drift angle on rudder performance

Special case corresponds to 0º drift angle, since straight rudder transverse force is higher than adapted rudder and indeed, it has the same sign of propeller force. Then, straight rudder would develop larger turn to the starboard side than adapted one, leading to more difficulties to keep the course. This can be explained if pressure coefficient for adapted rudder (right) and straight rudder (left) is analyzed (Figure 11). Looking that figure, the only difference between both rudders can be located on the lower leading edge, since the straight rudder has larger pressure gradient than the adapted rudder, giving rise to a higher positive force.
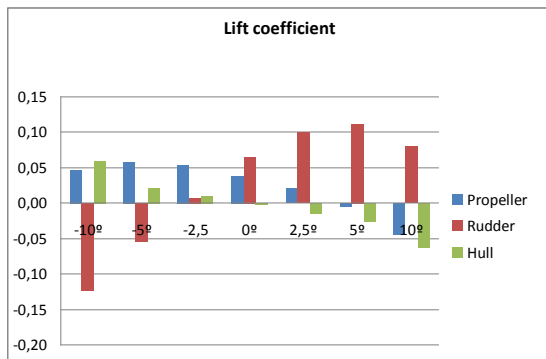
Figure 10. Lift coefficient of propeller, straight rudder and hull for each straight rudder angle configuration for pure drift
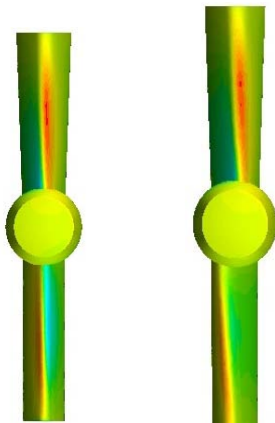
Figure 11. Pressure coefficient for straight rudder (left) and wake adapted rudder (right)

4. Conclusions and Future Works

In the present work RANS CFD has been used to perform numerical self-propulsion test for a vessel 45.9 m long equipped with a twisted rudder with bulb and a single propeller, in order to study the interaction between hull, propeller and rudder and their influence on ship's course and the capacities of manoeuvre, when the vessel sails at constant speed of 10 knots and propeller rotation rate of 205 rpm. Also, a straight rudder with the same bulb has been studied to know the effects of twisted rudder on those issues. Then, two configurations were analysed: static rudder and pure drift.

The numerical simulations for static rudder configuration ($0° < \delta < 10°$) shows that rudder transverse force increases with increasing the rudder angle and for propeller and hull keeps constant, being hull force negligible. For 0°, rudder force has opposite sign that propeller. Since the sum of moments is not null, a small turn to starboard side is developed.

Effect of drift angle (β) produces a symmetrical response for hull lift forces but not for propeller and rudder, due to interaction between then. For all studied drift angles, lift forces have opposite signs for rudder and propeller, except for small positive angles due to propeller clockwise rotations and lateral displacement of twisted rudder. This performance is due drift angle induces an unbalance of incoming velocities on the propeller, leading a higher propeller loading on blades with lower incoming velocities (enhance or not in function of propeller rotation sense). This asymmetric load distribution produces rudder lift force in the same sign of drift angle, with a little delay due to lateral displacement and rotation sense.

When both rudders are compared, almost the same performance is achieved although the lift curves from both rudders present a shift. For 0° drift angle, straight rudder develops higher yaw moment than adapted one and hence, worse performance from point of view of course keeping. Then, twisted rudders have better performance on ship's resistance and course.

Future work include the use of these forces (propeller and rudder as unit propulsion) in manoeuvring simulator developed by VICUSdt and carry out new numerical simulations in order to get deeper knowledge of the interaction by means of LES modelling.

5. References

[1] Bertram, V. *Practical Ship Hydrodynamics*. 2nd ed. Woburn: Butterworth-Heinemann, 2000

[2] Caldas, A., Meis, M., Sarasquete, A. *CFD validation of different propeller ducts on Open Water condition*. 13th Numerical Towing Tank Symposium, Germany, 2010

[3] StarCCM+ User's Manual

[4] Ferziger, J.H. & Peric,M. *Computational Methods for Fluid Dynamics*. 3rd ed. Springer-Verlag Berlin Heidelberg, 2002

[5] Peric, M. *Flow simulation using control volumes of arbitrary polyhedral shape*. Ercofat Bulletin. Nº 62, 2004

[6] Larsson, L. Ship Resistance and Flow. SNAME, 2010

Modeling the effect of rotor downwash on ship airwakes

Kavyashree Kalaskar
Llyods Register, London

Introduction

Helicopter ship deck landing is one of the most challenging tasks which presents severe unsteady flow field and requires precision tasking under confined spaces. This puts immense pressure on naval pilots to operate the aircraft safely. To help with this, several flight simulators have been developed in order to provide training facilities and develop operational envelopes, which enable the pilots to have prior knowledge of the dangers and the operating limits under such conditions.

The challenge, however, is to develop CFD models for these simulators, that can accurately replicate the real atmospheric conditions of the helicopter ship deck landings.

Objective and Scope of Work

The motivation for this project originated from the University of Liverpool flight simulator used for helicopter deck landing simulations. The flowfield in the simulator represents the ship airwakes generated from the superstructure of the ship. However, it does not account for any downwash effects resulting from the helicopter blade rotation. Hence, the objective was to develop a fully coupled CFD model that included both the airwakes and the downwash, and investigate the effects of this complex flow interaction on the landing deck region.

Methodology

The analysis was conducted on a Type 45 Destroyer with a Virtual Blade Model to induce the effect of rotor downwash. Detached Eddy Simulation (DES) was used in order to capture the turbulent dissipation accurately and the computation was run with FLUENT commercial software. The simulations were conducted at a wind speed of 20 m/s. The *'k-ε realizable'* model was selected for the initial steady state run with RANS solver and *SST k-ω RANS* turbulence model was chosen for the DES solver. (Geometry shown in Figure 1)

Results and Discussion

The project was started by performing a comparative study in order to validate the CFD model. This computation was performed on SFS2 frigate and compared with the experimental results obtained by Lee *et. al* [1]. Although the project is mainly focussed on Type 45 frigate, this initial step was conducted on SFS2 as there was no experimental data available for Type 45 destroyer.

Figure 2 shows the mean velocity components and turbulent intensities for SFS2 at Headwind condition. A reduction in the longitudinal velocity (u) is seen around the mid-deck region where the flow interacts with the wake from the hangar. This is also seen from the normal velocity component (w) which shows a downdraft as the flow approaches the

mid-deck position. The re-circulation around the mid-deck is seen from the two dips and raises seen in the normal velocity component. This phenomenon was also recorded from Zan's [2] experiments. The computational results are in good agreement with the experimental data and show similar trends. The slight variations could be due to the insufficient data sampling.

Figure 3 shows the formation of vortex at the deck region. The right image shows the vortex structures obtained from CFD computation and the left image shows an oil flow visualisation of SFS2 [2]. In both the images, the generation of vortex cores from the hangar can be seen clearly. A saddle point is seen around the mid-deck region where the vortex flows emerging from the corners meet and gets deflected. This variation in the flow field could severely affect the steadiness of an approaching helicopter leading to an increase in the pilot workload. From the above results, it could be concluded that the DES solver has been able to successfuly replicate and demonstrate the flow field characteristics that were encountered in the experiments.

The ship airwake analysis for the Type 45 was performed at two conditions - Headwind and Green 30 (30° from starboard side). Figure 4 shows the mean velocity components and turbulent intensities at both Headwind and Green 30 conditions. It can be seen that the Green 30 case has higher turbulent intensities towards the starboard side of the ship. The turbulent intensities reach up to 35% of the freestream velocity. This is due to the fact that, when the freestream flow approaches the ship, it hits the corner of the hangar and results in immediate shear layer separation forming large unsteady turbulent eddies.

The lateral velocity (v) for the Green 30 condition also increases rapidly around the mid-deck creating a strong crossflow for the approaching helicopter. This is shown in Figure 6.

There is a transition from high to low velocity towards the corner of the hangar. This is where the edge shear layer emerges and develops further as seen in Figure 6. This can also be seen from Figure 5 which shows the iso-surface of the mean velocity magnitudes at half the freestream velocity for Headwind and Green 30 conditions. The Headwind case showed 'burbles' i.e. bubble like structures emerging from the super structure and shed across the deck region. This behaviour was also seen from Polsky and Bruner's [3] work which showed similar burbles for an LHA ship.

Green 30 case shows severe turbulence emerging from the superstructures and the hangar. This forms strong vortices that extend throughout the deck region. This behaviour agrees with Bogstad et. al. [4] who also encountered the strongest velocity contours at Green 30 condition.

Images on the right side of Figure 6 show the vortices generating from the hangar for both the conditions. The Green 30 case shows the vortex generating from the corner of the hangar which develops as it approaches the mid-section of the deck. This then further moves across the deck towards the port side of the ship forming a long vortex streak. Unlike the Headwind case, this does not form a saddle point or a re-attachment around the mid-deck region. This behaviour was seen on the experiments conducted by Zan [2] with SFS2 model.

The ship airwake analysis of Type 45 Destroyer presented realistic flow

characteristics that are encountered in actual ship-deck landings. The results obtained agree with the findings of several other researchers for similar types of frigate.

A fully coupled model was then developed which incorporated a rotor induced downwash effect interacting with the ship airwakes. Figure 7 shows the mean velocity components (u, v, and w) obtained for the fully coupled and uncoupled flow. It can be seen that the normal velocity (w) of the fully coupled simulation shows a substantial dip around the mid-deck region when compared to the uncoupled case. This is due to the inherent rotor downwash affecting the flow field around that region. The maximum downward velocity (w) occurs at 90° and 270° azimuth of the rotor. There is also a slight increase in the longitudinal velocity (u) around the mid-deck region where the flow encounters the rotor for the first time and gets triggered to a higher velocity.

The downwash is shown on the right side in Figure 7 which gives the mean normal velocity. The downwash can be seen very clearly where the flow above is dragged in towards the rotor, being pushed downwards and then washed away with the freestream.

Figure 9 gives the unsteady turbulent intensities for the three velocity components (u, v and w) along a lateral line over the mid-deck position. It can be seen that the rms value peaks around the mid-deck region where the airwake encounters the rotor downwash. The rotor diameter exists from -0.3 to 0.3 (y/b). The normal component peaks around this region indicating high levels of flow unsteadiness. This could be further confirmed from Figure 8 which gives the

mean and rms longitudinal velocity contours for both the fully coupled and uncoupled case. It can be seen that the unsteady turbulence intensities are higher for the fully coupled model accompanied with several strong eddies especially near the mid-deck region.

The rotor pushes the flow towards the lee of the hangar and this causes the flow to re-circulate and form larger vortices. This is seen in the mean velocity contour plots on the left side of Figure 8. The downwash creates a lower pressure region towards the hangar of the deck, which could lead to a suction effect thereby making the landing even more unstable.

Conclusions and Further Recommendations

The results indicate a positive outcome for the fully coupled model. It was seen that the rotor model included in the flow field affects the ship airwakes to a large extent and contributes to a major portion of the flow. It affects the flow field around the deck region thereby increasing the turbulent kinetic energy. The model also featured strong turbulent eddies. A strong downward velocity component (w) was seen in the mid-deck region as shown in Figure 7. It was also seen that the presence of the rotor affects the vortex flow around the mid-deck region. It is believed that these unstable flow features will certainly affect the pilot workload activity and considerably increase it when compared with an uncoupled flow model.

At this stage, it can be said that this method of modeling the rotor downwash is certainly beneficial as it generated several changes in the flow field around the deck region of the ship. It would certainly be beneficial to perform the analysis at different wind conditions to see how the flow field varies and to what

extent the rotor downwash modifies the flow at these different wind angles. Further piloted trials with the fully coupled model in the simulator would indicate the fidelity of this technique. Acquiring the pilot workload ratings would indicate how close this model represents realistic flow physics.

References
1. Lee R.G., and Zan S.J., 'Wind Tunnel Testing of a Helicopter Fuselage and Rotor in a Ship Airwake', *Journal of the AHS*, Vol. 50, No. 4, 2005, pp. 326-337
2. Zan S.J., 'Surface Flow Topology for a Simple Frigate Shape', *Canadian Aeronautics and Space Journal*, Vol. 47, No. 1, 2001, pp. 33-43
3. Polsky S.A and Bruner C.W.S., 'A Computational Study of Unsteady Ship Airwake, *40th AIAA Aerospace Sciences Meeting and Exhibit*, Reno, NV, 14-17 January 2002
4. Bogstad M.C. et.al 'CFD Based Advanced Ship-Airwake Database for Helicopter Flight Simulators', *Journal of Aircraft*, Vol. 39, No. 5, 2002, pp. 830-838
5. Forrest J.S., 'Thesis: Predicting Ship-Helicopter Operating Limits using Time-Accurate CFD Ship Airwakes and Piloted Flight Simulation', University of Liverpool, July 2009.
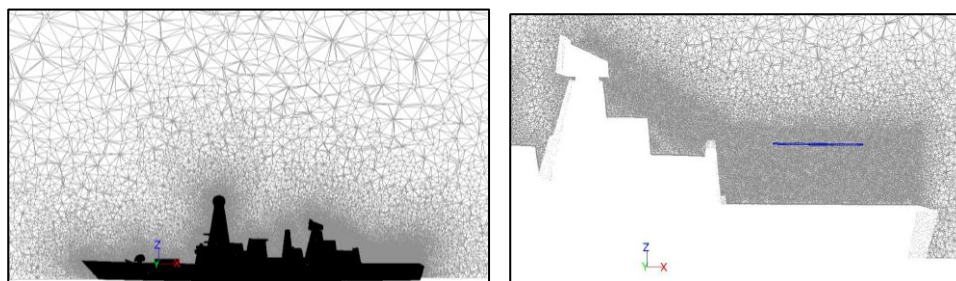
Figure 1 Images showing the domain and the refined mesh regions with the rotor over the deck
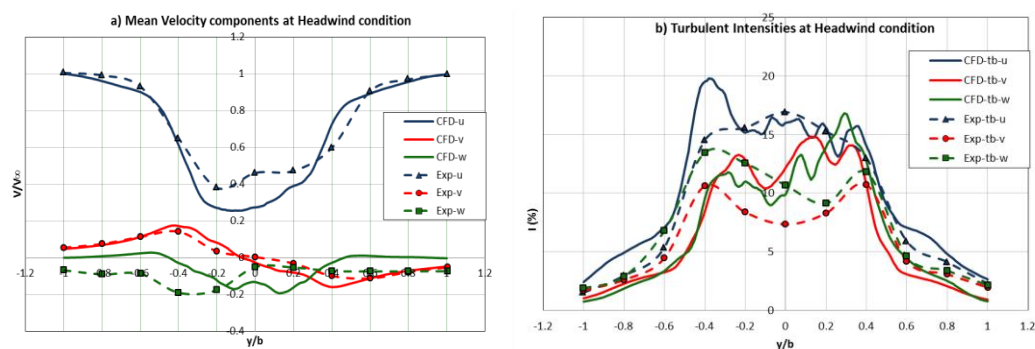
Figure 2 Mean Velocity components (a) and Turbulent Intensities (b) for SFS2 frigate showing CFD and Experimental data
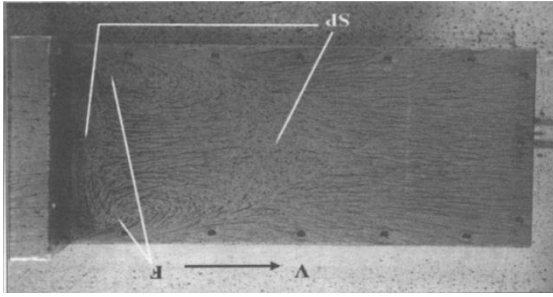
Experiment **CFD**
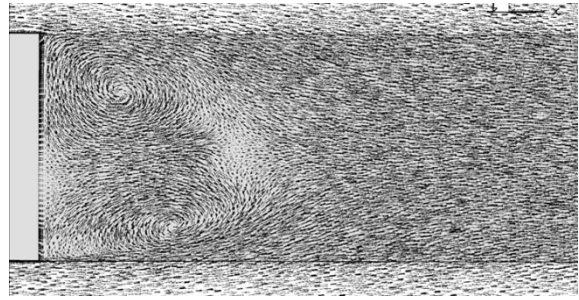
Figure 3 Left: Oil flow visualisation of the vortices; Right: Vortices over deck region captured from CFD analysis

(a) Mean Velocity Components along the lateral line for Type 45

(b) Turbulent Intensities along the lateral line for Type 45
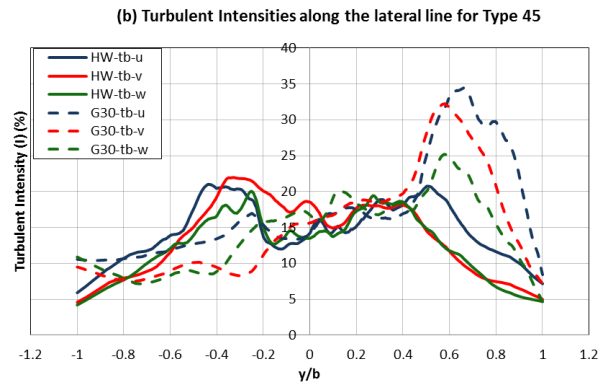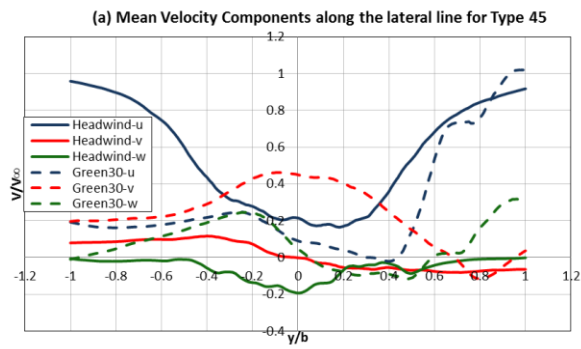
Figure 4 Mean Velocity components (a) and Turbulent Intensities (b) for Type 45 Destroyer at Headwind and Green 30
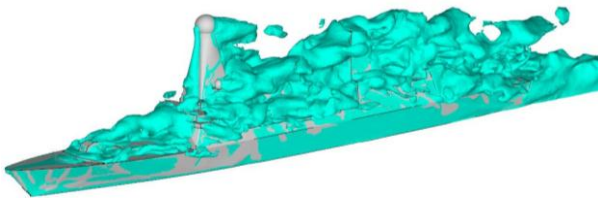
Headwind **Green 30**
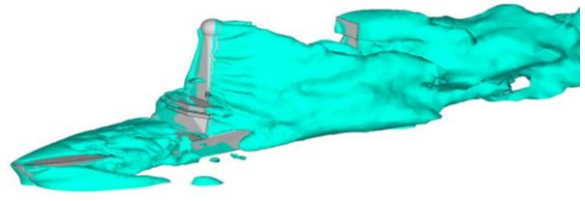
Figure 5 Iso surfaces showing vorticity for Headwind (left) and Green 30 (right)
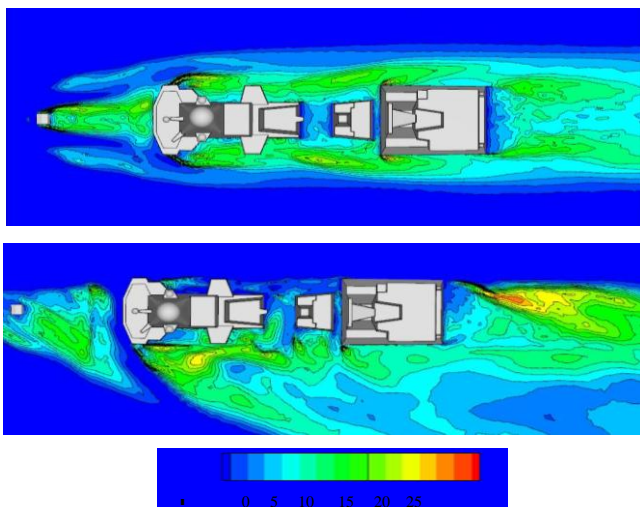
Headwind **Green 30**
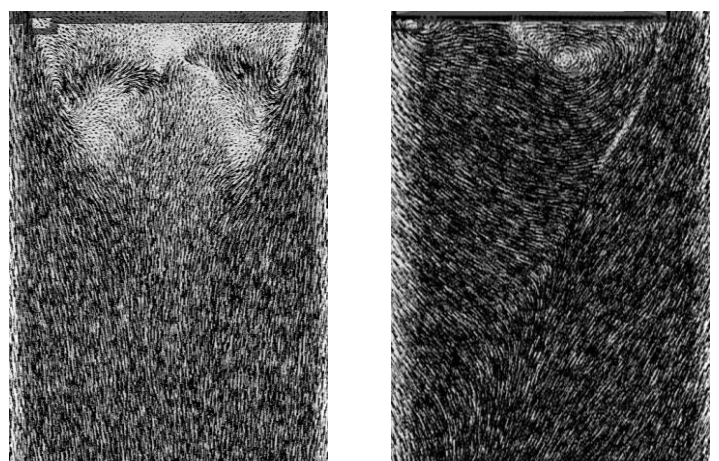
Figure 6 Turbulent Intensities shown for Headwind (top) and Green 30 (bottom) case (Contour plot on the left); Vortices captured over the deck region for the Headwind and Green 30 cases (right)
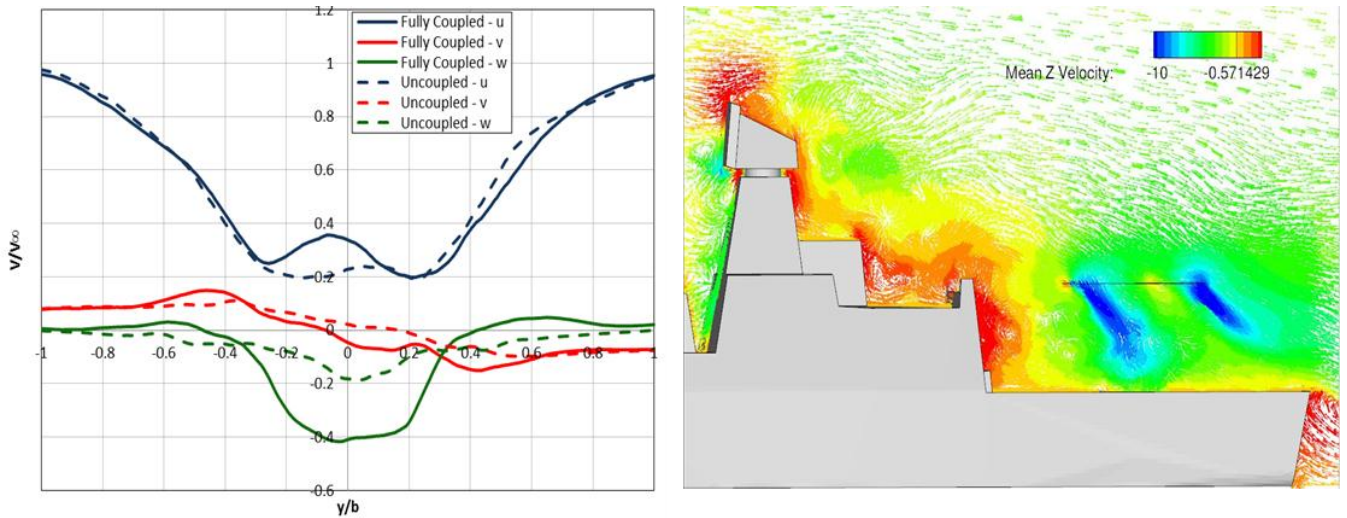
Figure 7 Graph showing the velocity components for Fully Coupled and Uncoupled model (left); Vector plot showing the downwash from the Root on the landing deck (right)
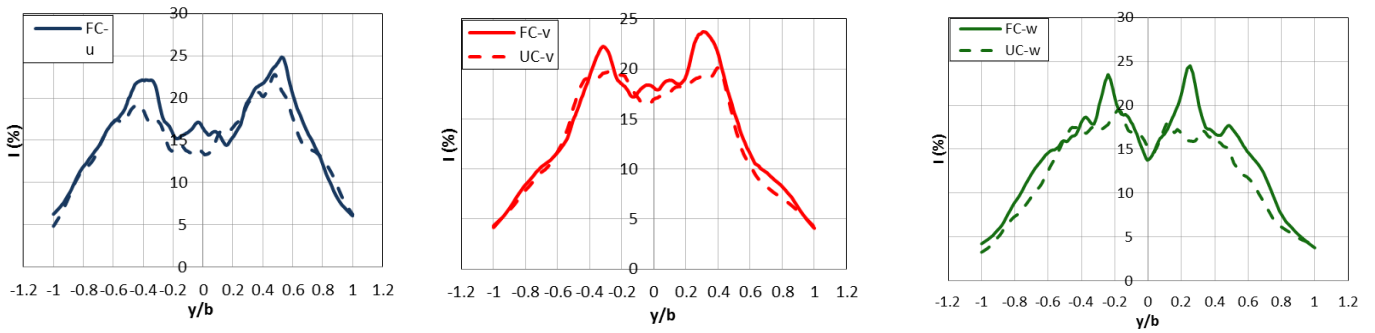
Figure 8 Turbulent intensities for u, v, and w component for fully coupled model
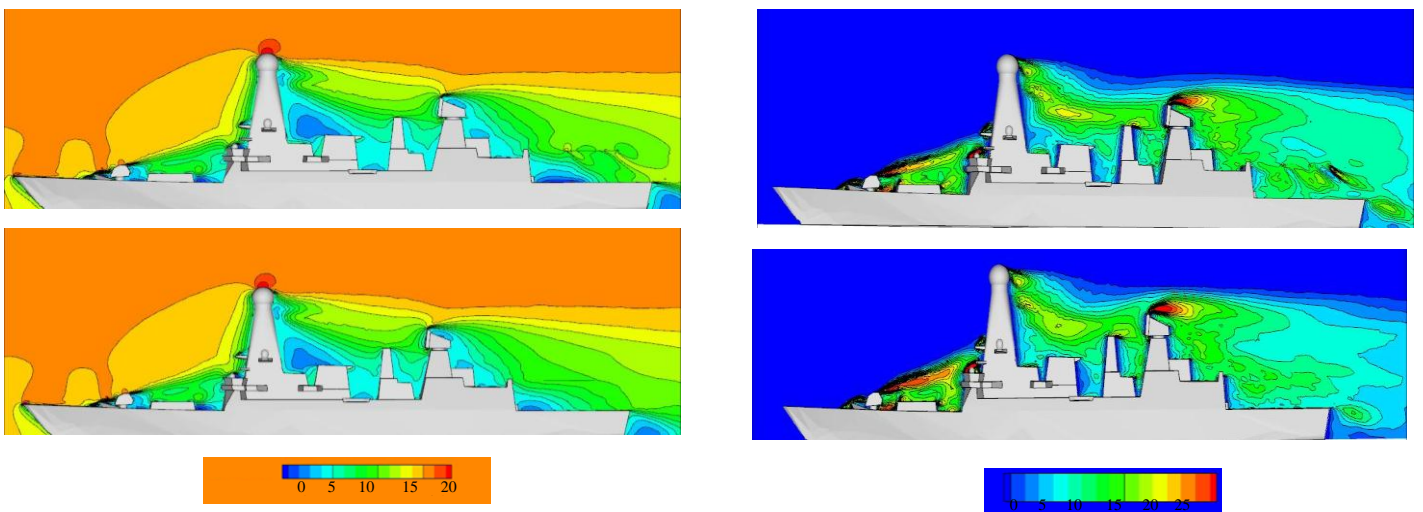
Figure 9 Contour plots showing mean longitudinal velocity (left) and rms longitudinal velocity (right) for coupled (top) and uncoupled (bottom) models

Influence on the numerical uncertainty of a generic submarine model by changing the wall-normal distribution of the wall-bounded grid cells

Maarten Kerkvliet, MARIN, Netherlands
m.kerkvliet@marin.nl

1 Introduction

MARIN is using Computational Fluid Dynamics (CFD) for engineering applications on daily practice. To establish the credibility of the results verification and validation is desired. As explained by Roache [1]: Verification is a purely mathematical exercise that intends to show that we are "solving the equations right", whereas Validation is a science/engineering activity that intends to show that we are "solving the right equations".

This paper focuses only on verification of CFD simulations performed with MARIN's viscous flow solver ReFRESCO [2, 3]. For this verification analysis the numerical uncertainty method of Eça and Hoekstra [4] is used, which is based on grid refinement studies of geometrical similar grids. The numerical uncertainty of a CFD prediction has three components, i.e., the round-off error, the iterative error and the discretisation error.

The aim of this paper is to get a better understanding of the relation between the numerical uncertainty estimation and the wall-normal distribution of the wall-bounded grid cells, since earlier work by, e.g., [5], showed unexpected trends in the order of convergence based on the discretisation method.

All simulations are performed for a generic submarine model which is described in the next section. Furthermore the programme of simulations is explained followed by the results and ending with conclusions.

2 Methodology

2.1 Geometry

The generic submarine model used for this study is based on suggestions by Joubert [6] and is used by the Submarine Hydrodynamics Working Group (SHWG) (www.shwg.org) to study hydrodynamic effects on submarine performance, e.g., manoeuvring, propulsion and signature. An overview of the geometrical shape of the submarine is given in Figure 1. The origin of the right-handed coordinate system is located at the intersection of the symmetry axis of the bare hull at midships. All forces and moments working on the submarine are based on this coordinate system. The integral forces X, Z and moment M are made non-dimensional with the overall length of the submarine L_{oa} using:

$$X', Z' = \frac{X, Z}{\frac{1}{2}\rho U_\infty^2 L_{oa}^2} \qquad M' = \frac{M}{\frac{1}{2}\rho U_\infty^2 L_{oa}^3} \qquad (1)$$
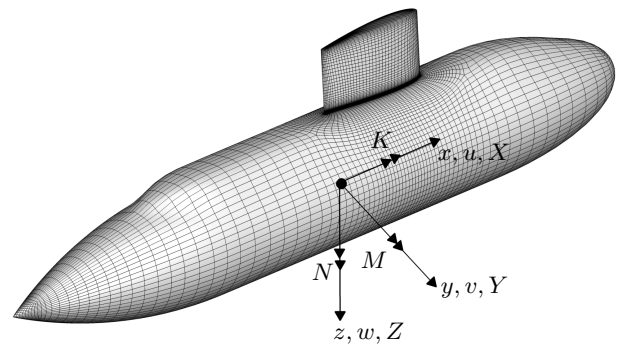
Figure 1: Submarine geometry with midships coordinate systems

2.2 Numerical grid

For the best performance of ReFRESCO, i.e., code efficiency, small numerical errors and to facilitate uncertainty analysis, multi-block structured O-O grids should be used. For this study the commercial grid-generation software PDC GridPro is used to construct the multi-block structured topology. An example of a course grid cell distribution on the submarine hull is given in Figure 1.

Grid cell size To be able to compute the actual velocity profile of the viscous boundary layer down to the wall, a certain amount of grid elements are needed in the region close to the wall. The aim of this study is to investigate the relation between the numerical uncertainty and the wall-normal distribution of the wall-bounded grid cells. The resolution of this near-wall region can be indicated by the non-dimensional y^+ and the type of distribution, e.g., equidistant or stretching function. The y^+ is defined as:

$$y^+ = \frac{u_\tau d}{\nu} \qquad (2)$$

with d the distance of the cell center to the wall and u_τ the friction velocity defined by,

$$u_\tau = \sqrt{\frac{\tau_w}{\rho}} \quad (3)$$

A stretching function is used to create a smooth transition from the small wall-bounded grid cells to larger elements in the surrounded region. The used stretching function in this study is based on a percentage growth of the adjacent cells (rate of stretching χ) in the wall-bounded blocks of the multi-block topology.

Series of geometrically similar grids To perform a numerical uncertainty analysis based on the method of Eça and Hoekstra [4], a series of geometrically similar grids is desired. GridPro has the possibility to generate a series of geometrically similar grids by starting from a fine grid and reducing the amount of grid cells in all directions by a constant coarsening factor ζ. Since a stretching function is used in the wall-bounded blocks, the rate of stretching χ will change over this series. This means that by coarsening the grid the rate of stretching χ will increase by a power function as can be seen in Figure 2, according to,

$$\chi_{(\zeta)} = \chi_{(0)}^{\zeta^{-1}} \quad (4)$$
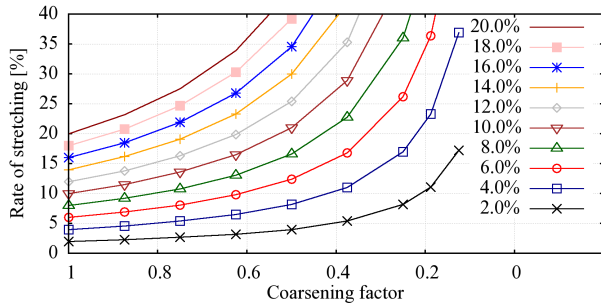
Figure 2: Rate of stretching as function of the coarsening factor

For example, if you start with a fine grid with an initial rate of stretching of 20% ($\chi_{(0)} = 1.2$) in wall-normal direction, the increase of the rate of stretching by a coarsening factor of $\zeta = 0.5$ is quadratically, i.e. 44%, which is undesirable. This relation should be taken into account by choosing the initial rate of stretching $\chi_{(0)}$, for the finest grid. Therefore a small initial rate of stretching, i.e. 4 or 5%, is desired when doing grid studies over a wide range of coarsening factors.

Domain size The domain size should be large enough to neglect the influence of the boundaries on the behaviour of the flow field in meaningful regions. For this study a cylindrical domain with a radius of approximately $4L_{oa}$ around the tip of the stern is

used. The top and bottom boundaries are located at approximately $3L_{oa}$ below and above the symmetry axis of the hull, see Figure 3.

Boundary conditions For this study all simulations were conducted for deep diving conditions. Therefore, deformation of the free-surface does not need to be incorporated. A pressure boundary condition is used as upper surface and for unrestricted simulations, i.e. far away from the bottom, a symmetry boundary condition is used as lower surface, see Figure 3. Furthermore, a no-slip wall boundary condition is applied on the hull and sail and the boundary conditions on the exterior domain are determined using an *automatic detect* boundary condition, which automatically applies inflow condition, pressure or outflow (Neumann) condition on the cell faces [5].
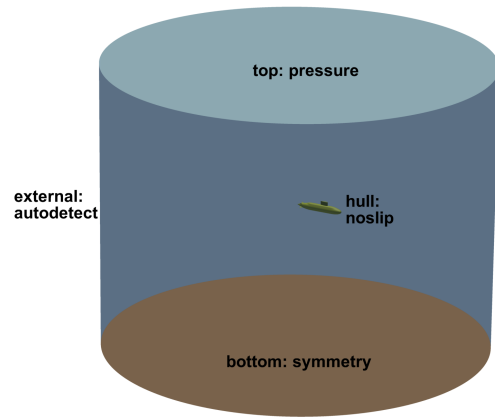
Figure 3: Numerical domain with boundary conditions

2.3 Numerical Solver

All simulations were accomplished with the MARIN in-house URANS (unsteady Reynolds averaged Navier-Stokes) code ReFRESCO. The governing equations were integrated down to the wall, i.e., no wall-functions are used. The coupled pressure/velocity solver is used with a QUICK type convective flux discretisation scheme with enabled excentricity correction. The turbulence models used for this study are the one-equation turbulence model by Spalart and Allmaras [7] (designated S-A), and the two-equations $k - \omega$ SST (1994) turbulence model by Menter [8]. The Dacles-Mariani streamwise vorticity correction, proposed by Dacles-Mariani et al. [9] is activated in both cases ($C_{prod} = 4$).

2.4 Numerical uncertainty

Without knowing the exact solution of the problem an estimation of the numerical error is required to indicate the quality of CFD. As described by Eça,

Hoekstra and Vaz [4, 3], the numerical uncertainty of a CFD prediction has three components, i.e., the round-off error, the iterative error U_i and the discretisation error U_d. The round-off error is a consequence of the finite precision of computers, but since all the computations are performed with double precision the round-off error is negligible. The iterative error comes from the non-linearity of the mathematical equations solved by CFD, which can also be neglected if the iterative error is two orders of magnitude smaller than the discretisation error. Finally, the discretisation error is a consequence of the approximations made to transform the partial differential equations into a system of algebraic equations.

The goal of the numerical uncertainty is to obtain an error band for a given calculation result such that the exact solution is within that band with 95% confidence.

3 Programme of simulations

The programme of simulations is given by Table 1 where the series are indicated by a Case number, Grid type, y^+ information of the finest grid and turbulence model. More detailed information of the series of grids are given in Table 3, which contains the: Name, Number of cells, Coarsening factor, Rate of stretching and y^+ values of each grid. The maximum y^+_{max} should not reach values above 5, since this is the threshold value for applying a wall-function scheme, where a blended scheme is active from 5 till 30. Note the very small y^+ values for grid C, which is used to analyse the influence of the ω parameter of the turbulence model, since it tends to infinity close to the wall. Grid C+ is a series of grids based on the $5M$ of the C-series. Within the C+ series, only changes are made in the boundary layer region. Furthermore, all calculations were performed at a model scale Reynolds number, $Re = 7.5 \times 10^6$.

Table 1: Programme of simulations

Case	Grid	y^+ $(\zeta = 1)$		χ	Turbulence
		Max.	Avg.	$(\zeta = 1)$	model
I	A	0.35	0.16	10.0%	$k - \omega$ SST
II	B	0.35	0.16	4.0%	$k - \omega$ SST
III	B	0.35	0.16	4.0%	S-A
IV	C	0.018	0.008	5.0%	$k - \omega$ SST
V	C+	0.034*	0.015*	10.3%*	$k - \omega$ SST

* This series is based on the $\zeta = 0.5$ of the grid C-series

4 Results

In this section the results of the numerical uncertainties will be discussed, using the procedure proposed by Eça and Hoekstra [4].

4.1 Iterative error

Theoretically, the iterative error can be decreased as far as the machine accuracy permits. However, in complex turbulence flows it is not guaranteed that this level of convergence can be achieved. The simulations in this study were run until the normalised residual between successive iterations has dropped well below 1×10^6 or when further iterative convergence was not obtained (stagnation), which was still well below 1×10^4 for all cases. The relative changes in the non-dimensional integral quantities (forces and moments) at the end of the simulations were well below 1×10^9 and the iterative errors are small, see Figure 4. Since this behaviour was seen for all cases only one representative simulation is shown, which is the 7.3M grid of Case II. Hence, the iterative error is two or more orders of magnitude smaller than the discretisation error (see subsection 4.2), the iterative error can be neglected and will not be discussed further in this paper.
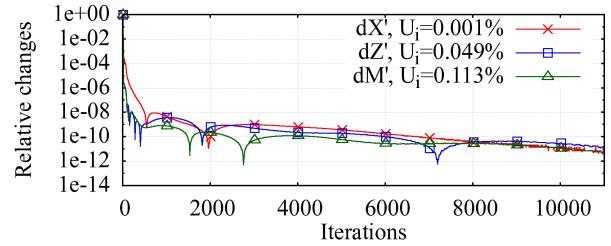
Figure 4: Iterative error

4.2 Discretisation error

Since the round-off error and iterative error in this study are negligible, the discretisation error equals the numerical uncertainty. The discretisation error of the forces X', Z' and moment M' can be found in Table 4 - 7, where the resistance force is divided into a pressure X'_p and frictional part X'_f. The other values ϕ_1 and ϕ_0 are the non-dimensional scalar quantities on the finest grid and the estimated exact solution, respectively. To analyse the origin of the discretisation error in more detail the separate parts of the resistance force is plot in Figure 5. Here, the relative step size is based on the number of grid cells of the finest grid n_1 and the course grids n_i according,

$$\text{Relative step size} = \sqrt[3]{n_1/n_i} \qquad (5)$$

The following statements are based on the given discretisation errors and the fitted curvature line.

General notes: all Cases

- The theoretical order of convergence based on the discretisation method is second order. For geometrically similar grids in the asymptotic range this
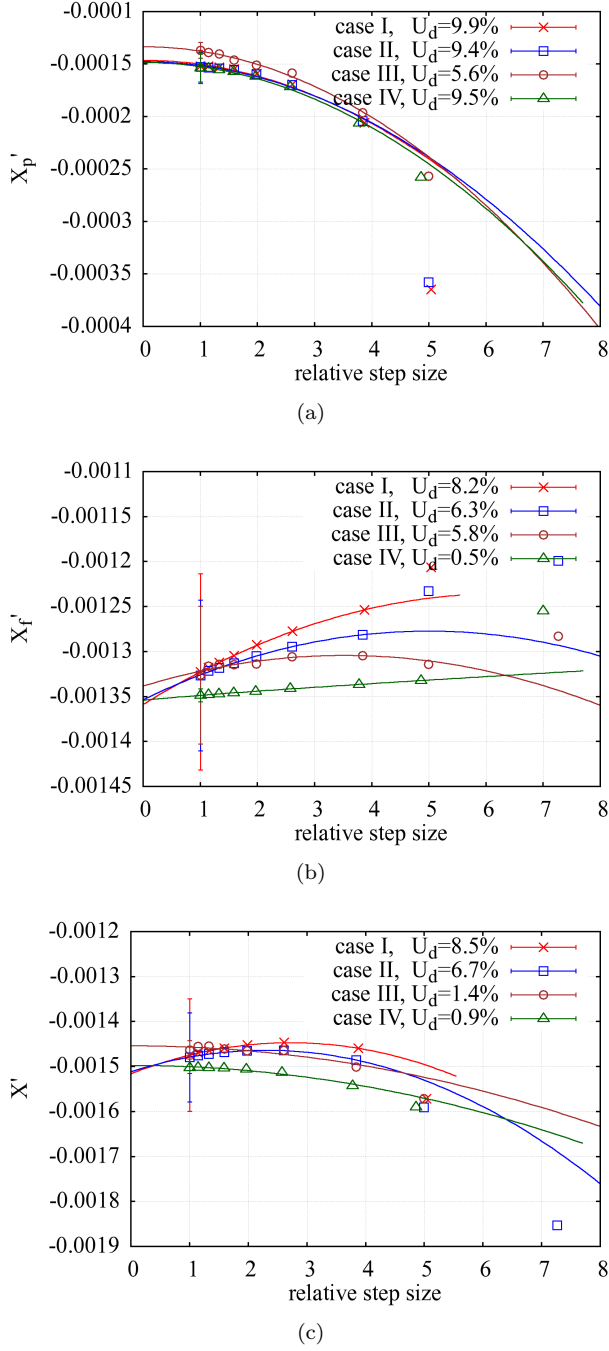
Figure 5: Discretisation error

will emphasize an independency of the result by further grid refinement. Unfortunately not all coefficients seem to fit in this asymptotic range.

- The pressure part of the resistance force X'_p shows an asymptotic behaviour towards grid refinement.
- High uncertainties can be found for Z' and M' coefficients, but since these coefficients are relatively small in straight flight, not too much attention should be given.

Compare rate of stretching: Case I and II

- The difference for these cases is the initial rate of stretching for the finest grid, i,e., 10% and 4% for

Case I and II, respectively.

- The polynomial behaviour of the curvature fit close to the finest grid is undesirable and not expected, since it assumes no asymptotic range with grid refinement.
- For both case the uncertainties are poor, e.g., the resistance forces are around $7-9\%$.
- Restriction of the uncertainty analysis to the resistance forces only, Case II, with the lower rate of stretching, shows marginal better results.

Compare turbulence model, Case II and III

- The difference for these cases is the turbulence modelling, i,e., $k-\omega$ SST and S-A for Case II and III, respectively.
- The resistance force X' shows an asymptotic behaviour towards grid refinement and therefore a low uncertainty ($U_d = 1.4\%$).
- The better order of convergence is probably due to the less grid-sensitivity of the S-A turbulence modelling, since this model has no grid dependent parameter like the ω equation in the $k-\omega$ SST model.
- Restriction of the uncertainty analysis to the resistance forces only, Case III, with the S-A turbulence modelling, shows better results.

Compare y^+ dependency, Case II and IV

- The difference for these cases is the initial value of y^+ for the finest grid, i,e., $y^+_{avg} = 0.16$ and $y^+_{avg} = 0.008$ for Case II and IV, respectively.
- The resistance force X' shows an asymptotic behaviour towards grid refinement and therefore a low uncertainty ($U_d = 0.9\%$).
- The better order of convergence is thought to be related to the higher values for ω close to the wall, which by Equation 6 tends to infinity by approaching the wall, see also Figure 6. The related eddy viscosity, given by Equation 7, goes to zero approaching the wall, since there is no turbulence activity in the close-wall viscous sub-layer.
- The uncertainties for Case IV are generally good. Analysing the uncertainties and asymptotic behaviour with grid refinement, Case IV, with the low values for y^+, shows the best results.

$$\omega_{wall} = 10 \frac{6\,\nu}{(\beta_1\,d^2)} \qquad (6)$$

$$\nu_T = \frac{\alpha_1\,k}{\max(\alpha_1\,\omega, SF_2)} \qquad (7)$$

with d the distance of the cell center to the wall.

4.3 Favourable wall-bounded grid cell height (y-plus)

The series of grids used for Case IV shows very good numbers for numerical uncertainty analysis. This uncertainty analysis shows that relative coarse grids can
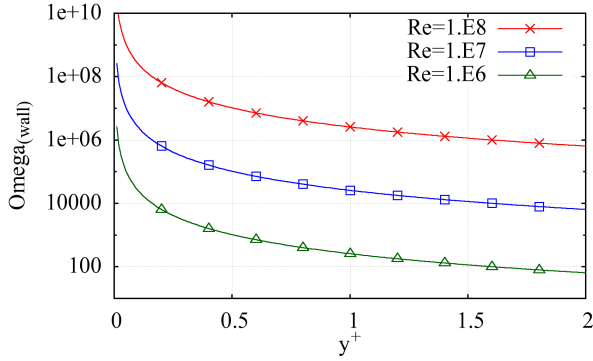
Figure 6: Specific dissipation rate ω as function of y^+

be used for analysing the forces and moments. The use of a coarse grid for CFD is desired on a practical base, since the very fine grids are very expensive in CPU power and memory consumption. This section describes how to choose a course grid which is sufficiently fine to satisfy the criteria of an absolute change in resistance force X' within one percent based on the finest grid C 38M.

Figure 7.a shows the forces X'_p, X'_f, X' and Z' and moment M' as a function of the average y^+ value, for the nine grids which are used in Case IV. Grid 38M with a $y^+ = 0.008$ is situated on the left of the figure while grid 110k with a $y^+ = 0.048$ is situated most right. The figure shows a gradually change of the quantities, except for the last grid. This steep change indicates a too coarse grid to capture the flow physics, even though the average y^+ value is still small. To make a good estimation for the wall-bounded gridcell height the flow physics should be captured well. Since the change in the X' from the finest grid (38M) to the fifth grid (5M) is only 0.2%, this medium fine grid is used as a reference grid for the grid C+ series. Detailed information about grid C+ series can be found in Table 3.

Figure 7.b shows the forces X'_p, X'_f, X' and Z' and moment M' as a function of the average y^+ value of the grid C+ series (Case V). The range of y^+ values varied from $y^+ = 0.015$ (C1) to $y^+ = 1.92$ (C8). All grids have a fixed percentage cell-stretching in the wall-bounded blocks, where the rate of stretching is approximately 10% or a bit less. Except for X' and X'_f all quantities show an horizontal line. The values for X' are summarized in Table 2, where the absolute change with reference to 38M and C1 are given by E_{38M} and E_{C1}. The first three grids of the C+ series $y^+ < 0.1$ show a small change $E < 1\%$ in X'. Larger changes $E > 4\%$ are seen for the last four grids where $y^+ > 0.4$. Hence, for this geometry and grid topology a medium fine grid with a rate of stretching of approximately 10% and an average $y^+ \approx 0.1$, is sufficiently fine to estimate the forces and moments within one percent with reference to a very fine grid

which has small numerical uncertainties.
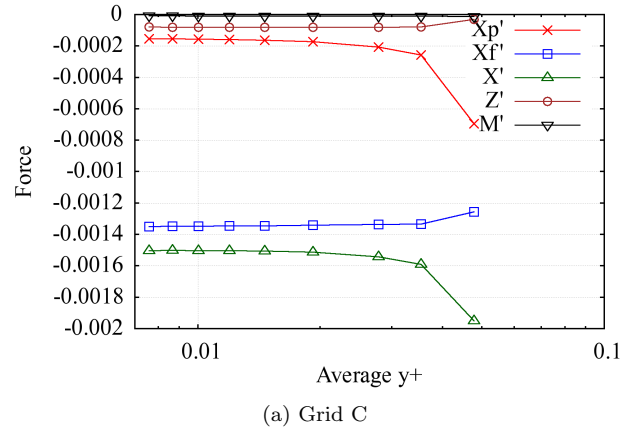
(a) Grid C
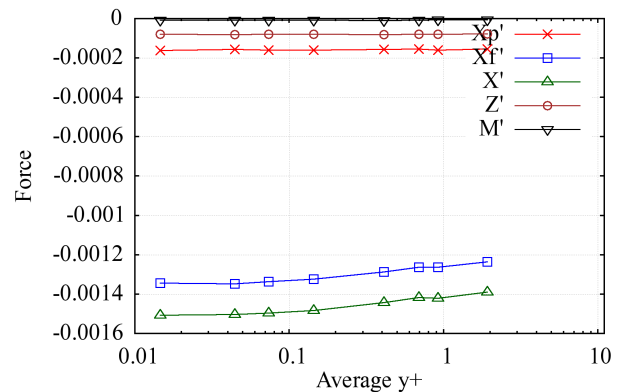
(b) Grid C+

Figure 7: Non-dimensional quantities as function of the average y^+ for grid series C and C+

Table 2: Absolute changes in X' of the grid C+ series

Grid	ID	X' ($\times 10^3$)	E_{C38M}	E_{C1}
C	38M	−1.50210	-	-
C+	C1	−1.50566	0.24%	-
C+	C2	−1.50279	0.05%	−0.19%
C+	C3	−1.49559	−0.43%	−0.67%
C+	C4	−1.48181	−1.35%	−1.58%
C+	C5	−1.44194	−4.01%	−4.23%
C+	C6	−1.41704	−5.66%	−5.89%
C+	C7	−1.42102	−5.40%	−5.62%
C+	C8	−1.39010	−7.46%	−7.68%

5   Conclusions

1. Using the numerical uncertainty method of Eça and Hoekstra [4], a clear influence on the numerical uncertainty is seen by changing the wall-normal distribution of the wall-bounded grid cells. Changing the stretching of the grid distribution within reasonable values didn't show much influence, whereas decreasing the height of the wall-bounded grid cells towards $y^+ \ll 1$ shows a significant decrease of the numerical uncertainties.

2. If the general research interest of the CFD simulation is to determine the forces and moments, a medium fine grid with a rate of stretching of approximately 10% and an average $y^+ \approx 0.1$, is sufficiently fine to estimate the forces and moments within one percent with reference to a very fine grid which has small numerical uncertainties.

References

[1] P. Roache. Verification of codes and calculations. *AIAA Journal*, Vol. 36(5):696–702, 1998.

[2] G. Vaz, F. A. P. Jaouen, and M. Hoekstra. Free-surface viscous flow computations. Validation of URANS code FreSCo. In *28th International Conference on Ocean, Offshore and Arctic Engineering (OMAE)*, number OMAE2009-79398, Honolulu, Hawaii, May 31–June 5 2009.

[3] L. Eça, G. Vaz, and M. Hoekstra. A verification and validation exercise for the flow over a backward facing step. In *Fifth European Conference on Computational Fluid Dynamics*, Lisbon, Portugal, June 2010. ECCOMAS.

[4] L. Eça and M. Hoekstra. Evaluation of numerical error estimation based on grid refinement studies with the method of the manufactured solutions. *Computers & Fluids*, 38(8):1580–1591, September 2009.

[5] S. L. Toxopeus. *Practical application of viscous-flow calculations for the simulation of manoeuvring ships*. PhD thesis, Delft University of Technology, Faculty Mechanical, Maritime and Materials Engineering, May 2011.

[6] P. Joubert. Some aspects of submarine design - part 2. Shape of a submarine 2026. Technical Report DSTO-TR-1622, Defence Science and Technology Organisation, Fishermans Bend, Victoria, Australia, October 2006.

[7] P. R. Spalart and S. R. Allmaras. A one-equatlon turbulence model for aerodynamic flows. In *30th Aerospace Sciences Meeting & Exhibit*, Reno, Nevada, January 1992. American Institute of Aeronautics and Astronautics.

[8] F. R. Menter. Two-equation eddy-viscosity turbulence models for engineering applications. *AIAA Journal*, Vol. 32(8):1598–1605, August 1994.

[9] J. Dacles-Mariani, G. G. Zilliac, J. S. Chow, and P. Bradshaw. Numerical/experimental study of a wingtip vortex in the near field. *AIAA Journal*, 33:1561–1568, September 1995.

Table 3: Information of the used grids

Grid	ID	Number of cells $\times10^{-3}$	Coarsening factor ζ	Rate of stretching χ	y^+ Max.	y^+ Avg.
A	24M	24093	1.0	10%	0.35	0.16
	16M	16158	0.875	11.5%	0.40	0.19
	10M	10221	0.75	13.6%	0.46	0.22
	6M	5993	0.625	16.5%	0.55	0.26
	3.1M	3088	0.5	21.0%	0.68	0.32
	1.4M	1353	0.375	28.9%	0.89	0.42
	415k	415	0.25	46.4%	1.41	0.63
	190k	189	0.1875	66.2%	1.71	0.79
B	28M	28263	1.0	4.0%	0.35	0.16
	19M	19011	0.875	4.6%	0.40	0.18
	12M	12036	0.75	5.4%	0.46	0.21
	7M	7038	0.625	6.5%	0.55	0.25
	3.6M	3647	0.5	8.2%	0.67	0.31
	1.6M	1604	0.375	11.0%	0.87	0.41
	500k	499	0.25	17.0%	1.30	0.58
	230k	227	0.1875	23.3%	1.58	0.73
	75k	74	0.125	36.9%	2.22	0.98
C	38M	38053	1.0	5.0%	0.018	0.008
	26M	25599	0.875	5.7%	0.020	0.009
	16M	16285	0.75	6.7%	0.023	0.010
	10M	9599	0.625	8.1%	0.028	0.012
	5M	5011	0.5	10.3%	0.034	0.015
	2.2M	2234	0.375	13.9%	0.044	0.019
	710k	708	0.25	21.6%	0.063	0.028
	330k	332	0.1875	29.7%	0.079	0.035
	110k	111	0.125	47.7%	0.113	0.048
C+	C1	5011	-	10.3%	0.034	0.015
	C2	4244	-	10%	0.099	0.044
	C3	3979	-	10%	0.161	0.074
	C4	3677	-	10%	0.312	0.144
	C5	3283	-	10%	0.89	0.41
	C6	3109	-	10%	1.49	0.69
	C7	3106	-	10%	1.95	0.92
	C8	3158	-	10%	4.30	1.92

Table 4: Numerical uncertainty Case I, Grid A

Item	ϕ_0	ϕ_1	U_ϕ
X'_p	-1.46×10^{-4}	-1.52×10^{-4}	9.9%
X'_f	-1.36×10^{-3}	-1.32×10^{-3}	8.2%
X'	-1.52×10^{-3}	-1.47×10^{-3}	8.5%
Z'	-8.02×10^{-5}	-7.90×10^{-5}	7.2%
M'	-8.35×10^{-6}	-7.56×10^{-6}	14.6%

Table 5: Numerical uncertainty Case II, Grid B

Item	ϕ_0	ϕ_1	U_ϕ
X'_p	-1.48×10^{-4}	-1.53×10^{-4}	9.4%
X'_f	-1.35×10^{-3}	-1.33×10^{-3}	6.3%
X'	-1.51×10^{-3}	-1.48×10^{-3}	6.7%
Z'	-8.12×10^{-5}	-7.96×10^{-5}	12.9%
M'	-1.02×10^{-5}	-8.06×10^{-6}	35.0%

Table 6: Numerical uncertainty Case III, Grid B

Item	ϕ_0	ϕ_1	U_ϕ
X_p	-1.33×10^{-4}	-1.37×10^{-4}	5.6%
X_f	-1.34×10^{-3}	-1.33×10^{-3}	5.8%
X	-1.45×10^{-3}	-1.46×10^{-3}	1.4%
Z	-7.46×10^{-5}	-7.39×10^{-5}	5.7%
M	-9.32×10^{-6}	-7.72×10^{-6}	127.9%

Table 7: Numerical uncertainty Case IV, Grid C

Item	ϕ_0	ϕ_1	U_ϕ
X'_p	-1.48×10^{-4}	-1.54×10^{-4}	9.5%
X'_f	-1.35×10^{-3}	-1.35×10^{-3}	0.5%
X'	-1.50×10^{-3}	-1.50×10^{-3}	0.9%
Z'	-7.94×10^{-5}	-7.88×10^{-5}	5.3%
M'	-7.80×10^{-6}	-7.76×10^{-6}	17.2%

Hydrodynamics Analysis of the Twin Fin Propulsion System

Olof Klerebrant Klasson[1], Simon Törnros and Tobias Huuva
(Berg Propulsion Production AB)
[1]email: olof.klasson@bergpropulsion.com

Introduction

Background

Today diesel-electric propulsion systems in Offshore Service Vessels are most commonly equipped with rotatable azimuth thrusters driven by electric motors. This eliminates the need for rudder and stern tunnel thrusters, but makes the vessel more vulnerable from a mechanical point of view due to the angle gears and other mechanical parts not being accessible from inside the vessel. In case of break down on azimuth thrusters, it is normally necessary to go into dry dock for repair.

An alternative to azimuth thrusters is the conventional diesel-electric or diesel-mechanical propulsion concept with a long shaft and machinery positioned inside the hull. This system is more reliable than azimuth thrusters, but requires more space for gear and electric motor in cargo area. This solution is also difficult to retrofit on an azimuth-fitted vessel.

In order to overcome these obstacles, Berg Propulsion, Grontmij and SMG have developed a compact design for diesel-electric twin propeller vessels based on well-tested components through many years of experience, well-proven to work in harsh environments such as in arctic areas. The system is developed for Offshore Service Vessels working in Dynamic Positioning mode, but will also be a competitive alternative for other twin propeller vessels where noise and vibration requirements call for diesel-electric systems, such as seismic or cruise vessels. The system is intended for both new buildings and for uncomplicated retrofits on existing azimuth-fitted vessels. Since the system prefabrication, the work and downtime at shipyard can be minimized.

Ice protection fins can be mounted on the twin fins as on single screw vessels and also as an ice knife ahead of the rudder. Inside, the system includes only one water-lubricated bearing, where the seal can be replaced from within the hull. The short propeller shaft has a hydraulically fitted shaft coupling connecting to the gearbox output shaft. Between the gearbox input shaft and electric motor output shaft a flexible coupling is fitted. The compartment is easily accessible from inside the hull, from where also the gear and electric motor can be removed.

The two separate propulsion units that substitute the azimuth thrusters consist, on starboard and portside, of controllable pitch propellers mounted as normally seen on single screw vessels with skeg. The CP propeller can be mounted with or without a nozzle depending on various vessel requirements.

The concept may include steering gear with rudder that can be of high efficient flap type, where maneuverability is required; and tunnel thrusters arranged in centre skeg, where Dynamic Positioning ability is required.

The overall hydrodynamic performance of the compact propulsion system with the Twin Fin Propulsion System needs to be investigated.

Objective

The purpose of this study is to compare the hydrodynamic performance of the Twin Fin Propulsion System with a conventional hull utilizing twin azimuth thrusters in a self propulsion test using CFD.

Test Cases and Software

The CFD computations were performed using OpenFOAM v2.0.x and v2.1.x. The used preprocessors were ANSA v14.0.0 and snappyHexMesh. All post processing was performed with FieldView v13.2 and OpenFOAM.

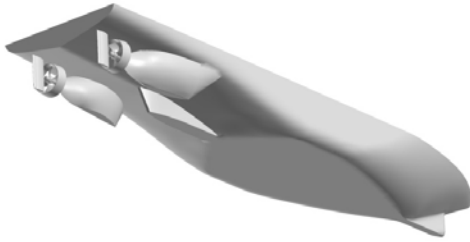The twin fin hull can be seen in Figure 1 and the azimuth hull can be seen in Figure 2.

Figure 1: Twin fin hull

Figure 2: Twin azimuth hull

The vessel is an offshore vessel with characteristics as can be seen in Table 1 for both the twin fin and the azimuth fitted hull.

Table 1: Characteristics of the hulls

	Azimuth	Twin fin
Lpp [m]	80	80
B [m]	20	20
T [m]	6.6	6.6
S [m^2]	2403	2568

The propeller characteristics of the azimuth unit and the twin fin propeller can be seen in Table 2.

Table 2: Characteristics of the propellers

	Azimuth	Twin fin
D [m]	3.5	3.8
RPM [-]	139	122
P07/D [-]	1.300	1.189
Z [-]	4	4
EAR [-]	0.551	0.531

Computational Methodology

All computations were performed using the Reynolds Averaged Navier-Stokes (RANS) approach with the Menter $k - \omega$ SST turbulence model, applying wall functions for near wall treatment. All grids in the study are of unstructured type with prism layers near the wall yielding $30 \leq y^+ \leq 100$.

Second order accurate schemes were used for all terms except for the turbulent quantities, where first order upwind was applied. Second order upwind was utilized for the convection term of velocity.

For pressure, a geometric agglomerated algebraic multigrid (GAMG) solver was applied and the velocity was solved with a diagonal incomplete-LU (DILU) operation Gauss Seidel solver. All turbulent quantities were solved with a preconditioned biconjugate gradient (PBiCG) solver.

For the transient calculations, convergence was considered reached when the mean variation in global force was small. For steady state calculations, convergence was considered achieved when the global force variation was small and the residuals where below 10^{-5}.

Hull Resistance Computations

The hull resistance of both hulls was computed using a transient two phase interface tracking volume of fluids (VoF) approach. A snipped hexahedron mesh with three million cells on the half hull was applied in the entire hexahedral domain made three ship lengths downstream, two ship lengths wide, one ship length upstream, 1.5 ship lengths below the expected free and 0.5 ship lengths above the expected free surface. The mesh can be seen in Figure 3.
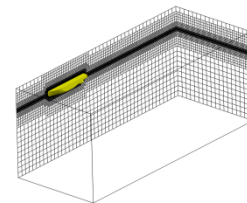

Figure 3: The computational domain of the hull resistance test

The bare hull calculations were performed with the Pressure-Implicit with Splitting of Operators (PISO) algorithm. The pressure velocity coupling was looped over multiple times, while no iterations

over the non-linear coupling was performed as proposed by (Issa, 1985)

The integrated pressure force was oscillative. The oscillations were found to be periodic with a constant mean value and amplitude and hence the calculations were stopped after three periodic oscillations. The pressure force was averaged over at least two periods. Each period approximately corresponds to one water particle passing the hull from bow to stern.

Open Water Computations
The open water calculations were set up in a cylindrical domain. The simulations were of steady state type using the SIMPLE algorithm for pressure velocity coupling.

The rotation of the propeller was modeled with MRF. For this a cylindrical MRF zone was used. The applied meshes were unstructured with triad surface mesh and mixed polyhedral volume elements, applying tetrahedrons and pyramids in the transition and hexahedral cells to the largest extent possible in the free stream region. The applied meshes were made with a total number of 3.5 million cells for the twin fin propeller and 7.7 million for the azimuth. An example of the mesh can be seen in Figure 4. The MRF zone was located inside the nozzle for each propeller.
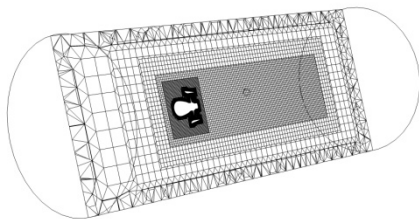
Figure 4: The computational domain of the open water test

The open water characteristics of the azimuth unit were calculated for the whole unit. A closer view of the mesh can be seen in Figure 5.
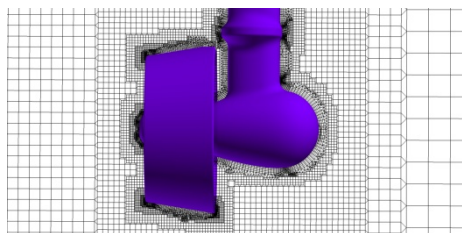
Figure 5: Centreplane cut of the volume mesh close to the propeller for the open water test

The present calculation methodology has been carefully investigated and validated for several different propeller calculation setups. See (Abdel-Maksoud, 2011), (Klerebrant Klasson, 2011), and (Huuva, 2011). The method has also been investigated and validated in internal work during propeller design.

In Behind Computations
In the in Behind condition, the computational domain consisted of the hull, shaft, rudders and propellers with nozzles. The setup was similar to the setup in the open water calculations. The applied twin fin mesh was made with 5 million cells and the applied azimuth mesh with 9 million cells. The mesh was unstructured and made by a similar approach as for the open water test. The mesh is visualized in Figure 6.
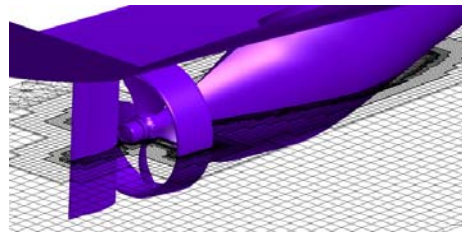
Figure 6: The mesh for the self propulsion test

The free surface was represented by a symmetry plane. The propeller rotation was modeled using MRF. The RPM of the propeller was altered until force equilibrium between the hull resistance and the propeller thrust was reached.

To account for the wave resistance, a bare hull calculation with symmetry plane as free surface was performed. The free surface in the self propulsion test was accounted for by increasing the power in the calculation until the thrust overcame the hull resistance increased by the difference between the symmetry plane and the VoF calculation.

Results

Hull Resistance

The oscillating pressure force can be seen in Figure 7. The amplitude and mean value is fairly constant. The plot is characteristic for all bare hull simulations.
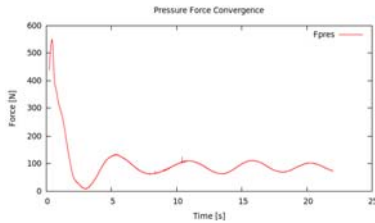
Figure 7: Oscillating pressure force from VoF simulation

The resistance from the bare hull calculation of the azimuth hull was compared to the model test results and the difference was small.

The bare hull resistance increased when comparing the conventional azimuth hull to the twin fin hull. This was an effect of the increased wetted surface, but also due to a separation area occurring downstream the fin as can be seen when comparing Figure 8 to Figure 9.
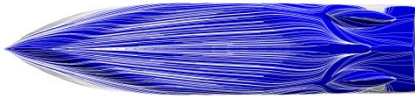
Figure 8: Streamlines on twin fin hull

Figure 9: Streamlines on azimuth hull

The resistance was increased further due to a low pressure region on the outside of the fin, caused by the acceleration of water due to the curvature. This low pressure region tended to create a wave on the fin as occurring in Figure 10, but not in Figure 11.
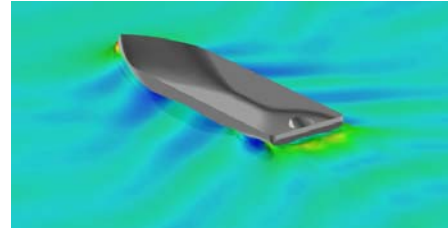
Figure 10: Wave elevation around the twin fin hull
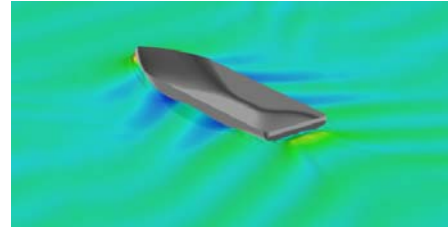
Figure 11: Wave elevation around the azimuth hull

The nominal wake of the azimuth and twin fin hull can be seen in Figure 12 and Figure 13 respectively. Note that the azimuth unit is not included for the azimuth hull, which explains the very low wake.
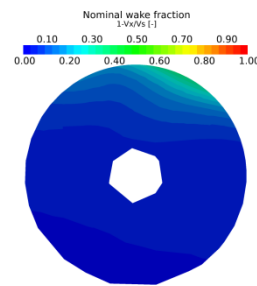
Figure 12: Nominal wake for the azimuth hull

The twin fin wake is fairly circular and evenly distributed.
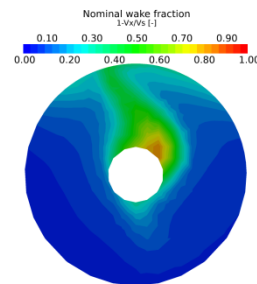
Figure 13: Nominal wake for the twin fin hull

Open Water

The open water performance of the azimuth was lower due to the fact that the propeller diameter was smaller and that the gear house was present in the calculation.

As can be seen when comparing Figure 14 and Figure 15, the water upstream accelerated towards the propeller suction side is forced to pass the gear house, yielding increased resistance in the azimuth case. Hence both increased drag and accelerated passing water are contributing to the lowered open water performance of the azimuth unit.
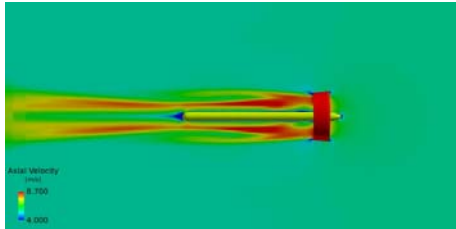
Figure 14: Axial velocity field at J=0.6 for twin fin propeller
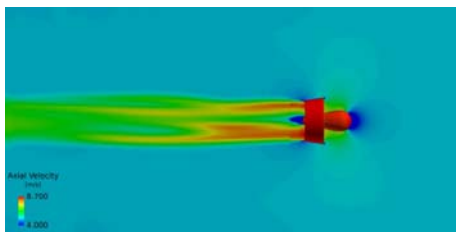
Figure 15: Axial velocity field at J=0.6 for azimuth unit

In Behind

The inflow to the propeller is improved for the twin fin solution by a more gradual and circular distribution of the wake as can be seen when comparing Figure 16 to Figure 17.
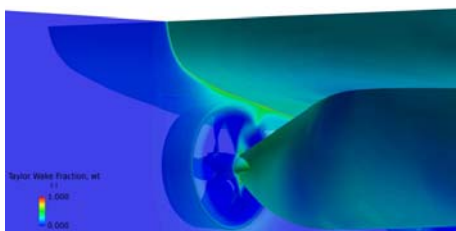
Figure 16: Inflow to the twin fin propeller
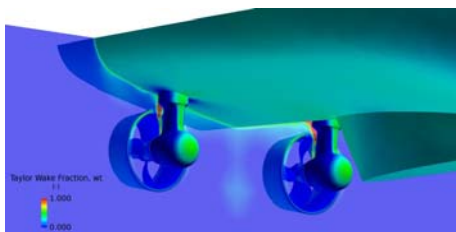
Figure 17: inflow to the azimuth propeller

The open water efficiency was significantly increased for the twin fin system compared to the azimuth unit, which is due to the definition of the applied open water test methodology. Further, the hull efficiency was increased due to the improved effective wake. The hull pressure distribution and velocity field for the twin fin and azimuth hull can be seen in Figure 18 and Figure 19.
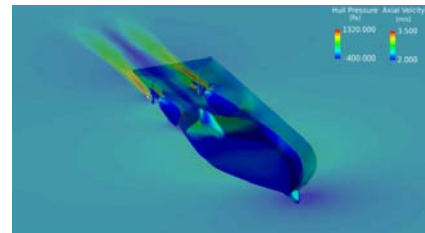
Figure 18: Pressure distribution on the hull and axial velocity field for the twin fin hull
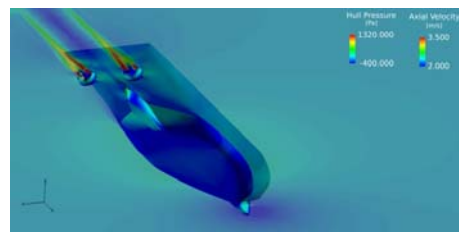
Figure 19: Pressure distribution on the hull and axial velocity field for the azimuth hull

The increased resistance from the hull, but the gains in propulsion and transmission efficiency, yields a higher total efficiency for the twin fin concept than the efficiency for the azimuth solution.

Conclusions

The following conclusions can be drawn from this study and applies to adding twin fins in comparison to the hull equipped with azimuth thrusters:

- The fins allow a larger propeller diameter, yielding higher open water efficiency
- The hull resistance increase, since the wetted surface increase when the fins are introduced
- The fins causes a separation area downstream, which yields higher resistance
- The fins increases resistance by creating a wave near the fins
- The inflow to the propeller is improved by the fins
- The hull efficiency is improved due to the increase in effective wake fraction
- The total consumed break power is decreased when applying the fins

References

Abdel-Maksoud M., "Proceedings of smp'11 Workshop on Cavitation and Propeller Performance", <u>The Second International Symposium on Marine Propulsors</u>, Hamburg, 2011.

Carlton J. <u>Marine Propellers and Propulsion</u>, 2nd ed., Elsevier Ltd, Burlington, Jun, 2007, pp. 89-135.

Holtrop, J. "A statistical Re-Analysis of Resistance and Propulsion Data", <u>International Shipbuidling Progress</u>, vol. 353, 1984, pp. 272.

Huuva T and Pettersson M, "Investigating the Flexibility of Twin Screw Vessels with Various Propulsion Concepts using CFD", <u>Proceedings of the 12th Numerical Towing Tank Symposium</u>, Cortona, 2009.

Huuva T, "Nozzle Design Using Automated Optimization Routines", <u>RINA - Developments in Marine CFD</u>, London, 2011.

Huuva T., "Green concepts for propulsion", <u>Proceedings of the 9th Green Ship Technology Conference</u>, Copenhagen, 2012.

Issa R. I., "Solution of the Implicitly Discretised Fluid Flow Equations by Operator-Splitting", <u>Journal of Computational Physics</u>, 1985, pp. 40-65

Klerebrant Klasson O., "A Validation, Comparison and Automation of Different Computational Tools for Propeller Open Water Predictions", June 2011, Chalmers University of Technology, Department of Shipping and Marine Technology, Göteborg.

Klerebrant Klasson O., Huuva T. and Pettersson M. "Automation of Propeller Calculations and Application to the Potsdam Propeller Test Case – PPTC", <u>Proceedings of the 14th Numerical Towing Tank Symposium</u>, 2011, pp. 86-91.

Larsson L. and Raven H.C., <u>Principles of Naval Architecture Series - Ship Resistance and Flow</u>, Society of Naval Architects and Marine Engineers (SNAME), New York, 2010.

Larsson L., Stern F. and Visonneau M., "CFD in ship hydrodynamics --- Results of the Gothenburg 2010 workshop", <u>Int. Conf. Computational Methods in Marine Engineering</u>, MARINE 2011, Lisbon, 2011.

Matin F., "A Validation, Comparison and Hydrodynamics of Conventional Propeller and Azimuth Thruster in Behind Condition", Februari 2011, Chalmers University of Technology, Department of Shipping and Marine Technology, Göteborg.

Sanchez-Caja A, Sipilä T.P. and Pylkkänen J.V. "Simulation of viscous flow around a ducted propeller with rudder using different RANS-based approaches", <u>Proceedings of the 1st Int. Symp. Marine Propulsors, SMP'09</u>, Trondheim, 2009.

Versteeg H.K. and Malalasekera W., <u>An Introduction to Computational Fluid Dynamics – The Finite Volume Method</u>, 2nd ed., Pearson Educational Ltd, Harlow, 2007, pp 64-67.

Identification of Hydrodynamic Derivatives for Ship Maneuvering Prediction in Restricted Waters

Philipp Mucha and Bettar el Moctar*

1 INTRODUCTION

This paper investigates the identification of hydrodynamic derivatives for ships sailing in restricted waters and discusses their influence on course keeping stability. Planar Motion Mechanism (PMM) tests are numerically replicated drawing upon the solution of the Reynolds-averaged Navier-Stokes (RANS) equations. Both lateral and vertical flow restrictions are considered in systematic pure sway and yaw tests. The powerful influence canal walls or river topologies exert upon ships is notorious among pilots and hydrodynamicists because these effects aggrevate both ship handling and maneuvering prediction. While new vessels in inland waterway shipping tend to grow in size, existing waterways do not - this in turn imposes increased challenges to ensure safe and easy traffic. In this context maneuvering prediction methods become more important.

Related Work. Abundant discussions of ship hydrodynamics in restricted waters and numerical methods for prediction can be found in Tuck (1978), Newman (1978) and reference therein. More recently, investigations covering both Boundary Element Methods (BEM) and RANS-CFD relate to the International Conference on Ship Maneuvering in Shallow and Confined Waters (*e.g.* Liu, 2011) or the SIMMAN workshop (Stern et al., 2008). For the present study, the work of Thomas and Sclavounos (2006) is of special interest since it expands on the subject of hydrodynamic interaction forces in light of their influence on dynamic stability.

Organization of the Paper. The addressed maneuvering theory, the PMM test method and the numerical technique to model the ship flow is introduced first. Then, the virtual PMM test method is applied to derive sway and yaw acceleration derivatives for a spheroid. These are compared to related theoretical values from the literature. Specific light is shed on the test parameters and the numerical technique involved. Drawing upon these results for unrestricted flow the influence of a vertical wall and underkeel clearance is investigated. Finally the method is applied to a typical vessel encountered on German inland waterways. The resulting set of hydrodynamic derivatives populates a simple linear maneuvering model for various restricted maneuvering environments. The influence on course keeping stability is addressed stemming from the analysis of the dynamic systems' eigenvalues.

2 MANEUVERING THEORY

Newtonian mechanics are applied to a ship under rigid body and constant mass assumption leading to the maneuvering equations of motion. Their formulation is given for a ship-fixed Cartesian coordinate system x, y, z the origin of which coincides with the ship's longitudinal and transverse midpoint dimensions. x is pointing forward, y to starboard and z downward. The ship trajectory is given for an earth-fixed reference system x_0, y_0, z_0. For maneuvering purposes the equations of motion in six degrees of freedom are reduced to describe only those motions in the horizontal plane:

$$m\left(\dot{u} - vr - x_g r^2\right) = X \quad (1)$$
$$m\left(\dot{v} + ur + x_g \dot{r}\right) = Y \quad (2)$$
$$I_z \dot{r} + m x_g \left(\dot{v} + ur\right) = N \quad (3)$$

In (1-3) m is the ship mass and I_z the moment of inertia about the vertical axis. The rigid body velocities in surge, sway and yaw are denoted by u, v and r, respectively. The center of gravity takes coordinates x_g, y_g, z_g. Temporal derivatives are denoted with a dot. X is the external force in longitudinal direction, Y in transverse direction and N the external moment about the ship's vertical axis, respectively. A customary and straightforward approach to express the external forces is their formulation in terms of a Taylor-series expansion about an equilibrium state. If only small deviations from this state are considered a linear framework will suffice to cast the system dynamics. Moreover, for constant forward speed the surge mode can be excluded. The quantities arising from the Taylor-series expansion and acting on the state variables are known as the hydrodynamic derivatives. The maneuvering equations can be rearranged to constitute a classic linear mass-damper system:

$$\begin{bmatrix} -Y_{\dot{v}} + m & -Y_{\dot{r}} + mx_g \\ -N_{\dot{v}} + \Delta x_g & -N_{\dot{r}} + I_z \end{bmatrix} \begin{bmatrix} \dot{v} \\ \dot{r} \end{bmatrix} +$$
$$\begin{bmatrix} -Y_v & -Y_r + (m - X_{\dot{u}})U_1 \\ -N_v + (X_{\dot{u}} - Y_{\dot{v}})U_1 & -N_r + (m - Y_{\dot{r}})U_1 \end{bmatrix} \begin{bmatrix} v \\ r \end{bmatrix} \quad (4)$$
$$= \begin{bmatrix} -Y_{\delta_R} \\ -N_{\delta_R} \end{bmatrix} \begin{bmatrix} \delta_R \end{bmatrix}$$

*Philipp Mucha is with the Institute of Ship Technology, Ocean Engineering and Transport Systems (ISMT, University of Duisburg-Essen) and the German Federal Waterways Engineering and Reserach Institute (BAW). Bettar el Moctar is with ISMT. Email: philipp.mucha@uni-due.de, ould.el-moctar@uni-due.de

Table 1: MOTION PARAMETERS FOR PMM TESTS WITHIN AN EARTH-FIXED FRAME

Motion	Pure sway	Pure yaw
u	u_0	u_0
v	$-y_{max}\omega cos(\omega t)$	$-y_{max}\omega cos(\omega t)$
r	0	$\psi_{max}\omega sin(\omega t)$

Figure 1: COORDINATE SYSTEMS FOR SHIP MANEUVERING

The subscripts in X, Y and N denote the quantities with respect to which the partial derivatives are taken. For ship-like bodies the hydrodynamic derivative $X_{\dot{u}}$ is considerably lower than the ship's mass and can be dropped from the equations. A way to identify these coefficients is the PMM method. Through dynamic tests in which a harmonic motion is superponed to a forward motion at constant speed, both acceleration and velocity derivatives can be found. The periodic time series of the measured or computed forces are then referred to the Taylor series and subjected to Fourier analysis. Within the linear framework the expression for Y in pure sway mode then reads

$$Y = Y_{\dot{v}}\dot{v} + Y_v v \tag{5}$$

In line with the motion formulation within an earth-fixed coordinate system provided by Table 1 its harmonic representation is

$$Y(t) = Y_{S1}sin(\omega t) + Y_{C1}cos(\omega t) \tag{6}$$
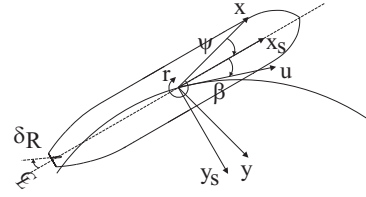
and the derivatives of interest are finally found from

$$Y_{\dot{v}} = \frac{Y_{S1}}{v_A\omega} \tag{7}$$

$$Y_v = -\frac{Y_{C1}}{v_A} \tag{8}$$

v_A is the sway velocity amplitude as per $y_{max}\omega$ where y_{max} is the lateral displacement and ω the frequency of the harmonic motion. The test parameters are chosen in accordance with the guidelines and recommendations of the ITTC (2005). For pure sway a nondimensional frequency $\omega'=\omega L/u_0$ of typically 1-2 and of 2-4 for pure yaw tests is suggested. L is the ship length. An extensive coverage of this procedure can be found in Yoon (2009). The linear assumption behind (5-8) is noteworthy: the force is assumed to be exclusively dependent on the contemporary velocity and acceleration, thus unaffected by memory effects.

3 NUMERICAL METHOD

A dynamic equation describing the motion of a viscous and incompressible flow is found from turning to the Navier-Stokes equations. The integral representation of the mass and momentum conservation equations satisfies

$$\frac{\partial}{\partial t}\int_V \rho\,dV + \int_S \rho\mathbf{v}\cdot\mathbf{n}\,dS = 0 \tag{9}$$

$$\frac{\partial}{\partial t}\int_V \rho\mathbf{v}\,dV + \int_S \rho(\mathbf{v}\mathbf{v})\cdot\mathbf{n}\,dS = \int_S \mathbf{T}\cdot\mathbf{n}dS + \int_V \rho\mathbf{b}\,dV \tag{10}$$

where $\mathbf{v}$ denotes the velocity vector, $\mathbf{n}$ is the normal vector of S which represents the area of the surface of the control volume V, $\mathbf{T}$ denotes the stress tensor and $\mathbf{b}$ a vector describing a force per unit mass.

The additional transport of momentum due to the turbulent nature of the flow is accounted for by expressing the flow quantities in terms of their time average and fluctuating parts leading to the RANS equations. A SST k-ω model (Menter, 1994), involving two more transport equations provides closure of the system of equations.

The flow equations are approximated by the Finite Volume (FV) method. The approximation of the flow equations for the entirety of control volumes (CVs) provides a set of algebraic equations. The flow equations are solved in a segregated fashion based on the Semi-Implicit Method for Pressure-Linked Equations (SIMPLE) algorithm. For an elaborate discussion the reader is referred to Ferziger and Peric (1996). An implicit temporal scheme of second order and three time levels is used for unsteady simulations. The present problem of conducting virtual PMM tests involves relative motions between the vessel and the spatial restrictions which calls for the modeling of transient mesh deformations (mesh morphing). The method redistributes mesh vertices following prescribed displacements of control points which are related to existing mesh vertices of the boundaries of the solution domain. The commercial solver STARCCM+ is used in the present investigation and a detailed formulation of the numerical method is given in Cd adapco (2013).

An inlet boundary condition is set one ship length upstream specifying the flow velocity and turbulent kinetic energy and disspiation rate. Two ship lengths downstream and one ship length away from the ship on the domain sides an outlet boundary condition holds where the pressure is given directly and velocities are found from the arithmetic average of neighboring cells. Inflow can be considered in terms of the normal component of boundary recirculation. If a lateral restriction

Table 2: MAIN PARTICULARS

	Length	Beam	Draft	c_B
Spheroid	2a=100m	2b=15m	7.5m	0.52
Vessel	110m	11.4m	3m	0.89

Table 3: GRID SENSITIVITY STUDY

CVs	$\frac{Y_{\dot{v}}}{\rho\nabla}$	$\frac{Y_v B}{\rho\nabla U}$	$\frac{N_{\dot{r}}}{0.2\rho\nabla(a^2+b^2)}$	$\frac{N_r B}{\rho\nabla UL}$
201894	-0.9538	-0.0382	-0.7472	-0.4228
252714	-0.9394	-0.0409	-0.7505	-0.4085
416824	-0.9422	-0.0408	-0.7560	-0.4079
Panels	$\frac{a_{22}}{\rho\nabla}$		$\frac{a_{66}}{0.2\rho\nabla(a^2+b^2)}$	
924	-0.9431		-0.7828	
1476	-0.9519		-0.7949	
3064	-0.9629		-0.8051	
Theory	-0.9600		-0.8000	

Figure 2: TIME STEP SENSITIVITY STUDY: NONDI-MENSIONAL SIDE FORCE AGAINST THE RATIO OF TIME t TO OSCILLATION PERIOD T

is considered the domain boundary on the starboard side of the vessel at distance d turns into a free slip wall (zero normal velocity component). The bottom and top boundaries are also given free slip wall conditions. If free surface flow is to be modeled the Volume of Fluid (VOF) technique is used (Ferziger and Peric, 1996). The ship boundary is a no-slip wall (zero tangential velocity component). For rigid body motions the ship boundary vertices are assigned respective velocities and the rigid free surface is allowed to experience in-plane deformations.

4   RESULTS AND DISCUSSION

The Spheroid. In lack of experimental data for validation purposes comparison can be drawn to results found from analytic scrutiny. Such information exists for added masses of simple bodies based upon potential flow theory (Newman, 1978). In three dimensions such a simple body is a spheroid the sway added mass a_{22} and yaw added moment of inertia a_{66} of which are quantified in the reference. The flow is assumed unbounded, it does not consider the influence of waves. The hydrodynamic forces arising from the body acceleration in sway and yaw mode of motion will be proportional to just the above quantities, it might be compared to the respective acceleration derivatives as present in (4). The comparison can serve as a check for the suitability of the numerical method albeit their identification is done within a viscous flow regime. The main particulars of the spheroid are given in Table 2.

Preliminaries. A forward speed of 3m/s corresponding to Reynolds-Number $Re=3\cdot10^9$ is used. Due to the low Froude Number (F_n=0.095) the free surface is consid-

ered rigid leading to the classical double-body flow. It is obvious from (5-8) that the hydrodynamic derivatives are functions of both test frequency and amplitude. In favor of reduced testing effort in the single-run PMM method only one test is conducted at low frequency, assumed to be sufficiently close to zero to obtain the slow motion derivatives. The periodic time series of the side force and yaw moment are smoothed by the moving average method before they are subjected to Fourier analysis. The oscillation is observed to be stable after one quarter of an oscillation and shows convergent behavior (constant amplitude oscillation) after three oscillations. Computations are performed on a High Performance Computer (HPC) cluster on four Intel(R) Sandy Bridge nodes (64 cores).

Sensitivity Studies. PMM tests are performed using three grids with a refinement factor of $\sqrt{2}$. The near wall discretization is chosen in accordance with the wall function used. It remains constant during the refinement. The test parameters are ω'=2 and y_A=1m for pure sway and ω'=4 and ψ_A=2.3° for pure yaw. Comparison is also drawn to a_{22} and a_{66} computed with the zero-speed Green Function method of the code GLRankine (Söding, 2012). Table 3 shows that the difference in $Y_{\dot{v}}$ between the grids is less than 2%. The result from the finest grid differs by 1.88% from the theoretical sway added mass. The sway velocity derivative Y_v deviates by 6.6% between the coarse and the fine grid —here there is no theoretical value available. For $N_{\dot{r}}$ the maximum deviation between the grids is less than 2% and for N_r its 3.5%. $N_{\dot{r}}$ computed with the finest grid is 5.5% less than the theoretical value. It has to be kept in mind that the frequency dependence is not considered yet. The zero speed Green Function method approaches the theoretical values with increasing body panels for both quantities. On the medium size FV grid the computational time for one period of oscillation T=104.72s with 800 time steps is approximately seven minutes. The
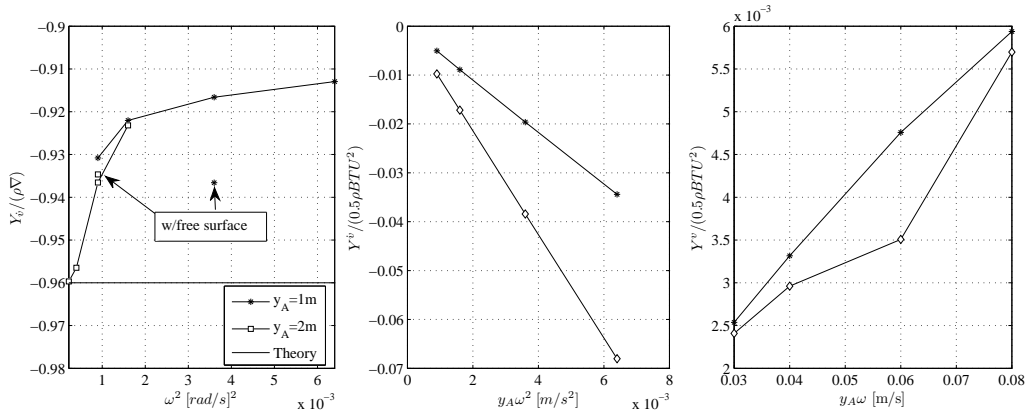
Figure 3: PARAMETER STUDY FOR SWAY FORCE DERIVATIVES

grid with free surface considered comprised $1 \cdot 10^6$ cells and for the case $\omega'=2$ the computational time is about 30 minutes per oscillation. The added masses found from GLR are readily available within less than a minute on a common desktop computer. The sensitivity to temporal discretization is checked by varying the time step to yield 400, 800 and 1600 steps per oscillation. Figure 2 illustrates the result of this study for a pure sway test. The trends for the two finer time steps do not show a marked difference in Y. 800 steps per oscillation and the medium size grid are chosen throughout forthcoming simulations.

Figure 3 illustrates the test paramter study for lateral force components found from pure sway tests. The left hand side plot shows $Y_{\dot{v}}$ as a function of ω^2 and for two amplitudes y_A. $Y_{\dot{v}}$ takes higher norm values the smaller the frequency gets, this trend approaches the theoretical value. The lowest frequency corresponds to the smallest ITTC reccomendation $\omega'=0.25$ and the highest frequency is equivalent to $\omega'=4$. Results scatter around the reference value by maximum 5%. For two cases the free surface has been taken into account and results differ by less than 3% compared to the double-body flow. The right hand side plots show the force contributions without normalization to derivative representation as a function of sway velocity $y_A\omega$ and acceleration $y_A\omega^2$ for the amplitudes considered. By varying the flow history memory effects and nonlinearities involved in the testing procedure can be identified (Renilson, 1986). The difference between the amplitude curves indicates memory effects. The deviation of these curves from a straight line reveals nonlinearities. The linear assumption appears to be well suited for $Y^{\dot{v}}$ and memory effects become pronounced for higher frequencies. For Y^v no such straight line is observed and more tests would be necessary to gain insight into the dependencies. Throughout forthcoming simulations pure sway tests are performed with $\omega'=1$ and $y_A=2$m. For pure yaw tests, $\omega'=4$ and $\psi_A=2.3°$ are used. In general amplitudes are kept low in light of the runs in laterally restricted flow.

Restricted Flow. Figure 5 depicts the linear sway force derivatives as a function of the nondimensional distance to the wall d/L. Both $Y_{\dot{v}}$ and Y_v increase in a nonlinear fashion. This trend agrees with investigations carried out for a slender ship-like body (Thomas and Sclavounos, 2006) with fore-aft symmetry similar to a spheroid. In the reference, sway added masses are found with the 3D Rankine source method SWAN. In essence, the change in the hydrodynamic properties is attributable to the fact that in bounded flow the acceleration of water particles in the vicinity of the ship hull is aggrevated and also associated damping becomes more pronounced. The presence of the wall raises the question whether reflecting waves might affect the results even at low Froude numbers. The most and least narrow cases are expanded on for this investigation. Results for the side force and yaw moment coefficients are plotted in Figure 5 additionally. It is seen that the sway force coefficients are less sensitive to free surface effects than the yaw moment coefficients. While $Y_{\dot{v}}$ and Y_v hardly differ at all from the double-body results $N_{\dot{r}}$ and N_r exhibit a deviation by approximately 10%. It is assumed that this trend is attributable to the choice of the test parameters for the pure yaw case ($\omega'=4$). In case of a vertical restriction the derivatives follow a similar trend when plotted against the ratio of water depth h to ship draft T. Here the boundedness of the flow also causes more fluid obstruction (Figure 5). The influence of heave and trim was not considered in the present investigation.

The Inland Waterway Vessel. Pure sway and yaw tests are now conducted for the inland waterway vessel (Table 2) in a narrow and shallow flow. The same time step and space discretization studies are performed. In what follows, given results are computed on a grid of $0.9 \cdot 10^6$ cells. The test parameters are $\omega'=2$, $y_A=1$m for pure sway and $\omega'=4$, $\psi_A=2.3°$ for pure yaw. Figure 6 shows that the trends seen for the spheroid are also observed for the ship. Besides that the plots show all other derivatives needed to populate the maneuvering model (4). In absence of rudder action or any other controls, the inherent stability behaviour of the dynamic system can be studied by turning to the eigenvalues of the system matrix $\mathbf{A} = -\mathbf{M}^{-1}\mathbf{N}$ where $\mathbf{M}$ is the matrix acting on $\dot{\mathbf{x}} = [\dot{v} \ \dot{r}]^T$ and $\mathbf{N}$ the matrix acting on $\mathbf{x} = [v \ r]^T$ in

(4) because a solution to (4) with zero right hand side is

$$\mathbf{x}(t) = e^{\mathbf{A}t}\mathbf{x}_0 \qquad (11)$$

It can be shown that the system matrices found for various restricted maneuvering environments all have one eigenvalue λ with positive real part $\Re(\lambda)$ giving way to unbounded amplification as a response to external excitation. In the considered environment, such an excitation can be suction forces generated by the presence of a canal wall or another ship. It is seen that the magnitude of the positive real part eigenvalues increases with decreasing water depth and distance to the wall (Figure 4). Mucha and el Moctar (2013) discussed the narrow water influence on the actual maneuvering trajectory for a large tanker and the related need for increased control action.

Figure 4: VESSEL: POSITIVE REAL PART EIGENVALUES AGAINST NONDIMENSIONAL WALL DISTANCE
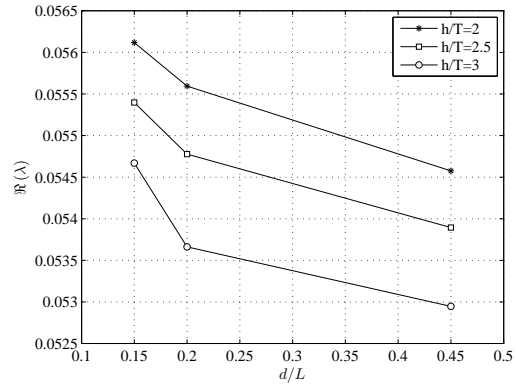
5 CONCLUSIONS

PMM tests were replicated by a numerical method based on the solution of the RANS equations. For a spheroid it was shown that it is possible to find hydrodynamic sway and yaw acceleration derivatives with satisfactory accuracy. The influence of lateral and vertical flow restrictions was shown to significantly increase these quantities. For low Froude numbers, and moderate test frequencies, it was observed that through the presence of a wall there is no significant influence of the free surface on the hydrodynamic derivatives. Further investigations expanded on the derivation of a linear set of maneuvering coefficients for a typical inland waterway vessel for various restricted maneuvering environments. It was shown that the narrow and shallow water effect have a destablizing effect on the motion of the vessel in the horizontal plane. The computational effort for the host of virtual PMM tests was remarkably high and in absence of appropriate computational resources prohibitive. A more sophisticated validation and verification methodology *e.g.* through comparison with model tests is needed to gain more insight into the suitability of the presented method for maneuvering prediction in restricted waters.

6 ACKNOWLEDGMENTS

7 REFERENCES

Cd adapco, 2013, *STARCCM+-User-Guide 8.04.007*

Ferziger, J., Peric, M., 1996, *Numerische Strömungsmechanik*, Springer

Liu, Z., Larsson, L., 2011, *CFD Prediction and Validation of Ship-Bank Interaction in a Canal*, Proceedings of the 2nd International Conference on Ship Manoeuvring in Shallow and Confined Water: Ship-to-Ship Interaction

Menter, F.R., 1994, *Two-Equation Eddy-Viscosity Turbulence Models for Engineering Applications*, AIAA Journal, Vol. 32, No. 8, pp. 1598-1605

Mucha, P., el Moctar, O., 2013: *Ship-Bank Interaction of a Large Tanker and Related Control Problems*, Proceedings of the 32nd International Conference on Ocean, Offshore and Arctic Engineering OMAE 2013

Newman, J.N., 1978, *Marine Hydrodynamics*, MIT Press

Renilson, M.R., 1986, *A Note on the Fluid Memory Effects and Non Linearities Involved in Oscillatory Ship Model Manoeuvring Experiments*, Proceedings of the 9th Australian Fluid Mechanics Conference

Söding, H., von Graefe, A., el Moctar, O. and Shigunov, V., 2012, *Rankine source method for seakeeping predictions*, Proceedings of the 31st International Conference on Ocean, Offshore and Arctic Engineering OMAE 2012

Stern, F., et al., 2011, *Experience from SIMMAN 2008: The First Workshop on Verification and Validation of Ship Maneuvering Simulation Methods*, Journal of Ship Research, Vol. 55, No. 2, pp. 135147

The International Towing Tank Conference - Recommended Procedures and Guidelines, 2005, *Testing and Extrapolation Methods Manoeuvrability Captive Model Test Procedures*, 7.5-02-06-02

Thomas, B. S., Sclavounos, P. D., 2006, *Optimal Control Theory Applied to Ship Maneuvering in Restricted Waters*, Readings in Marine Hydrodynamics, Volume Published in Honor of Professor J. Nicholas Newman

Tuck, E.O., 1978, *Hydrodynamic Problems of Ships in Restricted Waters*, Ann. Rev. Fluid Mechanics, No.10, pp. 33-46

Yoon, H., 2009, *Phase-averaged Stero-PIV Flow Field and Force/Moment/Motion Measurements for Surface Combatant in PMM Maneuvers*, Ph.D. thesis, The University of Iowa
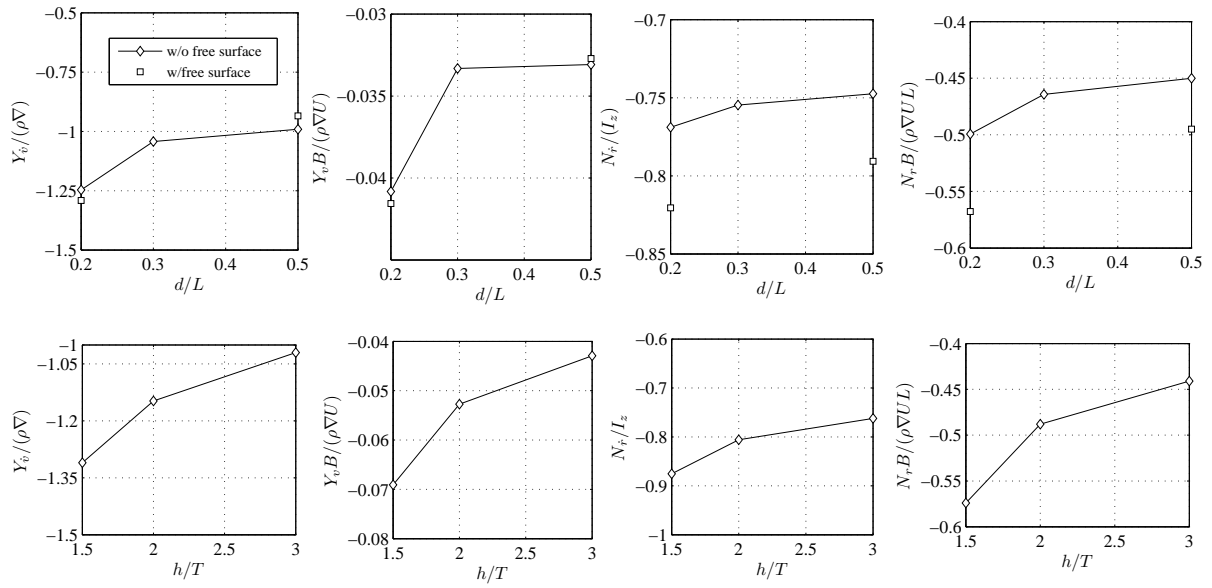
Figure 5: SPHEROID: SWAY FORCE AND YAW MOMENT DERIVATIVES AGAINST NONDIMENSIONAL WALL DISTANCE d/L AND WATER DEPTH-DRAFT RATIO h/T
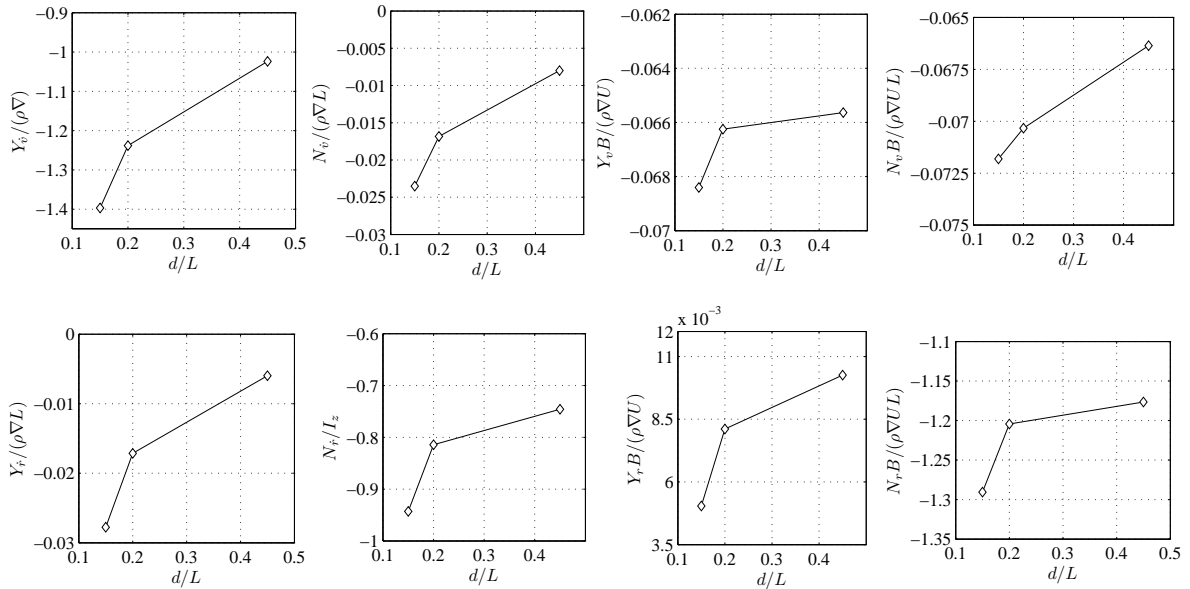
Figure 6: VESSEL: LINEAR HYDRODYNAMIC DERIVATIVES FOR SWAY AND YAW AGAINST NONDIMENSIONAL WALL DISTANCE d/L FOR h/T=2

FLOW AROUND FIXED CYLINDERS IN TANDEM

LINH TUAN THE NGUYEN[1*], PANDELI TEMAREL[1], JOHN CHAPLIN[2]

[1] *Fluid Structure Interaction Research Group*, [2] *Energy and Climate Change Research Group*,

Faculty of Engineering and the Environment, University of Southampton, UK

1. Introduction

As worldwide demand for energy increases, oil corporations are expanding subsea operations for oil and gas exploration and production. When risers are installed in arrays, simultaneous vortex- and wake-induced vibrations can create fatigue damage in the risers used in the offshore industry to bring oil and gas from seabed to the platform or floating vessel at the surface. With the development of computer resources, CFD provides a very useful tool for studying this interaction in conditions that may be very difficult or impossible to achieve experimentally.

In the present work, the unsteady viscous flow around stationary circular cylinders in a tandem arrangement is investigated numerically using a 2D CFD RANS code. The method adopted here is based on the Finite Volume Method using the commercial CFD package Ansys Fluent 14.0 (ANSYS, 2011). Simulations are presented for the subcritical Reynolds number (Re) 22,000, with cylinder separations L/D in the range 2 to 5, where L is the centre-to-centre distance and D the diameter. The simulations are carried out using different k-ε and k-ω turbulence models and different flow parameters such as the incident turbulence intensity I and the turbulent-to-laminar viscosity ratio β. This paper presents computed drag and lift coefficients and Strouhal numbers, and compares them with experimental measurements and other numerical predictions.

2. Methodology

In order to assess their degrees of validity, results based on four different turbulence models were compared: realisable k-ε (RKE), standard k-ω (SKW), SST k-ω, and k-k_1-ω. Furthermore, the sensitivity of computed results to the values of I and β were examined for the k-ε and k-ω models. Results are compared with measurements from Ljungkrona et al. (1991) and numerical predictions from Kitagawa and Ohta (2008), for Re of 20000 and 22000, respectively. A structured mesh of 75000 elements was used in this numerical study. Convergence tests confirmed that mesh dependency was negligible (Table 1) where the SKW turbulence model was used and UC and DC demote the upstream and downstream cylinder, respectively at L/D = 5.

Table 1: Verification of mesh dependency for cylinders in tandem at Re = 22000

Case	Grid resolution	Cd (UC)	Cd (DC)	% different in Cd (UC)	% different in Cd (DC)
mesh 0	39309	1.23	0.21	-	-
mesh 1	55700	1.19	0.238	3.36	-11.76
mesh 2	75000	1.165	0.24	2.15	-0.83
mesh 3	108700	1.163	0.238	0.17	0.84
mesh 4	145000	1.162	0.24	0.09	-0.83

3. Numerical simulation results

Turbulence intensity (I) and turbulent-to-laminar viscosity ratio (β)

Sensitivity tests for the influence of β and I on the drag coefficients of both upstream and downstream cylinders were carried out with the standard k-ω and SST k-ω turbulence models. Various turbulence intensities (I = 0.1%,

---

[*] Corresponding author's email: lttn1v11@soton.ac.uk

1.4%, 3.2%) and turbulent viscosity ratios (0.1 < β < 10) were run for 6 different spacing ratios *L/D* = 2, 2.5, 3, 3.5, 4, 4.5 and 5, shown in Figures (1, 2). Overall, the results indicate that predictions of the SKW model are more sensitive to the turbulence intensity and turbulence viscosity ratio than the SST *k*-ω model. So that, SKW turbulence model is used to investigate the variation in drag coefficient with the spacing and the turbulence intensity and make comparison with Ljungkrona et al. (1991)
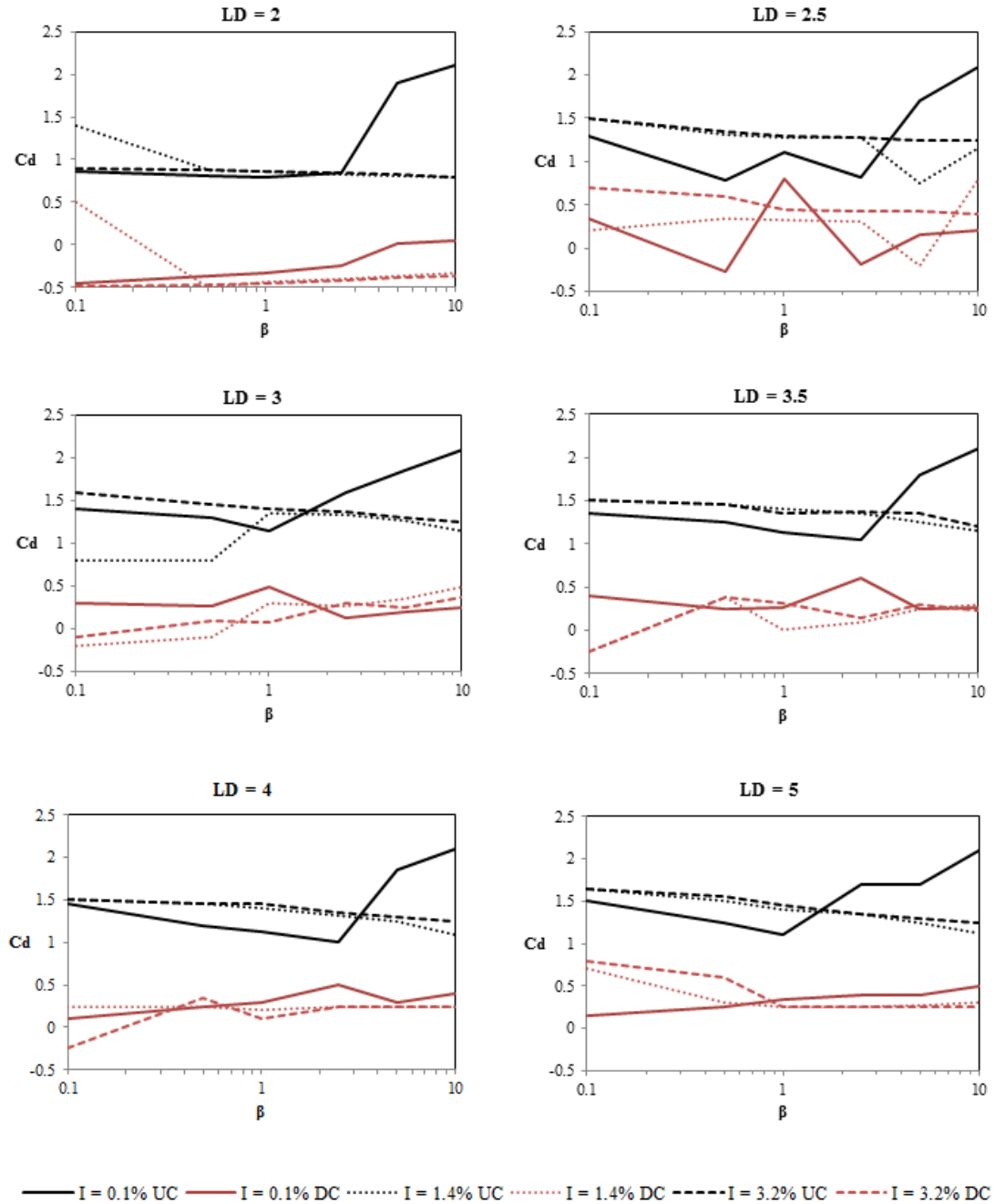
Figure 1: Effect of *I* and *β* on Cd for various cylinder spacings L/D, standard k − ω, Re = 22000

2
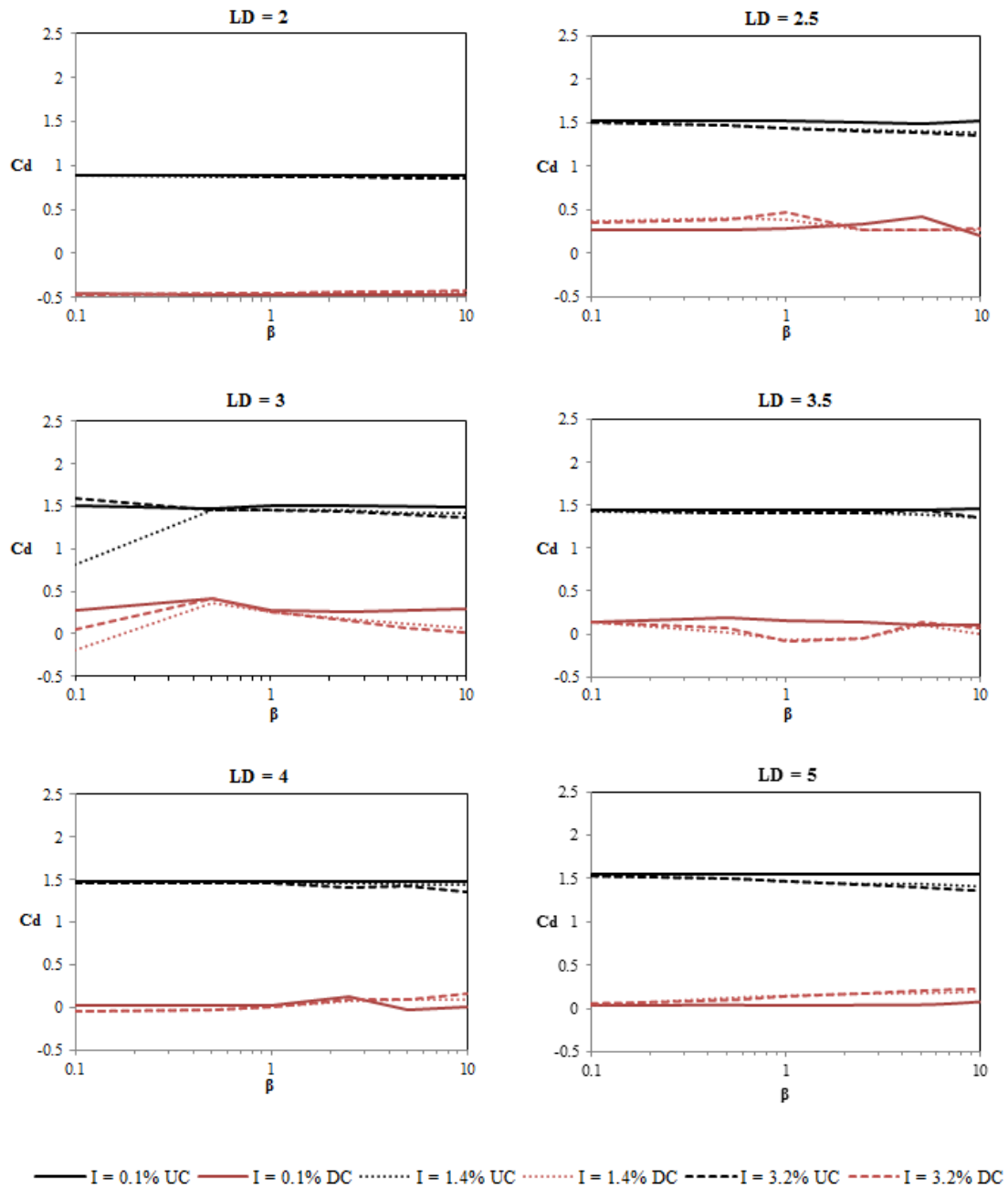
Figure 2: Effect of *I* and *β* on Cd for various cylinder spacings L/D, SST k – ω, Re = 22000

Drag coefficient, lift coefficient and Strouhal number

As shown in Figure 3 the RKE method predicts the general trend of the measurements, but underestimates the drag of upstream cylinders. Similar behaviour was seen in earlier runs for the case of a single isolated cylinder (Linh, 2012). In the flow around two cylinders, the RKE underestimates the drag coefficient for the upstream cylinder (UC), but for the downstream cylinder (DC) the results show better agreement with the study by Ljungkorna et al (1991). The jump in the drag coefficient of the downstream cylinder occurs at about *L/D* = 3.

This is the critical spacing where the vortices in the wake of the upstream cylinder change from quasi-stationary vortices, become unstable and start roll up in front of the downstream cylinder, causing a dramatic increase in the drag coefficient of the downstream cylinder. Drag coefficients obtained with the SKW method with very low incident turbulence intensity (typically *I* < 1%) compare well with those in the experimental results by Ljungkrona et al. (1991). There is also good agreement with drag coefficients computed by LES for the

3

downstream cylinder by (Kitagawa and Ohta, 2008). The SST k-ω turbulence model recommended by ANSYS. (2011) shows worse agreement with previous data than either of the other cases. It overpredicts the drag coefficient of the upstream cylinder and does not follow the trend seen in other numerical or experimental results.
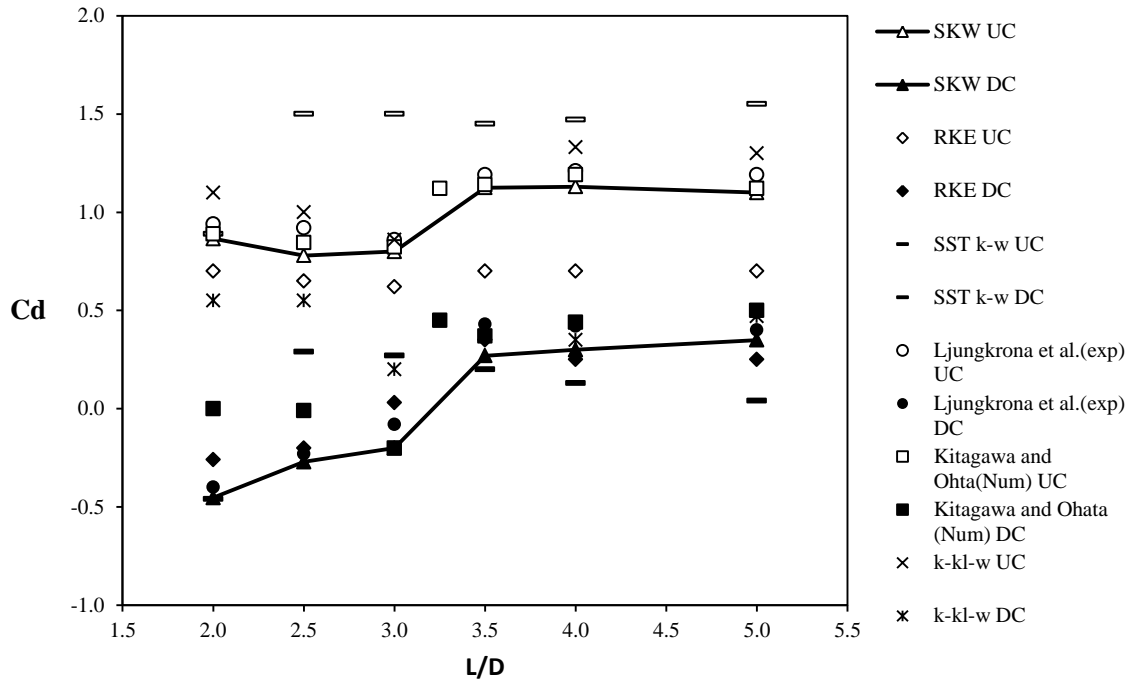
Figure 3: Variation of drag coefficient with cylinder spacing, L/D, at Re = 20000 and 22000

The lift coefficient, shown in Figure 4, agrees with the LES numerical simulation by Kitagawa and Ohta (2008) for the downstream cylinder and overpredicts for the upstream cylinder. The Strouhal number, shown in Figure 5, shows good agreement with the experimental results, including those by Ozono et al. (2001).
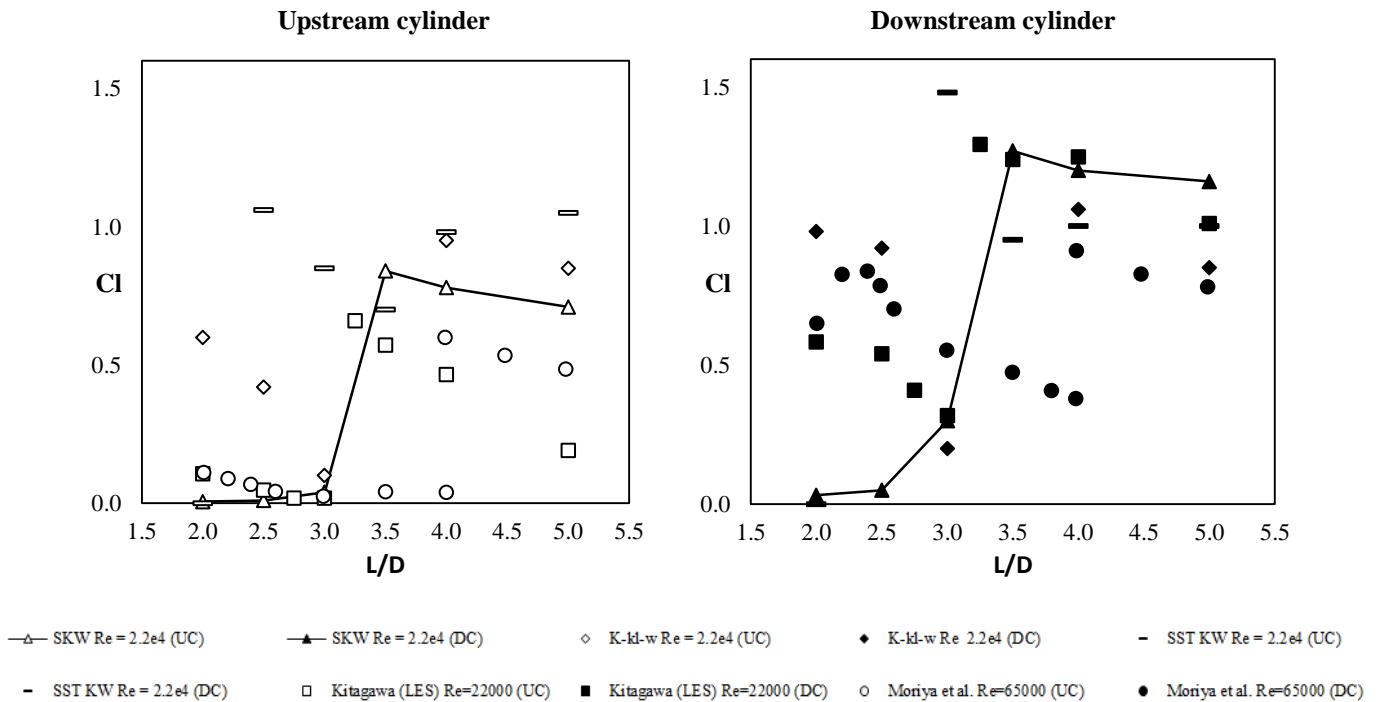
Figure 4: Variation of lift coefficient with cylinder spacing, L/D, for Re = 20000 and 22000
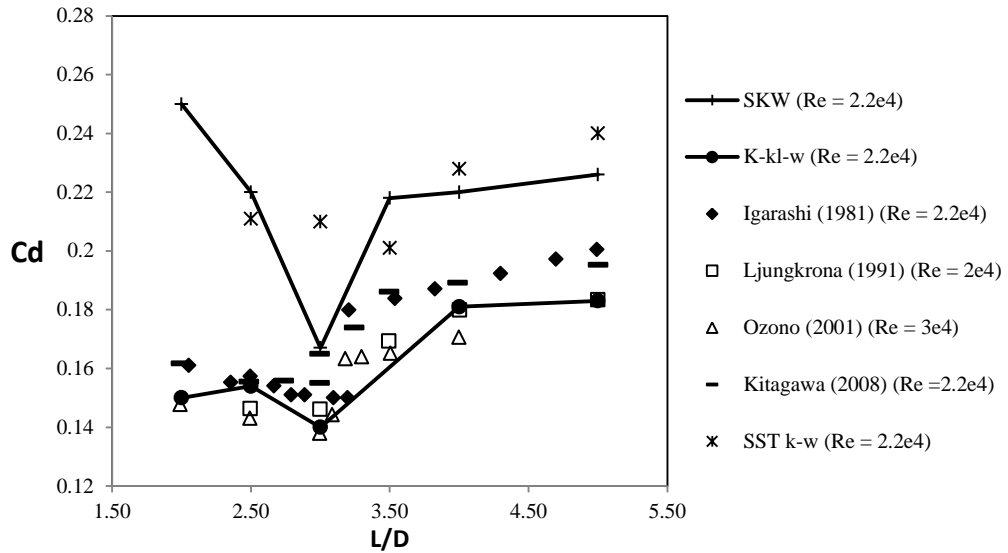
Figure 5: Strouhal number for different cylinder spacing L/D

Effects of turbulence intensity

Examining Figure 6 for the downstream cylinder, Cd showed the common trends as per Ljungkrona et al. (1991). Increase in turbulence intensity shortens the critical spacing region. The "jump" appears at L/D = 2.5 (with I = 1.4 and 3.2 %) instead of L/D = 3 (I = 0.1 %). The drag coefficient at L/D > 3.5 is close to the experimental results. For the upstream cylinder, trends similar to other studies can be observed. However, the drag coefficient is overpredicted in the region LD = 2.5 to 3 for I = 1.4 and 3.2%. The drag coefficient for the upstream cylinder shows good agreement when L/D > 3.5. In general, I = 0.1% shows reasonably good agreement for both UC and DC. Higher turbulence intensity I = 1.4 and 3.2%, shows acceptable agreement for the trends in DC, but not in UC.
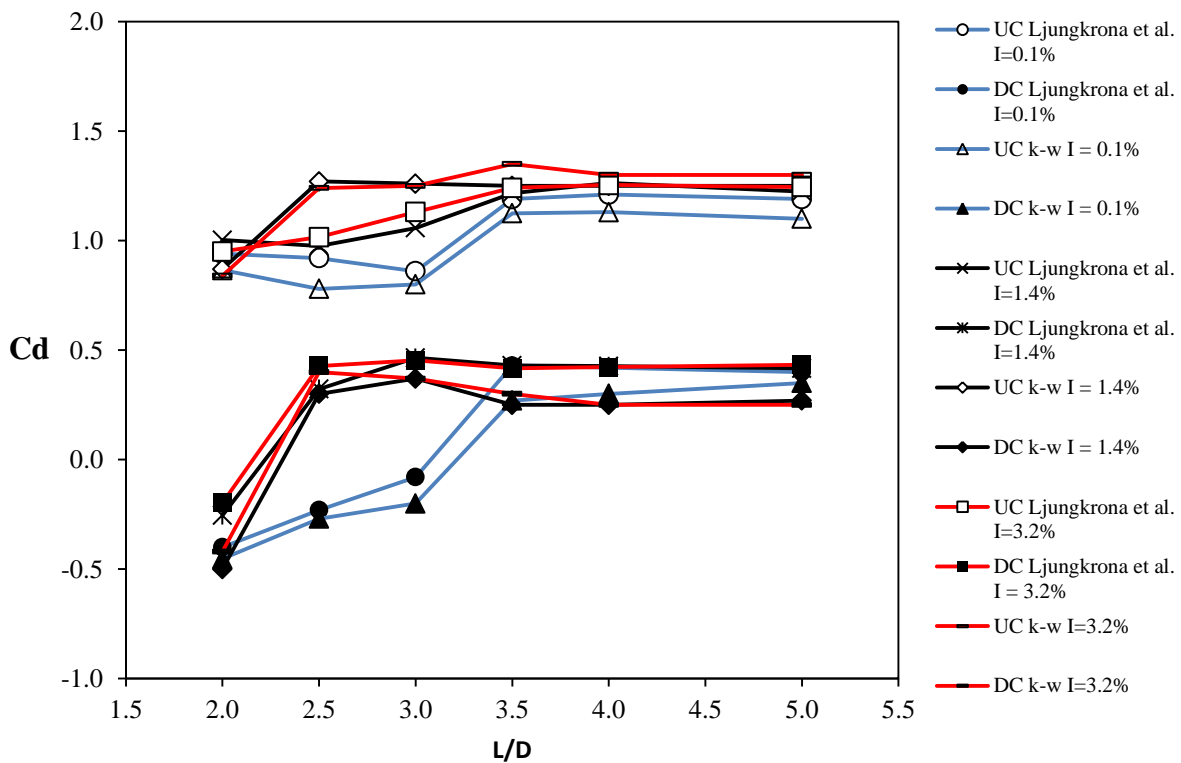
Figure 6: Variation of drag coefficient with cylinder spacing L/D at turbulent intensity 0.1%, 1.4% and 3.2% at Re = 22000, comparison with Ljungkrona experiments at Re = 20000

5

4. Conclusions

In this paper, different RANS based turbulence models have been used to simulate the flow around two fixed cylinders in tandem. Different gap spacings were used in order to investigate the effects of various turbulence parameters (I and β) and hydrodynamic forces acting on the cylinders. The most important conclusions in this report can be summarized as follows:

- The standard k - ω shows sensitivity to turbulence parameters I and β used for predicting force coefficients. The numerical results show that SKW can capture the general trends, especially, at the critical spacing region, with reasonably good values for both upstream and downstream cylinders.
- k–ε turbulence model can capture the trends of the drag coefficient for various cylinder spacings. However, in general, this model underpredicts the drag coefficient for the upstream cylinder.
- SST k - ω shows the worse results for this Reynolds number for this numerical study case. In general, SST k - ω overpredicts the drag coefficient for both upstream and downstream cylinders.
- The new numerical method k–k_l–ω, combination of k - ω with other transition equation and highly recommended by Ansys, also overpredicts the drag coefficient for L/D < 3. However, the predictions are closer to experimental results for L/D > 3.5. This method shows its reliability in predicting Strouhal number, and showed the best agreement with experimental results as far as Strouhal number is concerned.
- Finally, although none of the methods investigated provide total agreement with experimental results, some methods are shown to be highly suitable in predicting hydrodynamics parameters around cylinders. SKW is appropriate to carry out further numerical studies on flows around cylinders in tandem at subcritical Reynolds numbers.

5. References

ANSYS. 2011. *Ansys Fluent Manual, release 14.0*, ANSYS, Inc.

IGARASHI, T. 1984. Characteristics of the flow around two circular cylinders arranged in tandem 2nd report: unique phenomenon at small spacing. *Bulletin of JSME,* 27**,** 2380–2387.

KITAGAWA, T. & OHTA, H. 2008. Numerical investigation on flow around circular cylinders in tandem arrangement at a subcritical Reynolds number. *Journal of Fluids and Structures,* 24**,** 680-699.

LINH, T. T. N. 2012. 9 months reports. University of Southampton.

LJUNGKRONA, L., NORBERG, C. & SUNDÉN, B. 1991. Free-stream turbulence and tube spacing effects on surface pressure fluctuations for two tubes in an in-line arrangement. *Journal of Fluids and Structures,* 5**,** 701-727.

MORIYA, M., SAKAMOTO, H., KIYA, M. & ARIE, M. 1983. Fluctuating pressures and forces on two circular cylinders in tandem arrangement. *Transactions of the JSME* 49**,** 1364–1374 (in Japanese).

OZONO, S., ODA, J., YOSHIDA, Y. & WAKASUGI, Y. 2001. Critical nature of the base pressure of the upstream circular cylinder in two staggered ones in cross-flow. *Theoretical and Applied Mechanics,* 50**,** 335–340.

Fully Resolved Large Eddy Simulation as an Alternative to Towing Tank Resistance Tests – 32 Billion Cells Computation on K computer

Tatsuo Nishikawa, The Shipbuilding Research Centre of Japan, t_nishikawa@srcj.or.jp
Yoshinobu Yamade, **Masaru Sakuma**, Mizuho Information & Research Institute, Inc.
Chisachi Kato, University of Tokyo

1. Introduction

The demand for towing tank tests has been increasing due to the requirements of the EEDI (Energy Efficiency Design Index) imposed by IMO (International Maritime Organization) as a measure for controlling CO_2 emissions from ships.

Although numerical simulations by RANS (Reynolds-averaged Navier-Stokes) have been widely used in the early stage of hull design, the prediction accuracy has to be further improved for such simulations to become a complete alternative for towing tank tests. In particular, for resistance tests and self-propulsion tests, the relative error to the experimental data has to be reduced to 1%. By tuning the turbulence models, RANS simulations may provide such accuracy. But, it seems difficult for RANS simulations to always guarantee such accuracy for different types of ships.

With the recent speed-up of high-end computers, fully resolved large eddy simulation (LES), which directly computes the streamwise vortices in the turbulent boundary layer (TBL), is expected to become feasible within a few years. Fully resolved LES provides almost the same accuracy as DNS (Direct Numerical Simulation) and will probably achieve simulations with a relative error of 1% or smaller.

For towing-tank tests with a 5 m to 6 m long model towed at 1 m/s to 2m/s, the diameter of the streamwise vortices is estimated approximately 0.3 mm to 0.7 mm. To resolve such vortices, computational grids with 30 billion to a hundred billion cells are necessary.

In our previous work [1], we presented a fully resolved LES around KVLCC2 at Re=1.0×10^6 , which is about 5 times smaller than the test condition, with one billion cells. In the present paper, we present 32 billion cells fully resolved LES at the actual towing tank model-scale Reynolds number (4.6×10^6) [2][3], using the K computer, Japan's most powerful supercomputer [4].

2. Computational Method

The flow solver, called FrontFlow/blue (FFB), was developed in the "Innovative Simulation Software Project" sponsored by the Ministry of Education, Culture, Sports, Science and Technology (MEXT) of Japan. The solver simulates turbulent flows, adopting LES with second-order accuracy in terms both of time and space [5]. A dynamic Smagorinsky model (DSM) [6][7][8] was implemented for the SGS (sub grid scale) model.

To realize a very large scale industrial LES, there are two essential problems to overcome: grid generation and massively-parallel computation. It is impossible to generate a computational grid with over

100 million cells manually. Therefore, a run-time grid refinement method, which automatically divides a grid cell into two in each of the directions during the computation, is applied. During the grid refinement, the CAD data representing the geometry is being referred to. Thus the algorithm refines both spatial resolution and geometry representation. With the help of this method, a computational grid with a desired resolution is generated at run time.

FFB is fully tuned-up for the massively parallel architecture of K computer. Fig.1 shows result of a weak-scale benchmark on the K computer. The computational speed scales on the number of the nodes up to 80,000 nodes (640,000 cores) with a sustained performance of approximately 3% to the peak performance.
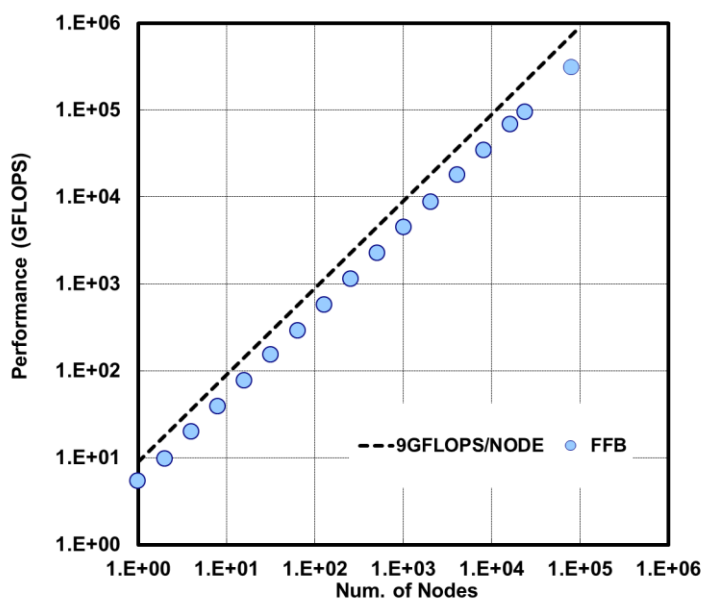
Fig. 1: Weak scale benchmark of the flow solver on K computer

The accuracy of FFB has been verified and validated in a number of fundamental benchmark tests as well as in various types of flow-related products. Interested readers may refer to [9][10].

3. Computational Model

The bare-hull KVLCC2 model is computed for double-body flow, Fig.2 and Table I. The effects of the free surface are secondary at this condition. Thus, a symmetry boundary condition was imposed at the still-water plane.
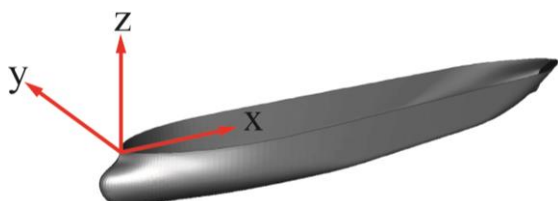
Fig. 2: Overview and coordinate system of computational model

Table I: Main dimensions of model ship

Length (L$_{PP}$)	Breadth	Draft	Block Coefficient
5.5172 m	1.0 m	0.3586 m	0.8098

The size of the streamwise vortices in a TBL is typically $x^+=300$, $y^+=30$, and $z^+=100$ where x^+, y^+ and z^+ are, respectively, streamwise, wall-normal and spanwise lengths in the wall unit.

The Reynolds number for the test case is $Re=4.6\times10^6$, the same as in the Gothenburg 2010 workshop [3]. For this Reynolds number, the size of the streamwise vortices normalized by L_{PP} is 1.0×10^{-4}, 1.0×10^{-3} and 3.5×10^{-4} in streamwise, wall-normal and spanwise directions, respectively. We arranged about 8 to 10 cells in each direction for one vortex. As a result, 32 billion cells are needed. To realize this computational grid, a 62 million cells grid, generated as a base grid, was refined three times in the flow solver.

4. Results

Fig.3 shows instantaneous distributions of the streamwise component of vorticity vectors on the ship surface for the base grid computation and refined grid computation. At the midship position, about 50 streamwise vortices are observed in the base grid result (c) and about 150 to 200 vortices are observed in the refined grid result (d). The estimated number of streamwise vortices is 184. The refined grid has fully resolved the streamwise vortices.

(a) Base grid

(b) Refined grid   (c) Base (d) Refined
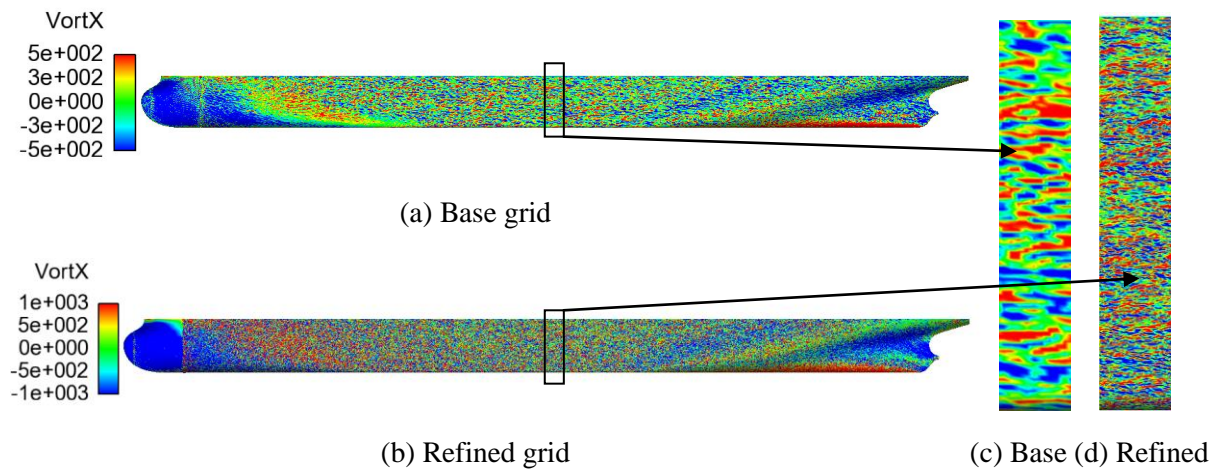
Fig. 3: Instantaneous distributions of the streamwise component of vorticity vectors on hull surface, close-up view of midship in (c) and (d)

Fig.4 and Table II compare the computed coefficients of pressure, friction and total resistance with those of a towing tank test done at Shipbuilding Research Centre of Japan. The Froude number that corresponds to $Re=4.6\times10^6$ in this experiment was 0.11 and the coefficient of wave making resistance (derived by three-dimensional method, i.e., $C_W=C_T-C_F(1+k)$, where the form factor $k=0.24$ is determined from the resistance tests at low speed range) is negligible as shown in Fig.5. Thus, one can directly compare the predicted and measured total resistance and the relative error of the refined grid computation is only 0.87%.

The coarse grid under-predicts both pressure resistance and frictional resistance. The reason for the under-prediction of the frictional resistance is related to the under-prediction of the thickness of the

TBL. This is shown in Fig.6, where velocity profiles at the propeller plane are compared. Note that the experimental data shown in Fig.6 are common benchmark results [2][3]. This under-estimation of the growth of the TBL also affects the generation of the hook at the propeller plane shown in Fig.7. The refined grid computation has captured the 'hook' very well. This typical wake feature for full hull shapes was not captured by coarse grid. For the base grid computation, since the growth of the TBL is under-predicted, the effective curvature at the aft part of the ship increases, resulting in over-prediction of the pressure recovery as seen in Fig.8.

Table II: Coefficients of total, pressure and friction ($\times 10^{-3}$) at Re=4.6×10^6

Coeffs.	Exp.	Base	Refined
Total	4.28	3.11	4.24
Prs.	-	0.60	0.98
Friction	-	2.95	3.26
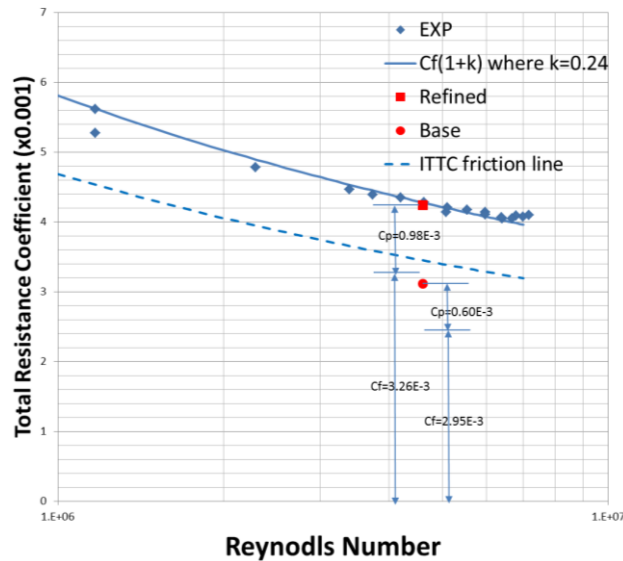
Fig. 4: Coefficients of total resistance
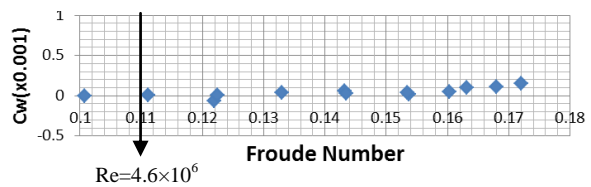
Fig. 5: Coefficients of wave making resistance of the experiment
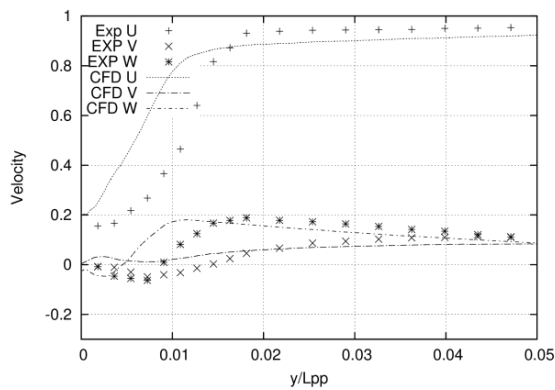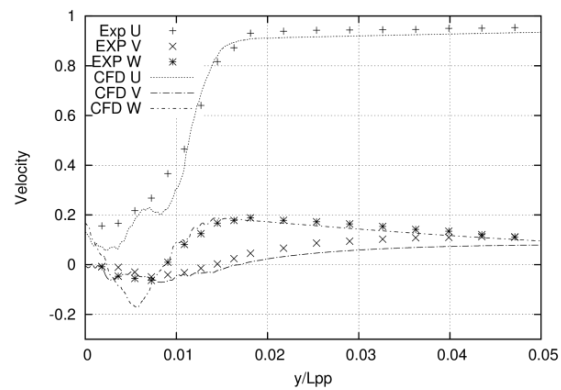
(c) Base grid (d) Refined grid

Fig. 6: Velocity in propeller plane (x/L$_{pp}$=0.9825) at z/L$_{pp}$=-0.05075

5.   Conclusions and Future Work

The turbulence boundary layers around a full hull shape have been successfully simulated with LES that resolves the streamwise vortices near the walls. Comparing with towing tank tests, it is confirmed that the resistance is accurately simulated within 1%. It is also confirmed that the density of the com-

putational grids strongly affects the accuracy of the computation. 32 billion cells seems an adequate grid density for the fully resolved LES.

Fully resolved LES with free-surface the rotating propeller and rudder is now underway as shown in Fig.9 and Fig.10. Verification with experiments is planned for late 2013.

(c) Base grid at Re=4.6×10^6 (d) Refined grid at Re=4.6×10^6
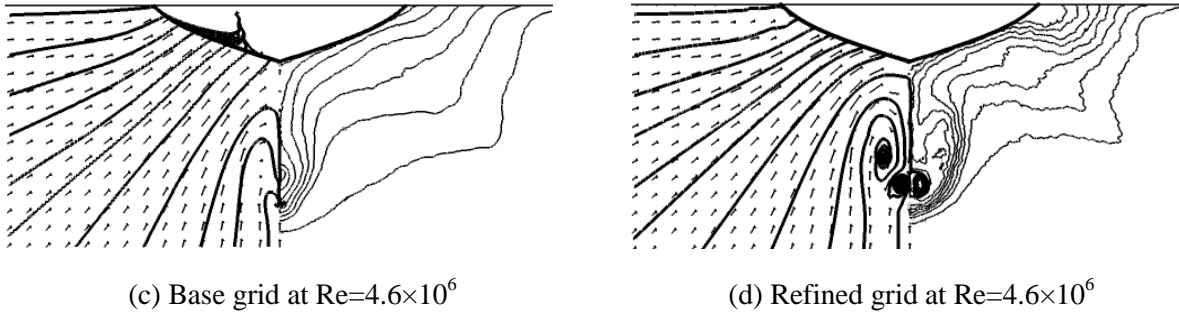
Fig. 7: Cross flow vectors and streamlines (left), U contours (right) at propeller plane (x/L$_{pp}$=0.9825)

(a) Base grid

(b) Refined grid
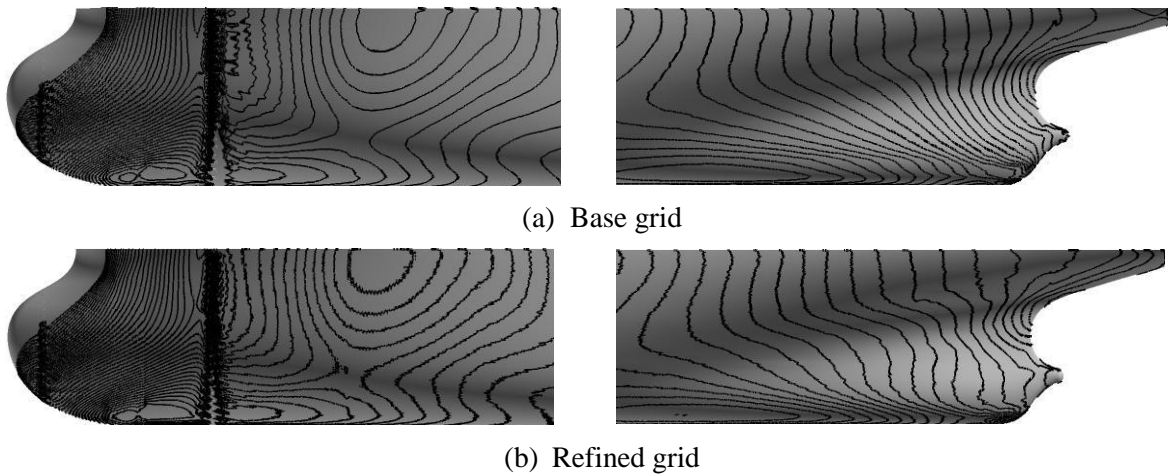
Fig. 8: Surface pressure distributions of fore part (left panel) and aft part (right panel).
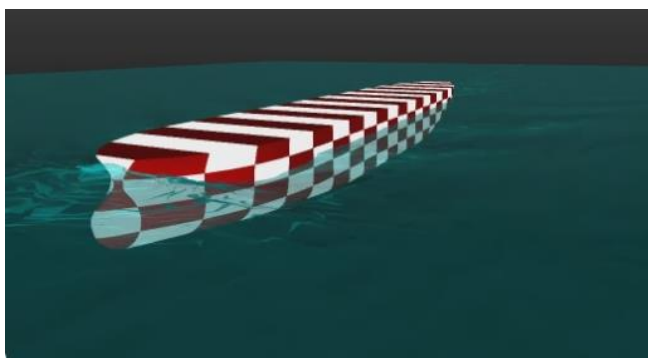
Fig 9: Free surface flow computation at Fn=0.142
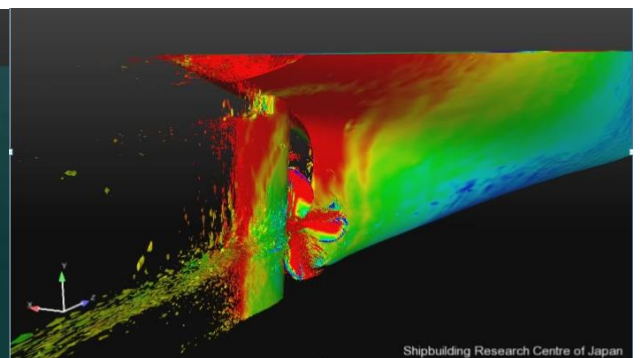
Fig 10: Self-propulsion computation (pressure distribution on body surface and second invariant iso-surface)

References

[1] Nishikawa, T., Yamade, Y., Sakuma, M., Kato, C., *Application of fully-resolved large eddy simulation to KVLCC2 －Bare hull double model at model ship Reynolds number－*, J. Japan Society of Naval Architects and Ocean Engineers 16, pp.1-10, 2012.

[2] Kim, W. J., Van, S.H., Kim, D.H., *Flow measurement around a 300K VLCC model*, Annual Spring Meeting, SNAK, Ulsan, pp. 185-188, 1998.

[3] Larsson, L., Stern, F., Visonneau, M., *KVLCC2 Case 1.1a*, CFD Workshop in Ship Hydrodynamics, Vol. 2, Gothenburg, 2010.

[4] Yonezawa, A., Watanabe, T., Yokokawa, M., Sata, M., Hirao, K., *Japanese national high-performance computing research institute and its 10-Petaflops supercomputer "K"*, Int. Conf. High Performance Computing, Networking, Storage and Analysis (SC'11), Seattle, 2011.

[5] Kato, C., Yamade, Y., Wang, H., Guo, Y., Miyazawa, M., Takaishi, T., Yoshimura, S., Takano, Y., *Numerical prediction of sound generated from flows with a low Mach number*, Computers & Fluids 36, pp. 53-68, 2007.

[6] Smagorinsky, J., *General circulation experiments with the primitive equations - I. the basic experiment,* Mon. Weather Rev. 91-3, pp. 99-164, 1963.

[7] Germano, M., Piomelli, U., Moin, P., Cabot, W. H., *A dynamic subgrid-scale eddy viscosity model*, Phys. Fluids A3-7, pp. 1760-1765, 1991.

[8] Lilly, D. K., *A proposed modification of the Germano subgrid-scale closure method*, Phys. Fluids A4-3, pp. 633-5, 1992.

[9] Uddin, A., Kato, C., Yamade, Y., Ohshima, N., Takahashi, M., Miyauchi, T., *large eddy simulation of homogeneous isotropic turbulent flow using the finite element method*, JSME Int. J. 49 B, pp.102-114.2006.

[10] Kato, C., *Application of full-resolved large eddy simulation to unsteady fluid flow and aeroacoustics predictions*, 7th Int. Symp. Turbulence and Shear Flow Phenomena, Ottawa, 2011.

Numerical Analysis of the Propeller with Economical Cap by CFD

Yoshihisa Okada*, Kenta Katayama* and Akinori Okazaki*

Propeller Design department, Nakashima Propeller Co.,Ltd.
688-1, Joto-Kitagata, Higashi-ku, Okayama 709-0625, Japan
E-mail: yoshihisa@nakashima.co.jp - Web page : http: // www.nakashima.co.jp

1.Introduction

In recent years, the ship speed and the propeller load increase more and more. Especially, the tendency is remarkable at container ship. When the horsepower per unit area is 700-800 kW/m^2 or more and the ship speed is 22-23 knots or more, Mikael Grekula et al.[1] pointed out that the rudder erosion should be occurred. Juergen Friesch[2] described the causes of rudder erosion were propeller tip-vortex cavitation, propeller hub-vortex cavitation and etc. and he introduced a new twisted rudder TW05 to reduce the risk of cavitation erosion in his paper. However, it is considered that the cavitation of the propeller should be disappeared in front of the rudder.

Yamasaki et al.[3] developed Non-Hub vortex(NHV) propeller. The features of this NHV propeller is confirmed an increase in efficiency due to the decrease of the hub vortex. Special propeller caps with similar characteristics are known, for example PBCF developed by Ouchi[4] et al. Kawamura et al.[5] investigated the characteristics of PBCF on model and full scale Reynolds number by CFD. Recently, there are special caps by some manufacturers, however there are no published paper for design of these special caps by CFD.

This paper describes that the development of economical propeller cap for prevention of rudder erosion. The authors carried out the optimaization of economical propeller cap by CFD, and the performance of the propeller with economical cap was confirmed by model test.

Keywords　　　CFD・Propeller・Economical Cap・Diffusion effect・Hub vortex・Rudder erosion

List of symbols

D	Propeller diameter	J	Advance coefficient $J=\dfrac{V}{nD}$	$\triangle K_T$	K_T economical cap／K_T contraction type	
V	Velocity of the flow	K_T	Thrust coefficient $K_T=\dfrac{Thrust}{\rho n^2 D^4}$	$\triangle K_Q$	K_Q economical cap／K_Q contraction type	
n	Propeller shaft speed	K_Q	Torque coefficient $K_Q=\dfrac{Torque}{\rho n^2 D^5}$	$\triangle \eta$	η economical cap／η contraction type	
ρ	Density	η	Propeller efficiency $\eta=\dfrac{J \cdot K_T}{2\pi K_Q}$	K_T	K_T blade + K_T boss + K_T cap	
ν	Kinematic viscosity	R_{nD}	Reynolds number $R_{nD}=\dfrac{nD^2}{\nu}$	K_Q	K_Q blade + K_Q boss + K_Q cap	

2.Analysis by CFD

2-1.Propeller Particulars and Analysis Models

MPNo.1&2 are analyzed by CFD, MPNo.1, has 6 blades, is for large container vessel and MPNo.2, has 5 blades, is for bulk carrier. Table1 and Fig.1 show the propeller particulars and profile. MPNo.1 has the large blade area and large skew angle and MPNo.2 has the small blade area and medium skew angle. These propellers are designed to confirm the difference regarding the performance of the propeller with cap by the difference of propeller profile.

Table 1. Propeller Particulars

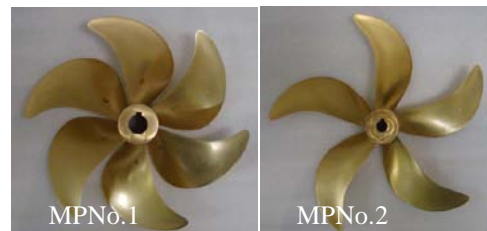|		MPNo.1	MPNo.2
Number of blades		6	5
Diameter (Model/Actual)	mm	240 / 9500	265 / 6700
Pitch ratio at 0.7r/R		1.043	0.833
Exp. Area ratio		0.81	0.44

Fig.1 Propeller Profile

RANS calculations are performed by SOFTWARE CRADLE SCRYU/Tetra Ver.10 which is a commercial CFD code and is based on a finite volume method with an unstructured grid. The Shear Stress k-ω model is applied to the turbulence model of the present simulations. The authors simulated the flow field around a propeller in non-uniform wake flow. The computational domain is composed of the inner rotational part including the propeller and the outer stationary part. The stationary part and the rotational part are connected discontinuously. Constant velocity and zero pressure are prescribed at the inlet and the outlet boundary, respectively. Fig.2 shows the computational domain. The numerical mesh is an unstructured grid, and basic cells are tetrahedral and prismatic cells are applied to near the blade surface for resolving the boundary layer. The first layer thickness of the prism layer was set to a non-dimensional wall distance for a wall-bounded flow (y^+ in short) =1. The total number of elements was about 32 million.
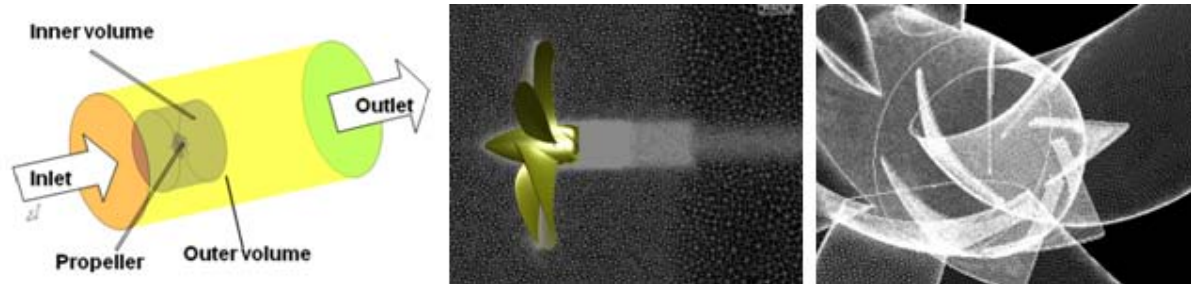
Fig2. Analysis Model for CFD

2-2.Analysis of General Propeller Caps

Firstly, the performance of the general propeller caps was analyzed by CFD. Fig.3 shows the profile of the general propeller caps. The contraction type is typically used in many propeller manufacturers. Straight type and diffusion type has sometimes adopted as countermeasure against hub vortex cavitation. In this analysis, Reynolds number is abt.2×10^6 considering calculation cost and scale effect
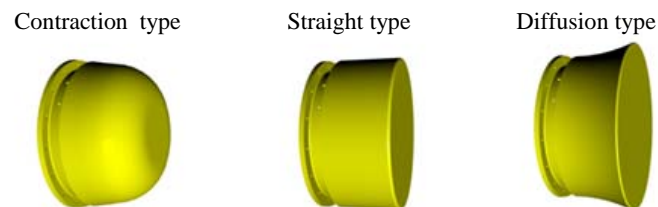
Fig.3 Profile of General Propeller caps

Fig.4 shows the pressure distribution behind the propeller caps by CFD result. The blue part represents the low pressure which is the cause of the hub vortex cavitation. In MPNo.1, contraction type generates the low pressure part behind the propeller cap. The low pressure part generated by straight type is smaller than contraction type and the part by diffusion type is still smaller. Compared with MPNo.1, the low pressure part in MPNo. 2 is smaller. Namely, it is estimated that the hub vortex generated by 5blades propeller is weaker than the vortex by 6 blades propeller. As well as MPNo.1, it is shown by Fig.4 that the reduction of the low pressure part by straight cap in MPNo.2. From above results, it can diffuse the hub vortex when the propeller cap is straight or diffusion type. However, these propeller caps still generate large low pressure part.

Next, it was visualized how hub vortex is generated by CFD for design of economical cap.
Fig.5 shows the isosurface which represents the flow of tangential direction of a certain velocity. The flow generated at trailing edge was concentrated at the center of propeller cap rear. If the concentration of tangential flows is prevented, it is expected that the hub vortex is weakened. It is named "diffusion effect" in this paper. In addition, it was confirmed that the low pressure part decreases on straight type or diffusion type due to diffusion effect.

MPNo.1

MPNo.2

| Contraction type | Straight type | Diffusion type | Contraction type | Straight type |
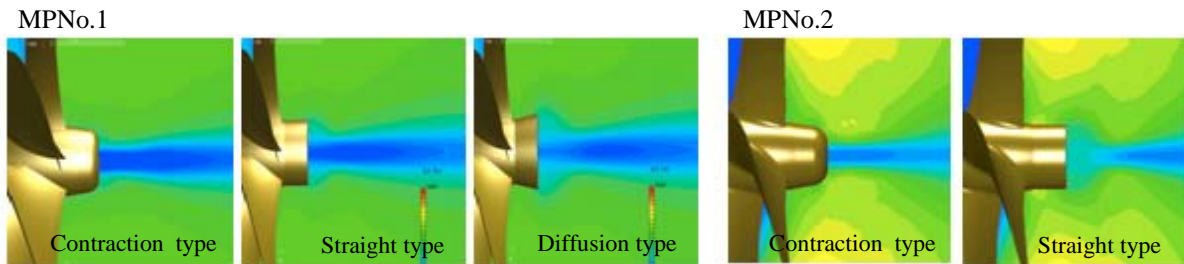
Fig.4 Pressure distribution behind the Propeller caps (MPNo.1&2)
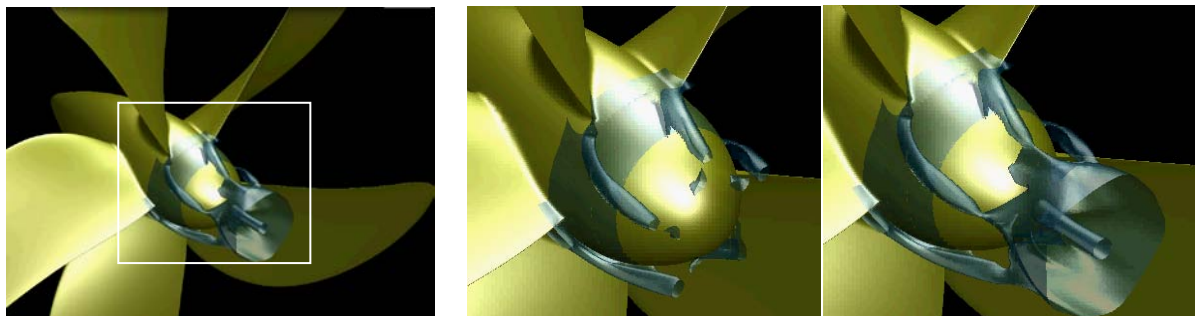
Fig.5 Visualization of Hub Vortex generation for MPNo.2

The authors confirmed the following items by numerical analysis of CFD.
1) The low pressure part on MPNO.1 has 6 blades is larger than on MPNo.2 has 5blades.
2) The cap of straight type or diffusion type can reduce low pressure part than contraction type by diffusion effect.
3) Hub vortex is occurred by concentration of several tangential flows generated from propeller blade root.

2-3.Design of Economical Cap

It is important to prevent the concentration of the tangential flow at the center of the propeller cap rear for a reduction of the hub vortex. Therefore, the design concept of an economical cap is prevention of the concentration of tangential flows, and the authors designed three economical caps as follows. Fig.6 shows the profile of the designed the economical caps.

Case-1 : Straight fins, and the end of fins is concentrated at the center of propeller cap rear.
Case-2 : Straight fins same as Case-1, and the end of fins is separated at the center of propeller cap rear.
Case-3 : Taper fins, and the end of fins is separated at the center of propeller cap rear.

Fig.6 Profile of Economical Propeller caps for MPNo.2

Fig.7 shows the isosurface of tangential flow visualized by same way of Fig.5 on the economical caps. In all of them, the diffusion effect is confirmed. In Case-1, weak hub vortex is occurred at the center of propeller cap rear,

and the tangential flows are induced to the part of concentration of the fins at cap rear. Therefore, the authors judged the edge of fins should be separated at the center of propeller cap for prevention of hub vortex. Fig.8 shows the pressure distribution of each economical cap, and the low pressure part (blue area) of each economical cap is reduced than the general caps. The effect of reducing the low pressure part of the CASE-3 is higher than Case-1 and Case-2. Therefore the authors designed the economical cap for MPNo.1&2 based on Case-3, and made a comparison between the economical cap and the contraction type about the propeller characteristics with those cap.

Fig.9 & 10 shows the comparison of the propeller characteristics with the economical cap and the contraction type, and the components of K_T & K_Q of the propeller characteristics for MPNo.1&2. K_T of propeller with economical cap is larger than with contraction type. Moreover, K_Q is smaller. As the results, the propeller efficiency became to increase. From the figure of the components of K_T and K_Q, the authors confirmed that K_T of propeller cap increased and K_Q of propeller cap decreased. In MPNo.1, K_Q of the boss is decreased in a range of high J. Regarding the propeller efficiency, MPNo.1 is increased max.1.23% and MPNo.2 is increased max.0.61 % by economical cap.

Fig.11 shows the pressure distribution of the propeller cap. The contraction type has the large low pressure part (blue area) at the propeller cap rear. In the economical cap, the high pressure part (yellow and red area) on the cap is increased by fins, and the low pressure part of the boss also reduced by economical cap.
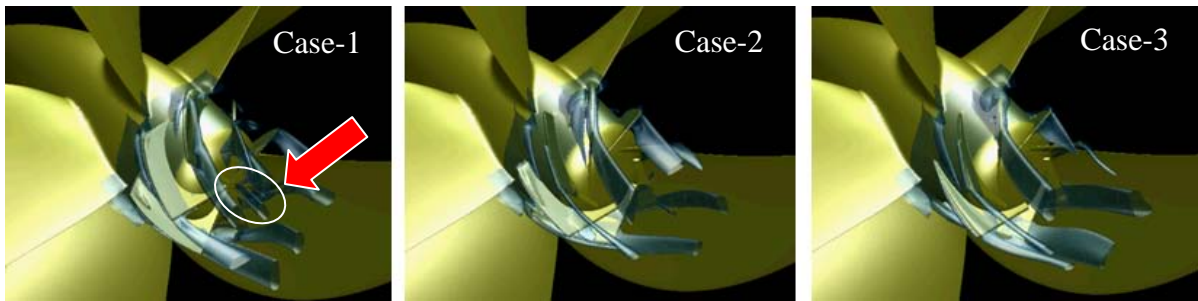
Fig.7 Tangential Flow of Economical caps for MPNo.2
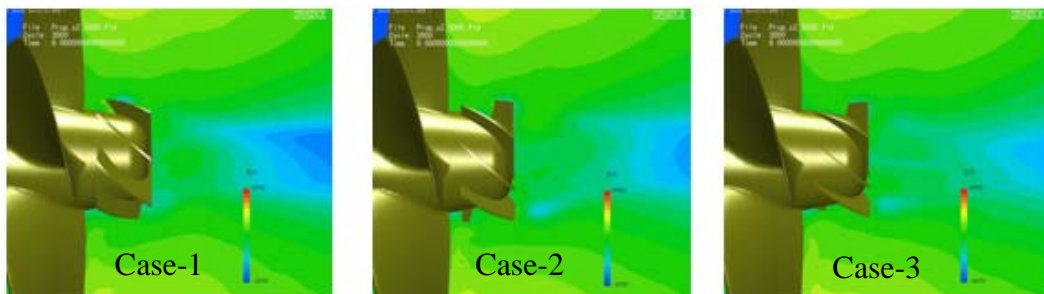
Fig.8 Pressure distribution behind Economical caps for MPNo.2
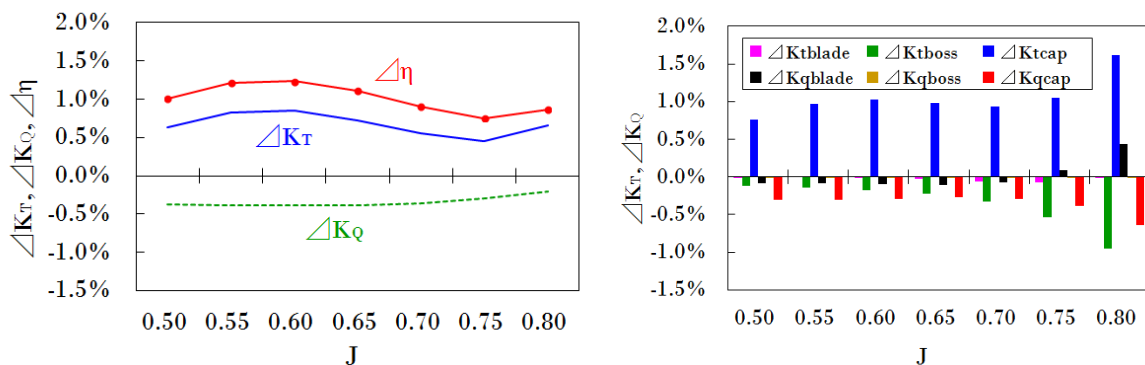
Fig.9 Comparison of Propeller Characteristics for MPNo.1 (Economical/Contraction)
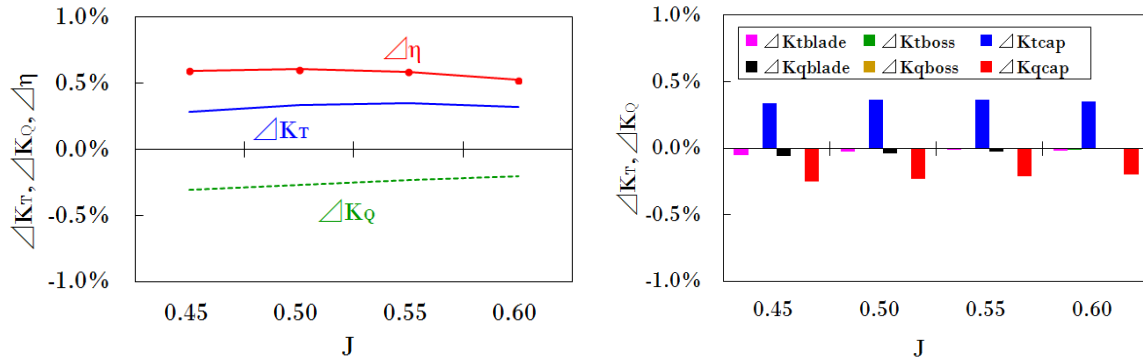
Fig.10 Comparison of Propeller Characteristics for MPNo.2 (Economical/Contraction)

Contraction type
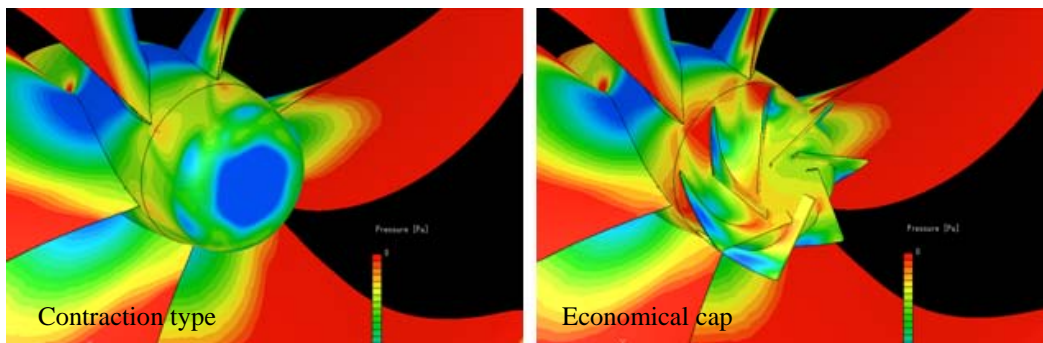
Economical cap

Fig.11 Comparison of Pressure distribution of Contraction type and Economical Cap for MPNo.1

3. Confirmation by Model Test

3-1. Procedure of Model Test

Fig.12 shows the measurement equipment for economical cap. Model test was carried out by circulating water channel in West Japan Fluid Engineering Laboratory Co., Ltd.. This model test was carried out at Reynolds number of abt.4×10^5, and was adopted reverse POT for measurement of the characteristics of the propeller with cap.

Flow direction

Fig.12 Measurement Equipments for the Propeller Characteristics by Reverse POT

3-2. Model Test Results

Fig.13 shows the comparison of the propeller characteristics by model test results. In MPNo.1, the propeller efficiency is increased max. 1.28% because Kt of economical cap is increased and K_Q is almost decreased. In MPNo.2, the propeller efficiency is increased max.0.69% because K_T is increased and K_Q is slightly increased. For the increase in propeller efficiency by model test, was almost the same as numerical analysis by CFD. However, on MPNo.2, the difference tendency between model test and CFD regarding K_Q was observed.
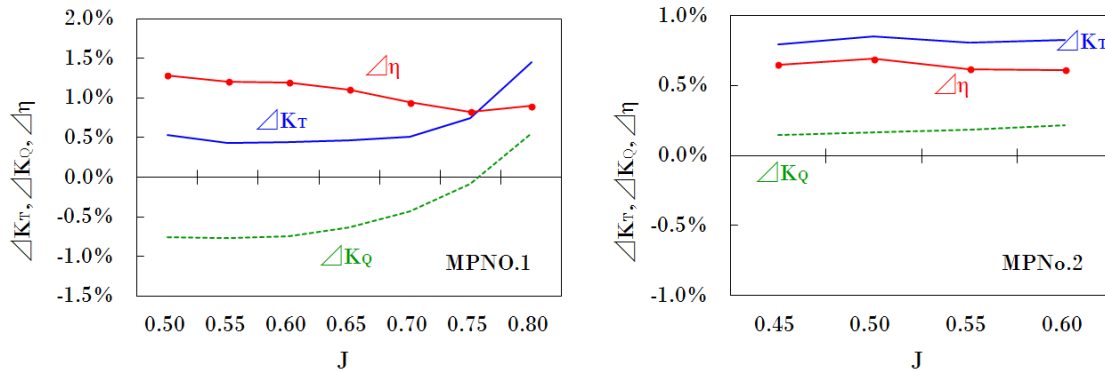
Fig.13 Comparison of Propeller Characteristics by Model Test (Economical/Contraction)

Fig.14 shows the photograph of flow visualization of the hub vortex. The flow visualization test by air injection method was conducted to confirm the strength of the hub vortex. In comparison with the contraction types, MPNo.1 generated strong hub vortex compared with MPNo.2. In the results of both propellers, the hub vortex was disappeared on the economical cap.

MPNo.1   MPNo.2
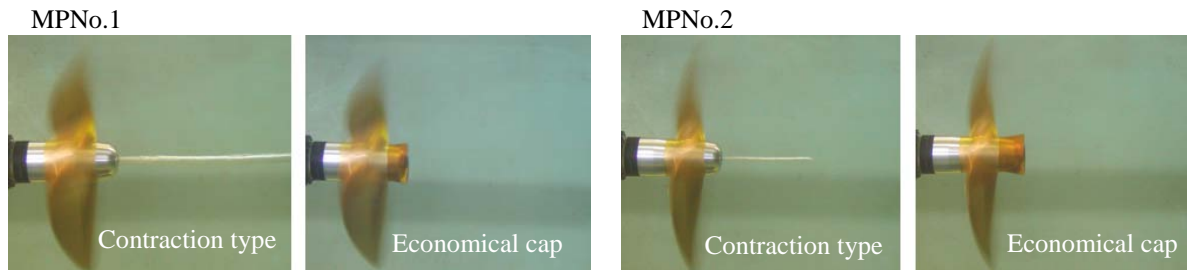
Fig.14 Flow Visualisation Test for the Hub Vortex

4. Conclusions

In numerical analysis by CFD and the motel test, the authors were confirmed that the following.

1) Diffusion effect of the hub vortex by economical cap was confirmed by CFD and the model test.
2) The increase of total efficiency by the economical cap was confirmed by CFD and the model test. According to CFD result, the effect of an improvement of the efficiency was by the fins on the economical cap.
3) About the increase of efficiency by economical cap in model test, MPNo.1 was max.1.28% and MPNo.2 was max.0.69%. In addition, almost the same results could be confirmed by CFD analysis.
4) Therefore, it is expected that prevention of rudder erosion and improvement of efficiency by economical cap.

After this, the authors will try the numerical analysis of economical cap including hull by CFD, and confirmation the efficiency in actual operation.

5. References

1. Mikael Grekula and Per Lindell, "Cavitation EROSION Damage on Semi-Spade Rudders", The Swedish Club Letter 1-2007
2. Juergen Friesch, "RUDDER EROSION DAMAGES CAUSED BY CAVITATION", CAV2006, Aug.,2006.
3. S.Yamasaki, "High Efficiency Propellers - NHV Propeller with Smallest Blade Area", IPS'10, Apr.,2010.
4. K.Ouchi, "Effect and Application of PBCF(Propeller Boss Cap Fins)", Journal of M.E.S.J., Vol.27, No.9, 1992.
5. T.Kawamura, "Model and full scale CFD analysis of propeller boss cap fins (PBCF)", Journal of Marine Science and Technology, Vol.17, Dec.,2012.

Simulation of Marine Propeller Vortex Flow

Heather Peng
Faculty of Engineering and Applied Science, Memorial University,
St. John's, NL, Canada
Email: hpeng@mun.ca

INTRODUCTION

The understanding of the detailed pressure field for propeller vortex flow is crucial to the prediction of cavitation inception. The detailed features of the tip vortex flow around a marine propeller configuration can be revealed by using advanced flow visualization and non-intrusive measurement techniques and numerical computations. For example, Chesnakas and Jessup (1998) used Laser Doppler Velocimeter (LDV) systems to obtain the detailed velocity measurements of a propeller at downstream locations. In spite of the success in measurement of propeller flow features, the pressure field still remains unclear due to the limitations of measurement techniques. It is desirable to provide the detailed pressure field by numerical simulations. RANS methods have been extensively used to evaluate performance of marine propellers. However, numerical studies on the tip vortex flow of open marine propellers are somehow limited except for some earlier studies, for example, Hsiao and Pauley (1999) and Chen and Stern (1998). Propeller flows involve a non-equilibrium boundary layer. The turbulence modeling is important in the computations of propeller tip vortex flow. There has been success in various degrees on the studies of the effect of turbulence modeling on the propeller tip vortex computations. Hsiao and Pauley (1999) applied a one-equation turbulence model on fine grids to compute the tip vortex flows of marine propellers. The discrepancy between the computational and experimental results in the far field indicated that the eddy viscosity computed from the Baldwin-Barth one-equation turbulence model might be too large within the tip vortex and led to an overly diffusive and dissipative tip vortex. Kim and Rhee (2004) also computed the tip vortex flow of a finite-span wing with several eddy-viscosity turbulence models and a Reynolds stress transportation model. Hsiao and Chahine (2008) further studied the tip vortex flow by improving the RANS solutions in a reduced computational domain with a direct Navier-Stokes simulation. The effects of the grid resolution and distribution on the computation of propeller tip vortex flow in the near field have been investigated by Qiu et al. (2013).

In this paper, the effects of various turbulence models, including eddy viscosity and Reynolds stress turbulence models, on the computation of propeller tip vortex flow in the near and far field have been investigated. The steady-state tip vortex flow at open-water condition generated by the David Taylor Model Basin (DTMB) 5168 propeller model has been computed using the RANS solver ANSYS-CFX. A spiral-like grid with grid concentration at the vortex core was generated based on the work of Hsiao and Pauley (1999). The eddy viscosity turbulence models, including one-equation models and two-equation models such as $k-\varepsilon$ and Shear Stress Transport (SST) $k-\omega$ models, along with various Reynolds stress models, were employed in the computations.

NUMERICAL METHOD

The governing RANS equations which consist of the continuity equation and the momentum equations in the rotating coordinate system are as follows:

$$\frac{\partial u_i}{\partial x_i} = 0$$

$$\rho \frac{\partial u_i}{\partial t} + \rho \frac{\partial u_i u_j}{\partial x_j} = -\frac{\partial p}{\partial x_i} + \frac{\partial}{\partial x_j}[\mu(\frac{\partial u_i}{\partial x_j} + \frac{\partial u_j}{\partial x_i} - \frac{2}{3}\delta_{ij}\frac{\partial u_l}{\partial x_l})] + \frac{\partial}{\partial x_j}(-\rho \overline{u_i' u_j'}) \tag{1}$$

Where the velocity components along x-, y- and z-axis are denoted by u_i, i=1,2,3, respectively; ρ is the water density; μ is the dynamic viscosity of water; p is the pressure; δ_{ij} is the Kronecker delta, $-\rho \overline{u_i' u_j'}$ is the turbulence term using the eddy viscosity models or the Reynolds stress solved from the transport equation based on Reynolds stress models. In the eddy viscosity models, the simple one-equation model, $(k-\varepsilon)_{1E}$ derived from the $k-\varepsilon$ model was used. In two-equation eddy viscosity turbulence models, $k-\varepsilon$, RNG

$k - \varepsilon$, $k - \omega$, and the blended $k - \omega$ (SST) models were chosen. In ε - based Reynolds stress models SSG Reynolds Stress Model (RSM) and the Launder-Reece-Rodi models (LRR): LRR-IP and LRR-QI were tested. The ω - based Reynolds stress models, such as the Baseline (BSL) RSM and the Omega Reynolds stress model, were also employed in the computations.

The conservative finite-element based control volume method is employed to solve the RANS equations in CFX. The pressure-velocity coupling scheme is used to solve the pressure and velocity equations as a single system. The high-resolution upwind difference scheme is employed to discretize the advection term. The transient term is discretized by the second-order backward Euler scheme. When the control volumes deform in time, the integral conservation equations are modified by applying the Leibnitz Rule. Based on the finite element method, shape functions are used to evaluate the spatial derivatives for all the diffusion terms and the pressure gradient term.

Based on the work of Hsiao and Pauley (1999), an H-type surface grid was first generated on the blade and hub surfaces with clusters at blade tip and root as well as leading and trailing edges. After the grid was generated on the blade surface and the boundary, a two-dimensional grid was created on each constant radial plane according to the blade surface grid using an algebraic scheme. Each two-dimensional grid was smoothed by applying an elliptic smoothing routine. The Three-dimensional initial grid was then set up by stacking all the two-dimensional grids and smoothed by a three-dimensional smoothing routine in the whole domain except the boundary layer region since the desired spacing and orthogonally has been assured in the initial grid generation, as shown in Figure 1. The computational domain was created by setting the inlet boundary at one propeller radius upstream and the outlet boundary one diameter downstream. The outer boundary in the radial direction was located at one propeller diameter. The boundary conditions were specified as follows. A no-slip wall condition was applied on the blades and the hub surfaces. A free stream condition was applied on the inlet boundary and the outer surface in the span-wise direction. The flow rate was specified at the outlet boundary. Rotational periodic conditions were applied on the periodic boundaries by the Fluid-Fluid Interface Modeling in ANSYS CFX.

VALIDATION STUDIES

The validation studies were carried out for the DTMB 5168 propeller model at the advance coefficient J = 1.1. Table 1 summarizes the propeller model geometry and operational conditions for the steady state. In the computations, the water density and viscosity are given as $\rho_{water} = 997 kg/m^3$

and $\mu_{water} = 8.89 \times 10^{-4} kgm^{-1}s^{-1}$.

TABLE I DTMB 5168 PROPELLER PARTICULARS

Diameter (m)	0.403
Inflow velocity (m/s)	10.70
Chord length at 0.7R (m)	0.175
Advance coefficient	1.1
Rotation speed (rps)	24.163
Combined velocity at 0.7R (m/s)	23.93
Reynolds number	$4.2*10^6$

A primary/secondary coordinate system as shown in Figure 2 was employed to better describe the tip vortex structure, in which the primary velocity, Vs, is defined in the axial-tangential x-t plane at the propeller pitch angle ϕ. The tangential velocity, Vc, and the radial velocity, Vr, are then on the secondary-flow plane (r - c plane) which is normal to the primary velocity. The primary and tangential velocities at each radial station are given as

$$V_s = V_x \sin\phi + V_t \cos\phi \qquad V_c = -V_x \cos\phi + V_t \sin\phi \qquad (2)$$

The tip vortex axis is normal to the secondary-flow plane and the structure of vortex core can be easily defined. Note that all velocity components presented below are nondimensionalized with respect to the inflow velocity. The computed axial, tangential and radial velocities, V_x, V_t and V_r in the tangential direction across the tip vortex centre at x = 0.2386R (R is the propeller radius) were compared with the experimental data (Chesnakas and Jessup,1998) in Qiu et al. (2013). It was shown that there were no significant differences in the predictions by using eddy viscosity or Reynolds stress turbulence models. In this work, these velocity components by

various turbulence models are computed and compared at x =0.1756R and far downstream x= 0.3963R in Figs. 3 to 4. Note that the center of the vortex core is defined at the location with minimum primary velocity Vs.

To examine the turbulence predicted by various models, the non-dimensional RMS fluctuation of velocity, q, was introduced. The computed q contours with the secondary streamlines are plotted in Figs. 5 and 6 and compared with the experimental results. As shown in the experimental results by Chesnakas and Jessup (1998), the size of high turbulence region around the vortex becomes larger as the flow moves downstream, from x = 0.1756R to 0.3963R. The relative coarse grid downstream may contribute to the dissipative tip vortex and the low turbulence levels. The tip vortex, which is strongly entangled with the blade wake at x = 0.3963R, was successfully predicted by the SST model, although the peak value of q is underestimated.

CONCLUSIONS

The tip vortex flow of a marine propeller at the steady state has been computed using the RANS solver ANSYS CFX on a spiral-like structured grid with grid concentration at the vortex core. Validation studies were carried out for the tip vortex flow. Eddy viscosity and Reynolds stress turbulence models were employed in the computations. All the turbulence models are able to predict similar axial, tangential and radial velocities. Various eddy viscosity turbulence models give good predictions of high turbulence region. The peak value of turbulence farther downstream is however under predicted by the eddy-viscosity and Reynolds stress models. Among these turbulence models $k - \varepsilon$ and SST models better predict the turbulence strength than the BSL and SSG Reynolds stress models. Further investigation will be conducted.

REFERENCES

Chen, B. and Stern, F., 1998, "RANS Simulation of Marine-Propulsor P4119 at Design Condition", Proceedings of 22nd ITTC Propulsion Committee Propeller RANS/PANEL Method Workshop, Grenoble, France.
Chesnakas, C.J. and Jessup, S.D., 1998, "Propeller Tip Vortex Measurements Using 3- omponent LDV," Proceedings of 22nd Symposium on Naval Hydrodynamics, Washington D.C., U.S.A.
Hsiao, C.-T. and Chahine, G. L., 2008, "Scaling of Tip Vortex Cavitation Inception for a Marine Open Propeller," Proceedings of 27th Symposium on Naval Hydrodynamics, Seoul, Korea.
Hsiao, C.-T. and Pauley, L.L., 1999, "Numerical Computation of the Tip Vortex Flow Generated by a Marine Propeller," ASME Journal of Fluids Engineering, Vol. 121, No. 3.
Kim, S.E. and Rhee, S.H., 2004 "Toward High-Fidelity Prediction of Tip-Vortex Around Lifting Surfaces," Proceedings of 25th Symposium on Naval Hydrodynamics, St. John's, Canada.
Qiu, W., Peng, H., Ni, S., Liu, L., Mintu, S., Hally, D. and Hsiao, C.-T., 2013, "RANS Computation of Propeller Tip Vortex Flow," International Journal of Offshore and Polar Engineering, Vol. 23, No. 1, pp. 73-79.
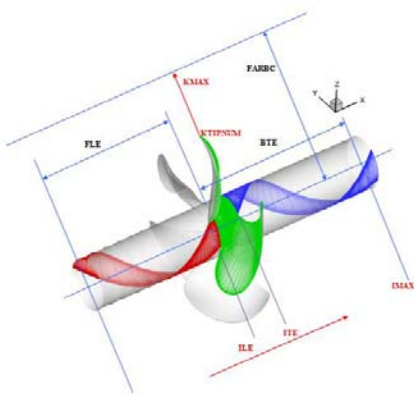
Figure 1 Computation domain
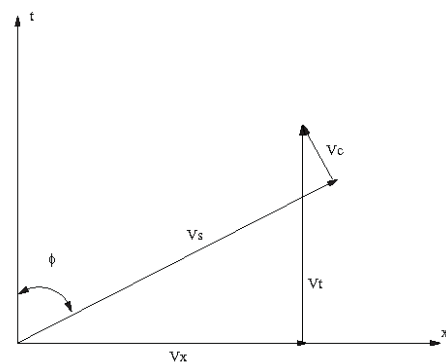
Figure 2 Primary and secondary coordinate system
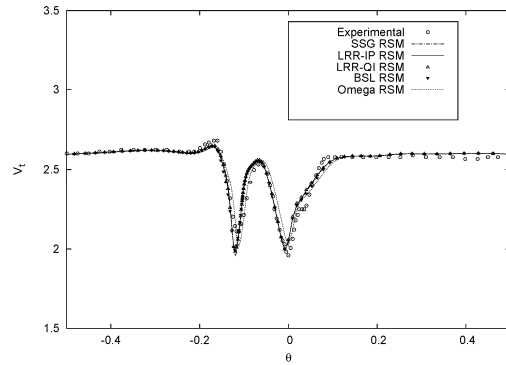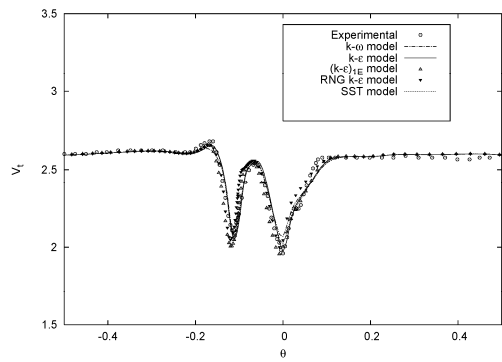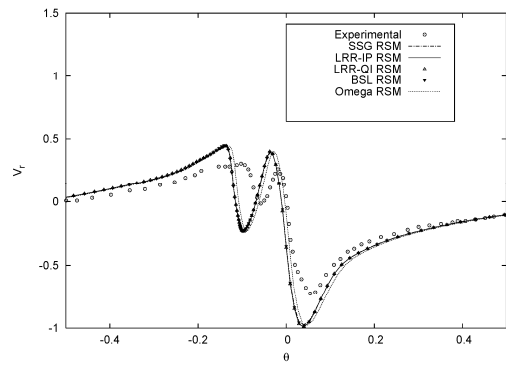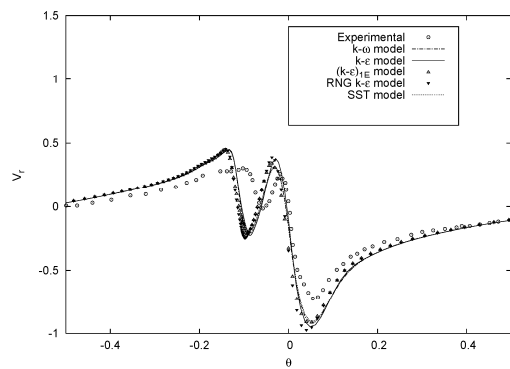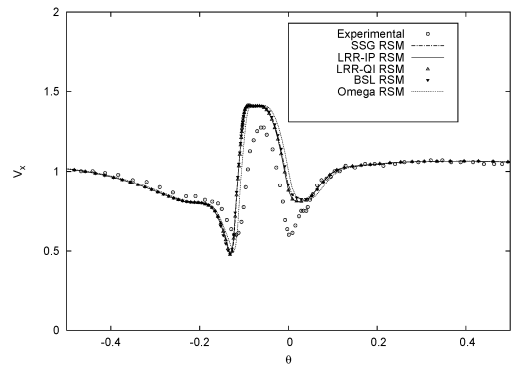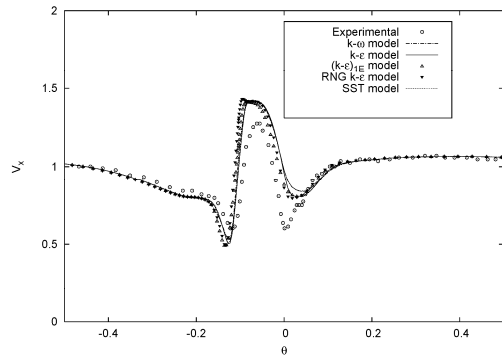
Figure 3 V_x, V_t and V_r verse θ across the vortex core at x/R=0.1756 with eddy viscosity turbulence models

Figure 4 V_x, V_t and V_r verse θ across the vortex core at x/R=0.1756 with Reynolds stress turbulence models
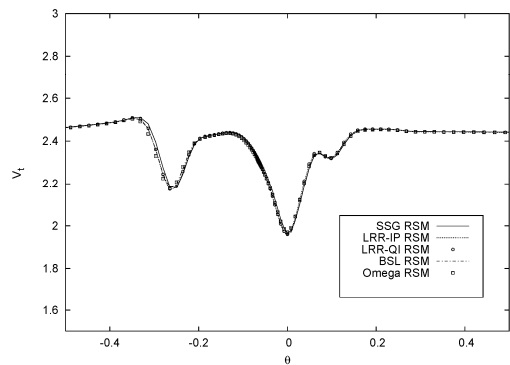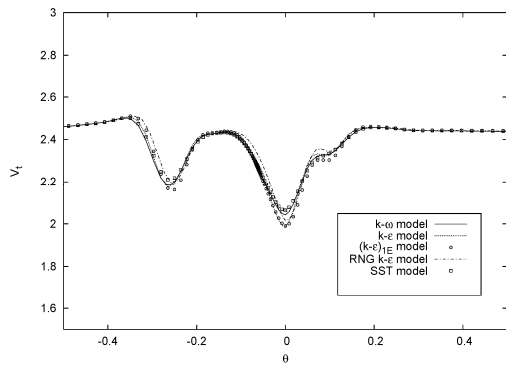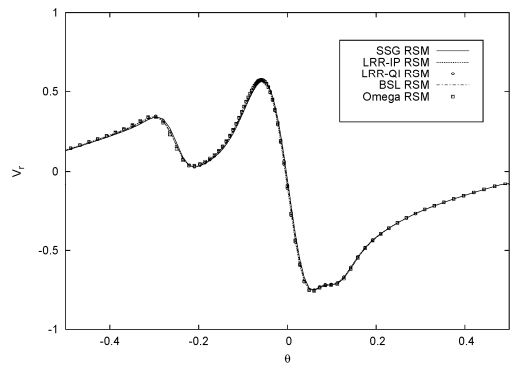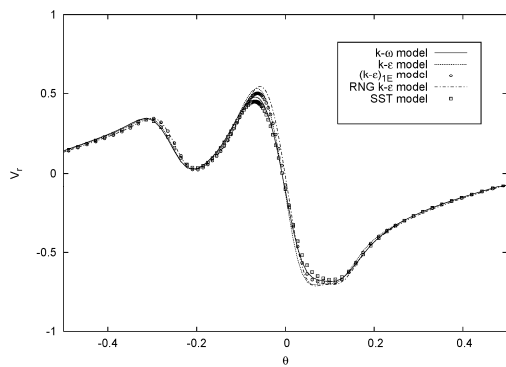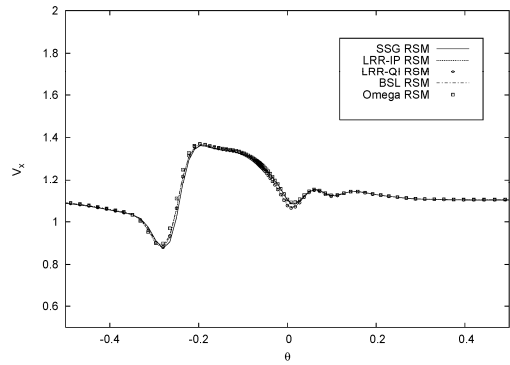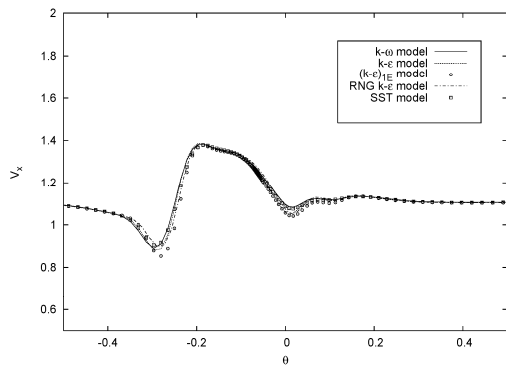
Figure 5 V_x, V_t and V_r verse θ across the vortex core at x/R=0.3963 with eddy viscosity turbulence models

Figure 6 V_x, V_t and V_r verse θ across the vortex core at x/R=0.3963 with Reynolds stress turbulence models
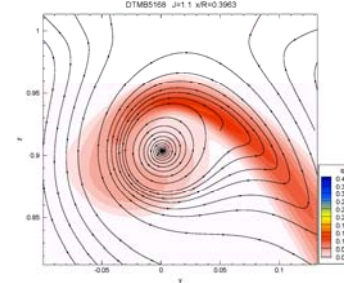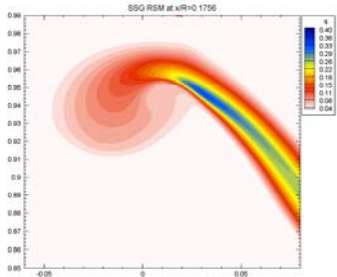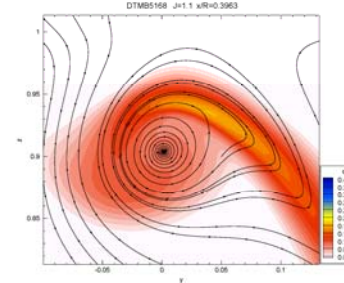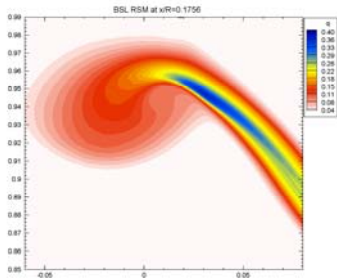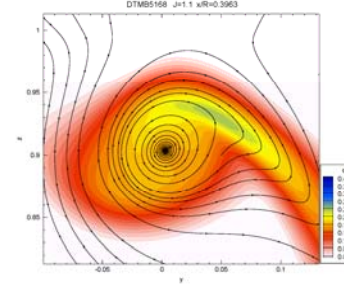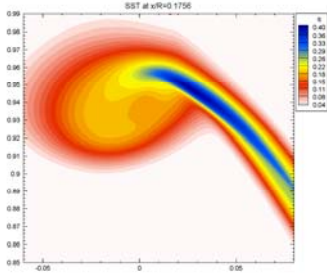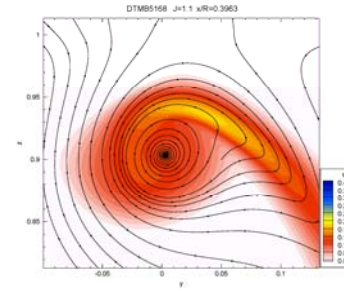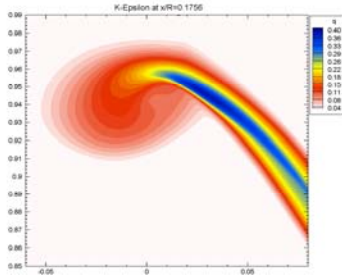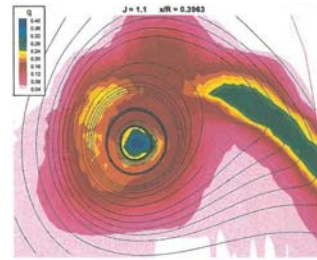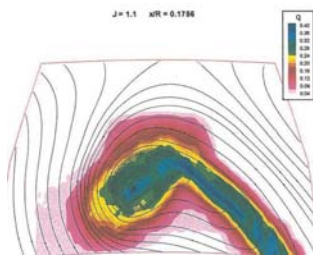
Figure 7: q contour at x/R=0.1756 with $k - \varepsilon$, SST, BSL RSM and SSG RSM model.

Figure 8: q contour at x/R=0.3963 with $k - \varepsilon$, SST, BSL RSM and SSG RSM model.

Applications of Wave Generation inside Solution Domain of Simulations Based on Navier-Stokes Equations

Robinson Perić

Hamburg University of Technology (TUHH)
Email: robinson.peric@tuhh.de

1. INTRODUCTION

When simulating free surface flows with the Navier-Stokes equations the standard procedure to create free surface waves is to prescribe the corresponding values for velocities and pressures at the inlet boundaries [2]. Alternatively, waves can be generated as in experiments, e.g. by imposing a flap-like movement on one or more boundaries of the solution domain. However, such wave generation mechanisms produce reflections when the wave generating boundary is hit by waves coming towards it.

To avoid reflections from the solution domain boundaries the most common and effective approach is a combination of coarsening the grid towards the corresponding boundary and applying a damping zone in the vicinity of the boundary, where – similar to a porous medium – the vertical fluid velocity component is damped by adding a source term into the corresponding equations for momentum conservation [1]. This approach is not applicable to wave creating boundaries since the created waves would experience damping as well.

In free surface simulations often very large or infinite domains are to be modelled, although only the solution in a small part of the domain is of interest. An example for this is the simulation of the wave pattern behind a moving ship on calm open sea, where only the water surface elevation in the vicinity of the ship is of interest. In simulations, the solution domain should be as small as possible, covering only the regions where the solution is of interest, and thus lowering the computational effort. For the solution inside the domain to be correct, the influence of the infinite domain has to be modelled directly at or near the boundary. For most applications this simply means that waves travelling out of the solution domain must not be reflected from its boundaries.

For free surface flow simulations around moving bodies, reflections from the wave-making boundaries can often be neglected, especially when the velocity of the bodies is higher than the characteristic wave propagation velocity in the liquid phase (i.e. Froude numbers $Fr \geq 1$). In these cases reflections are naturally transported downstream, i.e. away from the wave generating boundaries.

However, for simulations of the flow around bodies which do not move or move with a velocity lower than the characteristic wave propagation velocity of the liquid phase ($Fr \leq 1$), reflections are often a problem. Choosing a very large solution domain prolongs the time until reflections from the wave-making boundaries reach the body and create unrealistic disturbances in the solution results, but this approach drastically increases the computational effort and is not suitable for longer simulations.

The methods mentioned above are especially not suitable for simulating two wave fronts which meet under different angles.

In [4], a wave maker is presented which aims to overcome the limitations mentioned above. The method is suited for deep water conditions and generates surface waves by introducing mass source terms in box-shaped regions which can be placed at any desired location inside the solution domain. Thus wave damping can be applied at all domain boundaries and waves can travel through the wave maker without reflections. The derivation, advantages and limitations of the method and a general procedure for setting up the wave generation to produce waves with the desired characteristics (wavelength, amplitude, irregular/regular waves,..) is also given in [4].

The present paper presents selected examples of the application of this method to 3D simulations.

2. GOVERNING EQUATIONS AND SOLUTION METHOD

The governing equations for the simulations are the Navier-Stokes equations, which consist of the equation for mass conservation and the three equations for momentum conservation:

$$\frac{\mathrm{d}}{\mathrm{d}t} \int_V \rho \, \mathrm{d}V + \int_S \rho(\mathbf{v} - \mathbf{v}_g) \cdot \mathbf{n} \, \mathrm{d}S = \int_V \rho q_c \, \mathrm{d}V \quad , \quad (1)$$

$$\frac{\mathrm{d}}{\mathrm{d}t} \int_V \rho u_i \, \mathrm{d}V + \int_S \rho u_i (\mathbf{v} - \mathbf{v}_g) \cdot \mathbf{n} \, \mathrm{d}S =$$
$$\int_S (\tau_{ij} \mathbf{i}_j - p \mathbf{i}_i) \cdot \mathbf{n} \, \mathrm{d}S + \int_V \rho g_i \, \mathrm{d}V + \int_V q_i \, \mathrm{d}V \quad . \quad (2)$$

Here V is the control volume (CV) bounded by the closed surface S, $\mathbf{v}$ is the velocity vector of the equivalent fluid with the Cartesian components u_i, $\mathbf{v}_g$ is the velocity vector with which the CV surface is moving, $\mathbf{n}$ is the unit vector normal to S and pointing outwards, t is time, p is the pressure, τ_{ij} are the components of the viscous stress tensor, g_i is the gravitational acceleration in the direction of the Cartesian coordinate x_i and q_i is a volumetric source term. q_i takes the value $q^d_{x_i}$ for the x_i-velocity momentum equation inside the corresponding damping zone and is zero everywhere else. q_c equals the mass source term $s_i(t)$ inside source region i and is zero everywhere else.

The free surface is described with the volume of fluid method (VOF), see [3]. Air and water are assumed to have constant density and viscosity: $\rho_{\text{air}} = 1.2 \ \frac{\text{kg}}{\text{m}^3}$, $\rho_{\text{water}} = 1000 \ \frac{\text{kg}}{\text{m}^3}$, $\mu_{\text{air}} = 1.8 \cdot 10^{-5} \ \text{Pa} \cdot \text{s}$, $\mu_{\text{water}} = 0.001 \ \text{Pa} \cdot \text{s}$.
Therefore τ_{ij} takes the form:

$$\tau_{ij} = \mu \left(\frac{\partial u_i}{\partial x_j} + \frac{\partial u_j}{\partial x_i} \right) \quad .$$

The application of the method to simulations of the Reynolds-averaged NavierStokes or Euler equations is straightforward.

The formula for the source term to generate a wave with horizontal travelling direction $\mathbf{e}$ at an angle α for the simulations within this paper takes the form

$$s_i(t) = Q \sin\left(\omega t + kx\cos(\alpha) + ky\sin(\alpha) \right) \quad , \quad (3)$$

with wave frequency ω, wave number k and coefficient $Q = 2.4 \frac{1}{\text{s}}$ for the present simulations. The source term appears on the right hand side of the continuity equation for the grid cells inside the corresponding source region s_i. The setup for α can be seen in Fig. 1.
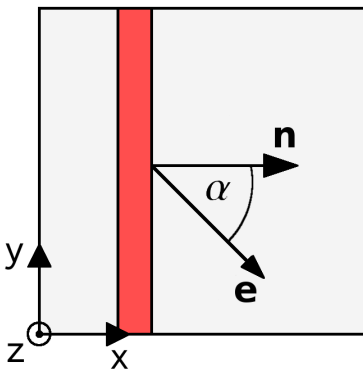
Figure 1: Top view of the solution domain with a single source region (red); $\mathbf{e}$ is the direction of propagation of the generated wave and $\mathbf{n}$ is the normal to the source region surface pointing towards the part of the solution domain where the solution is of interest

When u_i is the velocity component in x_i-direction, the damping is achieved as in [1] by adding a source term to the equation for the u_i-velocity:

$$q^d_{x_i} = \rho(f_1 + f_2 |u_i|) \frac{e^\kappa - 1}{e^1 - 1} u_i \quad , \quad (4)$$

$$\kappa = \left(\frac{x_j - x_{j,\text{sd}}}{x_{j,\text{ed}} - x_{j,\text{sd}}} \right)^n \quad . \quad (5)$$

Here x_j stands for the wave propagation direction with $x_{j,\text{sd}}$ being the start- and $x_{j,\text{ed}}$ the end-x_j-coordinate of the damping zone. The end coordinate is at the domain boundary to which the damping zone is attached and the start coordinate is located at a distance of $x_d = 120 \ \text{m}$ in boundary-normal direction from the end coordinate. f_1, f_2 and n are parameters of the damping model. For the present study, the parameter values were $f_1 = 10$, $f_2 = 10$ and $n = 2$. If not mentioned otherwise, only the u_3-velocity component (i.e. in z-direction) is damped.

3. SOLUTION DOMAIN, DISCRETIZATION AND SIMULATION SETUP

For some simulations the setup is slightly different to the one presented in this section. Any differences are pointed out in the text where they occur.

The solution domain for the simulations has the shape of a box with dimensions $(L_x, L_y, L_z) = (600 \ \text{m}, 600 \ \text{m}, 360 \ \text{m})$. The origin of the coordinate system is the bottom left corner of the box as depicted in Figs. 2 and 3. The domain is filled with water to a depth of $d = 330 \ \text{m}$. The rest of the domain is filled with air.
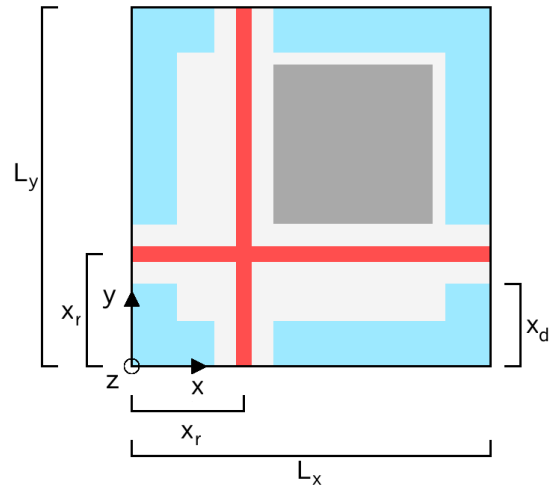
Figure 2: Top view of the solution domain for the case with two source regions, which cross each other at an angle of 90°; the u_3-damping zones are shown in blue and the location of the source regions are shown in red; the dark grey area denotes the zone with the finest mesh ((210 m < x < 480 m, 210 m < y < 480 m), where an agreeable solution is desired – the rest of the domain is for generating and damping of waves
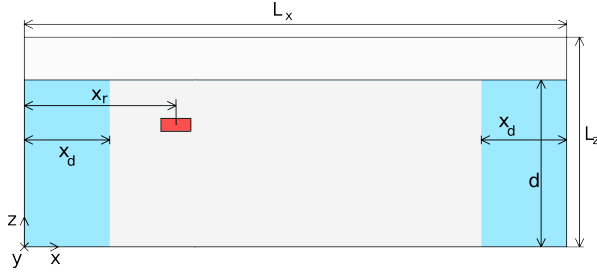
Figure 3: Cross-section of the solution domain through a source region with damping zones (blue) and source region (red)

The waves are generated at the two orthogonal source regions, which have the dimensions (174 m < x < 186 m, 0 m < y < 600 m, 309 m < z < 312 m) and (0 m < x < 600 m, 174 m < y < 186 m, 309 m < z < 312 m).

The distance of the damping zones from the domain boundaries is x_d = 120 m, and the distance of the u_3-damping zones to the center of the wave makers is 30 m. In the u_3-damping zones, the u_3-velocity component is damped, which provides damping to waves from all directions. For the parts of the domain boundary near the source regions where the damping zone is interrupted, there is also wave damping with the same damping distance x_d to the boundaries and the same procedure as in the damping zone described above, except that here only the velocity component normal to the wall is damped.

Alternatively, for some cases the waves are damped by extruding the grid for 600 m from the domain boundaries. The cell size in extrusion direction increases by a factor of 1.1 with each cell. This provides also acceptable damping. The z = 360 m boundary is a pressure outlet boundary, the other boundaries are no-slip boundaries.

In all simulations the wave makers generate waves with a wavelength of λ = 60 m and a wave amplitude of a = 1.2 m in deep water. Therefore the wave number is $k \approx 0.11 \; \frac{\text{rad}}{\text{m}}$, the wave frequency is $\omega \approx 1.0 \; \frac{\text{rad}}{\text{s}}$, the wave period is $T \approx 6.2$ s, the phase velocity is $c \approx 9.7 \; \frac{\text{m}}{\text{s}}$ and the steepness is $ka \approx 0.13$.

Due to the high computational cost of 3D wave simulations, a rather coarse computational grid was chosen. In the domain part where the solution is of interest (dark gray area in Fig. 2), the waves are discretized in the free surface zone with 38 cells per wavelength λ and 14 cells per wave height. In the rest of the domain, the grid is twice as coarse in z-direction in the free surface zone. With increasing distance to the undisturbed water surface, the grid is coarsened as well.

The wave amplitude directly above the source regions is twice the amplitude of the desired waves, since waves are created on both sides of the wave maker. Already at a distance of one wavelength from the source region the waves have the desired amplitude. To cre-

ate a desired wave, another unwanted wave is created, which travels in the opposite direction and has to be damped. The maximum velocity inside the wave directly above the source region can therefore be twice as large as everywhere else in the domain. The grid around the source region was twice as coarse in z-direction as in the zones with the finest mesh, so that the wave maker does not require a smaller maximum time step than other wave generation approaches.

For stability and accuracy reasons, it is advisable to keep the Courant number $C = \frac{u_i \Delta t}{\Delta x_i}$ at all times $C < 0.5$, i.e. a fluid particle travels less than half a cell per time step. Here u_i is the velocity component in x_i-direction, Δx_i is the minimum cell size in x_i-direction and Δt is the time step. Airy wave theory delivers an analytical prediction for the maximum velocity component values inside a wave as

$$u_{x,\text{max}} = u_{z,\text{max}} = \omega a \text{e}^{ka} \quad . \tag{6}$$

Using $u_{x,\text{max}}$ and taking Δx_i from the finest grid in the area of the water surface, the maximum Courant number can be approximated beforehand. In simulations where two waves meet, the water surface elevation is at some places $2a$; then $2u_{x,\text{max}}$ has to be used. If the waves are steep and interact with objects in the flow, it can be advisable to aim at even lower Courant numbers.

For better comparability and to reduce the effect of temporal diffusion on the wavelength and amplitude, the time step was chosen such that $C < 0.1$ for the present simulations. This resulted in a time step Δt = 0.015 s which corresponds to 413 time steps per wave period.

The governing equations are applied to each cell and discretized according to the Finite Volume Method (FVM). The resulting coupled equation system is then linearized and solved by an implicit segregated iterative solver. All schemes and approximations are of second order. The flow solver STAR-CCM+ was used for the simulations.

4. GENERATION OF A LONG-CRESTED WAVE IN 3D

In this section, wave generation with only one source region will be explored. Therefore the x-normal domain boundaries (i.e. the left and right boundaries in Fig. 3) have wave damping of the z-velocity component on the whole boundary. Furthermore, the area where the grid is finest is larger with (210 m < x < 480 m, 120 m < y < 480 m). The source term is Eq. (3) with $\alpha = 0°$.

4.1. Generation of a Single Long-Crested Wave

For this simulation, the source region has the dimensions (174 m < x < 186 m, 0 m < y < 600 m, 309 m <

$z < 312$ m). The $y = 0$ m and $y = 600$ m boundaries are symmetry boundaries and no wave damping is applied there. The resulting surface elevation in Fig. 4 after 20 periods shows that the wave generation works well. The waves appear to travel slower in the domain parts with the coarser grid. The flow has no component in y-direction, therefore the result is the same if in the vicinity of the $y = 0$ m and $y = 600$ m boundaries the u_2-velocity component of the flow is damped.
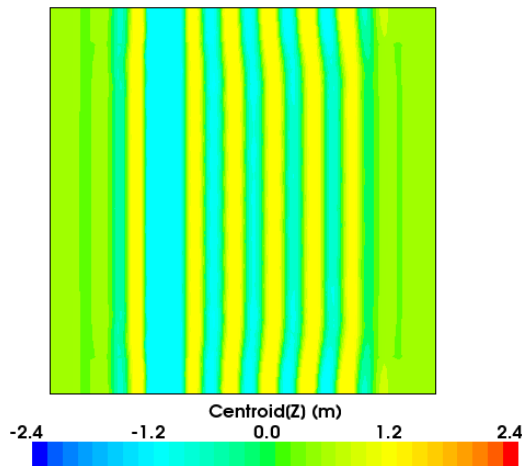
Figure 4: Surface elevation after 20 periods; no damping at $y = 0$ m and $y = 600$ m domain boundaries; source region extends from top to bottom wall

4.2. End Effects of Source Regions which do not Extend to the Domain Boundary

Figure 5 shows what happens if the simulation from Fig. 4 is repeated with additional damping of the u_3-velocity component of the flow in the vicinity of the $y = 0$ m and $y = 600$ m boundaries and a smaller source region of dimensions (174 m $< x <$ 186 m, 225 m $< y <$ 375 m, 309 m $< z <$ 312 m).
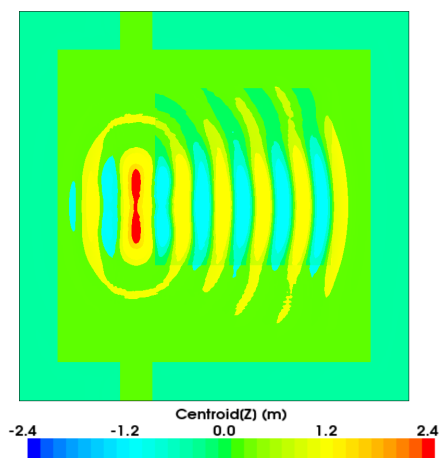
Figure 5: Surface elevation after 20 periods; damping of u_3-velocity component at all domain boundaries; source region does not extend into damping region

At both ends in y-direction of the source region the solution shows end effects. The generated waves are bowed and not parallel. Extending the source region into the damping zone produces a similar behavior. Decreasing the source region length in y-direction would increase this bowing, until for a quadratic cross-section of the source region in the x-y-plane the wave pattern for a point source would be obtained.

4.3. Generation of a Long-Crested Wave at an Angle in 3D

Waves can also be created in such a fashion that they leave the source region at an angle. For demonstration, the simulation from Fig. 5 is repeated with the source region extending from $y = 0$ m to $y = 600$ m, different source terms and damping on all domain boundaries. The influence of end effects on the results was less pronounced in these cases.

To generate waves which leave the source region at an angle α, the source term is set to Eq. (3) with α set to the desired value; see Figs. 6 and 7 for angles 20° and 45°, respectively.
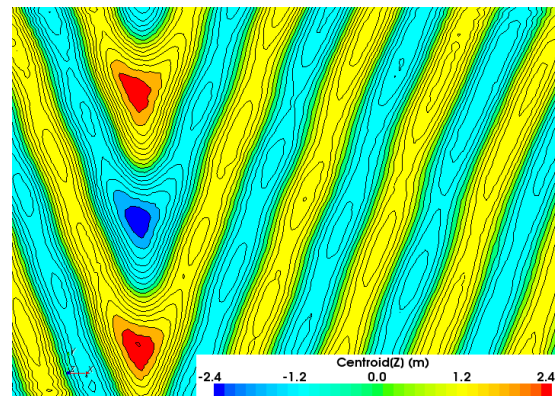
Figure 6: Surface elevation after 20 periods; the waves leave the source region at an angle of $\alpha = 20°$; wave peaks along the source region travel from top to bottom and waves are generated at both sides of the source region
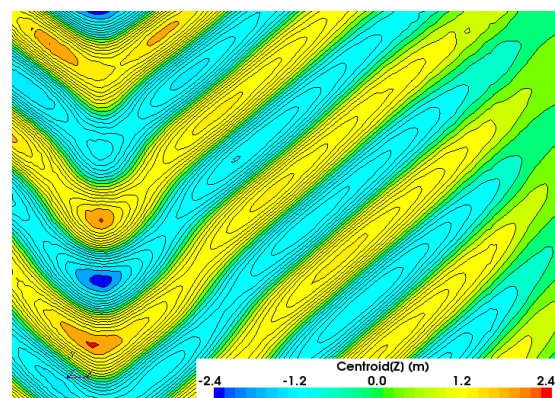
Figure 7: As Fig. 6, for $\alpha = 45°$

When generating waves at an angle $\alpha \neq 0°$, wave peaks and troughs travel along the source region and produce in this fashion waves at oblique angles. The larger the angle, the slower the movement. For large angles, the wave amplitude diminishes with increasing distance to the wave maker instead of remaining constant along the wave.

For angles of $\alpha \leq 45°$ this effect is less pronounced. This indicates that with increasing angle the method becomes less efficient. Simulations showed that a generation of a wave at an angle of $\alpha = 90°$ is not possible. It is therefore recommended to apply this procedure only to waves at angles of $\alpha \leq 45°$ and – if larger angles are required – to reposition the source region so that angles $\leq 45°$ can be used.

Although the wave maker succeeds to create waves at the desired angle, the wave crests do not form a straight line on all parts of the wave, but instead a straight line with one or more kinks in it. This is especially visible in Fig. 7, where at the top of the image the wave crests form a straight line from the source region outwards, whereas at the bottom of the image they form a line with a distinct bend. This behavior is further discussed in [4].

5. GENERATION OF SHORT-CRESTED WAVES BY CROSSING OF TWO LONG-CRESTED WAVES UNDER DIFFERENT ANGLES IN 3D

In this section, long-crested wave trains are generated that meet under the angles 90°, 120° and 180° using two source regions. When the two long-crested wave trains meet an angle other than 0° or 180° they generate characteristic patterns of short-crested waves. As regular waves are used, the results can be compared to analytical solutions from linear wave theory, here shown for a wave train travelling in positive x-direction which meets another wave train under the angle of β:

$$\eta(x, y, t) = a\sin(\omega t + kx) +$$
$$a\sin(\omega t + kx\cos(\beta) + ky\sin(\beta)) \quad , \quad (7)$$

with surface elevation $\eta(x, y, t)$.

Two orthogonal source regions are used to generate waves under angles between 0° and 135°. For larger angles, i.e. between 135° and 180°, two source regions opposite to one another are used. This way, two long-crested waves can be generated so that they meet at any desired angle. Unless mentioned otherwise, the source term is Eq. (3) with $\alpha = 0°$ for both source regions.

5.1. Generation of Standing Waves With Two Parallel Source Regions

The simulation setup corresponds to section 3, with two exceptions: The two source regions are located parallel to each other on opposite sides of the solution domain with (174 m < x < 186 m, 0 m < y < 600 m, 309 m < z < 312 m) and (414 m < x < 426 m, 0 m < y < 600 m, 309 m < z < 312 m). u_3-damping is applied on all boundaries except in a horizontal distance of 30 m to the source regions.

This setup generates two long-crested waves which meet at an angle of 180°, which produces a standing wave, see Fig. 8. The free surface between the two source regions oscillates between two extremes: flat surfaces and waves with the maximum amplitude twice the amplitude of the generated long-crested waves. The fact that the standing wave is still apparent without disturbances after 20 wave periods shows that waves can pass through the wave makers without being reflected and that the damping works well.
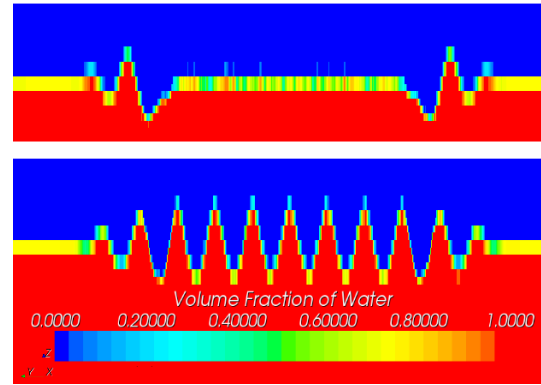
Figure 8: Volume fraction of water after 20 periods in a cross-section at $y = 300$ m when the two wave trains between the two wave makers cancel each other (top) and $0.25T$ later when the two wave trains show maximum amplification (bottom)

5.2. Generation of Short-Crested Waves With Two Orthogonal Source Regions

The domain setup is the one described in section 3. This corresponds to two long-crested regular wave trains of the same amplitude and wavelength meeting at an angle of 90°, which form the characteristic wave pattern in Fig. 9: a checkerboard-like arrangement of wave crests and troughs with twice the amplitude of the long-crested waves.

For an angle of 120°, the same setup can be used when changing the source term for the source region between the x-normal domain boundaries to Eq. (3) with $\alpha = 60°$. The resulting flow pattern in Fig. 10 looks like a stretched and rotated version of Fig. 9.

The simulation and analytical results in Figs. 9 and 10 agree well, despite slight differences in the color coding and the simulated waves being Stokes waves instead of Airy waves.
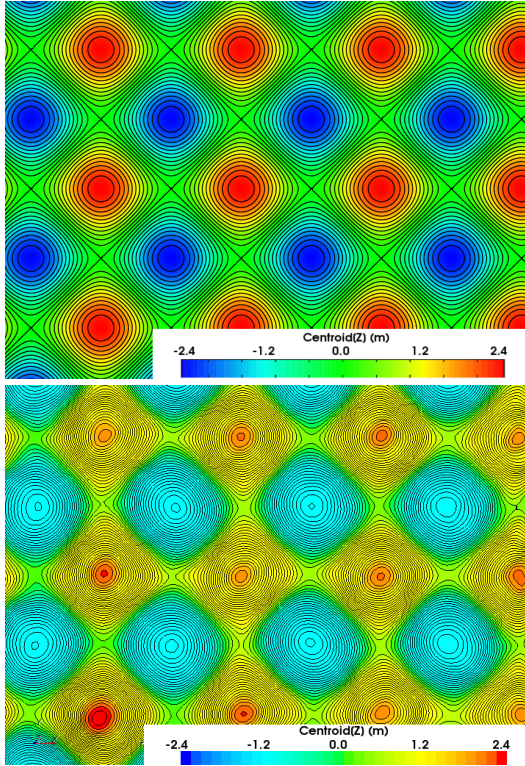
Figure 9: Analytical (top) and simulated (bottom) surface elevation after 20 periods of two long-crested wave fronts meeting under an angle of 90°
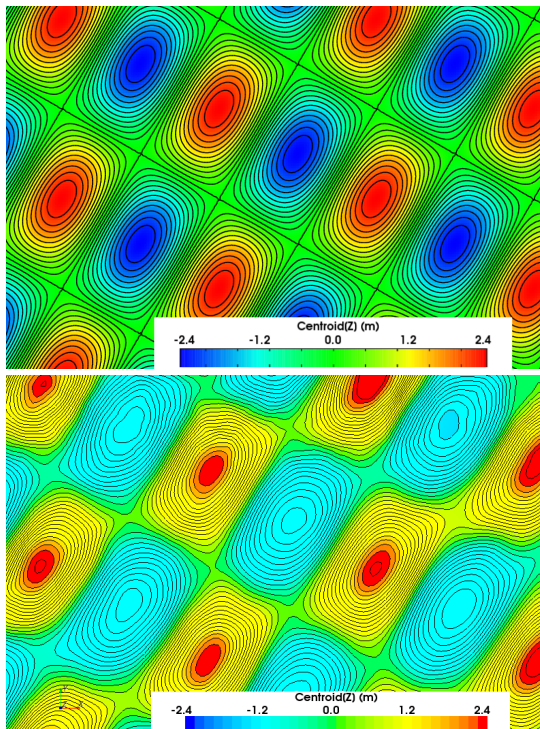
Figure 10: Analytical (top) and simulated (bottom) surface elevation after 20 periods of two long-crested wave fronts meeting under an angle of 120°

6. CONCLUSIONS

The aim of this study was to validate the method of wave generation by source terms in the continuity equation through comparisons of results with known or expected solutions. The value of the method is the ability to handle flow situations with additional complexity like wave interaction with bodies in the flow, breaking waves, effects of wind and current, and in particular reflections from walls that may radiate upstream-propagating waves. Since waves can pass over the source term zone unreflected, long simulations with natural interaction of incoming and reflected waves are possible. This is verified by the fact that two opposite wave makers can produce and maintain a standing wave between them. More applications, in particular involving wave reflections from solid bodies, are presented in [4].

References

[1] Choi, J., Yoon, S. B.: Numerical simulations using momentum source wave-maker applied to RANS equation model, *Coastal Engineering*, 56 (10), pp.1043-1060, 2009

[2] Ferziger, J., Perić, M.: Computational Methods for Fluid Dynamics, *Springer*, 2002

[3] Muzaferija, S., Perić, M.: Computation of free surface flows using interface-tracking and interface-capturing methods, *Nonlinear Water Wave Interaction*, Chap. 2, pp.59-100, WIT Press, 1999.

[4] Peric, R.: Internal wave generation and application to bodies in cross-sea, *Master Thesis at Hamburg University of Technology*, November 2013

Local Grid Refinement for Free-Surface Flow Simulations

Peter van der Plas[†] Henri J.L. van der Heiden, Arthur E.P. Veldman, Roel Luppes

University of Groningen, The Netherlands

1 Introduction

In offshore applications, extreme events of wave impact on rigid and floating structures are of high interest. In the past the CFD simulation tool ComFLOW [1, 2] has been successfully used for these applications. For an accurate prediction of wave run-up and wave loading on offshore structures high resolution is only required in the areas of interest, whereas in the far field coarse grids are sufficient. Up to now, further reduction of grid points was only possible by means of grid stretching which typically results in large deformation of grid cells and due to its poor locality is not very efficient. In the ComFLOW-3 project one of the aims is to increase numerical efficiency by introducing local grid refinement.

2 Discretization of the Navier-Stokes equations

An excellent model for incompressible fluid flow is provided by the Navier-Stokes equations, consisting of the continuity equation and the momentum equation

$$\mathcal{M}\mathbf{u} = 0, \tag{1}$$

$$\frac{\partial \mathbf{u}}{\partial t} + \mathcal{C}(\mathbf{u}, \mathbf{u}) + \mathcal{G}p - \mathcal{D}\mathbf{u} = \mathbf{f}, \tag{2}$$

based on the divergence operator $\mathcal{M} = \nabla\cdot$, the convection operator $\mathcal{C}(\mathbf{u}, \mathbf{v}) = \mathbf{u}\cdot\nabla\mathbf{v}$, the pressure gradient operator $\mathcal{G} = \nabla$, the diffusion operator $\mathcal{D}(\mathbf{u}_h) = \nabla\cdot\nabla\mathbf{u}_h$ and forcing term $\mathbf{f}$.

A finite-volume discretization is used in which the continuity equation (1) is discretized at the new time level

$$M\mathbf{u}_h^{n+1} = \mathbf{0} \tag{3}$$

Convection and diffusion are discretized explicitly in time and the pressure gradient is discretized at the new time level. If we denote the diagonal matrix containing the fluid volumes of the momentum cells by Ω, the discretized momentum equation is given by

$$\Omega\frac{\mathbf{u}_h^{n+1} - \mathbf{u}_h^n}{\Delta t} = -C(\mathbf{u}_h^n)\mathbf{u}_h^n + D\mathbf{u}_h^n - G\mathbf{p}_h^{n+1}. \tag{4}$$

Finding the solution to the system of equations (3) and (4) is split in two steps. First an auxiliary variable $\mathbf{u}_h^*$ is defined by the equation

$$\Omega\frac{\mathbf{u}_h^* - \mathbf{u}_h^n}{\Delta t} = -C(\mathbf{u}_h^n)\mathbf{u}_h^n + D\mathbf{u}_h^n. \tag{5}$$

Using this variable in (4) gives

$$\Omega\frac{\mathbf{u}_h^{n+1} - \mathbf{u}_h^*}{\Delta t} = -G\mathbf{p}_h^{n+1}. \tag{6}$$

Substitution of equation (6) in the continuity equation (3), gives rise to the following

$$\Delta t\, M\Omega^{-1}G\mathbf{p}_h^{n+1} = M\mathbf{u}_h^* \tag{7}$$

which is often referred to as the discrete pressure Poisson equation, as it can be viewed as a discretization of the equation $\mathcal{M}\circ\mathcal{G}\mathbf{p} = \mathcal{M}\mathbf{u}$. Note, however, that we are not directly discretizing the composed operator $\mathcal{M}\circ\mathcal{G}$ here,
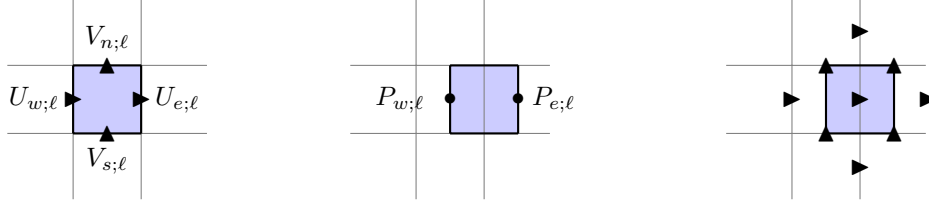
Figure 1: *Left:* Discretization stencil for the divergence in a continuity cell. *Center:* pressure gradient in a U-momentum cell. *Right:* convection and diffusion in a U-momentum cell.

but its separate parts $\mathcal{M}$ and $\mathcal{G}$. Hence, of sole importance is the accuracy of the discretization of the divergence and gradient operators $\mathcal{M}$ and $\mathcal{G}$, respectively. This should be kept in mind when assessing the accuracy of the method.

The Navier–Stokes equations are discretized on an Arakawa C-grid as illustrated in fig. 1. For brevity the third dimension, which is treated similarly, is omitted. The subscript ℓ is used to indicate the local refinement level, where $\ell = 0$ refers to the unrefined base grid.

In the regular parts of the grid the divergence operator is discretized as follows (for the subscript convention consult fig. 1)

$$M\mathbf{u}_h|_\ell = \Delta y_\ell (U_{\mathrm{e};\ell} - U_{\mathrm{w};\ell}) + \Delta x_\ell (V_{\mathrm{n};\ell} - V_{\mathrm{s};\ell}) \tag{8}$$

In order to let the discrete operators satisfy the adjoint condition,

$$G = -M^* \tag{9}$$

the pressure gradient is discretized as $G\mathbf{p}_h = -M^*\mathbf{p}_h$. This gives the following second-order central discretization:

$$(P_{\mathrm{e};\ell} - P_{\mathrm{w};\ell})/\Delta x_\ell \qquad\qquad (P_{\mathrm{n};\ell} - P_{\mathrm{s};\ell})/\Delta y_\ell \tag{10}$$

3   Local grid refinement

A semi-structured approach is followed in which a cell (i, j) at refinement level ℓ is *replaced* by a set of $r_i \times r_j$ smaller cells at refinement level $\ell + 1$, having indices $(r_i\, i + m, r_j\, j + n)$ at offsets $0 \leq m < r_i, 0 \leq n < r_j$. The semi-structured indexing system is illustrated in fig. 2. On block-shaped refinement regions the method is locally structured, hence the computational efficiency of the original array-based solution methods can be exploited as much as possible. Only at the boundaries of the refinement regions where the actual refinement takes place a new treatment is required.
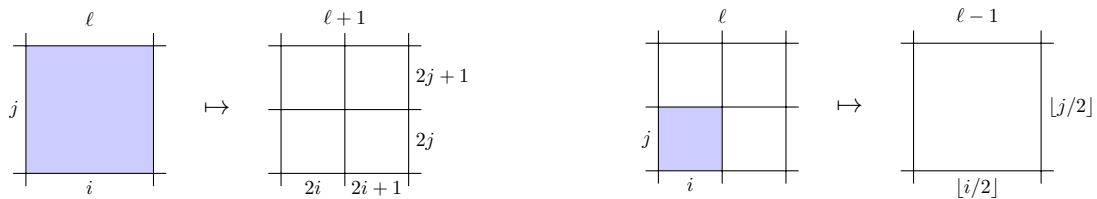
Figure 2: Two-dimensional illustration of semi-structured indexing for refinement ratios $r_i = 2, r_j = 2$. *Left*: From coarse to fine indices. *Right:* From fine to coarse indices.

For describing the grid layout an auxiliary array is introduced storing only one integer for each potentially occuring cell $(i, j; \ell)$ pointing at the memory location of the subgrid in which it is contained (or null if the cell does not exist). Along the lines of [3] a data structure results that allows for fast and efficient look-up when compared with typical tree-based storage methods.

Divergence and gradient near interfaces   Near refinement interfaces the discretization stencil is incomplete due to missing coarse or fine grid variables. Typically, a large stencil is used for the approximation of missing pressure

---

or velocity variables along the refinement interface. Interpolation of missing variables increases the number of non-zero coefficients in the pressure Poisson matrix, which might result in a non-symmetric matrix, putting higher demands on the solver. Most authors use a non-overlapping interface and apply linear (or even higher-order) interpolation for missing variables on the other side of the interface [4]. Another approach is to apply linear interpolation inside an overlapping interface [5]. In all cases the discretization results in a non-symmetric system of equations. In the present approach, a compact discretization scheme is designed, which results in a small and symmetric scheme for the discrete composition of M and G. This makes it possible to employ an efficient linear solver. Furthermore, it facilitates the use of adjacent refinement regions as well as the interface discretization near objects and free-surface boundaries.

There are two ways of organizing the variables at refinement interfaces. One way would be to place refined velocities at the interface and solve the momentum equation for each refined cell face (see fig. 3a). The discrete pressure gradient is different for each cell face. Missing refined pressure values would need to be interpolated which quickly results in large discretization stencils. (Several options have been examined but either resulted in complicated stencils or unstable behaviour.) Another approach, which is followed here, is based on unrefined velocities at the interface (see fig. 3b). The momentum equation is solved only on the coarse cell face and missing refined velocities are approximated by means of interpolation. This approach can be described as "using a constant pressure gradient along a refined cell face" and in some respects is similar to the one used in e.g. [6, 7].

(a) Approach with refined velocities

(b) Approach with coarse velocity (as followed here)

(c) Gradient operator in cell I

(d) Divergence operator in cell I_n
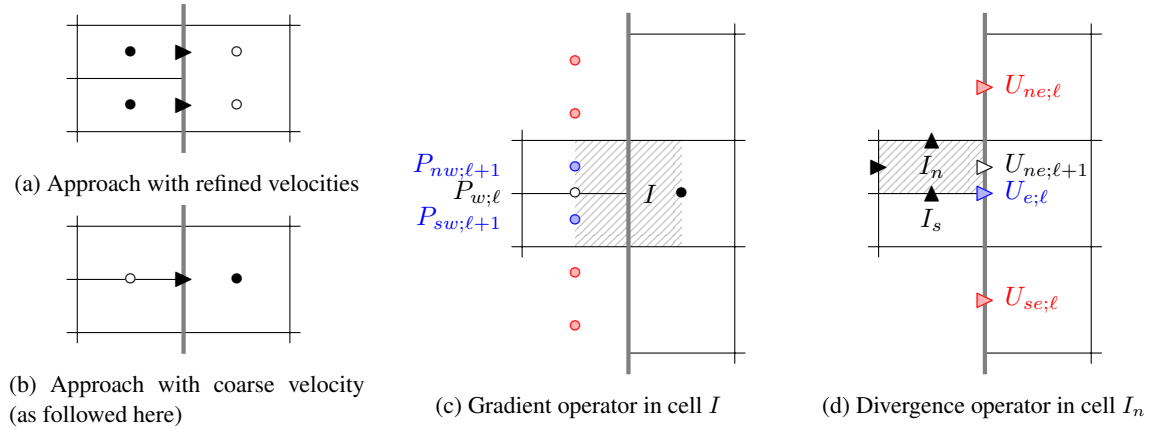
Figure 3: Illustration of the discretization stencils for the refinement approach with *coarse* velocities on the interface. Regular variables: ●, ▶, missing variables: ○, ▷, interpolants (lower order): ○, ▷, interpolants (higher order): ○, ▷.

The starting point for discretization is taken to be the regular central scheme for the divergence and pressure gradient as presented earlier, which from here on we denote by M^C and G^C. At interfaces the stencil is incomplete and an approximation needs to be found for missing variables (in fig. 3, only black variables are available and white variables need to be approximated). As a first step to complete the discretization at the interface, the pressure gradient operator is complemented by a linear approximation of the missing pressure value $P_{w;\ell}$ (using the blue variables in fig. 3c)

$$\overline{G}\mathbf{p}_h\big|_{I;\ell} = \Delta y_\ell \Delta z_\ell \left(P_{nw;\ell+1} + P_{sw;\ell+1}\right)/2 \tag{11}$$

It can be seen that the resulting pressure gradient operator $(G^C + \overline{G})\mathbf{p}_h$ is first-order accurate.

By means of the discrete adjoint condition (9) the completion of the divergence operator needs to satisfy $(M^C + \overline{M})^* \mathbf{u}_h = -(G^C + \overline{G}) \mathbf{u}_h$, which leads to the definition $\overline{M} := -\overline{G}^*$. The correction term $\overline{M}$ comes down to constant (first-order accurate) approximation of the missing mass fluxes $U_{ne;\ell+1}$ (in cell I_n) and $U_{se;\ell+1}$ (in cell I_s). Using a first-order accurate approximation of missing mass fluxes results in an inconsistent discretization of the horizontal velocity derivative and hence an inconsistent scheme for the continuity equation.

By using a linear approximation of the missing mass fluxes, the scheme can be made first-order accurate (hence consistent) again. To do so, a *symmetric* linear correction term is added to the divergence operator

$$\overline{\overline{M}}\mathbf{u}_h\big|_{I_n;\ell+1} = +\Delta y_{\ell+1}\Delta z_{\ell+1}\left(U_{nn;\ell} - U_{ss;\ell}\right)/8, \quad \overline{\overline{M}}\mathbf{u}_h\big|_{I_s;\ell+1} = -\Delta y_{\ell+1}\Delta z_{\ell+1}\left(U_{nn;\ell} - U_{ss;\ell}\right)/8$$

If the adjointness condition is to be satisfied this has also consequences for the gradient operator, because then a correction term needs to be added to the gradient operator as well, satisfying:

$$G^C + \overline{G} + \overline{\overline{G}} = -\left(M^C + \overline{M} + \overline{\overline{M}}\right)^* \tag{12}$$

After including all interpolation terms, the resulting discrete Poisson equation becomes

$$\Delta t \left(M^C + \overline{M} + \overline{\overline{M}} \right) \Omega^{-1} \left(G^C + \overline{G} + \overline{\overline{G}} \right) \mathbf{p}_h^{n+1} = \left(M^C + \overline{M} + \overline{\overline{M}} \right) \mathbf{u}_h^* \tag{13}$$

Because the composition of $\left(M^C + \overline{M} + \overline{\overline{M}} \right)$ and $\left(G^C + \overline{G} + \overline{\overline{G}} \right)$ yields a large number of non-zero coefficients it is beneficial to simplify it. Two observations can help with that. First of all, because the pressure gradient operator $G^C + \overline{G}$ is already first-order accurate (just as $G^C + \overline{G} + \overline{\overline{G}}$), the term $\overline{\overline{G}}$ can be removed without destroying the first-order accuracy. Secondly, one can consider removing the term $\overline{\overline{M}}$ from the left hand side of the Poisson equation. Doing so comes down to discretizing the continuity equation as follows

$$(M^C + \overline{M})\mathbf{u}_h^{n+1} + \overline{\overline{M}}\mathbf{u}_h^*, \tag{14}$$

which by using equation (6) can be rewritten as

$$(M^C + \overline{M})\mathbf{u}_h^{n+1} + \overline{\overline{M}}\mathbf{u}_h^* = (M^C + \overline{M} + \overline{\overline{M}})\mathbf{u}_h^{n+1} + \underbrace{\Delta t \, \overline{\overline{M}} \left[\Omega^{-1} \left(G^C + \overline{G} \right) \mathbf{p}_h^{n+1} \right]}_{} \tag{15}$$

It can be shown that the underlined "cancellation" term comes down to a first-order discretization error and hence does not affect the order of accuracy of the discretized continuity equation (which was already first-order accurate at interfaces). Furthermore, it is symmetric for each set of refined cells so that mass-conservation is ensured.   By dropping the terms $\overline{\overline{G}}$ and $\overline{\overline{M}}$ from the left hand side one ends up with the following Poisson equation,

$$\Delta t \, \left(M^C + \overline{M} \right) \Omega^{-1} \left(G^C + \overline{G} \right) \mathbf{p}_h^{n+1} = \left(M^C + \overline{M} + \overline{\overline{M}} \right) \mathbf{u}_h^*,$$

in which the *implicit* part of the interpolation stencil is reduced significantly (only the black and blue variables in fig. 3) and the Poisson matrix is still symmetric.

We remark that the correction operator $\overline{\overline{M}}$ is similar for other interface orientations. In the three-dimensional case the operator would also include a difference term in the secondary direction tangential to the interface.

4   Numerical results

In order to investigate the performance of the local grid refinement scheme, two-dimensional simulations of flow around a square cylinder have been performed. All simulations at Reynolds numbers 10 and 100 have been performed using a second-order central discretization.

cyl.	grid	L	# pts	C_d
2×4	80×80	0	6k	3.1374
	40×40	1	3k	3.1598
3×6	120×120	0	14k	3.2590
	60×60	1	6k	3.2589
4×8	160×160	0	26k	3.2918
	80×80	1	19k	3.2917
	40×40	2	4k	3.2908
6×12	240×240	0	58k	3.3138
	60×60	2	9k	3.3133
	30×30	3	3k	3.3099
12×24	480×480	0	230k	3.3297
	60×60	3	12k	3.3290
	30×30	4	5k	3.3243
24×48	960×960	0	922k	3.3383
	60×60	4	19k	3.3373
	30×30	5	9k	3.3323
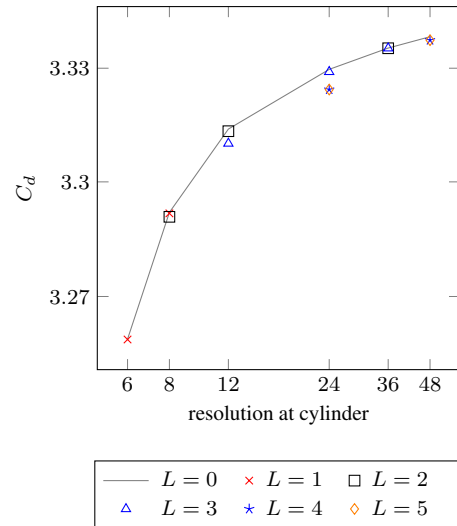
Table 1: Drag-coefficient predictions (C_d) for flow around a square cylinder (Re=10) on uniform, and locally refined grids. The column 'cyl.' displays the grid resolution at the boundary of the cylinder. The column 'grid' shows the resolution of the base grid to which the local grid refinement is applied. In all cases a refinement ratio of 2×2 is used and L indicates the number of local refinement regions. In the column '# pts' the total number of grid points is displayed.

In order to get a good view of the efficiency gain that is obtained with the local grid refinement approach, the analysis is best performed from a "coarsening" point of view. Near the object the grid resolution is kept constant while the grid is coarsened towards the boundaries of the domain.

Flow around a square cylinder   In this 2-D test case a square cylinder is placed of dimensions $[-0.5, 0.5] \times [-0.5, 0.5]$ in a computational domain covering the region $[-10, -10] \times [30, 10]$.

At a Reynolds number of 10 the flow readily converges to a steady-state solution. The resulting solution is smooth and is not expected to pose any difficulties for refinement interfaces. The numerical results presented in table 1 show that the drag-force predictions are accurate even on grids that are very coarse close to the boundaries of the domain. By accepting a 0.5% difference in the prediction of the drag force it is possible to reduce the computational time by up to factor of 100. The resolution of the grid close to the object is of main importance, and it is seen that good convergence behaviour is obtained when increasing the number of cells around the cylinder.

At a Reynolds number of 100 the flow is unsteady, as the flapping shear layer results in an oscillating drag and lift force on the cylinder. This test case clearly provides a more challenging test for the local grid refinement method. A local grid refinement ratio of 3×3 is used and the results of the locally refined grids are compared to their uniform counterparts. The results shown in table 2 illustrate again that the number of grid points can be reduced significantly while useful predictions for the drag and lift coefficients can still be obtained.

cyl.	grid	L	#pts	St	C_d	$C_{l,rms}$
6×12	240×240	0	58k	0.152	1.6275	0.2567
	80×80	1	19k	0.153	1.6273	0.2554
9×18	360×360	0	129k	0.150	1.5687	0.2231
	40×40	2	12k	0.150	1.5687	0.2208
18×36	720×720	0	0.5M	0.150	1.5234	0.2009
	80×80	2	48k	0.150	1.5232	0.1998
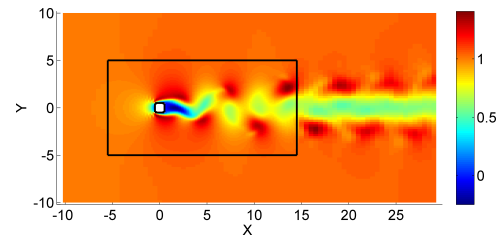
Table 2: Numerical predictions (time-averaged) of the Strouhal number (St), mean drag force C_d, and the root-mean-square of the lift coefficient $C_{l,rms}$ for flow around a square cylinder (Re=100) on uniform and locally refined grids. In all cases a refinement ratio of 3×3 is used. Again, the 'cyl.' denotes the grid resolution around the cylinder, 'grid' the resolution of the base grid, L the number of refinements, and '# pts.' the total number of grid points.

Dambreak experiment   To demonstrate the validity of the local refinement method for more practical cases, it is tested for the simulation of a breaking dam. ComFLOW has been used before for this classical test [1], therefore it provides good material for assessing the performance of the local refinement method.

As starting point a grid is used of $200 \times 36 \times 50$ points. In order to save computational time, the original resolution is only maintained around the block; to the right as well as towards the sides of the domain it is coarsened (as illustrated in fig. 4).
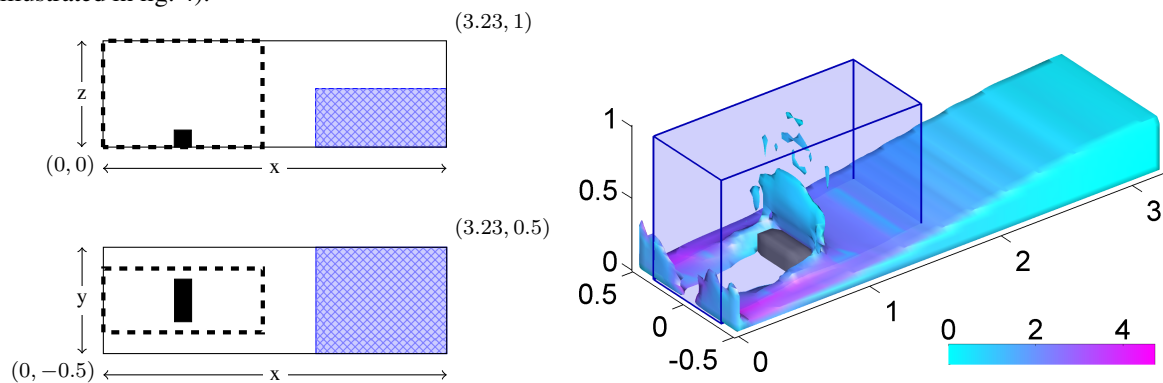
Figure 4: *Left:* Cross sections of the domain illustrating the grid configuration. The original resolution is only kept inside the dashed box. *Right:* Isosurface of the volume fractions colored by the absolute velocity of the free surface.

The simulation results show good correspondence to the measurements and it can be seen that coarsening in the region of the reservoir does not significantly affect the prediction of the impact pressure. The differences between the locally coarsened and uniform grid are much smaller than the actual modelling error while the computational time has been reduced from 8h05 to 0h38. This illustrates that for typical "impact" problems a significant computational saving can be made by coarsening in the far away regions.
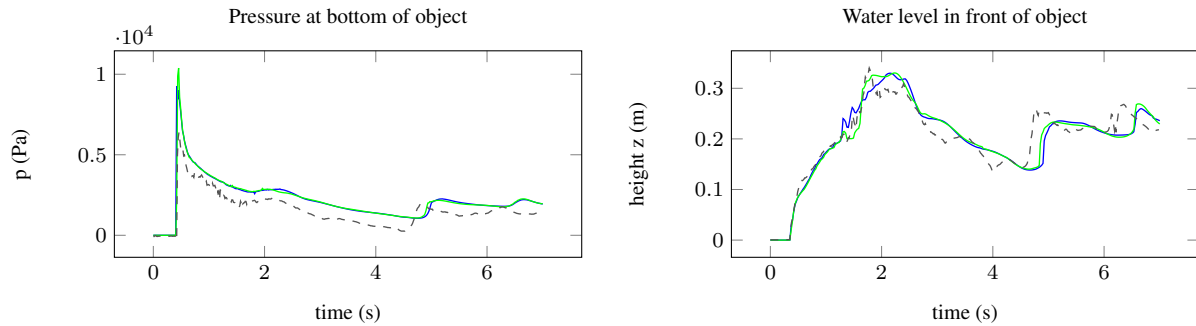
Figure 5: Numerical results and measurements for the 3-D dambreak experiment. *Legend:* —— coarsened grid; —— uniform grid; - - - experiment.

5 Conclusions

In this paper a local grid refinement approach has been presented for the simulation of free-surface flow. Special attention was paid to designing a compact stencil, because the method needs to be accurate and robust in a wide variety of settings. In particular this facilitates the interface discretization near cut-cells and the modification of the Volume-of-Fluid scheme. Furthermore, the compact interface scheme is easily adapted to support refinement corners that occur when concatenating rectangular refinement regions, hence allowing for even more efficient grid configurations.

The local refinement approach has been succesfully applied to the simulation of turbulent flow, wave simulations and (wave) impact problems. Several simulation results were presented to verify and validate the method. In particular for calculating drag forces or (wave) impact forces the reduction of computational costs can be significant. Currently the refinement method is being extended to support two-phase flow and moving objects.

References

[1] K.M.T. Kleefsman et.al. A volume-of-fluid based simulation method for wave impact problems. *Journal of Computational Physics*, 206(1):363–393, 2005.

[2] A.E.P. Veldman et.al. Extreme wave impact on offshore platforms and coastal constructions. *30th Conf. on Ocean, Offshore and Arctic Eng. OMAE2011, Rotterdam, Netherlands, June 19-24*, 2011.

[3] M.D. de Tullio et.al. An immersed boundary method for compressible flows using local grid refinement. *Journal of Computational Physics*, 225(2):2098–2117, 2007.

[4] M.L. Minion. A projection method for locally refined grids. *Journal of Computational Physics*, 127(1):158–178, 1996.

[5] Q. Liu. A stable and accurate projection method on a locally refined staggered mesh. *International Journal for Numerical Methods in Fluids*, 67(1):74–92, 2011.

[6] E. Uzgoren et.al. Computational modeling for multiphase flows with spacecraft application. *Progress in Aerospace Sciences*, 43(4):138–192, 2007.

[7] F. Losasso et.al. Simulating water and smoke with an octree data structure. In *ACM Transactions on Graphics (TOG)*, volume 23, pages 457–462. ACM, 2004.

The Surface Tension Challenge in Air-Water Interfaces
using the Volume-of-Fluid Method

Konstantinos Politis, LHEEA/CNRS, konstantinos.politis@ec-nantes.fr

Patrick Queutey, LHEEA/CNRS, patrick.queutey@ec-nantes.fr

Michel Visonneau, LHEEA/CNRS, michel.visonneau@ec-nantes.fr

The steadily increasing computing power, challenges modern CFD codes to take into account phenomena that are important in smaller scales. Specifically in naval engineering, modeling of spray/foam resistance phenomena or modeling the air-water interface behavior in air-assisted methods for drag reduction (air-cavity method, air-lubrication method), could prove of major importance in the pursuit of a more efficient ship. To this end, surface tension is an important phenomenon for inclusion in the CFD simulations.

In the literature, one comes across a large variety of different surface tension modeling approaches that can be directly coupled with a volume-of-fluid code. Although the performance of surface tension methods is traditionally demonstrated in static bubble test cases with exotic fluids, their numerical behavior is altered when an air-water interface is considered. This is due to large differences in the fluid density and viscosity. The purpose of this work is to demonstrate the numerical difficulties encountered in certain surface tension methods, discuss their strong and weak points in steady and unsteady simulations and propose new alternatives.

We will consider two classic surface tension methods and two methods which enforce the discontinuous nature of surface tension. The classic algorithms are the continuous surface force (CSF) method and the continuous surface stress (CSS) method. The first alternative algorithm is based on the discontinuous field reconstructions proposed by Queutey and

Visonneau (Queutey P., Visonneau M. (2007), An interface capturing method for free-surface hydrodynamic flows, Computer and Fluids). Finally, we propose a new algorithm which is based on geometrically reconstructing the air-water interface. The above algorithms are part of ISIS-CFD, an unstructured URANS-VOF flow solver, distributed commercially by NUMECA as the flow solver of the package FINE™/Marine.

Each of the previous methods is tested in following test cases: (a) the static bubble test case where we calculate the pressure jumps and compare to theoretical values and (b) the rising bubble test case where we calculate the terminal velocities for rising bubbles with radii spanning from R=0.6 mm to R=2 cm and compare with experimental results and numerical results found in previous studies (a small sample of the computations is presented in figures 1 and 2).

Each method's implementation, advantages/disadvantages and performance for the above cases are discussed in detail. The results demonstrate that, if surface tension loses its discontinuous nature, the dynamics of the interface are greatly affected and may result to unphysical behavior. The two proposed methods retain the discontinuous nature of the interface and perform very well in a wide range of relevant length scales to surface tension. Future work will be orientated towards evaluating the effects of surface tensions in flows encountered in naval engineering, using automatic grid refinement to reach small length scales where surface tension could have an important effect.
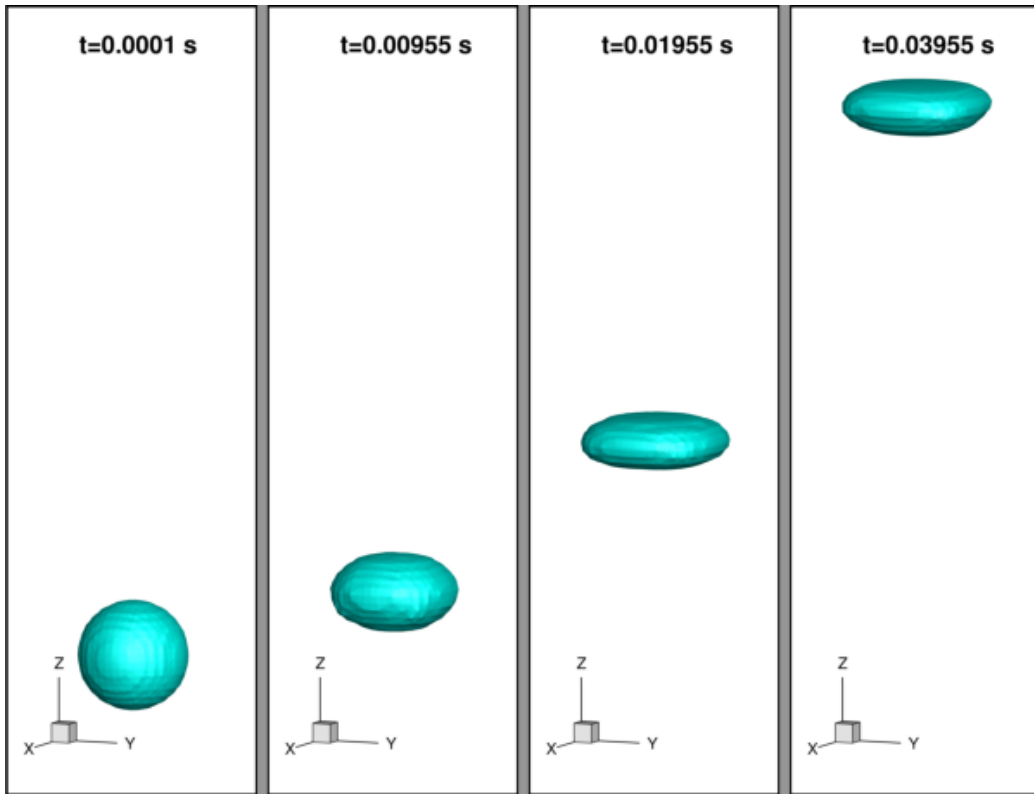
Figure 1.   Air-Water interface evolution for a rising bubble with R = 1 mm
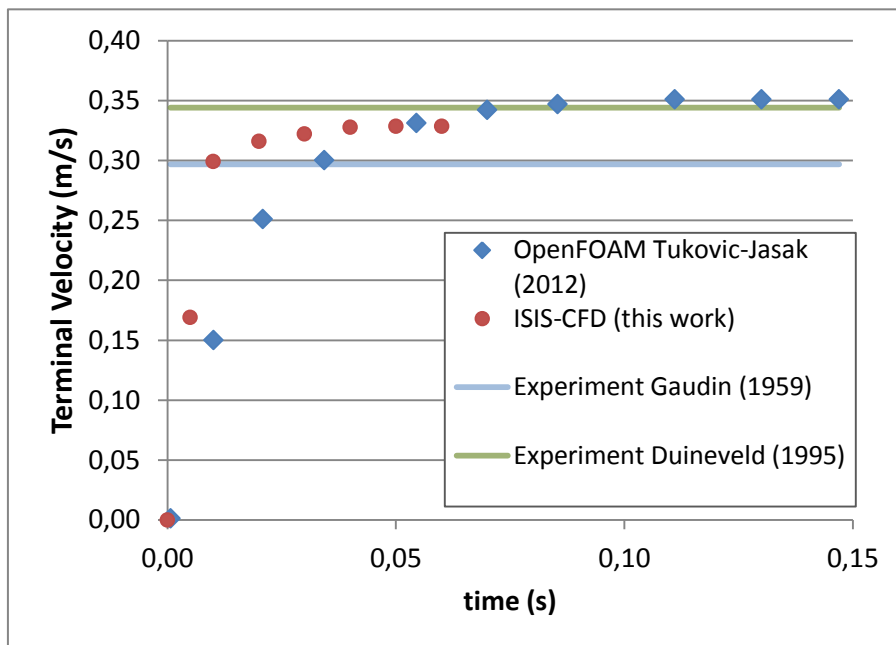
Figure 2.   Comparison of terminal velocity with previously published computations and experimental results.

Numerical Simulation of Tidal Turbines under Real Environmental Conditions

Dr. Dmitriy Ponkratov

Lloyd's Register EMEA, Technical Investigation department,

71 Fenchurch Street, London, EC3M 4BS

Dmitriy.Ponkratov@lr.org

Tidal energy is an attractive renewable resource because of its high predictability and robustness. However, in order to fully utilise such energy, different elements should be taken into account such as: locating turbines only at the sites with sufficiently high tidal resource; the size of the turbines depending on the water depth; the number and layout of turbines at a single site as there are strong interaction effects between them; the type and shape of the seabed as it affects the turbine arrangement and so on.

In comparison with wind turbines where typical layout is rectangular [1], a diamond arrangement is more effective for tidal turbines, as shown in the paper by Malki [2]. This paper shows that the influence of the wake could be quite significant and reach to the free surface. This conclusion is supported by the experimental results presented in the paper by Myers and Bahaj [3].

Waves can have a significant influence on the velocity of tidal flow, as can be seen in the paper by Norris & Droniou [4]. In addition, the importance of modelling the influence of waves on tidal turbines has been presented in the papers by Senat and Madasamy [5] and the paper by Barltrop et al [6].

Lloyd's Register (LR) Technical Investigation Department (TID) offers marine consulting, independent assurance and compliance services to all sectors of the maritime market. Apart from that, the department is actively engaged in different projects together with Lloyd's Register Energy with special emphasis on the tidal and wave sectors. One aspect of research covering the issues with regard to modelling tidal arrays is reported in this paper.

An important conclusion made in [7] that the vast majority of modelling aspects can be successfully simulated with modern Computational Fluid Dynamics (CFD) methods, is confirmed through internal research work within LR.

Current results are built on previous CFD experience Lloyd's Register has in water machinery interaction. For instance TID has worked on wave loading [8] and on water propeller interaction [9].

In the paper by Davies & Radosavljevic [10] Lloyd's Register previously presented a CFD method for modelling tidal turbine arrays using the moving reference frames (MRF) method. This was, however, only a proof of concept. Hence further development was needed, which is also reported in this paper.

The project used a CFD model of a 3x3 array of tidal turbines which had been previously created in STAR-CCM+. The turbine geometry (diameter 17.6m, distance from the axis to the seabed 14m) is presented in Figure 1. The diamond arrangement of the turbine 3x3 array is shown in Figure 2. The mesh sensitivity check had been performed within the previous project and was not included in the current work scope.

The CFD model was first run at a range of flow conditions. In the next stage the new CFD model was modified so that it could accommodate waves. Subsequently two wave conditions of different heights were modelled. These waves were chosen to have a significant impact on the turbine rotor, but not so large as to require the turbine to be shut down. These wave conditions were then combined with the tidal flow conditions already identified.

Figure 1. Tidal turbine geometry
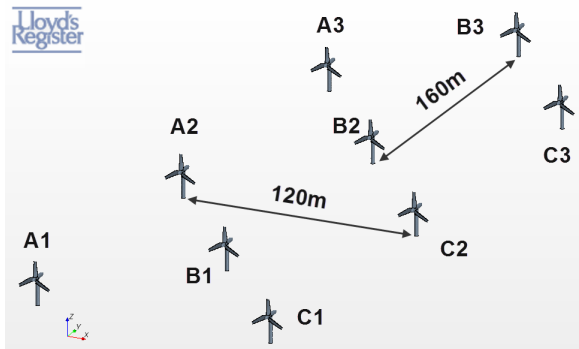
Figure 2. Turbines layout.

The investigations reported here included the following tasks:

1. Simulation of the 3x3 diamond shape array of turbines with different inlet velocity conditions without waves.
2. Simulation of two turbines with different wave conditions.
3. Simulation of the 3x3 diamond shape array of turbines with different wave conditions.

For the first task, the trimmed mesh has been built for the domain 560x540x45m with a fine resolution of turbine geometries. Every rotating part (blades and hub) was encapsulated within a cylinder 10m in diameter. The interface boundary conditions have been implemented on the borders of rotating and static parts. The thickness of the first cell close to the turbine geometry was set up in a way to keep the y+ values in a range from 30 to 800. In addition, an attempt to simulate a high realistic roughness of a

seabed was made for this task: the thickness of the first layer of cells close to the seabed was about 0.5m in order to apply the numerical roughness of 0.4m.

The system of the RANS equations for mass and momentum transfer is closed up with the k-ε Realizable turbulence model. The transport equations of the problem are solved by a segregated solution method with a SIMPLE-type algorithm for pressure-velocity coupling.

A separate issue is related to resolving unsteady simulation of the rotating blades. Similar to marine propeller implementation, it can be resolved using different solution methods such as Moving Reference Frame (MRF), Mixing Plane (MP) and Sliding Mesh (SM) [11]. Of these methods, only the time-accurate SM method provides a completely strict solution to the problem in hand, but it takes a significant amount of computation time. The quasi-steady MRF method and steady MP method can only be considered as approximations of the exact time-accurate solution. Depending on simulation targets these approximations may suffice objective of the study, to a larger or lesser extent.

Only the MRF method was exploited in the present study where just one position of rotor with its key blade at top vertical position (0 degrees) was considered. It should be noted that in tidal turbines modelling there is a principal difference compared to the simulation of a marine propeller: the rotation rate is developed by the flow and this value is initially unknown.

To cope with this uncertainty, an implementation of a quadratic Torque-RPM relationship algorithm which updates the RPM of each turbine until a convergence of the power balance is introduced.

This algorithm is based on the following steps:

1. The initial RPM is guessed (same for all turbines)
2. A quadratic Torque-RPM relationship for the drivetrain is assumed.
3. The simulation for a short time (~100 iterations) is run.
4. A new RPM for each turbine is calculated using:

$$\omega_{new} = \omega_{old} - \alpha(\tau_d - \tau_b) \qquad (1)$$

Where α is a constant/relaxation factor (typically 1e-6)

τ_d is the torque estimated on the drivetrain (from 2.)

τ_b is the torque calculated on the turbine blades.

5. Steps 3 and 4 are repeated until convergence of all the RPMs is reached.

The introduced algorithm showed a good convergence: Figure 3 presents the rotation rate convergence for the task 1: Simulation of the 3x3 diamond shape array of turbines without waves. The peaks show the points where the algorithm was updated.
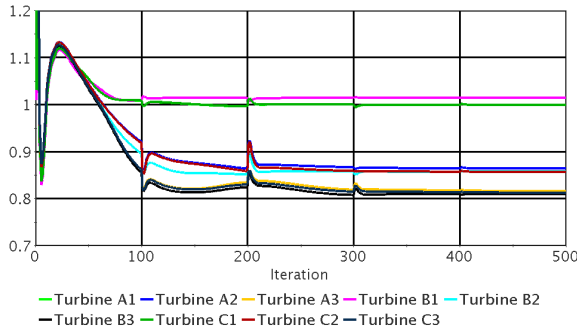
Figure 3. Rotation rate (rad/sec) convergence based on the Torque-RPM algorithm. No waves.

Another principal difference of the tidal turbine investigation compared to marine propellers simulation is the implementation of a sheared tidal flow. Undoubtedly, the vast majority of flow simulations in ship hydromechanics assume a deep water condition where the inlet flow is uniform. An attempt to perform calculations of tidal turbines in realistic environmental conditions with comparably shallow water leads to the implementation of a non-uniform inflow. One of the widely used velocity profiles for tidal currents was proposed by Hardisty [12] and can be described by the following formula:

$$Ud = Um \, (d^{1/\kappa V} / dm^{1/\kappa V}) \qquad (2)$$

Where Ud = mean velocity at depth "d"; Um = mean velocity at depth "dm", and κV Hardisty quotes a typical value of 5.2. However, other sources such as Myers & Bhaj [13] quote a value of 7.

In order to implement formula (2) in the CFD code a User Defined function has been used according to [14]. The validation of this approach was done for a preliminary task where no turbines were simulated in deep water conditions. The assessment of results showed that the inlet velocity profile was kept stable along the whole computational domain if there is no influence of turbines. Obviously, the presence of turbines will change the velocity profile dramatically. Figure 4 shows the velocity distribution in four vertical sections: Inlet, 10m before the first turbine, 10m before the second turbine and 10m before the third turbine.
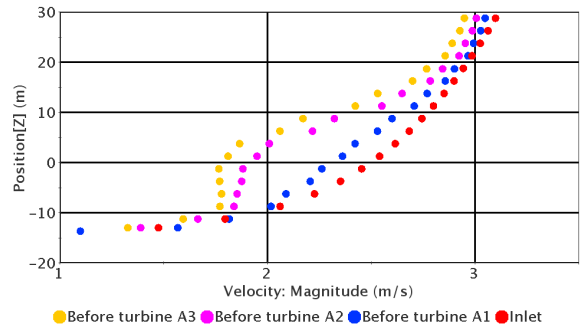
Figure 4. Velocity profiles at vertical sections 10m before each turbine. No waves.

As shown in Figure 4 the velocity profile before the first turbine is changed due to the blockage effect. A developed wake after the first turbine redistributes the velocities in the flow which goes to the second turbine. The final section shows the lowest flow due to a wakes combination from the first and second turbines.
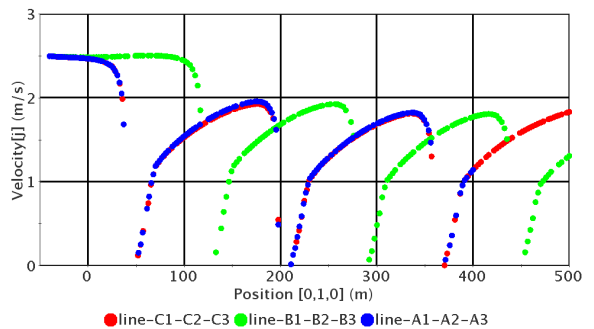
Figure 5. Velocities at hub height through each row of turbines. No waves.

Figure 5 shows a line plot at hub height through each row of turbines showing streamwise velocity as a function of streamwise distance. Here the same wake effect is presented in longitudinal form. It can be noted that the flow decelerates before the first turbine, almost recovers speed before the second turbine and then drops speed again before the third turbine.

A simulation with free surface and especially with waves requires some additional effort. Thus the mesh was rebuilt in order to create a region with a very fine mesh resolution where the waves were expected to be. The following requirements were needed to keep the stable wave propagation: the mesh resolution was 0.1m in vertical direction, 0.5m in longitudinal direction and 1m in transversal direction. This meant that a 3m height wave could be caught within 30 vertical cells. Together with high order wave representation it helped to keep the wave shape almost constant even for the high wave amplitude 3.5m as shown in Figure 6.
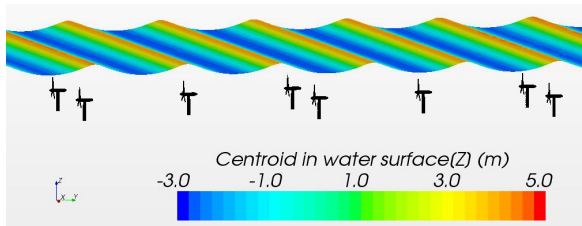
Figure 6. Waves of 7m above the turbines.

Apart from the mesh generation wave simulation requires a very accurate time scheme implementation. Hence the second order discretisation for time was used for these calculations. A time step of 0.0075 sec was set up, taking into a consideration that the wave period was 6 sec. Both the 1st and 5th order waves were implemented for the case with 3m wave height and showed comparable results in terms of revolution rates and torques. However, the implementation of the 1st order wave for the case with 7m wave heights was limited as the waves started to break up. Hence, the calculations for high waves were made mainly with the 5th order scheme implementation.

Another important point to discuss is the Hardisty [12] inlet profile condition together with wave induced velocities. According to wave theory the induced velocities decrease with water depth and it is taken into account by CFD models. However, as it was noted earlier the inlet profile was introduced by implementation of the User Defined Function. As a result, a new function summarising both the inlet velocity profile and wave induced velocities has been developed.

Figure 7 shows the velocity profiles in the vertical sections (same as in Figure 4): Inlet, 10m before the first turbine, 10m before the second turbine and 10m before the third turbine. It is important to note that despite the fact that the wave height is only 3m, the influence from the waves propagates down for about 30m. It can be seen from the figure that velocity profiles become similar below Z=0m. It is also important to note that the wave presence dramatically changes the wake after the turbine. Compared to Figure 4 where the velocity reduction behind the second and third turbines is clearly seen, the profiles in Figure 7 do not show such a reduction.
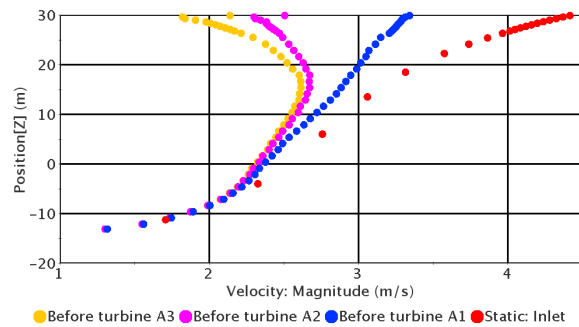
Figure 7. Velocity profiles at vertical sections 10m before each turbine. With waves H=3m, T=6s.

This phenomenon can be seen in Figure 8 where the velocities at hub height through each row of turbines are presented as a function of streamwise distance (same locations as in Figure 5). It can be concluded that even 30m below the water surface there are velocity fluctuations on the turbine axis. As it is an external influence on the whole domain, it recovers the flow behind the turbines quicker compared to the case without the waves. Hence, the velocity profiles before the turbines from the seabed to the turbine axis are in general very similar; however they fluctuate with the time step. It means that the rotation rate (and consequently the power) will be different at every time step.
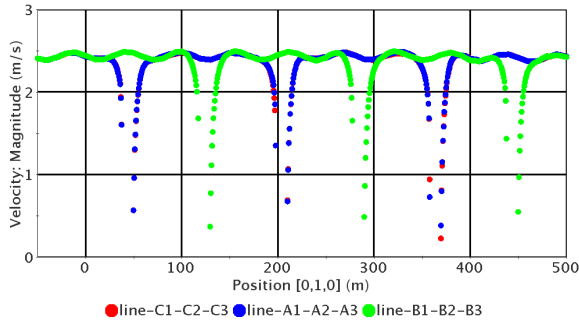
Figure 8. Velocities at hub height through each row of turbines. With waves H=3m, T=6s.

Figure 9 shows the convergence of rotation rates for all turbines. Compared to Figure 3 where the convergence is very stable, it can be noted here that the rotation rates fluctuate with the period about 4.5 sec. The peaks show the points where the Torque-RPM algorithm was updated.
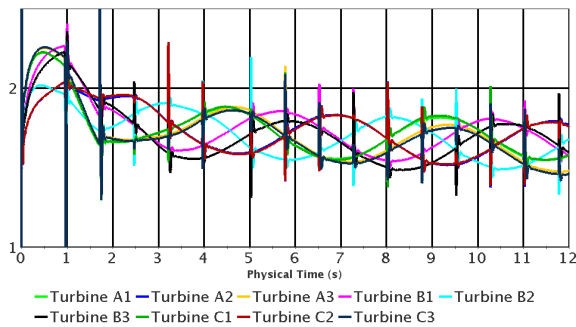
Figure 9. Rotation rate (rad/sec) convergence based on the Torque-RPM algorithm. With waves H=7m, T=6s.

This result closely matches with the investigation performed by Hedges and Lee [15] and proposes using an equivalent current to calculate the modified wave speed and so produces an equivalent wave which would exist in that current. So for the present current conditions a wavelength of 56.2m would produce a 6 sec wave in an equivalent current, and to a stationary observer this would appear to have a period of 4.52 sec.

As a result the power of each turbine for this case will not be a constant value; it will change with the period of 4.52 sec. An example is presented in Figure 10 where the powers of all 9 turbines are collected with the dependence of physical time. The peaks again show the points where the algorithm was updated.
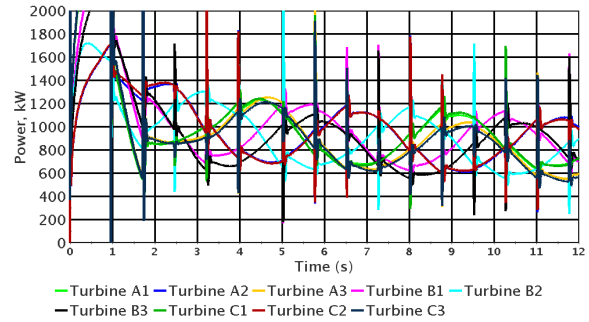
Figure 10. Power of turbines.

The following conclusions can be made:

1. The developed quadratic Torque-RPM relationship algorithm, which updates rotation rates of each turbine until a convergence of the power balance, showed very good convergence both for the case without waves and the case with waves.
2. The numerical implementation of the sheared current velocity profiled described by Hardisty [12] was found to be appropriate. A new velocity profile which takes into accounts both the Hardisty profile [12] and velocities from waves has been introduced.
3. The implementation of the realistic roughness on the sea bed was found to be appropriate for the full scale simulations.
4. The implementation of the 1st and 5th order waves with different combinations of wave heights has been investigated.
5. Results are in line with expectations and some field observations, however it is hoped that more full scale data will become available in the near future in order to validate the developed algorithms.

References.

1. MANWELL, J. F., McGOWAN, J. G., ROGERS, A. L., Wind Energy Explained, 2006 John Wiley & Sons Ltd.
2. MALKI, R., MASTERS, I., WILLIAMS, A.J., CROFT T.N., The Influence of Tidal Stream Turbine Spacing on Performance - European Wave and Tidal Energy Conference 2011.
3. MYERS, L.E. and BAHAJ, A.S., 2010. Experimental analysis of the flow field around horizontal axis tidal turbines by use of scale mesh disk rotor simulators. Ocean Engineering, 37(2-3), pp. 218-227.
4. NORRIS, J.V. and DRONIOU, E., 2007. Update on EMEC activities, resource description, and characterisation of wave-induced velocities in a tidal flow, Proceedings of the 7th European Wave and Tidal Energy Conference 2007.
5. SENAT, J., MADASAMY, A. Simulation and prediction of loads in marine current turbine full-scale rotor blades, Proceedings of the ASME 2011 30th International Conference on Ocean, Offshore and Arctic Engineering, 19-24 June, 2011, Rotterdam.
6. BARLTROP, N, VARYANI, K.S., GRANT, A., CLELLAND, D. and PHAM, X., Wave-current interactions in marine current turbines, Journal Engineering for the Maritime Environment. Vol 220 2006.
7. NICHOLLS-LEE, R.F., TURNOCK, S.R., The use of Computational Fluid Dynamics in the optimisation of marine current turbines, 10th Numerical Towing Tank Symposium, 23-25 April 2007, Hamburg, Germany.
8. CARDEN, E.P., ZEGOS, C., DURLEY-BOOT, N. J., MAGUIRE, J. R., RADOSAVLJEVIC, D., WHITWORTH, S., Modelling of Full Scale Wave Impacts on the Sloshel Mk III Test Panel, Proceedings of the Twenty-first (2011) International Offshore and Polar Engineering Conference Maui, Hawaii, 19-24 June, 2011.
9. RADOSAVLJEVIC, D., WHITWORTH, S. , ZEGOS, C. , Stern challenge – getting it right RINA Conference - Developments in Marine CFD 22-23 March 2011, London.
10. DAVIES, P. G., RADOSAVLJEVIC, D., A review of modelling techniques for tidal turbines, RINA Marine & Offshore Renewable Energy Conference, 26 – 27 September 2012, London.
11. KRASILNIKOV, V., PONKRATOV, D., CREPIER, P, A numerical study on the characteristics of the system propeller and rudder at low speed operation, Second International Symposium on Marine Propulsors, SMP'11, Hamburg, Germany, 2011.
12. HARDISTY, J., 2009. The Analysis of Tidal Stream Power. First Edition ed. Chichester, West Sussex: John Wiley & Sons Ltd.
13. MYERS, L. E., BAHAJ, A. S., Experimental analysis of the flow field around horizontal axis tidal turbines by use of scale mesh disk rotor simulations, Ocean Engineering 2010.
14. STAR-CCM+ v.7.06 User Guide, CD-Adapco.
15. HEDGES, T.S., LEE, B.W., The equivalent uniform current in wave-current computations, Coastal Engineering, 16 (1992), page 301-311.

The Design and Numerical Demonstration of a New Energy Saving Device

Bart Schuiling, b.schuiling@marin.nl

R&D Department, Maritime Research Institute Netherlands (MARIN)

1 Introduction

For more than 30 years Energy Saving Devices (ESDs) have been designed and built to improve the fuel efficiency of ships. Even though the maritime world has always been fascinated by ESDs, with the current challenging world economy, increasing oil prices and the upcoming new EEDI regulations, the interest in ESDs is strongly increasing.

Many papers have been published over the years, introducing new ESD designs, their profits and the working principles responsible for the energy saving. For a good overview of ESDs, see Carlton [1].

The present paper presents results from the ongoing European Project GRIP. In this paper not only a numerical demonstration will be presented, it also discusses the important steps that have been taken in the design process of the ESD and explains the working principle in detail.

2 The Concept Design

The first step in a design process is the identification of the design problem (section 2.1). The second step is the definition of the design function (section 2.2). The design function of a device describes what it must do to solve the problem. From the function follows the actual form of the device (section 2.3). The last step, the evaluation of the performance using CFD, in other words, how well the design fulfils its function, shall be discussed in the results section (section 4).

2.1 The Design Problem

Although the term 'Energy Saving Device' suggest that the main purpose of an ESD is to save energy, this is not completely correct. An ESD is installed on a ship to reduce fuel costs and to be profitable. Therefore, the optimal ESD is the one which has been the most profitable after its lifetime. This may seem self-evident, but is critical for the design of an ESD. The design problem is stated as follows: Design an upstream device which yields a significant power reduction leading to profits exceeding the installation costs.

2.2 The Design Function

The design function of an ESD describes what the device must do to reduce the power demand. In other words, the main working principle of the device that will result in energy saving.

Many possible working principles of ESDs can be found in literature published over the years. For a detailed overview of working principles, refer to Terwisga 2013 [2].

In this paper, an ESD is designed based on re-directing the flow in axial direction as its main function. By observing a propeller in oblique flow, it will be demonstrated that changing the transversal velocity field towards the propeller can lead to an increase of the propeller efficiency.

A propeller in oblique flow can be seen as a simplified case of a propeller in in-behind condition. Many papers have been published describing model tests and computations for a propeller in oblique flow, therefore details of the computations performed for this study shall not be discussed in detail here. However, the effect of the inclined flow on the propeller efficiency and the physical explanation for this will be discussed in this section.

To compare the efficiencies of a propeller for different inclination angles, it is very important to have a solid definition of the reference system and efficiency. The reference system, like model tests are often performed, is shown in Figure 1.
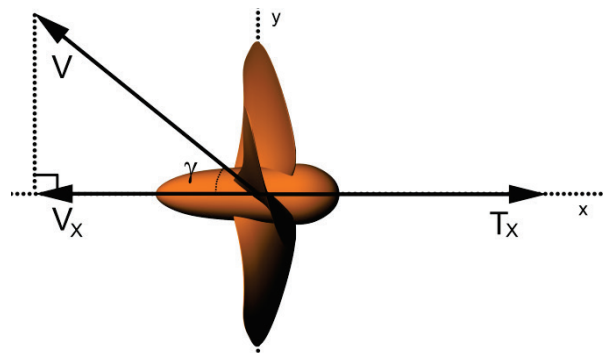
Figure 1: *The Reference Frame for a Propeller in Oblique Flow*

A definition for the efficiency is:

$$\eta = \frac{V_X \cdot T_X}{2\pi \cdot n \cdot Q} \qquad \text{2-1}$$

In this definition, the axial velocity (m/s) is denoted as V_X; T_X is the thrust (N) in axial direction as; n is the rotation rate (rev/s); and the torque (Nm) as Q.

A propeller operating in an oblique flow, will experience a varying blade loading during a revolution. With the presented system of reference in mind, if the flow is directed upwards, the thrust of the downward going blade will increase, while the thrust of the upward going blade will decrease. This effect is illustrated in Figure 2. The axial velocity V_X is constant, the only velocity component varying is the tangential velocity component

V_T. For the upward going blade V_T will be positive, resulting in a smaller angle of attack **α**. For the downward going blade, the V_T is negative, resulting in a larger effective angle of attack.
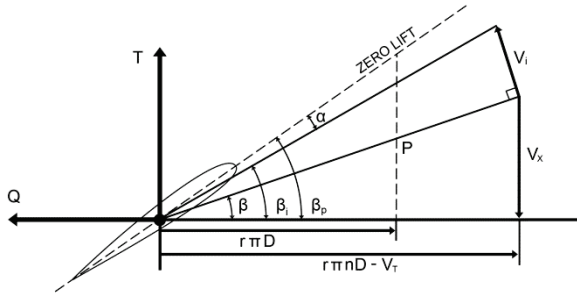
Figure 2: *Velocities and Forces Diagram*

If the induced velocities V_i of a propeller are neglected, the angle of attack α equals the hydrodynamic pitch angle β minus the propeller pitch angle β_p. Since the propeller pitch angle is constant, the change in α is then approximately equal to the change in β, which is defined as follows:

$$\beta = \arctan\left(\frac{V_X}{r\pi nD - V_T}\right) \qquad \textbf{2-2}$$

From this approximation, two conclusions can be derived. First, a change in V_T will have the largest influence on α for the inner radii of the propeller. Therefore, the largest changes in circulation due to variation in V_T can be expected at the inner radii. This will change the radial load distribution of the propeller.
Secondly, the downward going blade will be affected more than the upward going blade. This effect is illustrated in Figure 3, which presents the load variation of a single blade during one revolution for different values of inflow angle γ. The effect of an inclined flow on the propeller efficiency is presented in Figure 4.
The effect of an inflow angle on the efficiency of an open water propeller appears to be small, except for extreme angles. This trend in small but positive efficiency change is confirmed by model test results, published in 1964 by Gutsche [3].
The wrong conclusion can be drawn, that it would not be beneficial to re-direct the flow in axial direction. However, the increase in efficiency for increasing oblique inflow angles results from the choice of the reference frame and the comparison between the different angles for equal constant advance coefficient; this implies that the total velocity goes to infinity when the oblique inflow angle ɣ approaches 90°.
Nevertheless, the overall effect on the propeller efficiency is too small to explain the large differences in power obtained with ESDs in model tank tests [4]. Re-directing the flow with an ESD seems to be a dead end.
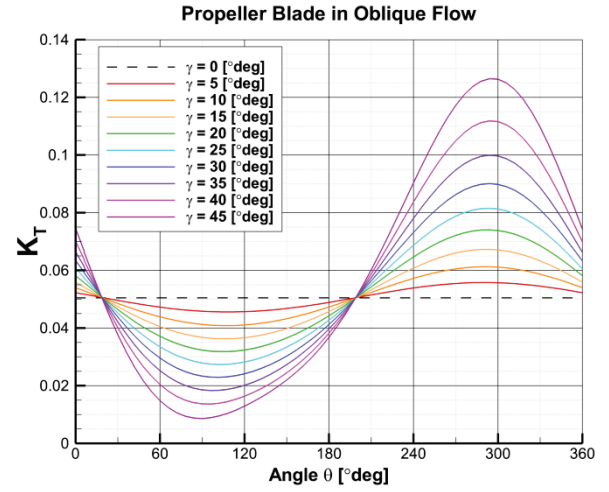
Figure 3: *The Variation in Thrust Coefficient for an Arbitrary Propeller in Oblique Flow for Constant Apparent Advance Coefficient*
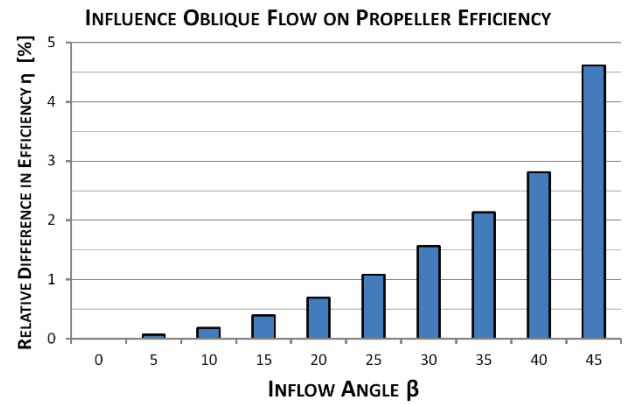
Figure 4: *The change in propeller efficiency as function of inflow angle γ*

However, quite the opposite is true. The explanation why the efficiency of the propeller is hardly affected is actually the key to the energy saving principle. Therefore, instead of observing the total efficiency of the propeller, a new efficiency is defined: the instantaneous propulsion blade efficiency. The definition is presented in equation 2-3.

$$\eta_B = \frac{V_{AVG\_X} \cdot T_{Blade}(\theta)}{2\pi \cdot n \cdot Q_{Blade}(\theta)} \qquad \textbf{2-3}$$

The definition implies, that the blade is observed as an independent system, rotating with a rotation rate n and travelling with a constant velocity V_{AVG_X}. The instantaneous blade efficiency is plotted in Figure 5.
This graph demonstrates that although the total propeller efficiency is hardly affected by the oblique inflow, the local blade efficiency variation is very high. Because the gain and loss in efficiency almost cancel, the total propeller efficiency stays nearly constant.
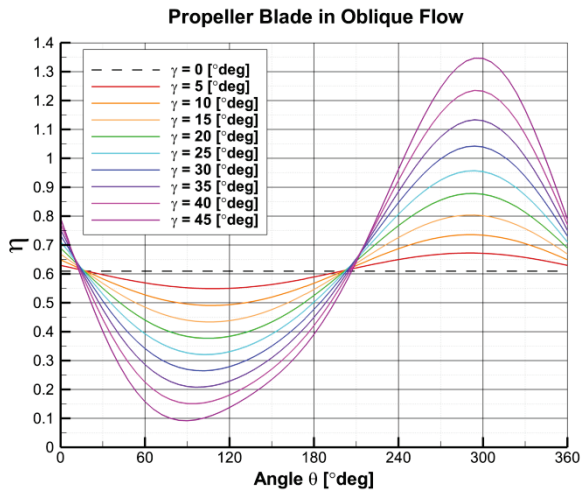
Figure 5: *The Variation in Blade Efficiency for an Arbitrary Propeller in Oblique Flow for Constant Apparent Advance Coefficient*

The gain in efficiency originates from a more favourable orientation of the lift vector of the section of a blade. This results in a larger increase of the thrust than the increase in torque.

Figure 5 reveals what an ESD must do in order to increase the propeller efficiency. If an ESD can influence the flow towards the propeller in the range θ=0...180, preventing the efficiency from decreasing, a higher propeller efficiency can be obtained.

An axi-symmetric ESD would increase the efficiency in one region of the propeller, while decreasing it in the other, resulting in no change, or even a decrease, in propeller efficiency. This suggests that an ESD with as function to increase propeller efficiency must be asymmetrical.

That an asymmetrical ESD is more effective was already discovered by Schneekluth [5]. He stated that an important parameter for the effectiveness of a WED is the axial inclination of both half ring ducts, which is to be set at different angles for both sides.

Generating pre-swirl is not the only important aspect which determines the effectiveness of an ESD. Influencing the flow towards the propeller can result in a higher total resistance. This is a negative effect which will result in an energy loss.

To conclude this section, the function of the ESD is presented in Figure 6.
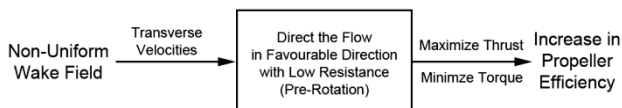
Figure 6: *The Function for the ESD*

2.3   The Design Form

The function of the ESD determines the form and the form enables the function. As the function of the ESD is defined, the shape of the ESD can be explained.

According to the hypothesis, the most promising ESD to fulfil the design function is asymmetrical and generates pre-rotation. This effect could be obtained by re-directing the flow in axial direction with an asymmetric pre-duct or by generating pre-swirl with

pre-stators. Although the forms are different, the actual function of both methods is the same. The concept ESD presented in this paper, called the BSD, is effectively a combination of a semi-duct and pre-stator.

A schematic drawing of the BSD can be found in Figure 7. As can be seen, the camber is varying along the chord of the BSD. Both sections B-B and D-D must bend the flow in axial direction and to do this effectively, the camber changes of sign in section C-C. This is also convenient for the stators, because A-A and E-E have to generate pre-swirl in equal tangential direction. The horizontal stator is somewhat smaller than the other stators, to fit nicely within the duct. To have a correct alignment with the flow, the pitch of the duct is varying from section B to section D.

The position of the BSD with respect to the propeller is chosen based on the possible gain in blade efficiency; in the rest of the propeller disc the blade efficiency is already relatively high. It is also less optimal to generate pre-swirl on starboard side for a right handed propeller, due to the orientation the total force vector on the pre-stator blade, resulting in a high resistance penalty.

The upper stator is not positioned vertically, because then it would be located in the wake peak, reducing the capability to generate pre-swirl. The lower stator is not positioned vertically due to an unfavourable interaction with the hull, resulting in a large pressure resistance increase.

The BSD is positioned concentric with the propeller shaft and the chosen diameter is approximately equal to the propeller diameter. A 3D rendering of the BSD can be seen in Figure 8.
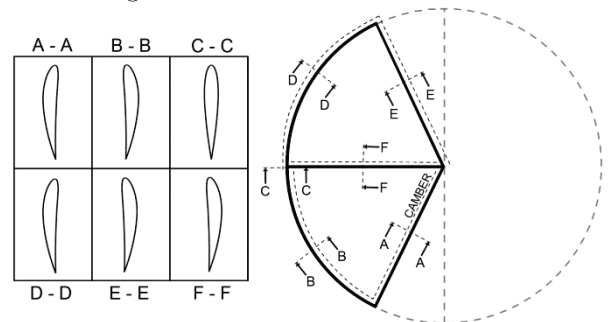
Figure 7: *Schematic View of the Camber Distribution of the BSD seen from Behind for a Right Handed Propeller*
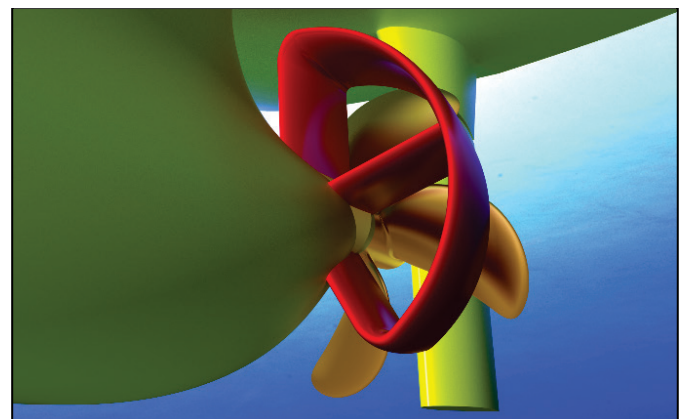
Figure 8: *A 3D rendering of the BSD*

3 Numerical Demonstration

3.1 Test-Case

To demonstrate the possible reduction in power with the BSD, a model scale design has been made for the single screw chemical tanker used in the European Project STREAMLINE. For the ship and propeller particulars, and the operations conditions, refer to Queutey [6].

3.2 The RANS Solver and Important Settings

The RANS solver used in this study is the MARIN in-house developed CFD code ReFRESCO. ReFRESCO solves the multiphase unsteady incompressible RANS (Reynolds Averaged Navier Stokes) equations, which are discretised using a finite volume approach with cell-centred collocated variables. The code is developed, optimized and validated exclusively for maritime applications [7].

Using the 'Sliding Interface' (SI) technique, recently implemented in ReFRESCO, both the ship and propeller are fully modelled in the RANS calculations. The first computation is performed time independent, often referred to as a 'Frozen Rotor' (FR) approach. The computation time is relatively low, the solution can be used as first analysis for the performance of the ESD. Subsequently, the acquired computational solution is used as start-up for the fully unsteady RANS calculation with a rotating propeller. The time step used in the SI simulations corresponds to the propeller turning 2 degrees.

The absolute differences are large between the FR and the SI calculations, but fortunately the best performing configuration using FR, seems also to be the best using SI. This makes designing an ESD a lot less time and CPU expensive.

The turbulence model used for all simulations is Menter k-ω SST version from 2003 [8] and the boundary layer is fully resolved. The second-order Quadratic Upwind Interpolation for Convective Kinetics (QUICK) is used for the convection term discretization [9]. The second-order Backward Differencing scheme (BDF) is used for the implicit time integration [10].

3.3 The Computational Domain and Boundary Conditions

To model the viscous interaction between the ship and propeller as complete as possible, both are fully modelled in the RANS calculations. This is done by generating two grids; a large unstructured grid containing the complete ship and BSD made with the grid generation software HEXPRESS [11] and a small structured grid for the propeller created with GridPro [12]. The grid characteristics are presented in Table 1 and Figure 9 gives an indication of the grid density.

Since computation times for unsteady simulations can become high, the used grids are relatively coarse. Consequently, the solution may not be grid independent. Nevertheless, since the structured propeller

grid is identical with and without BSD, and the unstructured grid is kept as similar as possible for both configurations, the relative numerical errors will be small.

Table 1: *Grid Characteristics*

	# Elements	# Surface Elements	Max y^+
GRID1 Ship	**14.3E6**	-	-
Ship	-	1.2E5	0.41
ESD	-	7.8E4	0.63
Rudder	-	3.4E4	0.82
Headbox	-	2.0E5	0.59
GRID2 Propeller	**1.8E6**	-	-
One Blade	-	1.0E4	0.31
Hub	-	2.1E4	0.38

The main function of the BSD depends on the transverse wake velocities. The influence of the ship's generated waves on the transverse velocities is large for the STREAMLINE Tanker and therefore included in the simulations. For the sake of simplicity and accuracy, the wavy surface is calculated with a different in-house RANS code called PARNASSOS [13] and subsequently simulated as a fixed surface in the ReFRESCO simulations. As a consequence, a possible interaction between the free surface and the BSD is not included in the simulation.

At the inflow boundary of the ship domain, uniform constant velocity is prescribed. At the outflow boundary an outflow condition is applied, stated the gradient of the velocity must be equal to zero. At the far fields a constant pressure is set. For the ship, pre-duct and propeller a no-slip boundary condition is used, without using wall functions. At the fixed wavy surface, a free-slip boundary condition is applied. As initial condition, the flow velocity is in the domain equal to the inflow velocity.
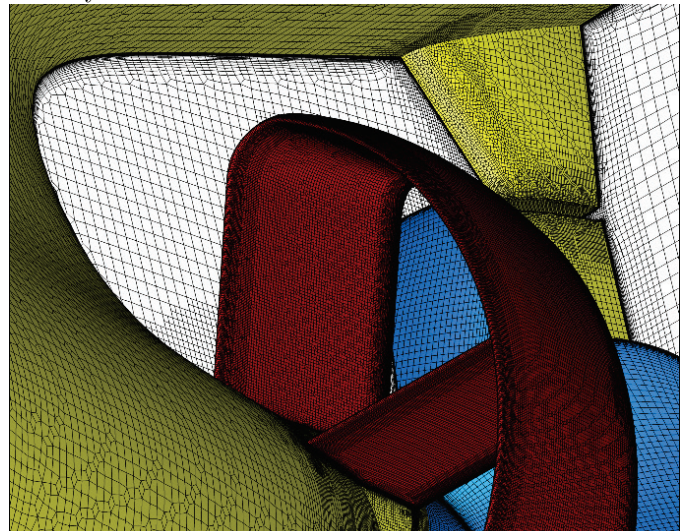
Figure 9: *An illustrative view of the grid including the BSD*

4 Results

In this section we evaluate the performance results of the BSD obtained with the unsteady RANS simulations using SI. Table 2 summarises the important propulsion results for STREAMLINE Tanker equipped with and without BSD. The results for the STREAMLINE Tanker without BSD correspond quite well with the results obtained by Queutey [6].

Table 2: *The Propulsion Prediction*

Propeller Performance		No-BSD	BSD	Difference [%]
Model Speed	m/s	1.773	1.773	0.0
Thrust	N	56.72	57.60	+1.6
Torque	N	2.24	2.234	0.0
Rot. Rate	rps	9.062	8.720	-3.8
Prop. Efficiency	-	0.79	0.83	+5.5
Power	**W**	**127.3**	**122.5**	**-3.8**

As can be seen in Table 2, the required power reduces with 3.8% for the STREAMLINE Tanker equipped with the BSD. The magnitude of the power reduction is comparable to values published for comparable ESDs.

As discussed previously, the energy saving originates from a higher propeller efficiency. The propeller efficiency in Table 2 is defined as in 2-1, where V_X is equal to the model speed V_M. The output of a propeller is the delivered thrust at a certain ship speed divided by the delivered hydrodynamic power.

This efficiency definition differs from the conventional in-behind propeller efficiency. The choice for a new propeller efficiency is justified as follows. Using the classical approach for a pre-swirl device, by determining the propulsion efficiency with the BSD considered to be part of the propulsion system, would lead to confusing efficiency changes. Since the thrust increases and the rotation rate decreases, the well-known thrust coefficient K_T increases. Subsequently, the effective Taylor wake fraction would increase with a BSD. This is rather strange, since the BSD hardly affects the axial wake velocities. A higher wake fraction implies a lower open water propeller efficiency. Since the rotation rate decreases, while the torque stays constant, also the relative rotative efficiency decreases. On the other hand, the hull efficiency increases significantly, implying that the BSD improves the propeller hull interaction. This does not contribute to the understanding of the working principle of the BSD and may explain why there had always been so many questions left unanswered regarding the working principles of ESDs.

The higher propeller efficiency implies that the BSD enables the propeller to generate more efficiently thrust. This is illustrated by plotting the ratio of thrust over torque, see Figure 10.

The ratio of thrust over torque becomes significantly higher in the section $\theta = [0..180]$, which results in a higher propeller efficiency. The propeller blade can generate more efficiently thrust, due to a more favourable lift over drag, as presented in Figure 2, and

an improvement of the radial loading distribution, see Figure 11. As derived in the section 2.2, the inner radii are effected more by the BSD than the outer radii.
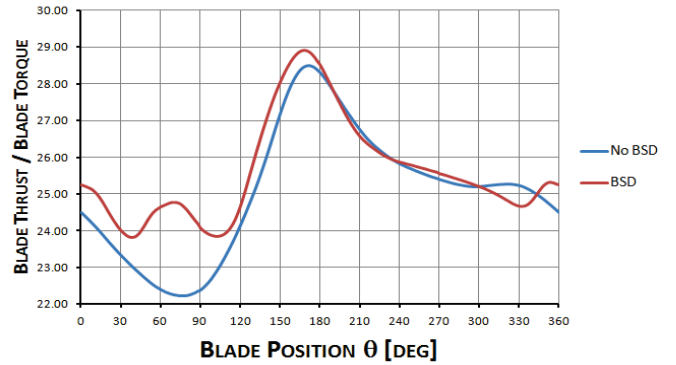
Figure 10: *Comparison in the ratio of Thrust over Torque for a single Blade during one revolution.*
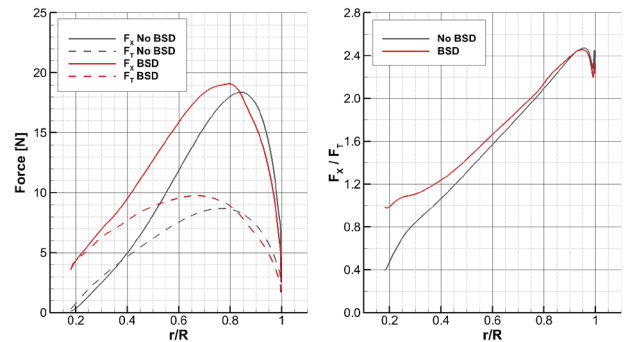
Figure 11: *The Radial Loading Distribution of a Propeller Blade at $\theta = 45°$*

Due to the more favourable thrust over torque ratio, the rotation rate of the propeller can decrease with 3.8%. Otherwise the propeller would generate almost 12% too much thrust. The power reduction is equal to the rotation rate reduction, since there is no difference in torque for both configurations in self-propulsion.

As mentioned earlier, it is highly likely an increase in propeller efficiency comes with a penalty in the form of an increase in resistance; in this case the propeller has to generate 1.6% more thrust. Table 3 gives a detailed summary of the changes in the forces acting on the different components.

Table 3: *An overview of the forces*

Forces	No-BSD [N]	BSD [N]	Percentage of Thrust [%]
Ship	-67.37	-68.35	-1.68
Rudder	-1.64	-2.23	-1.03
Head Box	0.32	0.42	+0.26
Hub	-0.32	0.15	+0.96
BSD	-	0.07	+0.11
Total	**-69.01**	**-69.92**	**-1.60**

The total force acting on the BSD is practically zero. However, the increase in resistance of the ship is rather large with 1.68%, as a percentage of the total thrust. The explanation is rather simple; by generating pre-swirl, the flow accelerates flow near the hull, decreasing locally the pressure on the ship hull, resulting in a higher pressure resistance.

Furthermore, the rudder resistance increases with 1%, which is not completely unexpected. It is commonly known that the rudder acts as a post-stator and by generating pre-swirl, the performance of the rudder as post-stator can be severely reduced.

An unforeseen positive effect occurs at the hub. The pressure recovery at the hub improves, resulting in a lower pressure resistance. This phenomenon is interesting, since the circulation at the inner radii increases, which should lead to a stronger hub vortex, combined with a lower pressure at the hub. The opposite appears to be true. Further research is needed here.

Overall, by equipping the STREAMLINE Tanker with the BSD, the total resistance increases with 1.6%. However, this loss factor is well compensated by the increase in propeller efficiency, resulting in a power reduction.

5 Conclusions

In this paper the working principle and design of a novel ESD concept design, the BSD, is presented. By redirecting the flow in axial direction, the propeller efficiency increases at the cost of a small increase in resistance. The obtained power reduction with the BSD for the STREAMLINE Tanker at model scale is according to CFD simulations 3.8%. Further research is needed to determine whether an even higher power reduction can be realised. If the BSD is still as effective on full scale must still be investigated.

The working principle of the BSD is demonstrated on the basis of a propeller in oblique flow. The transverse velocities have a large influence on the local instantaneous blade efficiency. By redirecting the unfavourable transverse flow into axial direction, a propeller efficiency gain can be obtained.

Besides reducing power demand, also the maximum thrust loading and variation is reduced. This can have a positive effect on the cavitation behaviour of the propeller and subsequently vibration problems.

It is important to note that the presented BSD is only a prototype, designed to proof the working principle presented in this paper. Manufacturability was left out of the scope of this study. Also the propeller correction, needed to correct back to the original propeller demand curve, was left out of this study.

The insight in how the propeller efficiency can be influenced and evaluated, can possibly lead to more effective ESDs than the one presented in this paper.

6 Acknowledgements

7 References

[1] J. Carlton, Marin Propellers and Propulsion Third Edition, Oxford: Butterworth-Heinemann, 2012.

[2] T. Terwisga, „On the Working Principles of Energy Saving Devices," in *Third International Symposium on Marin Propulsors (SMP '13)*, Launceston, Tasmania, Australia, 2013.

[3] F. Gutsche, „Untersuchung von Schiffsschrauben in schräger Anströmung," *Schiffbauforschung,* vol. 3, pp. 97-122, 1964.

[4] J. Dang, „An Exploratory Study on the Working Principles of Energy Saving Devices (ESDs) - PIV, CFD Investigations and ESD Design Guidelines," in *OMAE*, Rio de Janeiro, 2012.

[5] H. Schneekluth, „Wake Equalizing Ducts," *The Naval Architect,* 1986.

[6] P. Queutey, G. B. Deng, E. Guilmineau en F. Salvatore, „A Comparison Between Full RANSE And Coupled RANSE-BEM Approaches in SHip Propulsion Performance," in *OMAE2013*, Nantes, 2013.

[7] D. Rijpkema en G. Vaz, „Viscous Flow Computations on Propulsors: Verification, Validation and Scale Effects," in *RINA*, 2011.

[8] F. Menter, M. Kuntz en R. Langtry, „Ten Years of Industrial Experience with the SST Turbulence Model," *Turbulence, Heat and Mass Transfer,* vol. 4, 2003.

[9] B. Leonard, „A Stable and Accurate Convective Modelling Procedure Based on Quadratic Upstream Interpolation," *Computerl Methods in Applied Mechanical and Engineering,* vol. 19, pp. 59-98, 1979.

[10] J. Ferziger en M. Peric, Computational Methods for Fluid Dynamics, New York: Springer, 2002.

[11] „Numeca HEXPRESS," June 2013. [Online]. Available: www.numeca.be.

[12] „GridPro," June 2013. [Online]. Available: www.gridpro.com.

[13] B. Starke, A. v. d. Ploeg en H. Raven, „Viscous Free Surface Flow Computatuions for Self-Propulsion Conditions using Parnassos," in *A Workshop on CFD in Ship Hydrodynamics*, Gothenburg, 2010.

Application of OpenFOAM® to Prediction of Ship Squat in Restricted Waterways

I. Shevchuk* and N. Kornev

Chair for Modelling and Simulation, University of Rostock, 18057 Rostock, Germany

INTRODUCTION   Prediction of ship squat is a well known problem in ship hydrome-chanics. According to Bernoulli's law, acceleration of water in a return flow of a moving ship causes the pressure drop on the hull and this results in a suction force and mo-ment which make a vessel sink and trim. By definition, squat is an overall reduction of under-keel clearance caused by described above effect.

Change of a ship draught caused by hydrodynamic effects is observed both in deep and shallow waterways (confined and unrestricted). However, for deep water this effect is usually not of a high significance, since it is less pronounced and can not lead to groundings [1]. In fairways with depth restriction the described effect is strongly intensified, while the effective cross-section of a channel decreases. Satisfying the continuity equation, velocity should increase in order to keep the same flow rate through the smaller cross-section. Under such circumstances, the excessive squat can cause groundings. There are numerous methods presented in literature, which allow for prediction of this effect with different levels of accuracy and different computational demands [2, 7]. In restricted waterways ship squat is always considered for safety reasons.

The current research is additionally triggered by another reasons. As it is known, the restriction of depth intensifies the unsteady effects in the ship wake. One of these effects, which indicates the proximity of the bottom, is the strong ship stern vibration [1]. Preceding simulations, carried out by LeMoS group [6], showed that the intensity of vortex structures in the wake of a full-bottomed ship highly depends on the keel clearance. Strong vortex structures sufficiently change the axial velocity field at propeller plane. The oscillations of axial velocity in turn induce the periodic forces on propeller and may lead to vibration. Thus, in order to gain the proper insight into unsteady effects, taking place in the stern of ships with high blockage coefficients, the accurate prediction of under-keel clearance(UKC) should be obtained.

Previous analysis of unsteady effects in shallow water was performed in one-phase for-mulation using pisoFoam solver from OpenFOAM CFD toolkit [6]. In that work doubled body approach was used, which is not suitable for UKC prediction. Moreover, in one-phase flow the influence of wave pattern on unsteady structures in a wake is not accounted for, even though it can be significant due to strong separations [9]. Thus, such problems should be generally solved in two-phase formulation with simultaneous calculation of ship squat effect and this means that the interFoam family solvers should be utilized.

---

*ivan.shevchuk@uni-rostock.de

Modeling of free-surface ship flows in deep water using OpenFOAM has been widely carried out. Some works were aimed at modeling of ship resistance, some of them at estimating of ship seakeeping qualities [3], [5], [8]. Research on dynamic trim and sinkage prediction has also been conducted by LeMoS group and the results were presented at 15th Numerical Towing Tank Symposium. However, results of OpenFOAM application to shallow water ship flows have not been presented in literature.

It is known, that the restriction of depth leads to elongation of waves and to the widening of a wave pattern [4]. In computational sense this means that the domain should be enlarged in order to avoid the influence of the truncation boundaries on the solution. In order to test OpenFOAM capabilities for such simulations and to find the proper computation methodology, the following test case was used.

(a)   (b)
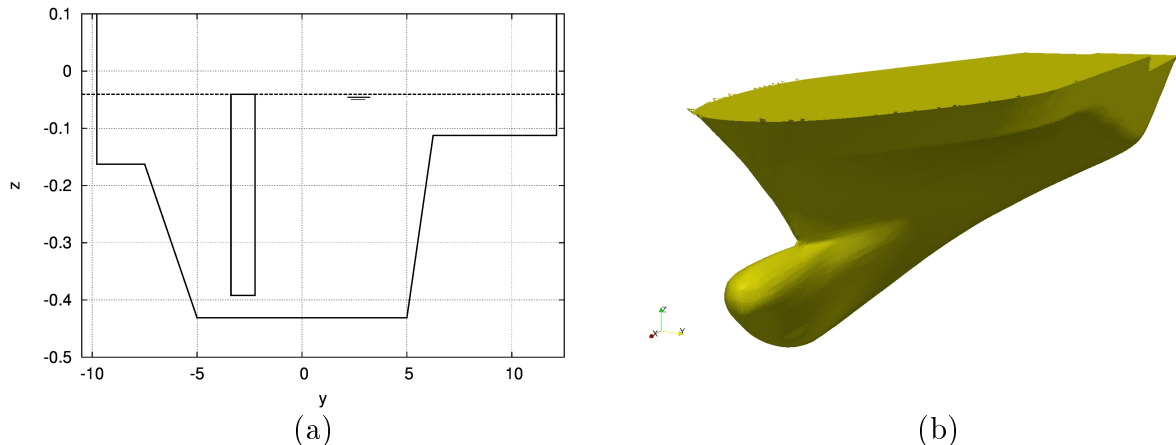
Figure 1: (a) channel cross section, rectangle shows the ship position in the channel, (b) PPM46 bow

TEST CASE The only accessible data for validation were the model tests for PPM46 post-panamax container ship, carried out by BAW (Federal Waterways Engineering and Research Institute) Hamburg at a scale 1:40. In the table 1 one can see the parameters of the mentioned vessel. Measurements of trim and sinkage were performed for 9 speeds, corresponding to depth Froude numbers from 0.256 to 0.51. Six of these regimes were chosen for the test case. The conditions considered in simulations are summarized in table 2. The experiment was carried out for complicated channel geometry, which had different cross-sections along the model path [7]. For the sake of simplicity the averaged cross-section with simplified banks was considered in the simulation (see fig. 1,a). Cross section area was kept constant. It is believed, that the slight change of channel geometry away from the ship would not cause a significant discrepancy in squat prediction.

Unfortunately, this validation case is restricted to subcritical flow regimes occurring at $Fn_H < 1$.

NUMERICAL METHOD AND SETUP In the present work the local-time stepping quasi steady state two-phase URANS solvers LTSInterFoam and LTSInterDyMFoam were used because of their relatively low computational demands compared to fully unsteady interFoam and interDyMFoam. Within these solvers the time-step field is calculated depending on a local Courant number in each cell. In order to avoid instability due to conservation errors time-step field is smoothed. Even though this approach violates

Table 1: PPM46 main characteristics		
	Full scale	Model scale
T_{fp} [m]	13.80	0.35
T_{ap} [m]	13.80	0.35
B_{wl} [m]	46.00	1.15
L_{oa} [m]	352.40	8.81
L_{pp} [m]	331.43	8.29
V [m^3]	121166.60	1.89

Table 2: Considered conditions			
Case No.	Speed [m/s]	Fn_H [-]	Fn [-]
1	0.51	0.257	0.056
2	0.55	0.280	0.061
3	0.66	0.336	0.073
4	0.81	0.414	0.090
5	0.97	0.497	0.108
6	1.00	0.510	0.111

the conservation laws (in the same way, like under-relaxation does), it allows for faster convergence to steady state and thus provides comparably fast solution.

LTSInterFoam is a standard solver of OpenFOAM. LTSInterDyMFoam, used for modeling of ship motion, was taken from Voith Advanced Propulsion extensions library and updated for the latest OpenFOAM 2.1.x revision from git repository. Initial version of steady-state boundary conditions for displacement of the points on the ship patch, allowing for 2DoF ship motion were also borrowed from the mentioned library and slightly modified.

Solution technique was as follows. First, the convergence of forces and the wave pattern was obtained for a fixed ship using LTSInterFoam, then the ship motion was considered in LTSInterDyMFoam.

Meshes for the simulation(3-3.5 mln cells) were generated using Hexpress®. Length of the computational domain was equal to $9L_{pp}$: $4L_{pp}$ in front of the ship and $4L_{pp}$ behind the ship. The height of the cells at free surface was 2mm. Cells at the inlet and at the outlet of the computational domain were stretched in longitudinal direction in order to damp the wave reflection from the boundaries. The y$^+$ value at the ship patch was about 30 in order to apply $k - \omega$ SST model with wall functions. Grading of boundary layer cells was 1.3.

Boundary conditions, applied to dynamic pressure ($p - \rho g h$) and velocity are summarized in table 3. Velocity at the sides, bottom and inlet was set equal to the ship speed. No wall functions were utilized at the bottom patch.

Table 3: Boundary conditions for dynamic pressure and velocity

Patch	p_rgh	U
bottom	fixedFluxPressure	fixedValue
atmosphere	zeroGradient	zeroGradient
sides	fixedFluxPressure	fixedValue
inlet	fixedFluxPressure	fixedValue
outlet	fixedValue 0	zeroGradient
slip	zeroGradient	no-slip / movingWallVelocity

Mesh motion was performed using velocity laplacian and displacement laplacian morphing algorithms. Since the maximum trim angles were no higher than 0.2° the mentioned techniques worked well. However, at high speeds the excessive decrease of UKC caused problems with mesh deformation, because the built-in algorithms for mesh motion diffusivity calculation caused appearance of negative volume cells. In order to solve this

problem, a new type of mesh diffusivity scheme was implemented as well as the diffusivity freezing algorithm. These improvements allowed for flexible treatment of mesh deformation problems.

RESULTS AND ANALYSIS   In the figure 2 one can see the convergence history for case No. 3. Plots for other cases are omitted for the sake of space-saving. Relaxation factors were applied to the forces and moments in order to achieve monotonic behavior of sinkage and trim. Monotonicity in this case is much more important than convergence rate because of extremely low distance to the bottom (in the case No. 6 resulting UKC in simulation was 2 cm for 8 meter model). Under such circumstances overshoots could lead to crash, because of the patch collision.

(a)   (b)
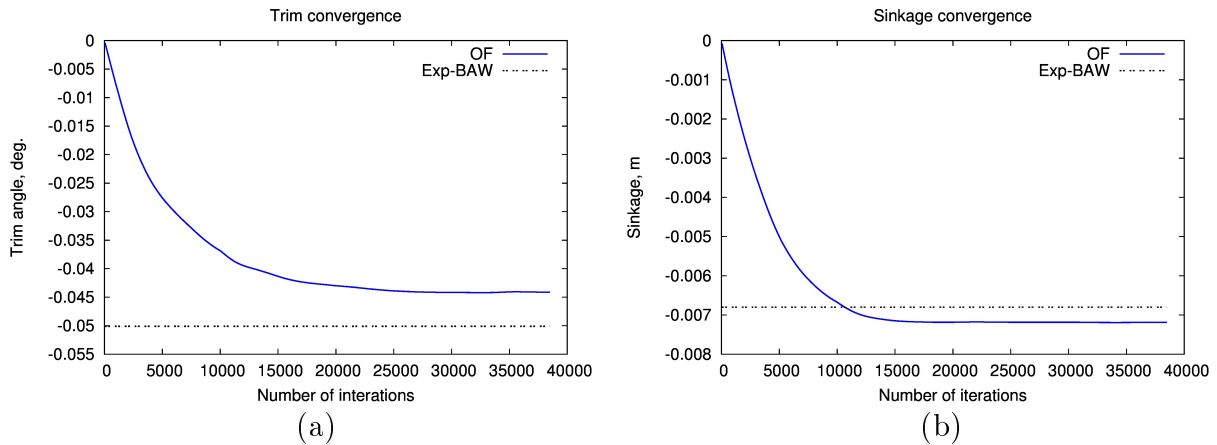
Figure 2: Convergence of trim and sinkage at CoG for the case No. 4

The computational results were compared to experimental (BAW) and numerical (GL-Comet) data [7] for sinkage at fore and aft perpendiculars. Comparison for the values, converted to full scale can be seen in the figure 3. Discrepancy analysis is presented in table 4.

As one can see, OpenFOAM predictions are in a satisfactory qualitative and quantitative agreement with experimental data both for FP and AP draught change, which is an encouraging result.

(a)   (b)
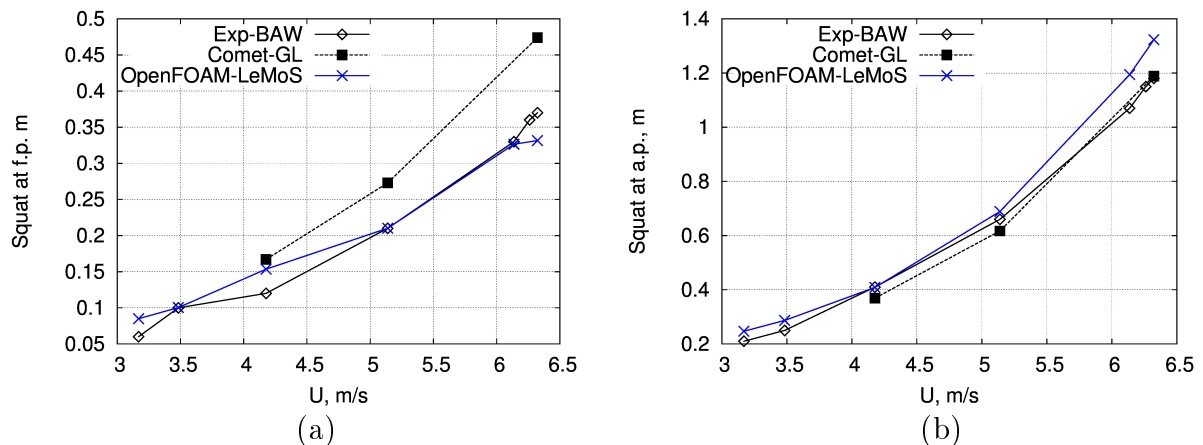
Figure 3: Comparison of experimental and computational results for sinkage at FP and AP, (converted to full scale)
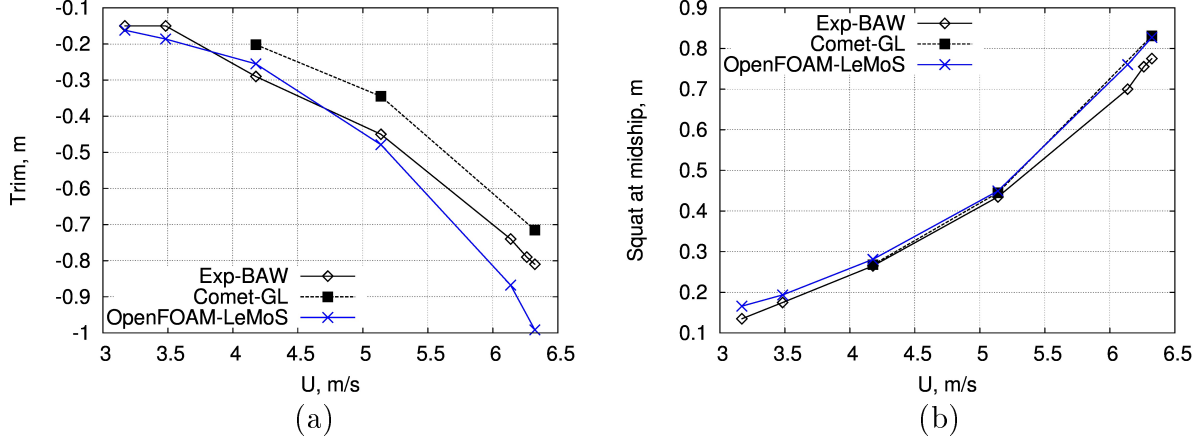
Figure 4: Comparison of experimental and computational results in terms of trim and midship sinkage (converted to full scale)

It is hard to compare prediction accuracy of the two viscous solvers and draw any conclusions, because Comet simulations were carried out on a somewhat "coarser" grids of maximum 2.5 mln cells. Exact information on mesh resolution and domain parameters is missing. But for this particular case it can be clearly seen, that both codes predict almost identical and equally accurate sinkage at midship, but considerably different trim value with different signs of discrepancy (see fig. 4). This difference, however is not significant, because the maximum squat (at AP) is predicted well by both viscous codes.

Squat modeling using OpenFOAM took 4 to 7 days of total simulation time on 32 cores (AMD6172). As stated in [7], simulation with another RANSE code required 2 days to one week using 8 processors, while GL Rankine simulation takes about 15 minutes per speed. However, neither the processor model, nor exact mesh resolution used for Comet simulations are known, and thus authors can not compare the computational efficiency of present methodology with another software described in [7].

Table 4: Discrepancy for sinkage at FP and AP (converted to full scale)

Case No.	Speed, [m/s]	Discrepancy, abs. [m] (rel. [%])			
		OpenFOAM-LeMoS		Comet-GL	
		Squat at FP	Squat at AP	Squat at FP	Squat at AP
1	3.18	0.02 (+41.62)	0.04 (+17.59)	-	-
2	3.48	0.00 (+0.36)	0.04 (+14.69)	-	-
3	4.18	0.03 (+27.97)	0.00 (-0.29)	0.05 (+39.16)	0.04 (-10.00)
4	5.13	0.00 (+0.07)	0.03 (+4.41)	0.06 (+26.06)	0.05 (-7.77)
5	6.14	0.00 (-1.07)	0.12 (+11.60)	-	-
6	6.32	0.04 (-10.41)	0.14 (+12.11)	0.11 (+28.82)	0.01 (+0.99)

CONCLUSION LTSInterFoam and LTSInterDyMFoam solvers have been successfully applied to a squat prediction of a container ship in restricted fairway. Present research gave promising results and showed that OpenFOAM with developed modifica-

tions can be used for simulations of under-keel clearance. This in turn allows for proper modeling of unsteady effects in a ship wake under such conditions.

On the other hand, numerical efficiency of the utilized solvers in comparison with the other viscous and potential methods [7] is still a question. And thus, it might be not the optimal solution for large series of computations. But for the needs of the further research on ship stern vibration in shallow water this methodology will be suitable.

References

[1] B. Barras. *Ship design and performance for masters and mates.* Butterworth-Heinemann, 2004.

[2] M. Briggs, P. Debaillon, K. Uliczka, and W. Dietze. Comparison of PIANC and numerical ship squat predictions for rivers Elbe and Weser. In *Proceedings of 3rd Squat-Workshiop: Nautical Aspectis of Ship Dynamics*, 2009.

[3] J. Höpken and N. Stuntz. Simulation of a Ship's Roll Decay with OpenFOAM. In *Proceedings of 12th Numerical Towing Tank Symposium* , 2009.

[4] T. Jiang. *Ship Waves in Shallow Water.* Fortschr.-Ber., VDI Reihe 12. Nr. 466. VDI Verlag 2001.

[5] D. Schmode, V. Bertram, and M. Tenzer. Simulating Ship Motions and Loads using OpenFOAM. In *Proceedings of 12th Numerical Towing Tank Symposium*, 2009.

[6] I. Shevchuk and N. Kornev. Numerical simulation of a ship wake in shallow water using hybrid URANS-LES method. In *Proceedings of 15th Numerical Towing Tank Symposium*, October 2012.

[7] A. von Graefe, B. O. el Moctar, V. Shigunov, H. Söding, and T. Zorn. Squat computations for containerships in restricted waterways. In *Proceedings of the 2nd International Conference on Manoeuvring in Shallow & Coastal Waters*, 2011.

[8] B. Winden, Stephen B. Turnock, and D. Hudson. Validating Force Calculations using OpenFOAM on a Fixed Wigley Hull in Waves. In *Proceedings of 15th Numerical Towing Tank Symposium*, 2012.

[9] Ed.by Y.I.Voitkounski. *Ship Theory Handbook, In 3 Volumes. Vol I. Hydromechanics, Resistance of Ship, Ship Propulsion Devices.* Leningrad, Sudostroenie, 1985.

CFD simulation on Kappel propeller with a hull wake field

Keun Woo Shin[1] (keun.shin@man.eu), Poul Andersen[2] (pa@mek.dtu.dk),
Rasmus Møller Bering[1] (rasmusm.bering@man.eu)

[1]MAN Diesel & Turbo, Frederikshavn, Denmark
[2]Department of Mechanical Engineering (MEK), Technical University of Denmark (DTU), Kgs.Lyngby, Denmark

INTRODUCTION

Marine propellers are designed not for the open-water operation, but for the operation behind a hull due to the inhomogeneous hull wake and thrust deduction. The adaptation for the hull wake is important for the propulsive efficiency and cavitation risk especially on single-screw ships.

CFD simulations for a propeller with a hull model have showed acceptable agreement with a model test result in the thrust and torque (Larsson et al. 2010). In the current work, a measured hull wake is applied to the simulation instead of modelling a hull, because the hull geometry is mostly not available for propeller designers and the computational effort can be reduced by excluding the hull. The CFD simulation of a propeller flow with a hull wake is verified in order to use CFD as a propeller design tool.

A Kappel propeller, which is an innovative tip-modified propeller, is handled. Kappel propellers are characterized by non-planar lifting surfaces and blade tips smoothly curved towards the suction side. An accurate analysis of the Kappel propeller using CFD is important due to the more complicating blade shape than the conventional propellers.

The propeller model is verified by comparing the open-water characteristics. The hull wake field is simulated without the propeller flow to check whether it is preserved at the propeller plane or not. Propeller flow simulations are made with mean axial wake varying only along the radius (i.e. circumferentially uniform), whole axial wake and upstream transverse wake. It is investigated how the accuracy is improved, as the wake field is modelled more precisely. The thrust variation and pressure distribution on the blade from the CFD simulation with the hull wake model are also analyzed.

1. COMPUTATIONAL MODEL

A 5.8m Kappel propeller on a 35,000 DWT tanker is simulated in model scale in CFD simulations. The results of self-propulsion and cavitation tests for conventional and Kappel propellers on two vessels including the case considered in the current work are summarized by Andersen et al (2005).

A quarter-cylinder domain with a single blade and the periodic boundary condition is used for the open-water simulation. A whole cylinder domain with the whole 4-blade propeller and a rudder is used for the simulation with a hull wake field. Two upstream distances of 3D and 4D from the propeller plane to the inlet boundary are applied to the open-water simulation domain, where D is the propeller diameter. The downstream distance is 6D and the domain radius is 4D.

An inner domain around the propeller is defined for the rotating motion. The upstream and downstream distances of the inner domain are 0.5D and the radius is 0.6D. The upstream and downstream distances are reduced to 0.2D in the simulation with the rudder.
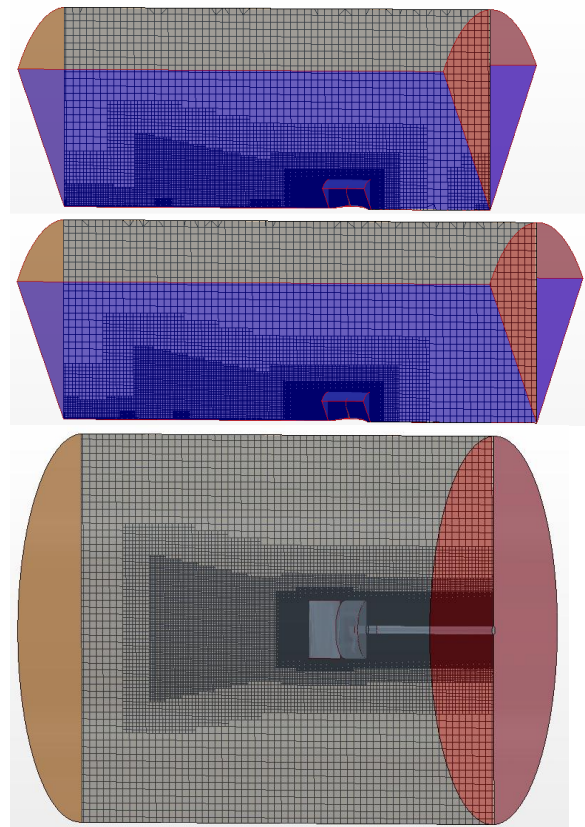
Fig. 1: *Computational models for a blade with an upstream distance of 3D (top) and 4D (middle) and for the whole 4-blade propeller with a rudder (bottom)*

In the open-water simulation, the propeller rotation is generated by using the moving reference frame (MRF). In MRF, fictitious volume forces corresponding to inertial forces from the propeller rotation are applied to the inner domain without an actual propeller rotation. In the simulation with the wake field, the propeller rotation is made by the rigid body motion and sliding mesh.

The hub with an upstream hubcap and a downstream shaft is applied to the open-water simulation in the same way as in the open-water model test according to the ITTC recommendation (2008). The actual hub and the rudder are applied to the simulation with the wake field.

Fig. 2: *Propeller surface mesh in the open-water simulation (top) and the simulation with the wake field and rudder (bottom)*

The surface of the blade, hub and rudder has a grid size of $\Delta x = 0.002D$-$0.004D$ and the no-slip boundary condition. The shaft surface has $\Delta x = 0.005D$-$0.01D$ and the slip boundary condition. 6 prism layers with a thickness of about $0.001D$ are applied to all the surfaces.
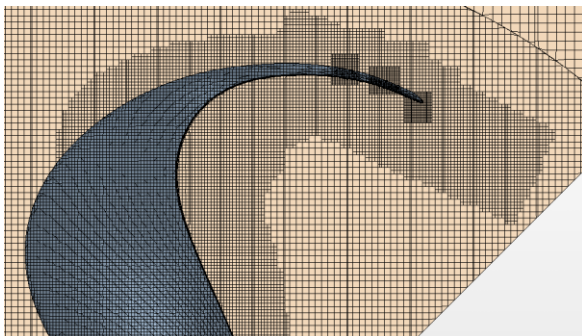
Fig. 3: *Sectional view of the volume mesh along the blade tip*

The volume mesh is mostly hexahedral and partially tetrahedral. The mesh grid size is gradually increased from the wall surface to the outer boundary. The fine volume mesh encompassing the inner domain has $\Delta x \approx 0.01D$. The intermediate volume mesh defined by

a larger cylinder and a cone downstream from the inner domain has $\Delta x \approx 0.025D$. In the simulation with the wake field, the fine volume mesh is extended to the inlet boundary. A finer volume mesh of $\Delta x \approx 0.005D$ is applied to the trace of the tip vortex along the tip to refine the vortex flow.

CFD computations are made by using StarCCM+ RANSE solver with k-ω SST turbulence model. All simulations are made in model scale and they are compared to the model test result without a scaling.

2. OPEN-WATER PROPELLER SIMULATION

Open-water simulations are made to verify the discretized model of the propeller geometry. Two domains with different upstream distances of 3D and 4D are applied to the open-water simulation.

Compared to the model test result, the CFD results from both domains have discrepancies of less than 3.4%, 5.3% and 3.0% in the thrust/torque coefficients K_T, K_Q and open-water efficiency η_O, respectively, for the advance ratio of $J=0.2$-0.5. The discrepancies are less than 4.5% at the design advance ratio. The CFD results from both domains differ from each other by less than 0.3%.

The open-water simulation shows acceptable accuracy at the design condition. Two domains with different upstream distances have equivalent accuracy, hence the following simulation with the wake field proceeds with the shorter domain to reduce the diffusion of the wake field on its way from the inlet boundary to the propeller plane.
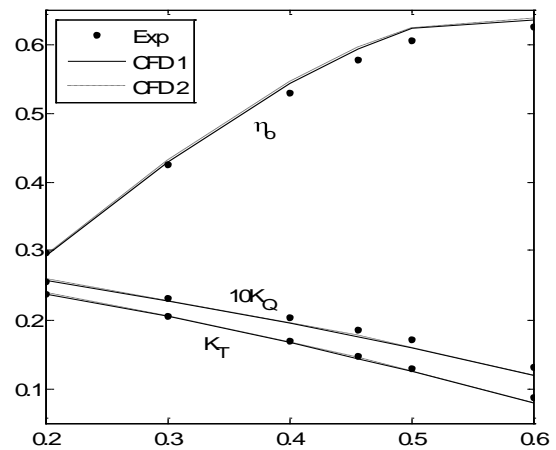
Fig. 4: *Open-water curve from the model test (Exp) and CFD with the upstream distance of 3D (CFD 1) and 4D (CFD 2)*

3. WAKE-FIELD SIMULATION

Before trying the propeller simulation with the wake field, the wake field is simulated without a propeller flow by applying it at the inlet. The sectional flow field on the propeller plane is checked to see how the applied wake field is varied on its way.

Since the measured wake field from the target ship is confidential, a dummy wake field from another single-screw low-speed U-form ship is demonstrated. In the following propeller simulation with the wake field, the wake field from the actual target ship is used.
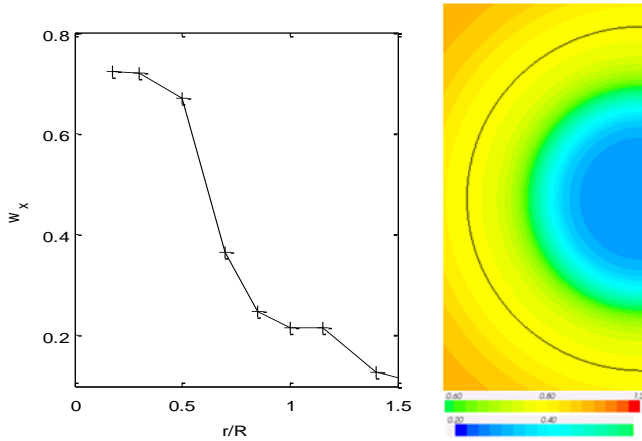
Fig. 5: *Mean wake fraction as a function of relative radius from the measurement (left) and axial wake component on the propeller plane in CFD with Wake 1 (right)*
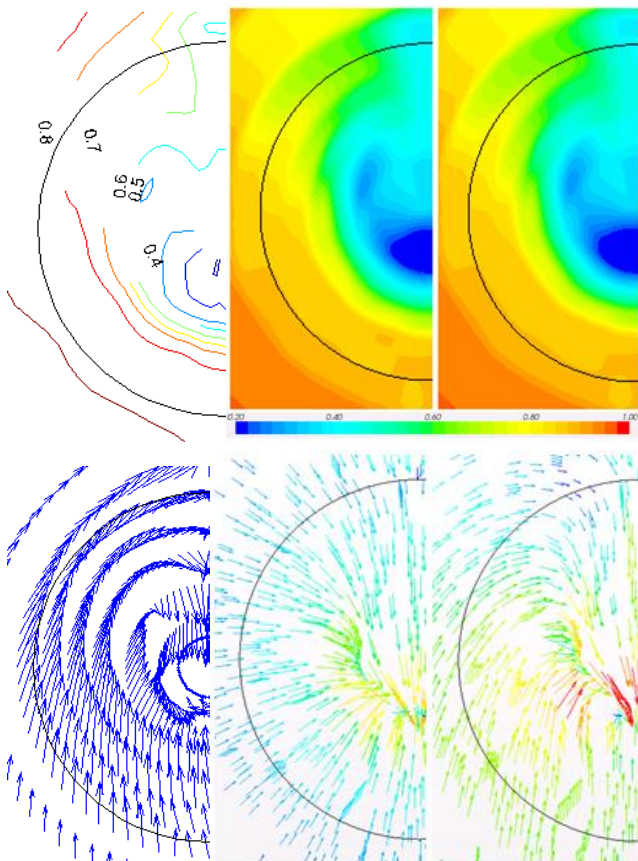
Fig. 6: *Axial component (top) and transverse component (bottom) of hull wake field on the propeller plane: measurement (left), simulations with Wake 2 (center) and 3 (right)*

The wake field behind a single-screw ship is characterized by high axial wake at inner radii and at the top central area, the upward flow in the lower half of the propeller disc and the bilge vortex in the upper half.

Three wake-field models are tried: mean wake varying as a function of radius and circumferentially uniform (Wake 1), whole axial wake field (Wake 2) and axial wake field together with an upward flow of $0.05V_S$ (Wake 3), where V_S is the ship speed. The average transverse wake on the propeller disk is about $0.05V_S$ in the upward direction. When the inhomogeneous transverse wake from the measurement is applied directly to the input wake together with the axial wake, the wake flow is destroyed to be chaotic. It is the reason why the uniform upward flow is tried instead of the whole transverse wake.

The axial and transverse wake components are taken at the propeller plane 3D downstream from the inlet. The simulation with Wake 1 shows that the axial wake on the propeller plane varies only along the radius and is uniform circumferentially. Wake 2 shows that the axial wake distribution is preserved well without a significant diffusion. The transverse wake from Wake 2 has an inward flow due to the low axial velocity in the inner radii, but it shows no characteristic upward flow and bilge vortex.

Wake 3 shows equivalent axial wake as Wake 2. The transverse wake has upward flow and bilge vortex qualitatively similar to the measured wake, but the center of the bilge vortex is a bit away from that in the measured wake. The overall magnitude of the transverse flow is about twice smaller than that in the measured wake.

4. PROPELLER SIMULATION WITH WAKE FIELD

Propeller simulations are made with three different wake models tried above. Unsteady-state computations are conducted with rigid body motion and sliding mesh. The time step of $\Delta t = 2.9 \cdot 10^{-4}$s corresponds to 1 deg propeller rotation and each time step has 5 inner iterations.

The design condition of $V_S = 15.5$kn and n=120rpm is considered. The effective wake fraction w in CFD is adjusted to reach the thrust T at the design V_S from the self-propulsion test, where w is the Taylor wake fraction, $V_A = V_S \cdot (1-w)$ and V_A is the advance velocity at the propeller plane.

Before applying the wake model, an open-water simulation is made again. The difference from the previous open-water simulations above is that the unsteady-state computation is made with the actual hub used in the self-propulsion test. While K_Q is underestimated by 4.0% and η_O is overestimated by 1.8% in the previous computation, K_Q is overestimated by 2.4% and η_O is underestimated by 1.3%. K_T at the design J in the model test is reached at slightly lower J, which implies that K_T is underestimated at the same value of J. In general,

steady- and unsteady-state computations do not result in significant differences for open-water propeller flow simulations. It is mainly due to the different hub.
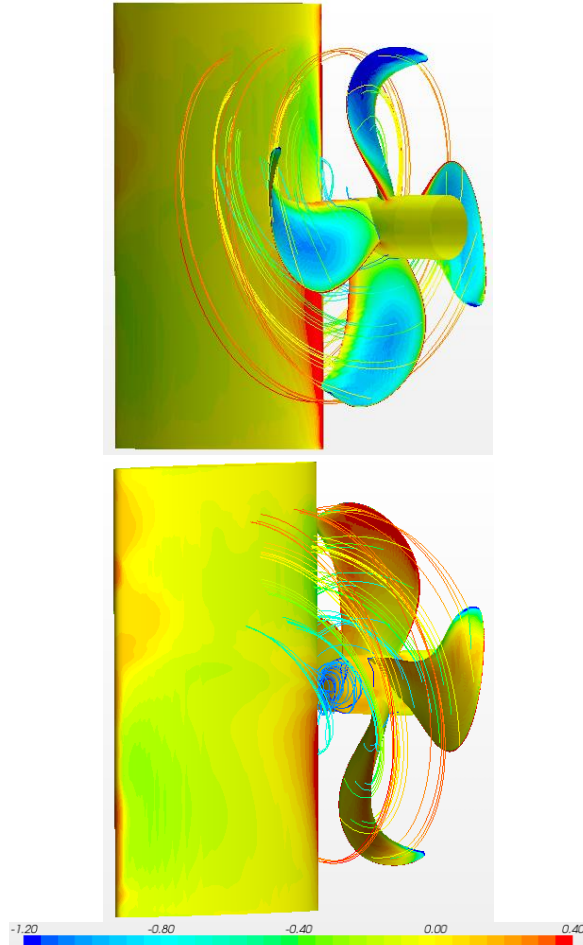
Fig. 7: *C_P on the propeller and rudder and streamlines with velocity magnitude for Wake 3*

Discrepancy [%]	ΔJ	ΔK_Q	$\Delta \eta_O$	$\Delta \eta_R$
Open-water	-0.6	2.4	-1.3	
Discrepancy [%]	Δw	ΔK_{QB}	$\Delta \eta_B$	$\Delta \eta_R$
Wake 1	-10.1	4.0	-3.9	-3.5
Wake 2	14.9	4.4	-4.2	-3.9
Wake 3	0.6	4.1	-4.0	-3.6

Table 1: *Discrepancies of CFD results with respect to the self-propulsion test results*

In Table 1, the discrepancies of the CFD results in w, K_{QB}, η_B and η_R are presented with respect to the self-propulsion test results, where K_{QB} is the behind-hull torque coefficient, η_B and η_R are the behind-hull and relative rotative efficiencies, respectively,

$$\eta_B = \eta_O \cdot \eta_R = \frac{J_A \cdot K_{TB}}{2 \cdot \pi \cdot K_{QB}}, \quad J_A = \frac{V_A}{n \cdot D}.$$

The thrust at the design V_S is reached at a 10% lower value of w for Wake 1 and at a 15% higher value for Wake 2, but w for Wake 3 is close to the effective wake fraction from the self-propulsion test with less

than 1% discrepancy. While V_A at $K_T=K_{TB}$ is taken from the open-water curve and w is calculated from the ratio of V_A to V_S in the model test report, w is calculated by integrating the wake on the propeller disk at the inlet boundary in this computation.
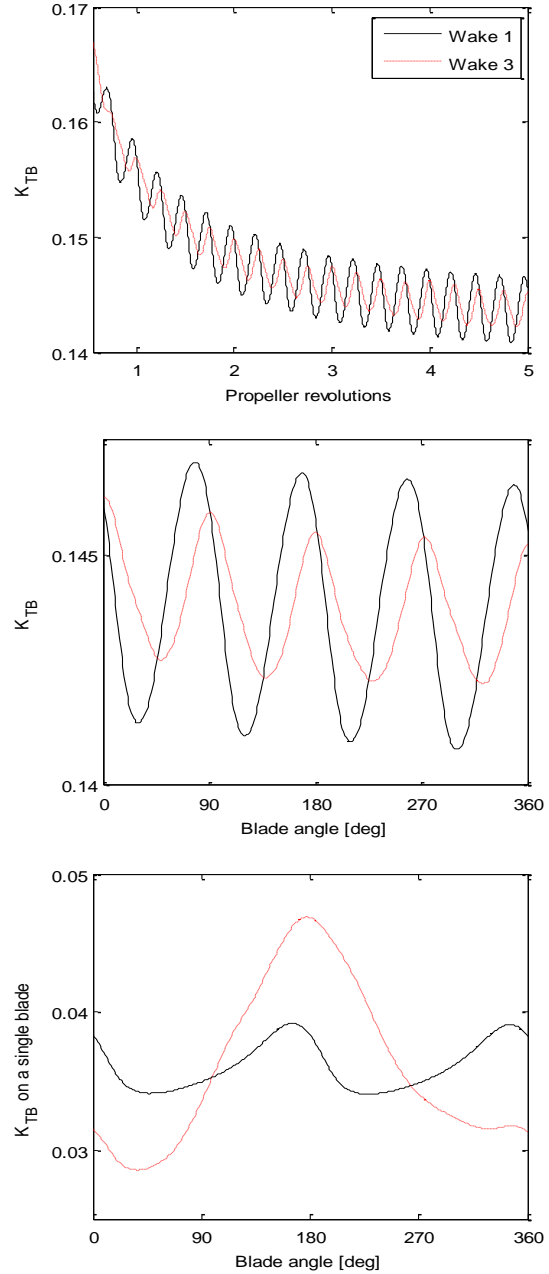
Fig. 8: *K_{TB} as a function of the propeller revolution (top), K_{TB} as a function of the blade angle (middle) and K_{TB} on a single blade as a function of the blade angel (bottom), where 180deg is 12 o'clock position*

In calculating η_B, V_A is assumed to be the same as in the self-propulsion test, because the simulations are for the same thrust. Although $\Delta \eta_B$ does not vary significantly for different wake models, it can be said that Wake 1 and 3 are a bit more accurate in estimating K_{QB} and η_B than Wake 2. Since the open-water simulation has an underestimation of $\Delta \eta_O$=-

1.3%, the underestimation of η_R becomes less than that of η_B. It implies that a portion of $\Delta\eta_B$ is due to the open-water discrepancy.

Wake 1 shows an equivalent accuracy to Wake 3. Wake 1 can be readily prepared using the wake data from a similar type of ship without a complicating wake measurement. But Wake 1 has a wide discrepancy in w, which implies that it has low accuracy in predicting K_{TB} at a certain value of J_A.

The thrust variation and pressure distribution are analyzed to investigate the influence of the wake models. Only Wake 1 and 3 are on the analysis, because Wake 2 shows a bit lower accuracy.

As the propeller flow is developed with more revolutions, K_{TB} is converged. K_{TB} on the whole propeller varies with a period of 90deg. The variation amplitude is 1.8 times higher for Wake 1 than for Wake 3. The wake input in Wake 1 does not vary along the blade angle and the variation of K_{TB} is caused mainly by the interaction of the rudder and propeller. When the downstream flow is decelerated by the rudder at the 0 and 90deg blade position, K_{TB} is increased. A symmetric rudder with a uniform sectional profile is used. When two blades are aligned with the rudder leading edge, K_{TB} is maximized.

Fig. 10: *C_P on the suction side for Wake 1 (top) and 3 (bottom)*

In contrast, the variation amplitude of K_{TB} on a single blade is 3.6 times higher for Wake 3. It is the highest at 180deg blade angle corresponding to the wake peak at the outer radii and the lowest at 30deg blade angle corresponding to the relatively lower wake. For Wake 1, K_{TB} on a single blade varies with a period of 180deg just due to the rudder influence. Since the wake does not vary along the blade angle, the variation amplitude is lower for Wake 1.

For Wake 1, C_P on the pressure side is slightly higher at 0 and 180deg blade positions than at 90 and 270deg. It is also noticeable that C_P at the outer radii of the suction side becomes lower at 0 and 180deg blade positions due to the rudder influence. The C_P distributions on both sides are almost the same at 0 and 180deg, because the wake is circumferentially uniform.

For Wake 3, the highest pressure on the pressure side and the lowest on the suction side are shown at 180deg blade position as usual on single-screw ships. $-C_P$ on the suction side becomes the lowest at 0deg. Therefore, the thrust is the highest at 180deg and the lowest near 0deg.

Fig. 9: *C_P on the pressure side for Wake 1 (top) and 3 (bottom)*

5. CONCLUSION

The computational geometry of the Kappel propeller is validated against the open-water curve from the model test. Based on the open-water simulation, the upstream distance of the computational domain is reduced from 4D to 3D.

The axial flow simulation with the behind-hull wake models without a propeller flow shows that the input wake is preserved well without a significant diffusion from the inlet boundary to the propeller plane.

Unsteady-state simulations with the rigid body motion of the propeller and sliding mesh are made for three hull wake-field models. The simplified wake model with a mean wake, which varies as a function of radius and is circumferentially uniform, shows slightly higher accuracy in estimating the torque and efficiency in the behind-hull condition. But the simplified wake model has a wide discrepancy in the wake fraction at the same thrust, which implies that the accuracy is low in predicting the thrust at a certain advance ratio.

The precise model with a whole axial wake field and an additional upward flow resulting in the bilge vortex shows accuracy in estimating both the thrust and torque. The thrust variation and pressure distribution in different blade angle also shows general characteristics of single-screw ship propellers.

The CFD simulation with the wake model can be more accurate and efficient in computational effort than the simulation with a ship hull. It can be a useful tool for the propeller design in the behind-hull condition. But the hull wake model has a limitation in predicting the hull efficiency and the wake field data are required. More simulations with the wake model for other cases with various ship types and propellers need to be made continuously to improve the robustness of the wake model.

REFERENCES

1. Andersen P., Friesch J., Lundegaard L., Patience G., 2005, Development of a marine propeller with nonplanar lifting surfaces, Marine Technology, Vol. 42, No. 3

2. ITTC, 2008, ITTC- Recommended procedures: Testing and extrapolation methods propulsion, propulsor open water test

3. Larsson L., Stern F., Visonneau M., 2011, CFD in ship hydrodynamics- results of the Gothenburg 2010 workshop, MARINE 2011, Lisbon, Portugal

Numerical Simulations of Particle-Laden Wake Flows

Håkon Strandenes[*], Bjørnar Pettersen[*] and Helge I. Andersson[**]

[*]Department of Marine Technology
[**]Department of Energy and Process Engineering

Norwegian University of Science and Technology, Trondheim, Norway
E-mail: {hakon.strandenes, bjornar.pettersen, helge.i.andersson}@ntnu.no
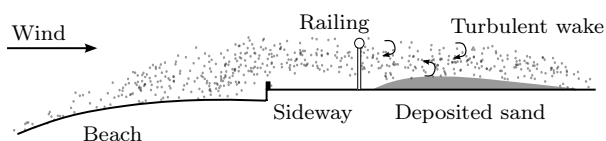
1 Introduction

Transport mechanisms for different substances are vital for our understanding of many important phenomena. One class of transport systems are particle-laden flows, that is flows with discrete particles. These particles can be biological matter, such as algae in the oceans or pollen in the air, pollution in the form of airborne dust from traffic or power plants, or it might be sand and soil in water or air.

Wake flows behind bluff bodies are a class of flow of great interest. They appear in many areas in nature, society and industry. Flows around cars, trucks, ships and offshore structures can all be placed in this category. One very simple geometrical case, however yielding highly complex flow patterns, is flow around circular cylinders. Even at very low Reynolds numbers the flow destabilize and the famous von Karman vortex shedding process is observed.

The presence of an unsteady wake can significantly alter the transport of particles. One example is a new sideway, with railing (manufactured of circular pipes) that was built along a road next to a beach in Sola, Norway. After the railing was put up, it suddenly became a huge problem with sand depositing on the road next to it [1]. Without further investigation, one might suspect that this deposition is triggered by the turbulent wake behind the railing.

Sand in the oceans close to the sea bed can behave in the same way as sand in air. The mechanisms of sedimentation and scour is of special engineering importance in the vicinity of offshore installations, wellheads, piles, sub-sea pipelines and anchor lines. It is vital to make sure that the installation of a pipeline does not trigger any scouring, as this might lead to long, free-hanging spans, in which the pipe might crack or burst due to the increased tension or fatigue damage because of vortex induced vibrations.

This work is a first step to study details of the dynamics of discrete, solid particles in the wakes behind bluff bodies. As a first step and a well-known flow case, the laminar flow around a circular cylinder without gravity is used. Even tough the case is simple, a lot of reference data exist for the flow, and it exhibits many of the same phenomena as turbulent flows, such as unsteadiness and vortices.

2 Mathematical Modelling

2.1 Flow Equations

The flow is assumed to be incompressible and isothermal with a Newtonian fluid, satisfying the Navier-Stokes equations:

$$\nabla \cdot \mathbf{U} = 0 \tag{1}$$

$$\frac{\partial \mathbf{U}}{\partial t} + \mathbf{U} \cdot \nabla \mathbf{U} = -\nabla \tilde{p} + \nu \nabla^2 \mathbf{U} + \mathbf{b} \tag{2}$$

where $\mathbf{U}$ is the fluid velocity vector, $\tilde{p} = p/\rho$ is the kinematic pressure, $\mathbf{b}$ is a body force and ν is the kinematic viscosity.

Together with the appropriate boundary conditions, this equation system is solved numerically with the open-source CFD tool OpenFOAM. This software uses the finite volume method to solve transport problems. In this work a special-purpose solver has been developed and used, however the flow solution process is the well-known PISO-algorithm [2], as implemented in `pisoFoam`. The chosen discretization is 2nd order in both space and time, with pure central differences for the spatial terms and a Crank-Nicholson temporal scheme. No further details on the mathematics of solving the Navier-Stokes equations are given here, but the interested reader is encouraged to read references [3] and [4].

2.2 Particle Modelling

The particles used throughout this work is solid, spherical particles treated as point masses. For every

Figure 1: Principle sketch of deposition of sand in the turbulent wake behind a railing.

timestep of the solution process, the forces on each particle are calculated, and Newton's second law of motion, $\sum \mathbf{F_i} = m_p \mathbf{a}$, is solved for each individual particle to find the new velocity and position.

The forces on the particles can roughly be divided in two parts: the contact forces, i.e. the forces originating from the physical contact with the fluid, and any field forces, such as gravity. The forces acting on the particles from the fluid can again be separated into many different contributions:

- Drag
- Buoyancy
- Lift
- Added mass
- Pressure gradient forces
- Basset (history) forces

In this work, some simplifications have been made, namely that we work with a fictitious fluid with high viscosity and low density. If the particle density ρ_p is much higher than the carrying phase (fluid) density ρ_c, such that $\rho_c/\rho_p \ll 1$, all of the force contributions listed above except the drag force can be neglected [5].

The particle behaviour is characterized by the Stokes number, which is a typical response time for the particle τ_p relative to a characteristic time scale in the carrying fluid τ_c [6]. If one assume that the only force on the particle is the Stokes drag force, a characteristic response time of a particle is given as:

$$\tau_p = \frac{\rho_p d_p^2}{18\mu} \qquad (3)$$

and then the Stokes number Stk become

$$Stk = \frac{\tau_p}{\tau_c} \qquad (4)$$

To determine the numerical values of the particle parameters, the Stokes number is selected first. Keeping the diameter fixed, to ensure that the flow always is within the Stokes flow regime, that leave us with the particle density ρ_p as one single variable to adjust to get the desired Stokes number.

3   Convergence Study

An extensive convergence study has been carried out for the fluid flow alone in order to assure that the flow field is converged in all important aspects before proceeding with the fluid-particle simulations. The following parameters are recorded and used to assess convergence:

- Strouhal number St
- RMS of lift force C_L'
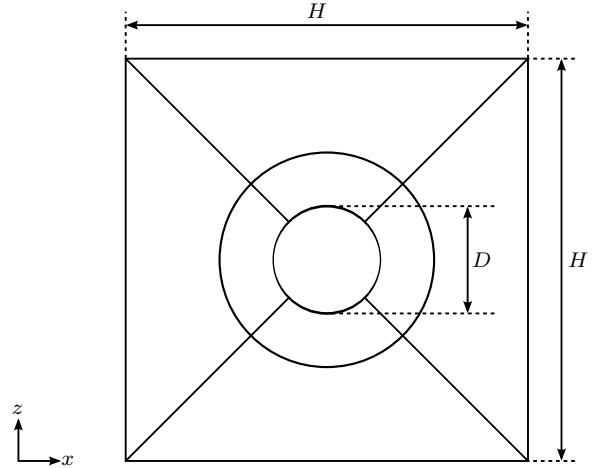
Figure 2: Illustration of the mesh block configuration for a simple, modified O-type grid. The inner layer is a pure O-grid, and then the grid is stretched to a square domain in the outer, far-field region. The origin is located in the cylinder centre, and the axis system is an xz-system as indicated on the figure.

- RMS of fluctuating drag force C_D'
- Mean drag force $\overline{C_D}$
- Mean base pressure coefficient $-\overline{C}_{pb}$

The Reynolds number for the flow is set to $Re = 100$. The cylinder has a diameter D of unity, and the inflow velocity U_∞ is also unity. To achieve the desired Reynolds number, the kinematic viscosity become $\nu = 0.01$.

The convergence study has been done in several stages, each running for over 100 vortex-shedding cycles to get enough data for statistical convergence. The parameters studied are (in order):

1. Mesh size near cylinder
2. Equation solver tolerances
3. Domain size H
4. The number of PISO-loops and non-orthogonal correctors
5. The necessary far-field grid size in order to preserve vortices in the far downstream region.

In each stage of the convergence study, the result from the previous simulation is used as an initial condition, either by direct transfer of the final flow field or by interpolating the field on a new grid. This is to make sure that the flow is fully developed.

The last stage, the necessary far-field grid size needed to preserve the vortices downstream, deserve some further discussion. The reason for studying this parameter is that the purpose of this work is to simulate the particle behaviour in the wake, hence we need sufficient resolution in the wake to avoid excessive numerical diffusion of the vortices. In order to assess the convergence in this area, the pressure
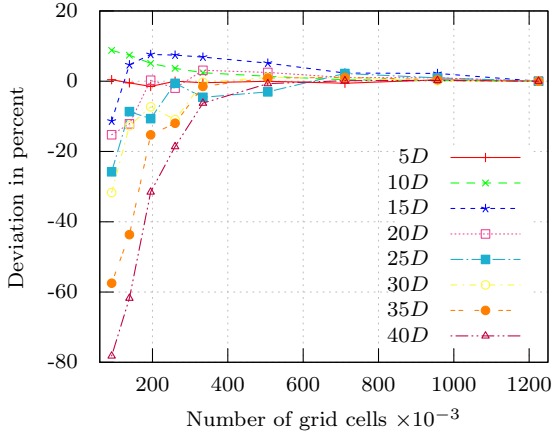
Figure 3: Wake pressure RMS values in the far-field against grid resolution. Ordinate axis value in per cent of value on finest mesh.

Table 1: Final grid and simulation setup

Grid Design		
Number of cells	506×10^3	
First cell height	1×10^{-3}	D
Cell size in wake	0.16	D
Domain size H	120	D
Time step	0.5×10^{-3}	D/U_∞
Numerical Setup		
Tolerance for p	1×10^{-7}	
Tolerance for $\mathbf{U}$	1×10^{-6}	
PISO-loops	2	
Non-orth. correctors	0	

was recorded in points along a line at $z = -1D$, starting from $x = 5D$, with one point every $5D$ until $x = 40D$ downstream of the cylinder center. The mesh is refined by keeping the cell size near the cylinder constant, and only refine the cells in the far-field region. As shown in figure 3, a rather high number of grid cells were needed to reach convergence far behind the cylinder.

The final grid and simulation setup for the flow solution is given in table 1. The recorded values for the converged flow simulation are in good agreement (within 4%) of reference values found in [7–10].

4 Particle-Fluid Simulations

The Lagrangan particles were injected with velocity $\mathbf{V} = U_\infty \mathbf{i}$ along a line of 20 001 discrete injection points between $(x, z) = (-10D, -10D)$ and $(x, z) = (-10D, 10D)$. When a particle collide with the cylinder, the particle is removed from the simulation. This is to avoid the additional physics associated with the collision problem. A one-way coupling

particle model is used, that means the particles are influenced by the flow, but there is no back-coupling into the momentum equation. The flow field is exactly the same as if there were no particles present. This can be considered physically realistic if the particle concentration is low. In these simulations however, we can neglect this, as there are neither a coupling from the particles back into the flow nor a particle-particle (collision) coupling. This effectively makes all particles 'invisible' for both each other and the flow. The results should thus be interpreted as if the particle-fluid flow is highly dilute.

The simulations procedure is as follows:

1. The simulation is started, and 50 particles are injected every timestep during 80 time-units

2. After 80 time-units, the particle distribution is believed to have reached a fully developed state, and the average particle volume fraction $\bar{\Theta}$ is calculated and updated each timestep.

3. Snapshots of the velocity field and particle locations together with information about the state of the particles are stored for every 5 time-units.

4. After exactly 20 vortex-shedding cycles, that is 121.698 time-units after the start of the averaging process, the simulation is stopped, and the final average particle volume fraction $\bar{\Theta}$ is written to disk.

The fluid density is assumed to be unity, and the particle diameter is set to $d = 1 \times 10^{-4}$. To gain the desired Stokes number, the density of the particles are adjusted as described previously in paragraph 2.2.

4.1 Particle Distribution

The instantaneous particle distribution for three selected Stokes numbers at the final time step of the simulation are shown in the figure 4. In this visualization, only 300 000 randomly selected particles of approximately 6 millions present are visualized. The colouring is the particle velocity magnitude $|\mathbf{V}|$. It is evident that the particles are repelled from the core of the vortices, and this effect is stronger for the heavier particles.

The shape of the particle voids at $Stk = 0.1$ and $Stk = 1$ are quite close to the shape of the isocontours for vorticity. For the heaviest particles with $Stk = 100$ the particle distribution in the wake is probably not fully developed, even at 60 cylinder diameters downstream. For this case a larger outlet length should have been used to see if the particles were transported fully away from the vortex cores.

4.2 Slip Velocity

The drag forces on the particles are only dependent on the slip velocity $\mathbf{U_S} = \mathbf{V} - \mathbf{U}$, as all other
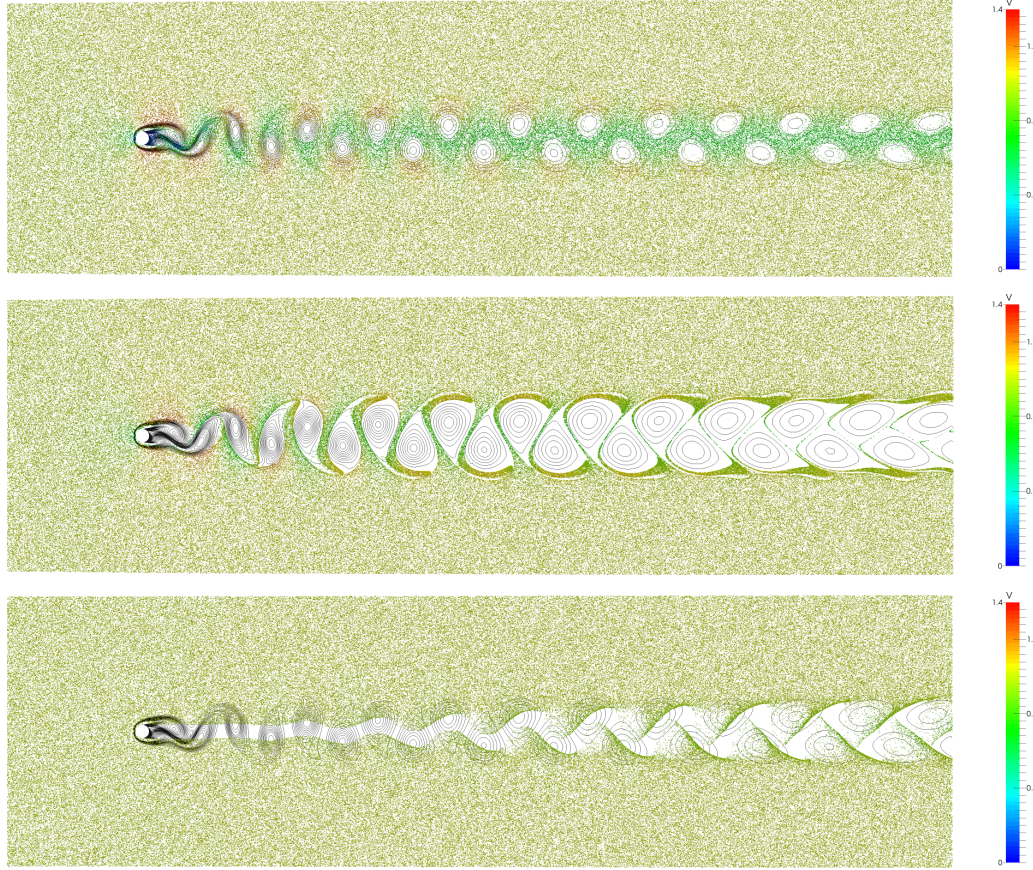
Figure 4: Instantaneous particle distribution for $Stk = 0.1$ (top), $Stk = 1$ (middle) and $Stk = 100$ (bottom). Only 300 000 (randomly chosen) out of about 6 million particles are displayed. The color scale is the particle velocity magnitude $|\mathbf{V}|$, and isocontours for vorticity magnitude is added for reference. The vorticity magnitute at the outermost contour is $|\omega| = 0.1$.

parameters in the force model, such as fluid density, viscosity, and particle diameter are constant for all particles in all cases.

In figure 5 the transverse (z) component of the slip velocity has been shown. These plots have a double logarithmic scale, and a threshold filter. This is done to emphasis the direction of the force, which is not possible with a single logarithmic scale. The log-scale is necessary due to the large variation in the orders of magnitude of the velocity. The blue-to-green color scale is for the particles with negative slip velocity, and the red-to-green scale is for the positive velocities. The particles with zero or almost zero transverse component of the slip velocity (i.e. that falls beyond the range of both scales) are not displayed, this can be seen as voids surrounded by a strong green color.

The figures show how the particles are 'dragged' out of the centre of the wake. The particles are dragged upward and downwards in an alternating fashion, with decreasing magnitude as the distance from the cylinder increases. This is how the void regions in the vortex cores are created.

4.3 Particle Age

Another variable that is recorded and stored is the particle 'age'. This is the time passed since the particle was injected in the simulation, i.e. the time of the snapshot minus the time of the initial injection of each particle. As a particle travelling with the undisturbed, freestream velocity will 'get older' proportionally with the distance travelled downstream with a velocity U_∞, one can construct a 'corrected particle age', that is the particle age of a certain particle, minus the age for an imaginary particle transported with the freestream velocity in the same point. This variable is shown in figure 6.

Figure 6 can give us insight in how the particles are transported in the wake for different Stokes numbers. For the lowest Stokes numbers, it is clear that there is a region in the back of the cylinder where there is a number of particles 'trapped'. Closer inspection of the data in the simulation reveal that these particles might stay there for a long time, as even some of the very first particles injected are found here at the end of the simulation (after about 200 time-units). However, there seems to be a transport of particles out of this region, that is within the high-vorticity
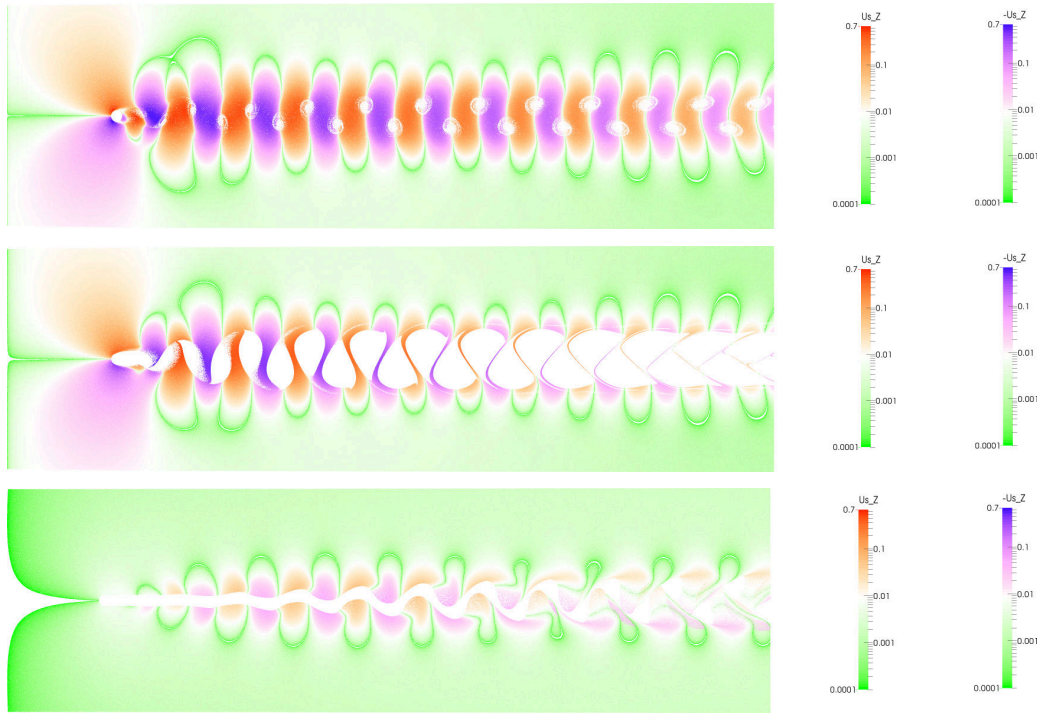
Figure 5: Transverse (z) component of slip velocity $\mathbf{U_S}$ for $Stk = 0.1$ (top), $Stk = 1$ (middle) and $Stk = 100$ (bottom). Note the use of two logarithmic scales, one for the positive values and one for the negative. The particles that fall beyond the range of both scales are not displayed.
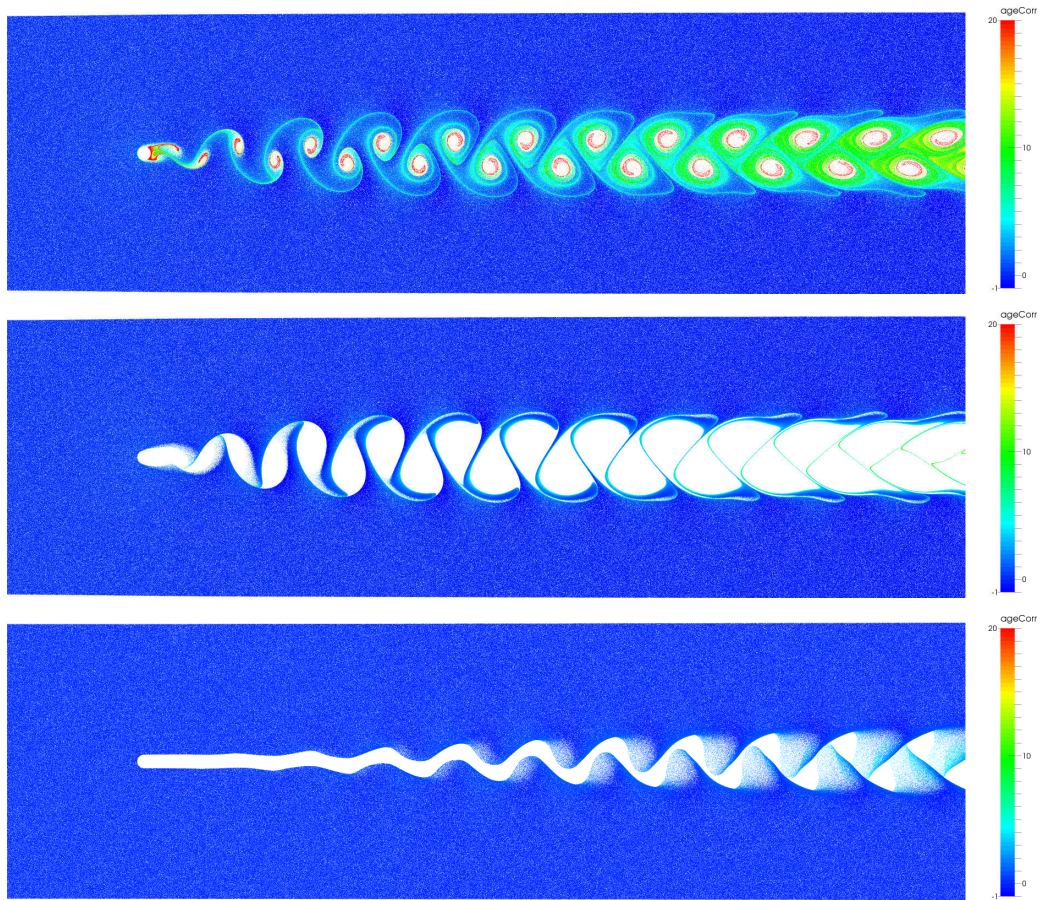
Figure 6: 'Corrected particle age' age $- (x + 10)/U_\infty$ for for $Stk = 0.1$ (top), $Stk = 1$ (middle) and $Stk = 100$ (bottom). All particles present are visualized.

regions in the vortex cores. Each time a vortex is shed from the cylinder, some of the particles trapped in the recirculation region is captured and dragged downstream.

The heavier particles are not that colourful, but one interesting phenomena is that particles in the wake is overtaken by particles coming from outside of the wake, which due to their large inertia maintain their higher velocity for some time. This is seen in the very end of the wake for the case with $Stk = 100$. In many cases figure 5 and 6 are complements that display much of the same physics, but in different ways.

5   Concluding Remarks

An efficient framework for simulating particle-laden flows has been established and tested. Different methods of visualization have been tried, and all give different insight into the physical phenomena involved. The visualization and also possibly quantification of the results are difficult topics that also need to be explored further.

From the simulations, we observe that the heavier particles are repelled from the vortex centres. The heavy particles have a time-scale that is much larger than the fluid time scale. This is visible in the particle concentration behind the cylinder, where the heavy particles create an almost straight 'particle shadow' region behind the cylinder. The light particles on the other hand, are observed in the immediate vicinity behind the cylinder.

In a retro-perspective view, an even finer grid should have been applied in the far-field. This is not because we do not believe in the results of these simulations, but simply because it was found that the majority of the computing time was spent on simulating the about 6 million particles present at each time instant. Because the particles are unevenly distributed in the domain, this leads to computational imbalances where a few processes with a lot of particles to track are the limiting factors when it comes to performance. Increasing the grid resolution even further would probably have given more accurate results at a marginal cost.

References

[1] Norwegian Broadcasting Corporation (NRK). Kjørte seg fast i sand på veien langs Solastranden. `http://www.nrk.no/rogaland/sand-i-veien-pa-sola-1.11057939`, 2013.

[2] R. I. Issa. Solution of the implicitly discretised fluid flow equations by operator-splitting. *Journal of Computational Physics*, 62(1):40–65, 1985. URL `http://dx.doi.org/10.1016/0021-9991(86)90099-9`.

[3] H. G. Weller, G. Tabor, H. Jasak, and C. Fureby. A tensorial approach to computational continuum mechanics using object-oriented techniques. *Computers in Physics*, 12(6):620–631, 1998.

[4] H. Jasak. *Error Analysis and Estimation for the Finite Volume Method with Applications to Fluid Flows*. PhD thesis, Imperial College, 1996.

[5] M. R. Maxey and J. J. Riley. Equation of motion for a small rigid sphere in a nonuniform flow. *Physics of Fluids*, 26(4):883–889, 1983. URL `http://dx.doi.org/10.1063/1.864230`.

[6] G B. Jacobs and K. Armstrong. Inertial particle dispersion in the lagrangian wake of a square cylinder. In *47th AIAA Aerospace Sciences Meeting*. Americal Institute of Aereonautics and Astronautics, 2009. URL `http://arc.aiaa.org/doi/abs/10.2514/6.2009-1026`.

[7] C Norberg. Fluctuating lift on a circular cylinder: review and new measurements. *Journal of Fluids and Structures*, 17(1):57–96, 2003. URL `http://dx.doi.org/10.1016/S0889-9746(02)00099-3`.

[8] O. Posdziech and R. Grundmann. A systematic approach to the numerical calculation of fundamental quantities of the two-dimensional flow over a circular cylinder. *Journal of Fluids and Structures*, 23(3):479–499, 2007. URL `http://dx.doi.org/10.1016/j.jfluidstructs.2006.09.004`.

[9] L. Qu, C. Nordberg, L. Davidson, S. H. Peng, and F Wang. Quantitative numerical analysis of flow past a circular cylinder at Reynolds number between 50 and 200. *Journal of Fluids and Structures*, 2013. URL `http://dx.doi.org/10.1016/j.jfluidstructs.2013.02.007`. In press.

[10] Y. Li, R. Zhang, R. Shock, and H. Chen. Prediction of vortex shedding from a circular cylinder using a volumetric Lattice-Boltzmann boundary approach. *The European Physical Journal Special Topics*, 171:91–97, 2009. URL `http://dx.doi.org/10.1140/epjst/e2009-01015-9`.

Self propulsion in waves using a coupled RANS-BEMt model and active RPM control

Björn Windén[1*], **Charles Badoe**[1], **Stephen Turnock**[1], **Alexander Phillips**[1] **& Dominic Hudson**[1]

[1]Fluid-Structure Interactions Research Group University of Southampton, Southampton, UK. SO17 1BJ

1   Introduction

The flow over a ships stern is very complex, involving a thick boundary layer, viscous-inviscid interaction, a complex turbulent flow-field and the action of a propulsor (ITTC, 1990). Reviewing these flow features numerically is a challenging task, since it requires not only accurate prediction of resistance and wake flow, but also good prediction of the propulsor. When considering self propulsion in waves, more complexity is introduced in the form of ship motions and unsteadiness introduced by the passing waves. One simplification in the analysis of the above system without compromising the predictive accuracy is to couple a propeller performance code in an iterative manner to predict the combined flow field.

Several twoway coupling approaches have been developed by various authors with different levels of complexity for investigating ship stern flows. An example of such an approach was presented by Badoe et al. (2012), who described a coupling using a body force model and a load distribution based on the Hough and Ordway (1964) circulation to determine the propeller forces.

Other possibilities involving coupling of a potential flow code to a RANS code has been described by Laurens and Cordier (2003) using the velocity field calculated in the near-field downstream flow from the propeller, simulated by the resolution of the potential problem as inlet boundary conditions within the RANS calculation. Each of these approaches have advantages in terms of accuracy, computational efficiency and level of detail.

The present paper aims to present a methodology for coupling a RANS code and a Blade Element Momentum theory (BEMt) model for the propeller. This is done as part of the development of a self propulsion modelling framework in the open source software package OpenFOAM. Ultimately, the goal is to acquire efficient numerical tools for modelling self propulsion in waves of realistic hullforms as well as propeller-rudder interaction.

2   Self propulsion framework

Modelling propulsion of a ship travelling in waves requires some form of control regulating the balance between hydrodynamic loads on the hull and the thrust and torque generated by the propeller. For this reason, a control framework has been created for OpenFOAM with three purposes:

- To determine/control the propeller RPM

- To handle information exchange between the flow solver, the propeller model and the dynamic mesh solver

- To have a modular definition of the propeller model and control function

2.1   Modular system

The last purpose is added to allow for an easy expansion of the framework. The definition of the propeller model as well as the control function is made as a selectable option. This means that the definition of the propeller model is independent of the information exchange. To introduce a new propeller model, a user would only have to clone an existing one, rename it and change the code to have a new selectable option for propeller modelling. The information exchange of the framework is shown in Figure 1.

---

corresponding author's e-mail: b.winden@soton.ac.uk
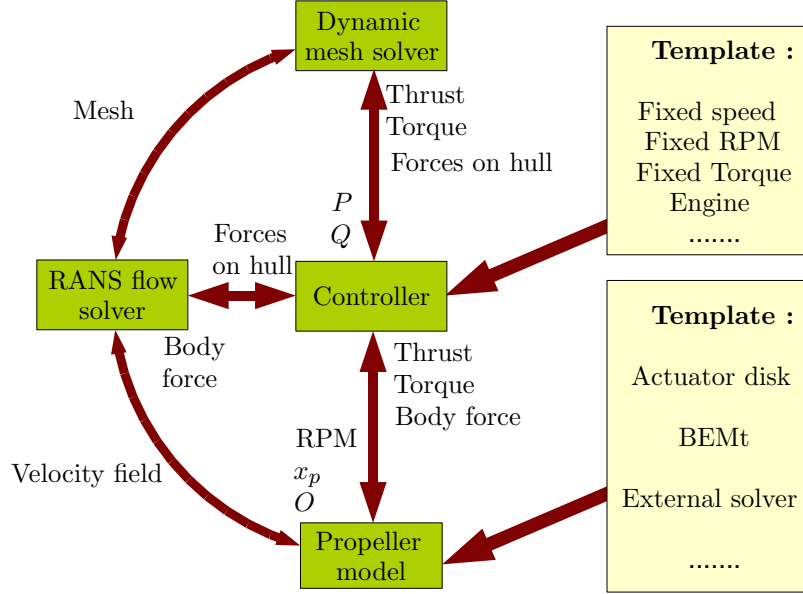
Figure 1: Self propulsion framework for OpenFOAM

3 Ship motions and cell identification

The ship motions in this model are based on forces and moments acting on the hull (including the propeller thrust and torque) and the equations of motion for a rigid body in 6 DOF. The forces and moments calculated with the RANS modelling technique used here were validated against experiments for a fixed hull in waves by Windén et al. (2012). The body force due to the propeller is introduced as an extra term in the unsteady RANS equation and is non-zero only in those cells which lie within the extent of the propeller disk. This means that these cells and their relative location within the propeller disk needs to be known.

The mesh is deformed using a Laplacian function on node displacement and keeping the moving hull and the domain edges as rigid boundaries as described by Jasak and Tukovic (2007) and Jasak (2009). The motion of points is diffused based on the inverse distance from the hull. This means that cells close to the hull are practically moving as part of the rigid body to ensure minimal distortion of boundary layer cells and other important mesh features near the hull. It also means that the body force distribution in the mesh should stay mostly constant since the cells inside the propeller disk are relatively close to the hull. They should therefore mostly move as part of the rigid body for moderate motions. Despite this, in the interest of developing a more generalised method, the cell identification process to determine where the body force should be added is handled and updated in run-time.

3.1 Relative location handling

The position of the propeller centroid x_p, the orientation of the propeller disk $O = (O_1, O_2, O_3)$ for an arbitrary ship orientation (defined by the rotation tensor Q and the offset P) is shown in Figure 2 and are calculated using the original centre of gravity CG_0 and the original orientation tensor O_0 as

$$xp = CG_0 + P + Q \cdot (xp_0 - CG_0) \tag{1}$$

$$O = Q \cdot O_0 \tag{2}$$

The the relative position of a cell I with its centroid located at coordinate x_I is given as

$$R_I = \begin{bmatrix} O_2^2 + O_3^2 & -O_1O_2 & -O_1O_3 \\ -O_1O_2 & O_1^2 + O_3^2 & -O_2O_3 \\ -O_1O_3 & O_2O_3 & O_1^2 + O_2^2 \end{bmatrix} (x_I - x_p) \tag{3}$$

$$d_I = (x_I - x_p) \cdot O \tag{4}$$

Here, R_I is the radius from x_I to the propeller axis and d_I is the distance from x_I to the propeller centre plane (Windén et al., 2013). Using this definition, active cells can be identified as fulfilling $r_H < R_I < R$ and $d_I < d/2$ where R is the tip radius, r_H is the hub radius and d is the disk thickness.
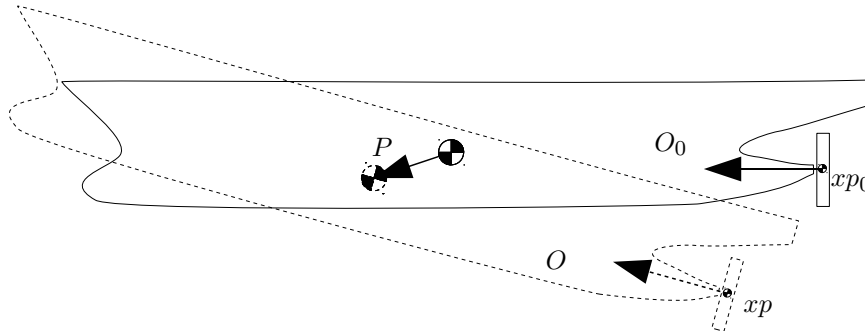

Figure 2: Movement of propeller region due to arbitrary ship motions

4 BEMt propeller model

In this paper the use of the BEMt approach in the self propulsion framework is studied. Blade element momentum theory combines both the blade element theory and the momentum theory. The combination of these two theories alleviates some of the difficulties in calculating the induced velocity of the propeller. Solution to this problem can be achieved if the part of the propeller between radial elements r and $(r+\delta r)$ is analysed by matching forces generated by the blade elements, as 2D lifting foils to the momentum changes occurring through the propeller disc between these radii. An actual propeller is not uniformly loaded as assumed by Rankine and Froude actuator disc model, thus to analyse the radial variation of loads along the blade, it is ideal to divide the flowfield into radially independent annulus stream tubes.

An existing BEMT model, (Molland and Turnock, 1996) was modified and coupled with a RANS solver. The local nominal wake fraction can be determined by running the code in open water conditions and behind model conditions until they yield the similar thrust coefficient. Effective wake can then be determined from the differences in advance coefficient for the two conditions. This can be expressed as

$$J_{ow} = J_{bm}(1 - wt) \tag{5}$$

where J_{ow} and J_{bm} are the advance coefficients in open water and behind model respectively, and wt is the effective wake fraction.

4.1 Propeller Open water characteristics

The open water performance shown in Figure 3 calculated from the BEMt code is compared with values provided by Molland and Turnock (2007), and that of Badoe et al. (2012) who carried out similar investigation on the same propeller using an Arbitrary Mesh Interface method (AMI). The agreement for KT was good with difference of less than 1% between both models. The trends with varying advance ratios are also well predicted.

Variations in KQ also showed under prediction for the BEMT model. CFD solutions over or under predict torque, and discrepancies increases with increasing propeller advance coefficient, J, when using a propeller model based on the momentum theory. This tendency seems to be prevalent in the open water plot below. This has also been reported by Uto (1993) who carried out RANS simulations involving marine propellers. These over predictions might be unavoidable due to experimental conditions such as tunnel wall, inflow speed nonuniformity and hub and boss configurations hardly conformable in CFD.

4.2 Computational effort

An important factor governing the choice of propeller modelling technique is the computational effort. Table 1 compares the associated cost in computation for a propeller-rudder interaction study by Badoe et al. (2012) and Phillips (2009) using an AMI, an actuator disk model and the BEMt model. It is clearly seen here that the BEMt and the actuator disk is far superior to the AMI approach in terms of computational effort.
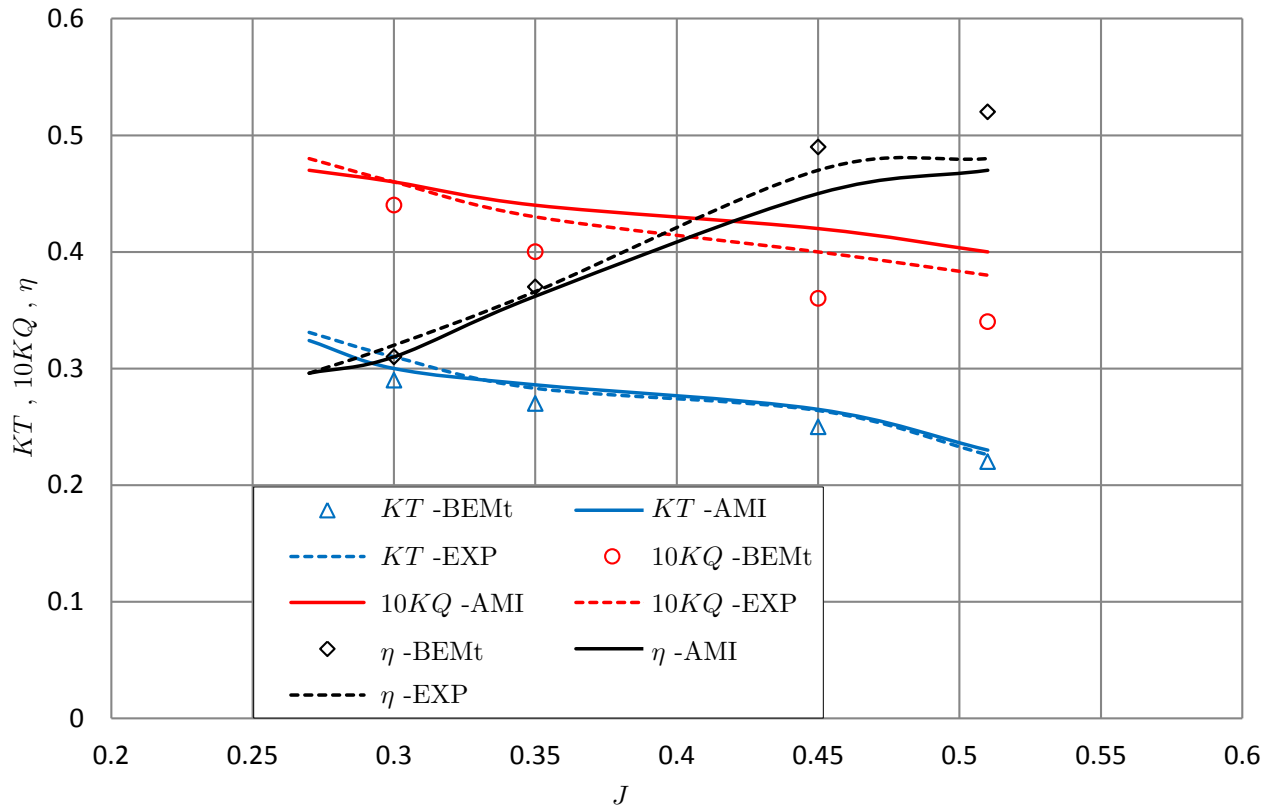
Figure 3: Comparison of propeller characteristics in open water. Experimental data by Molland and Turnock (2007).

Table 1: Computational cost comparison between different propeller modelling alternatives

Parameter	AMI Propeller	Actuator disk model	BEMt model
Mesh size	4-6M	4-6M	4-6M
Computer	Iridis 3 Linux Cluster	Iridis 3 Linux Cluster	Iridis 3 Linux Cluster
Resources utilised	6x8 processors	6x8 processors	6x8 processors
Simulation time	20-22 h	1.5-2.5h	3-4 h

5 Determination of wake fraction

The success of the body force approach relies on how accurately the relation between the ship wake and the propeller performance can be modelled. The unsteadiness of the nominal wake of a ship travelling in a seastate inevitably affects the thrust and torque delivered by the propeller and thus the self propulsion performance of the ship (Molland et al., 2011). This means that changes in the propeller inflow due to ship motions, passing waves and unsteady flow separation at the stern must be taken into account in the model. The propeller advance velocity can be easily corrected for ship motions through the movement of the ship centre of gravity and the global rotation tensor as shown in Figure 2. However, the variations in the wake due to waves, separation and motions can only be captured by probing the propeller inflow velocities in run-time.

5.1 Probe locations

For each cell I in the active body force region, an estimate of the local inflow condition is needed to determine local advance ratio. Considering the fact that the propeller might be tilted relative to the freestream, the probe location should be somewhere along a line parallel with the normal vector to the propeller disk. This way, if the propeller is tilted, only the component of the inflow velocity that is parallel with the propeller axial direction will be considered as the axial wake for cell I, the rest would be considered as tangential wake components. Furthermore, it has to be decided where along this line the probing should take place. The possible positions for probing the inflow velocity for cell I is shown in Figure 4.

The probe point x_{probeI} can be found as
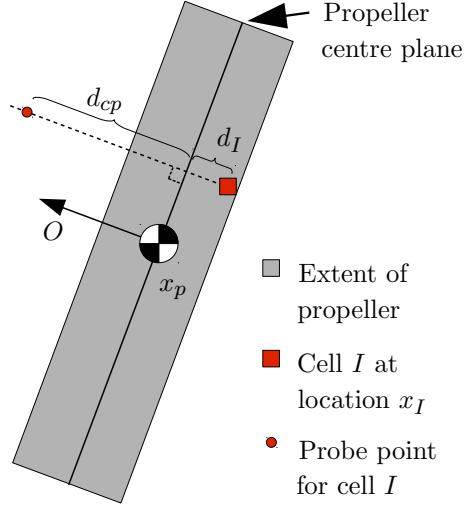
Figure 4: Location of probing point for cell I

$$x_{probeI} = x_I - (d_{cp} + d_I)O \qquad (6)$$

Using this definition, the effect of the wake velocities on the body force acting on cell I can be discussed. By using an active probing of the velocity field in run-time, both the axial and tangential components of the wake can be considered something that will add more realism to the thrust and torque distributions (Molland et al., 2011).

From the formulation in Equation 6, several options for the location of each probe are available:

- Probing in the centroid of cell I : $d_{cp} = -d_I$

- Probing on the propeller centre plane : $d_{cp} = 0$

- Probing on the propeller disk front face : $d_{cp} = d/2$

- Probing some distance in front of the propeller disk front face : $d_{cp} > d/2$

6   Preliminary results

Although the aim of this paper is to use a full implementation of the BEMt in the self propulsion framework, initial results are shown here for an actuator disk. The framework shown in Figure 1 was used with an actuator disk to study the response to different types of controller by Windén et al. (2013). Results for different values of the maximum permitted RPM acceleration for a ship encountering a regular wave train using an actuator disk propeller model is shown in Figure 5. Furthermore, to show the potential of the BEMt model, apart from the open water characteristics shown in Figure 3, data from a propeller-rudder interaction study by Badoe et al. (2012) and Phillips (2009) is presented in Figure 6.
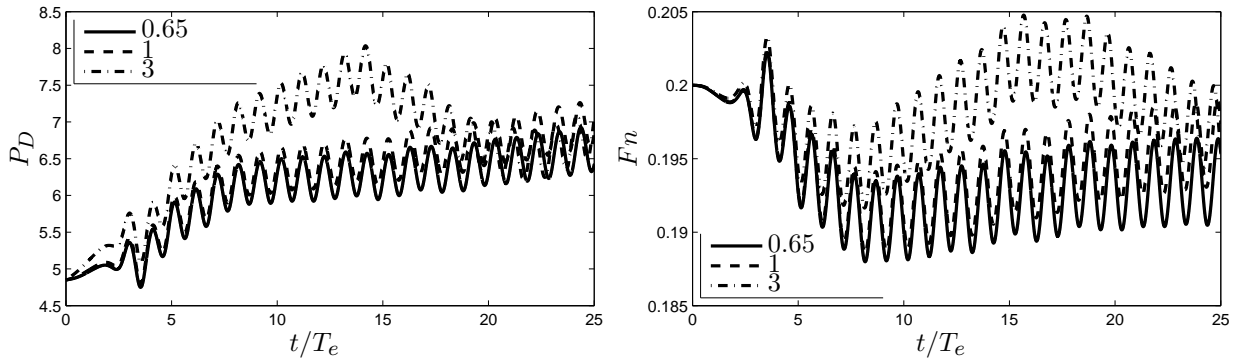
Figure 5: Changes in delivered power and forward speed when encountering a regular wave train with different values of $\partial RPM/\partial t$ allowed

Figure 6: Force data on rudder, $J = 0.35$, (Experimental data by Molland and Turnock (2007).)

This demonstrates that the wake field generated by the BEMt agrees well with experimental values of lift and drag on a rudder placed aft of the propeller at different angles. The final paper will present results from the fully coupled model as well as the influence of probing location and the manner in which the inflow velocities and the tangential wake is dealt with by the BEMt.

References

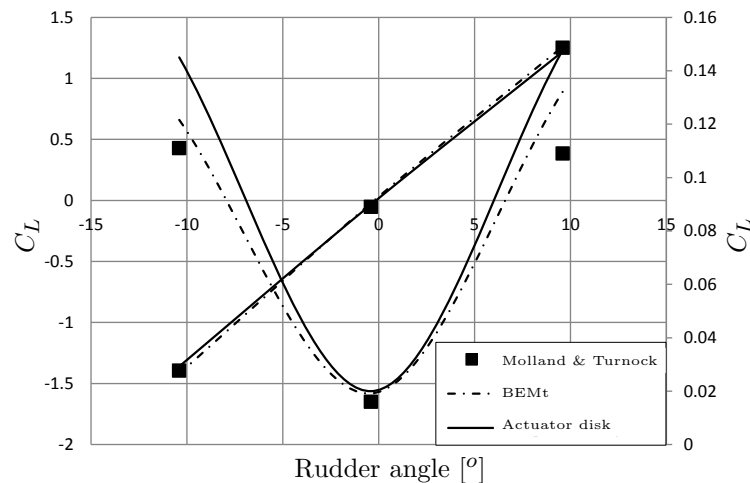Badoe, C., Phillips, A. and Turnock, S. (2012), Influence of drift angle on rudder propeller interaction, *in* 'Proceedings of the 15th Numerical Towing Tank Symposium, Cortona, Italy 7-9 October'.

Hough, G. and Ordway, D. (1964), The Generalized Actuator Disk, Technical report, Technical Report TARTR 6401, Therm Advanced Research, Inc.

ITTC (1990), Report of the Resistance and Flow Committee, *in* 'Proceedings of the 19th International Towing Tank Conference, Madrid, Spain'.

Jasak, H. (2009), Dynamic mesh handling in OpenFOAM, *in* '47th AIAA aerospace sciences meeting, Orlando'.

Jasak, H. and Tukovic, Z. (2007), 'Automatic Mesh Motion for the Unstructured Finite Volume Method', *Transactions of FAMENA* **30**(2).

Laurens, J. and Cordier, S. (2003), Numerical Simulation of Propeller-Rudder interface, *in* 'Proceedings of the 8th Symposium On Numerical Ship Hydrodynamics'.

Molland, A. and Turnock, S. (1996), Wind tunnel tests on the effect of a ship hull on rudder-propeller performance at different drift angles, Technical report, Technical report, University of Southampton Ship Science Report No. 76.

Molland, A. and Turnock, S. (2007), *Marine rudders and control surfaces: principles, data, design and applications*, Butterworth-Heinemann, Oxford.

Molland, A., Turnock, S. and Hudson, D. (2011), *Ship Resistance and Propulsion: Practical Estimation of Ship Propulsive Power*, Cambridge University Press.

Phillips, A. (2009), Cost Effective Hydrodynamic Design of Autonomous Underwater Vehicle, Ph.d. thesis, University of Southampton.

Uto, S. (1993), 'Computation of incompressible flow around a marine propeller', *Journal of Naval Architecture* **173**.

Windén, B., Turnock, S. and Hudson, D. (2012), Validating Force Calculations using OpenFOAM© on a Fixed Wigley Hull in Waves, *in* 'Proceedings of the 15th Numerical Towing Tank Symposium, 7-9 October, Cortona, Italy', pp. 170–175.

Windén, B., Turnock, S. and Hudson, D. (2013), A RANS modelling approach for predicting powering performance of ships in waves, *in* '12th International Symposium on Practical Design of Ships and Other Floating Structures (PRADS13), Changwon City, Korea', Pending review.

Adaptive Mesh Refinement in Viscous Flow Solvers: Refinement in the Near-wall Region, Implementation and Verification

Jaap Windt, MARIN, Netherlands

j.windt@marin.nl

1 Introduction

MARIN's viscous flow code ReFRESCO [1] is used in a daily routine to analyze the flow around offshore constructions, ships and propellers. ReFRESCO is able to solve the Reynolds averaged Navier-Stokes equations for multi-phase unsteady incompressible flow. Several one- and two-equation eddy-viscosity turbulence models and cavitation models are available. The code is based on a finite-volume method with cell-centred, colocated variables. The code is face based and cells with arbitrary number of faces are allowed. The free surface is solved using an interface-capturing method. This paper focuses on the implementation of an adaptive mesh refinement method in ReFRESCO. The current work is inspired by previous work done by Wackers et al. [2],[3] and is part of the Streamline [4] project, partly funded by the 7th Framework Programme of the European Commission. Windt and Klaij [5] demonstrated ReFRESCO's adaptive mesh refinement capability, which is in development, for two kinds of flows using two different criteria for refinement. Here, we focus on one specific aspect, the refinement close to walls, i.e. inside the boundary layer. In the next section we will discuss this, followed by a section that describes the testing programme of the implemented method. Next results are presented. The paper ends with conclusions.

2 Adaptive mesh refinement in the near-wall region

To capture the high gradients in the boundary layer, grids need to be clustered towards the wall. The aspect ratio of cells close to the wall can be very high. Without the use of wall functions, aspect ratios can easily exceed 1 million when calculating the flow around a ship at model scale and will be even higher for full scale (Re $= 10^9 - 10^{10}$). Straightforward isotropic refinement (dividing a cell in 8) leads to numerical problems because eccentricity will be too high; construction of the cell face variables from the cell centre variables will be inaccurate. As an example consider the boundary layer mesh plotted in the left part of Fig. 1. Due to a certain mesh refinement criterion a cell is refined while the adjacent cell is not. To avoid this, adjacent cells are refined as well as shown in the right part of the figure. Hence the column structure of the boundary layer mesh is maintained.

A second aspect in reducing numerical errors, is that cells are not split up in the direction parallel to walls. The decision to refine a cell isotropically or anisotropically is done by checking the angle between the face normal vector and the line connecting the cell and face centre or by checking the aspect ratio. The aspect ratio components of a cell are calculated by $a_i = \max(h_j)/h_i$ for $j = 1..3, j \neq i$ and with h_j the distance between two opposite faces. A third aspect is refinement on the walls itself. With local refinement the resolution of the wall mesh increases and consequently the geometry will be described more accurately. But this is only true if the newly created boundary nodes are projected to the exact geometry. If the nodes are not projected, it can lead to peculiar results even if the initial grid is rather dense. An example of such a solution is presented in Fig. 2. The figure shows the mesh on a tanker hull with and without adaptive mesh refinement. The top figure plots the unstructured initial mesh. The grid is very coarse, especially at the bilge of the ship. The dashed circle denotes a rather distorted cell due to the insufficient resolution in this region. The middle figure plots the mesh after several refinement steps. The curved bilge region is now much better modelled
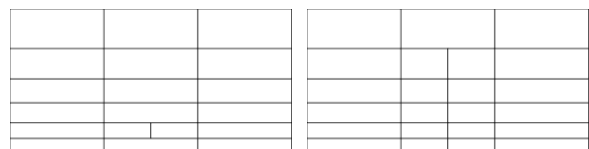
Fig. 1. *2D example of refinement in the boundary layer grid. Left figure: not robust, right figure: robust.*

by the mesh. The two bottom figures show a closer view of the region inside the dashed circle. It shows what happens without projection. The thicker lines show the mesh without refinement. The mesh is refined but this leads to a dent in the surface. The cell marked by the dots is refined, edges are split in two and new nodes are created on the straight edges. The new node on the middle of the original face follows from the new edge nodes and is located quite far from the original geometry. After the first refinement even more resolution was added to solve the gradients at the edge of the dent. Of course in this example the
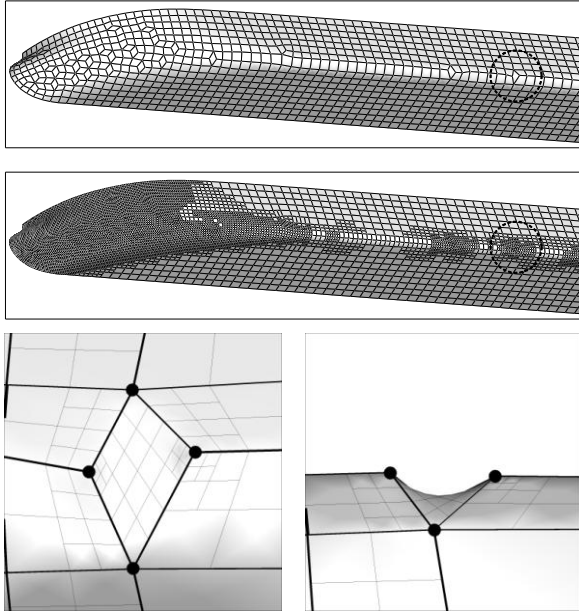
Fig. 2. *Example of adaptive mesh refinement with and without (bottom figures) wall node projection.*

initial mesh is much too coarse to model the curvature of the surface, but in principle this always happens without projection, although at a smaller scale. At MARIN, for ReFRESCO, we mainly build meshes using two commercial available packages, GridPro [6] and HEXPRESS [7]. GridPro generates block structured grids with good quality, especially near the body. HEXPRESS generates unstructured, fully hexahedral based meshes, with reasonable-quality inflation layers to capture the near-wall flow. Both packages use the STereoLithography (STL) format. STL describes unstructured triangulated surfaces. The number of triangles can be huge so projection needs to be fast. It is done as follows:

- Search for the closest vertex of the STL surface. This can be efficiently done using an octree structure which is much faster ($O(logN)$) than a simple linear search ($O(N^2)$).
- Calculate the closest distance between the node and all triangles connected to this closest STL vertex. The minimum distance between a point and a triangle is calculated by finding the minimum of the function describing the distance between any point on the triangle and the node [8].
- If the projected point is on the interior of one of the triangles a good projection is found. If the projected point is on the edge of the group of triangles, the projection might be outside the group. In this case an extensive (simple but slow) search is performed through all the triangles of the STL surface.

3 Testing method

To test several methods of refinement inside the boundary layer, we consider the flow around a sphere at a Reynolds number equal to 100 [9]. At this Reynolds number the flow is steady. The flow separates from the sphere and forms a closed recirculating wake in the shape of an axi-symmetric vortex ring. Fig. 3 plots the limiting streamlines on the sphere and the axial velocity field at an y-constant plane through the centre of the sphere. The testing consisted of using different initial meshes, different refinement strategies and different levels of refinement:

A. Use 4 different initial grids:
  1. Multi-block structured, extremely coarse but with near-wall clustering (4.448 hexahedral elements);
  2. Multi-block structured, coarse and near-wall clustering (28.672 hexahedral elements);
  3. Unstructured mesh, extremely coarse and near-wall clustering (6.384 hexahedral elements);
  4. Multi-block structured, extremely coarse and NO near-wall clustering: near-wall spacing about 0.5 times the radius (R) of the sphere (2.048 hexahedral elements).
B. Use 3 different refinement strategies:
  1. Isotropic refinement, do not touch the boundary layer grid: exclude cells from refinement if the minimum edge length is below 2% of R;
  2. Anisotropic refinement, preserve column structure, NO projection to STL;
  3. Anisotropic refinement, preserve column structure, projection to STL.
C. Use 3 different levels of the threshold parameter for the refinement criterion:
  1. $J_e = 1 \times 10^{-3}$
  2. $J_e = 1 \times 10^{-4}$
  3. $J_e = 1 \times 10^{-5}$

A. Grid generation

Although the flow is axisymmetric the computational domain consists of a rectangular three-dimensional domain. The sphere has a diameter of $1m$ and its centre is located at the origin. The sphere is placed in a tunnel with the inflow boundary 10m upstream and the outflow boundary 20m downstream the sphere. The tunnel walls are located at 12m away from the centre. A free slip condition is imposed on the tunnel walls. A straightforward multi-block grid was built (32 blocks). The mesh is clustered towards the sphere with a near-wall cell size equal to $10^{-3}m$ using geometrical progression with common ratio equal to 1.2.

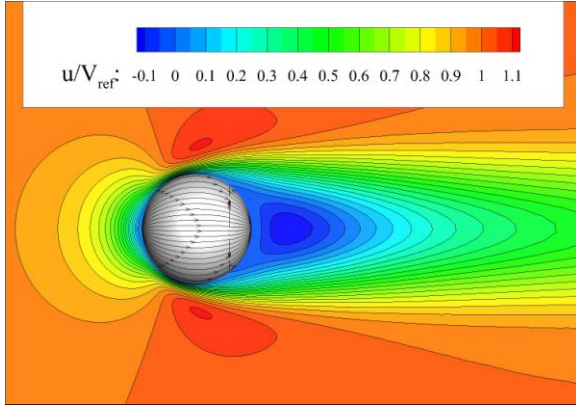The near-wall spacing is deliberately quite small ($y^+ < 0.02$) to test the grid adaptivity in the near-

Fig. 3. *Flow around a sphere at $Re = 100$. Limiting streamlines and axial velocity at the symmetry plane.*

wall region. The number of cells (before the stretching) is equal in all blocks and differs from $4 \times 4 \times 4$ for the coarsest grid to $80 \times 80 \times 80$ for the finest grid. In total, 16 grids are generated. The unstructured mesh is built using HEXPRESS. It is also extremely coarse: the initial cell size is set to $3m$ in all directions. The mesh is refined locally around the sphere using 3 refinement levels only. The near-wall mesh consists of 24 layer with using similar settings as the structured mesh.

B. Refinement strategy

The first calculation, using adaptive mesh refinement, was without any special treatment of the near-wall mesh. The calculation was not successful: after the first refinement step convergence of the solver decreased significantly and after the second step the solver diverged. High aspect ratio cells in the vicinity of the sphere were marked for refinement while cells adjacent to the sphere were not. One way to regain convergence is to prevent grid refinement close to walls. This was done by excluding cells from refinement if the minimum edge length of a specific cell was below $10^{-2}m$. This is refinement strategy B1 presented earlier. The second refinement strategy (B2) is using anisotropic refinement. As explained, refinement parallel to the wall is not allowed if aspect ratios are high. Besides that the column structure of the near-wall grid is maintained. The third strategy (B3) is similar to B2 except that now the new wall faces nodes are being projected. The geometry is described by an STL-surface consisting of 62.248 triangles. The maximum edge length of the triangles is below $0.6\% R$ and the maximum angle between two triangles is below 1.7°.

C. Refinement criterion

The criterion used is an error estimator. In the streamline project, Eskilsson and Bensow [10] introduced this finite element estimator in a finite

volume setting. The error estimator, based on jump values, following Bernard [11], is defined as:

$$J_e = \sqrt{\frac{e_e^2}{2\|\Phi\|_{L^2}^2}}$$

with e_e the local error of an element and $\|\Phi\|_{L^2}^2$ the L^2 norm of a scalar variable. The local error of an element is approximated by:

$$e_e^2 = \frac{\Delta}{4N} \sum_{k=1}^{N} (\Phi_L - \Phi_R)^2$$

with N the number of element faces and Δ the volume of the element. The left and right values of a face, Φ_L and Φ_R , are simply given by the face neighbouring cell values. In the calculations presented here, the pressure and velocity magnitude are used as quantities for the jump estimator.

4 Results

Before showing calculations using adaptive mesh refinement, a systematic grid study is presented. These calculations, using the series of structured grids, are used to qualify the computations using adaptive mesh refinement. All calculations have been done using ReFRESCO and have been converged very well. Maximum residuals (L_∞) have been reduced at least nine orders and the maximum (dimensionless) changes between two consecutive iterations are below 10^{-8}. For the calculations with adaptive mesh refinement this is six orders and 10^{-5} respectively. For all calculations discretisation of convective fluxes is done using the QUICK [13] scheme.

Two aspects of the flow are considered. The drag of the sphere and the size of the wake. The drag of the sphere is defined as:
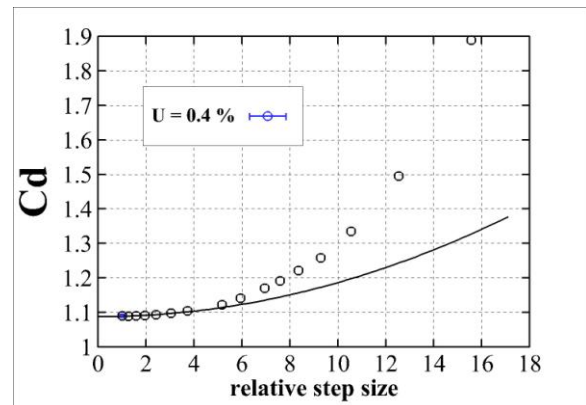

Fig. 4. *Resistance versus relative step size.*

$$Cd = \frac{F_x}{\frac{1}{2}\rho V^2 \pi R^2}$$

with F_x the total force in the direction of the flow, ρ density, V the inflow velocity and R the radius of the sphere. The calculated drag coefficient Cd can be separated in the frictional part Cd_f and pressure part Cd_p. The size of the wake is defined as the non-dimensional length of the recirculating wake given by the distance between the back of the sphere and the point on the axis where the axial velocity changes sign, divided by the diameter of the sphere.

Fig. 4 plots a result of the systematic grid study. The figure shows the calculated resistance coefficient versus the relative step size. Following [12] the numerical uncertainty is estimated with power series expansions as a function of the typical cell size. These expansions, of which four types are used, are fitted to the data in the least squares sense. The selection of the best error estimate is based on the standard deviation of the fits. The figure also shows the fit through the six finest solutions. The estimated uncertainty is 0.4%. Hence the predicted drag coefficient Cd is equal to 1.090 ± 0.005. This is in good agreement with Jones and Clarke who found a drag coefficient of 1.087 and nearly equal to results of Tabata and Itakura [4] who found 1.0900 ± 0.0003. The calculated length of the wake is slightly more depending on the grid density. We find 0.86 ± 0.02. The prediction however is good enough to demonstrate the accuracy of the grid adaptivity method quantitatively.

Next, calculations using adaptive mesh refinement are presented. A refinement step is started if the maximum residuals have been reduced below 10^{-8} or if the maximum of 1000 iterations per refinement step is reached. The number of refinement steps depends on the case and varies from 2 to 10. First, we illustrate the three different refinement strategies in the near-wall region. Fig. 5 shows the face distribution on the sphere and a contour plot of the number of refinement levels at the vertical symmetry plane. The top figure (method B1) shows that cells adjacent to the sphere are not refined. The number of refinement levels increases with increasing distance from the sphere. It also shows that faces on the sphere itself are not refined. Hence the shape of the geometry is determined by the initial grid. In this case the initial grid is very coarse and obviously the flow around this kind of geometry is not realistic. However, in general it is difficult to know in advance what resolution is required to obtain a certain accuracy. Therefore grid refinement close to walls is mandatory.

The middle figure shows the results using method B2. Now the cells close and adjacent to the sphere are refined as well. The mesh on the whole sphere is
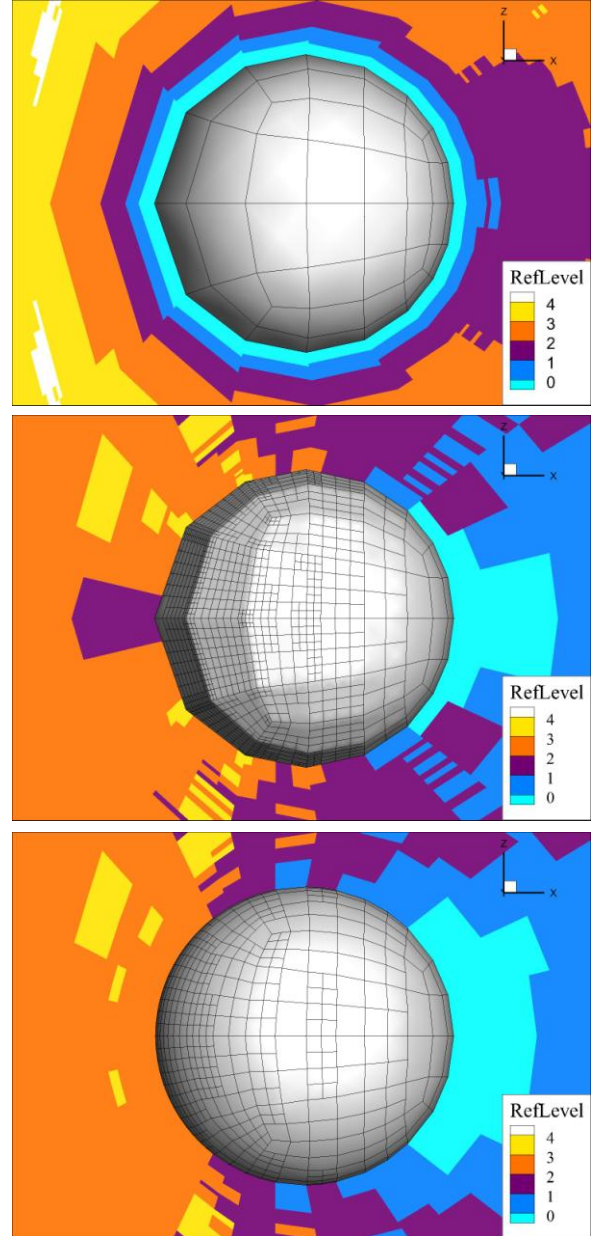
Fig. 5. *Faces on the sphere and a contour plot of the number of refinement levels. From top to bottom: calculation A1-B1-C2, A1-B2-C2 and A1-B3-C2.*

refined except for the downstream part. The newly created nodes on the sphere are not projected on the sphere but are still located on the geometry described by the initial wall grid. Reassuring is that at the knuckle lines the mesh becomes extra fine to solve the higher gradients in the flow.

The third method (B3) is shown in the bottom figure. Now the geometry of the sphere is much better described by the final wall grid.

Table 1 gives an overview of the calculated drag coefficients and wake length. 6 plots the calculated drag coefficient versus the final number of cells. In the table, the percentages present the error, relative to the solution obtained with the finest structured grid, using no adaptive mesh refinement. The results obtained with projection to the exact geometry are shaded (table) or filled (figure). All calculations show that reducing the threshold parameter J_e of course increases the final number of cells, but more interesting, differences between consecutive results (using different threshold parameters) reduce significantly. The pressure part of the drag is more dependent on the grid density than the frictional part. The most sensitive to the grid is the wake length. Although all calculations converge to a constant value, only in case of projection to the exact geometry, the drag and wake length end up with the correct value. No projection leads to an under prediction of the resistance. Also with a non-clustered initial mesh the calculated forces are quite accurate, but the number of cells increase rapidly because many (low aspect ratio) cells are added close to the wall. The calculations also show that with a finer initial mesh the difference between projection or no projection is smaller. In general we conclude that with adaptive mesh refinement a certain accuracy can be obtained using considerably less elements than with a structured mesh.

5 Conclusions

Adaptive mesh refinement of the near-wall grid has been implemented in ReFRESCO successfully. The method is demonstrated for the flow around a sphere. The calculations show that without local refinement on the wall and without projection of new face nodes on the exact geometry, results will be inaccurate. With projection an accurate solution is obtained using considerably less cells compared to calculations without adaptive mesh refinement.

ACKNOWLEDGEMENTS

References

[1] Vaz G, Jaouen F, Hoekstra M. Free-Surface Viscous Flow Computations. Validation of URANS Code FreSCo. In: ASME 28th International Conference on Ocean, Offshore and Arctic Engineering, OMAE2009, June 2009.

[2] Wackers J, Ait Said K, Deng GB, Queutey P, Visonneau M. Adaptive Grid Refinement Applied to RANS Ship Flow Computation. In: 28th Symposium on Naval Hydrodynamics, September 2010.

[3] Wackers J, Leroyer A, Deng GB, Queutey P, Visonneau M. Adaptive grid refinement for hydrodynamic flows. Computers & Fluids 55, 85-100 (2012).

[4] Streamline http://www.streamline-project.eu; May 2012.

[5] Windt J, Klaij, CM. Adaptive Mesh Refinement in MARIN's Viscous Flow Solver ReFRESCO: Implementation and Application to Steady Flow. In: MARINE 2011, IV International Conference on Computational Methods in Marine Engeneering, September 2011.

[6] GridPro http://www.gridpro.com; May 2012.

[7] HEXPRESS http://www.numeca.com; May 2012.

[8] http://www.geometrictools.com/Documentation/DistancePoint3Triangle3.pdf; May 2012.

[9] Jones DA, Clarke DB. Simulation of Flow Past a Sphere using the Fluent Code. Maritime Platforms Division, DSTO Defence Science and Technology Organisation, Australia, December 2008.

[10] Eskilsson C, Bensow RE. A Mesh Adaptive Compressible Euler Model for the Simulation of Cavitating Flow. In: MARINE 2011, IV International Conference on Computational Methods in Marine Engineering, September 2011.

[11] Bernard PE. Discontinuous Galerking methods for geophysical flow modelling. PhD thesis, Université catholique de Louvain, 2008.

[12] Eca L, Hoekstra M. A Procedure for the Estimation of the Numerical Uncertainty of CFD Calculations based on Grid Refinement Studies. To be published. Submitted to Journal of Computational Physics.

[13] Hoekstra M. Numerical simulations of ship stern flows with a space-marching Navier-Stokes method. PhD thesis, Delft University, 1999.

[14] Tabata M, Itakura K. A precise computation of drag coefficients of a sphere, Int. J. Computational Fluid Dynamics 9, 303, 1998.

Table 1. *Adaptive mesh refinement study. Calculated drag coefficient and recirculating wake length for the sphere at Re = 100.*

| Init. grid	Ref. strat.	Ref. level	# of cells	Cd_p		Cd_f		Cd		Wake length	
A1	B1	C1	9.404	0.70557	(17.70 %)	0.56516	(-1.09 %)	1.27073	(16.61 %)	0.525	(-39.10 %)
		C2	137.420	0.58708	(6.82 %)	0.49872	(-7.18 %)	1.08580	(-0.36 %)	0.773	(-10.32 %)
		C3	907.090	0.55092	(3.50 %)	0.50953	(-6.19 %)	1.06045	(-2.69 %)	0.801	(-7.08 %)
	B2	C1	5.824	0.83480	(29.55 %)	0.59660	(1.80 %)	1.43141	(31.35 %)	0.528	(-38.75 %)
		C2	124.100	0.56095	(4.42 %)	0.52609	(-4.67 %)	1.08704	(-0.25 %)	0.798	(-7.42 %)
		C3	2.040.790	0.52916	(1.51 %)	0.53069	(-4.25 %)	1.05984	(-2.74 %)	0.825	(-4.29 %)
	B3	C1	5.824	0.75038	(21.81 %)	0.62951	(4.82 %)	1.37989	(26.62 %)	0.514	(-40.37 %)
		C2	99.064	0.52602	(1.22 %)	0.57770	(0.06 %)	1.10372	(1.28 %)	0.816	(-5.34 %)
		C3	1.513.553	0.51335	(0.06 %)	0.57792	(0.08 %)	1.09127	(0.14 %)	0.857	(-0.58 %)
A2	B2	C1	6.601	0.71835	(18.87 %)	0.61037	(3.06 %)	1.32872	(21.93 %)	0.235	(-72.74 %)
		C2	56.646	0.57195	(5.43 %)	0.52938	(-4.37 %)	1.10133	(1.06 %)	0.648	(-24.83 %)
		C3	760.167	0.52460	(1.09 %)	0.53353	(-3.99 %)	1.05812	(-2.90 %)	0.808	(-6.26 %)
	B3	C1	6.601	0.71831	(18.86 %)	0.61030	(3.05 %)	1.32860	(21.92 %)	0.235	(-72.74 %)
		C2	41.553	0.52484	(1.11 %)	0.58385	(0.63 %)	1.10870	(1.74 %)	0.664	(-22.97 %)
		C3	477.549	0.51359	(0.08 %)	0.57673	(-0.03 %)	1.09032	(0.05 %)	0.849	(-1.51 %)
A3	B2	C2	67.914	0.55701	(4.06 %)	0.57429	(-0.25 %)	1.13129	(3.81 %)	0.808	(-6.26 %)
		C3	1.036.512	0.51799	(0.48 %)	0.56743	(-0.88 %)	1.08542	(-0.40 %)	0.851	(-1.28 %)
	B3	C2	61.705	0.53957	(2.46 %)	0.58319	(0.57 %)	1.12276	(3.03 %)	0.801	(-7.08 %)
		C3	791.590	0.51355	(0.07 %)	0.57685	(-0.01 %)	1.09040	(0.06 %)	0.858	(- 0.46 %)
A4	B3	C1	11.722	0.44038	(-6.64 %)	0.57317	(-0.35 %)	1.01355	(-6.99 %)	0.415	(-51.86 %)
		C2	169.234	0.50348	(-0.85 %)	0.57347	(-0.32 %)	1.07696	(-1.17 %)	0.889	(3.13 %)
		C3	3.566.306	0.50764	(-0.47 %)	0.58203	(0.46 %)	1.08967	(-0.01 %)	0.887	(2.90 %)
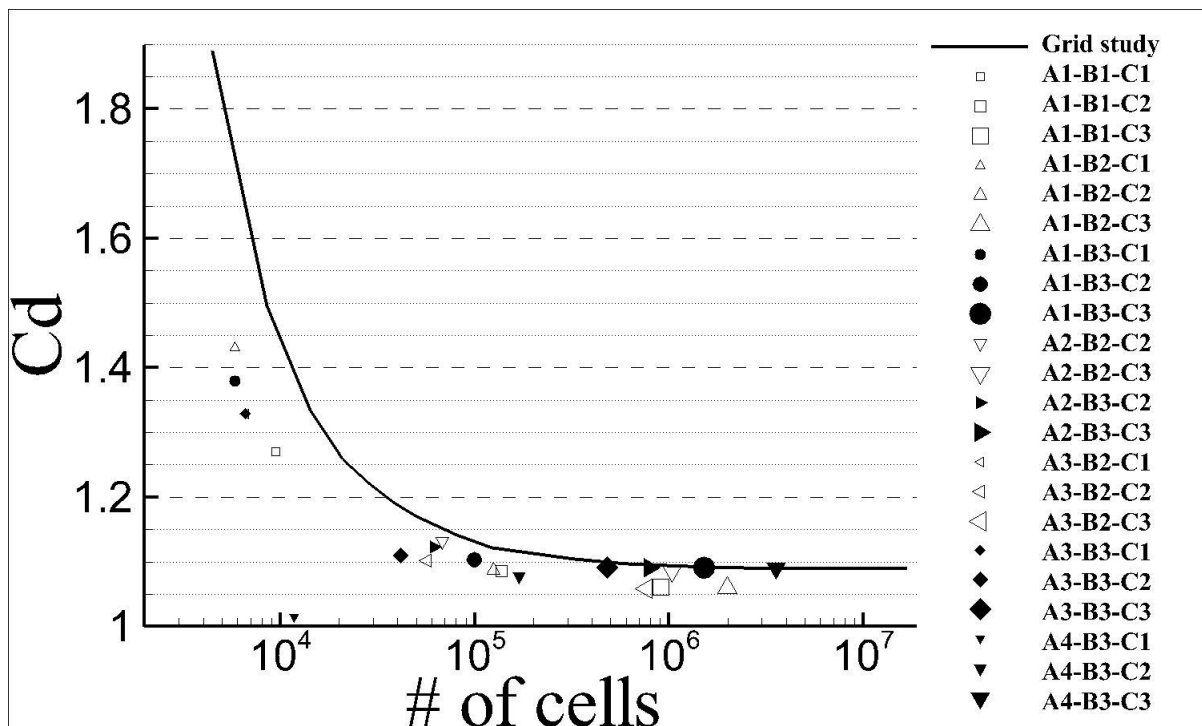
Fig. 6. *Drag coefficient versus the number of mesh elements.*

Co-simulation in fluid-structure interaction problem with rigid bodies

Camille Yvin[1,2], Alban Leroyer[1] and Michel Visonneau[1]

camille.yvin@eleves.ec-nantes.fr

[1] *Laboratoire de recherche en Hydrodynamique, Energétique et Environnement Atmosphérique, École Centrale de Nantes, CNRS-UMR 6598, 44321 Nantes Cedex 3, France*

[2] *Sirehna/DCNS Research, 44321 Nantes Cedex 3, France*

1 Introduction

Co-simulation (Co-operative simulation) is a simulation methodology that allows several numerical solvers to work together in order to solve a complex problem [Jürgens, 2009]. It will be one of the biggest change in work methods that will appears in engineering during the next years. It is possible and interesting because current numerical methods are enought mature to solve complex models in specific science fields (structural dynamics, fluid dynamics, thermodynamics, combustion, electromagnetism etc.). Fluid-structure interaction problems are commonly encountered in naval architecture and co-simulation can be employed to efficiently study this kind of situations.

Co-simulation is not only a method which allows scientist to resolve a general problem but an efficient work method too. Indeed, the usage of different solvers permits a very strong numerical adaptation for each elementary problem [Kassiotis, 2009] and naturally allow collaboration between different development team. From a practical point of view, the validation and maintenance of the solvers are also more efficient [Hou et al., 2012].

Fluid-Structure Interaction (FSI) problems can be seen as a unique global problem and the resolution can be performed with a monolithic approach (usely with a unique solver) [Hübner et al., 2004], [Heil, 2004], [Wick, 2011]. This approach is difficult to implement and the resolution is not an easy task [Dunne and Rannacher, 2006], [Longatte et al., 2009]. The partitioned approach (or block-iterative method [Cervera et al., 1996]) is most often used because of its simplicity of implementation. It consist in solving the fluid and structure problems in a segregated way. This approach is used here because it can be used in a co-simulation context. However, its the convergence can be slow [Degroote et al., 2009] and the coupling algorithm stability is not guarantee [Wall et al., 2006] so additional works have to be done before its application.

In this work, two different general solvers are used : one to solve the fluid problem and another to solve the structure solver. They are respectively ISIS-CFD and MBDyn. Section 2 and section 3 briefly describe these two solvers. Section 4 introduces the FSI problem and the coupling algorithm used. Section 5 describes how the added mass effect is taken into account and section 6 explicits the evaluation of the relaxation operator. An application case is proposed at section 7.

2 ISIS-CFD solver

ISIS-CFD is available as a part of the FINE[TM]/Marine computing suite which is dedicated to marine applications. It is an incompressible unsteady Reynolds-averaged Navier-Stokes (RANS) solver developed by the ECN-CNRS [Queutey et al., 2012]. This solver is based on the finite volume method to build the spatial discretisation of the transport equations. Pressure-velocity coupling is obtained through a Rhie & Chow SIMPLE-type method : in each time step, the velocity updates come from the momentum equations and the pressure is given by the mass conservation law, transformed into a pressure equation. An Arbitrary Lagrangian Eulerian (ALE) formulation is used to take into account modification of the fluid spatial domain. It is associated with robust and fast grid deformation techniques [Leroyer and Visonneau, 2005].

The discretisation is face-based. While all unknown state variables are cell-centered, the systems of equations solved within a implicit time stepping procedure are constructed face by face. Fluxes are computed in a loop over the faces and the contribution of each face is then added to the two cells next to the face. This technique poses no specific requirements on the topology of the cells. Therefore, the grids can be completely unstructured and cells with an arbitrary number of arbitrarily-shaped faces are accepted. Free-surface flow is addressed with an interface capturing method, by solving a conservation equation for the volume fraction of water, discretised with specific compressive discretisation schemes [Queutey and Visonneau, 2007]. The code is fully parallel using the MPI (Message Passing Interface) protocol. An automatic adaptive grid refinement technique is also included [Wackers et al., 2012].

3 MBDyn solver

MBDyn (Multy-Body Dynamics), is an open-source solver under the GNU'S GPL license developed at the *Dipartimento di Ingegneria Aerospaziale* of the *Politecnico di Milano*. It is intended for the simultaneous solution of multi-discipline problems including non-linear dynamics, aero-servo-elasticity, smart piezo-structural components, electric and hydraulic components. It aims at the modelling of complex systems [Ghiringhelli et al., 1999].

To solve the kinematics laws of a multi-body mechanical system, the Redundant Coordinate Set (RCS) formulation is used. This means that every inertial body has 6 rigid body Degrees of Freedom (DOF) even if they are constrained by joints for instance. Additional constraint equations are added which introduce algebraic unknowns that are analogous to the Lagrange multipliers and directly represent the reaction forces and couples [Masarati, 1999]. All these equations are written in form of a set of first order Algebraic Differential Equations (ADE). Thus every rigid body is represented by 12 equations (6 equations that represent the momenta and 6 others the Newton's law that link the rate change of momenta with forces). The RCS formulation leads to very sparse system matrices which need to be handled by specific linear algebra solvers. The ability to take into account multidisciplinary complex systems and the simplicity of implementation are the main advantages of this formulation.

4 FSI problem in general

FSI problems can be seen as a particular application of decomposition domain methods which consist in solving a boundary value problem by splitting it into smaller boundary value problems on subdomains. Theses methods are suitable for parallel computing but also for FSI problems because the interaction occurs only at the interface between the fluids and the solids. It is the reason why it's interesting to express this problem with the Steklov-Poincaré operator and its inverse. These operators can be seen as the fluid or the solid solver.

Thus, the physical domain $\bar{\Omega}$ is split in a fluid $\bar{\Omega}^{\mathrm{f}}$ and solid domain $\bar{\Omega}^{\mathrm{s}}$. The Steklov-Operator operator $\mathcal{S}$, and its inverse $\mathcal{S}^{-1}$, are defined for each domain as :

$$\mathcal{S}_{\mathrm{d}}\left(\mathbf{x}^{d}\right) = \boldsymbol{\lambda}^{d} \qquad \mathcal{S}_{\mathrm{d}}^{-1}\left(\boldsymbol{\lambda}^{d}\right) = \mathbf{x}^{d} \qquad (4.1)$$

where the superscript d represents the domain in consideration, $\mathbf{x}$ is the position vector and $\boldsymbol{\lambda}$ the stress. At the fluid-structure interface $\Gamma = \bar{\Omega}^{\mathrm{f}} \cap \bar{\Omega}^{\mathrm{s}}$, the interface continuity and the action-reaction principle have to be respected :

$$\mathbf{x}^{s} = \mathbf{x}^{f} = \mathbf{x}^{\Gamma} \quad \text{and} \quad \boldsymbol{\lambda}^{s} + \boldsymbol{\lambda}^{f} = \mathbf{0} \qquad \text{on } \Gamma \quad (4.2)$$

These two equations can be expressed with the operators previously defined in different formulation as for instance the Steklov-Poincaré, the Picard (fixed-point) or the Newton (root-finding) formulation [Deparis et al., 2006]. The first one is suitable when the time simulation to solve the fluid and the structure problem are on the same order because the parallelization is naturally obtained ($\mathcal{S}_{\mathrm{s}}$ and $\mathcal{S}_{\mathrm{f}}^{-1}$ or their inverse are not composed). This is not the case here because the fluid problem needs more computation time than the solid problem. This is due to the high number of unknowns in the fluid problem. To use a Newton strategy, the problem Jacobian must be computed or approximated. It can be must costly than solving a simple fixed-point equation because of the non-linearity of the coupling terms [Dettmer and Perić, 2008]. In this work, a simple implicit Block Gauss-Seidel (BGS) approach is used to solve the following fixed point formulation :

$$\mathcal{S}_{\mathrm{f}} \circ \mathcal{S}_{\mathrm{s}}^{-1}\left(-\boldsymbol{\lambda}^{f}\right) = \boldsymbol{\lambda}^{f} \qquad (4.3)$$

The coupling and time iterations are respectively denoted as i and n. A simple implicit BGS algorithm, as the one presented at the Fig. 1 or Eq. (4.5) and (4.5), is easy to implement but need a lot of coupling iteration before reaching convergence and can be rapidly unstable when the added-mass effect become important [Förster et al., 2007].

$$\mathbf{x}^{\Gamma}\big|_{n+1}^{i+1} = \mathcal{S}_{\mathrm{s}}^{-1}\left(-\boldsymbol{\lambda}^{f}\big|_{n+1}^{i}\right) \qquad (4.4)$$

$$\boldsymbol{\lambda}^{f}\big|_{n+1}^{i+1} = \mathcal{S}_{\mathrm{f}}\left(\mathbf{x}^{\Gamma}\big|_{n+1}^{i+1}\right) \qquad (4.5)$$

In order to reduce the simulation time, Aitken Δ^{2} relaxation technique is often used [Küttler and Wall, 2008]. This technique is based on a geometrical approximation (tangent method) of the coupled problem. To be efficient, the solvers have to produce physical results, and so, each operator needs to be solved accurately. This means that for an implicit coupling algorithm, the fluid problem has to be solved several times at each time-step which is not a good solution.

In this work, the classical Steklov-Poincaré operator for the fluid problem is modified to reduce CPU time of this part. This new operator, denoted as $\mathcal{S}_{\mathrm{f}}^{*}$, doesn't represent a global fluid resolution any more but only one Picard iteration of the fluid solver. It can be seen as a linearised version of the Steklov-Poincaré operator. In a few words, the fluid-problem converged during the coupling loop.

5 Added-mass effect

The added-mass effect often occurs in naval architecture because the density of the water is not negligible with respect to the structure one. To take into

account this destabilising added-mass effect, the artificial added-mass technique is often used. To illustrate this point in a co-simulation context, a one-dimensional case is presented. A rigid body of mass m has one degree of freedom in translation x. The fluid force and the structure force (gravity, joints, etc.) are respectively denotes as f_f and f_s and respectively computed by the fluid and the structure solver. The added mass effect is the part of the pressure fluid force which is proportional and opposed to the acceleration of the body. The fluid force is splitted accordingly and the added mass part is denoted by $-m_a \cdot \ddot{x}$ and the other part by $\bar{f}_f$. This splitting is just for the presentation because in reality a classical CFD solver can't separate the added mass effect from the total fluid force. The equations which has to be solved is then :

$$m \cdot \ddot{x} = f_s + f_f = f_s + \bar{f}_f - m_a \cdot \ddot{x} \qquad (5.1)$$

The original artificial added mass technique affects the inertia of the body by an artificial added mass coefficient $\overline{m_a}$ and thus decrease the dependency of the right hand member with the acceleration. The corresponding equation is :

$$(m + \overline{m_a}) \cdot \ddot{x}\,\big|_{n+1}^{i+1} = f_s\,\big|_{n+1}^{i} \qquad (5.2)$$
$$+ \bar{f}_f\,\big|_{n+1}^{i} - m_a \cdot \ddot{x}\,\big|_{n+1}^{i} \qquad (5.3)$$
$$+ \overline{m_a} \cdot \ddot{x}\,\big|_{n+1}^{i} \qquad (5.4)$$

A theoretical lower limit for the artificial added mass coefficient in order to guarantee the stability of the coupling algorithm can be found [Söding, 2001]. Discussion about it's optimum value can be found at the next section. The last term in the left member acts as a force and must be given by the coupling algorithm. In a co-simulation context, this not a good solution because the structure solver has to be modified due to the modification of the left member in the previous equation. To correct this, the relaxation factor α is introduced (Eq. (5.5)) and the acceleration term of the right member is approximated (Eq. (5.6)) in order to obtain a modified equation (Eq. (5.7)).

$$\alpha = \frac{1}{1 + m/\overline{m_a}} \qquad (5.5)$$

$$\overline{m_a} \cdot \ddot{x}\,\big|_{n+1}^{i} \approx f_s\,\big|_{n+1}^{i-1} + f_f\,\big|_{n+1}^{i-1} \qquad (5.6)$$

$$m \cdot \ddot{x}\,\big|_{n+1}^{i+1} = \alpha \cdot f_s\,\big|_{n+1}^{i} + (1-\alpha) \cdot f_s\,\big|_{n+1}^{i-1}$$
$$+ \alpha \cdot f_f\,\big|_{n+1}^{i} + (1-\alpha) \cdot f_f\,\big|_{n+1}^{i-1} \qquad (5.7)$$

This equation shows the link between the artificial mass technique and a simple relaxation method applied to forces. This method is still not truly satisfying in a co-simulation context because the term

$f_s\,\big|_{n+1}^{i-1}$ is generally unknown. But it can be shown that the relaxation step can be applied not to forces but to kinematics in the same way which is easier to implement.

The final fluid-structure algorithm is summarised by Eq. (5.8) and presented at Fig. 1 where $\mathbf{R}$ is the 6 DOF relaxation operator previously defined for a 1 DOF problem (Eq. (5.5)) and $\tilde{\mathbf{x}}^s$ is the interface position before the relaxation step. It's named BGS-ICF (Block Gauss-Seidel - Internal Coupling Fluid) algorithm. It can be noticed that at the first iteration of a time-step, the kinematics of the interface fluid-structure is given by a prediction of order 2 at constant acceleration.

$$\mathcal{S}_f^* \circ \mathbf{R} \circ \mathcal{S}_s^{-1}\left(-\boldsymbol{\lambda}^f\right) = \boldsymbol{\lambda}^f \qquad (5.8)$$
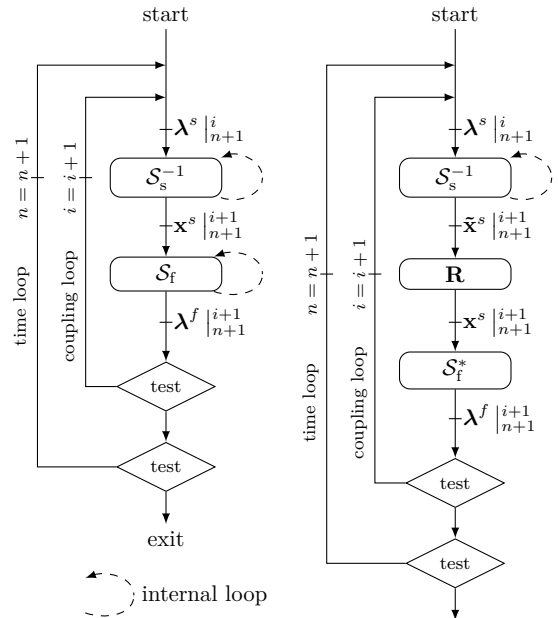

Figure 1: BGS (left) and BGS-ICF with relaxation (right) algorithms

6 Evaluation of R

As it was shown, the artificial added mass technique is not stricky similar but very close to a relaxation method. As every relaxation method, it's important to find a correct value in order to not deteriorate the convergence speed. The first numerical experiences show that a good convergence behaviour is obtained if the artificial added mass is close to the "physical" added mass.

Added mass effect is sometimes hard to tackle because reference values are not always available and furthermore it can change during the simulated time of the simulation (spatial configuration, free surface modification, etc.). This is the reason why,

an added mass pressure equation has to be implemented in ISIS-CFD to compute the added mass effect which can be represented by a square matrix of dimension 6 [Söding, 2001].

The corresponding equation can be derived from the Navier-Stokes equations by removing all terms linked to the fluid velocity (Eq. (6.1)). By taking the divergence of this equation and because the fluid velocity is divergence free, the acceleration term also vanished (Eq. (6.2)). The Green-Ostrogradski theorem is used to get an surface equation which is integrated over all the volume controls (Eq. (6.3)).

$$\frac{\partial}{\partial t} \iiint_{\Omega_a} \rho \mathbf{u} \mathrm{dv} = - \iiint_{\Omega_a} \overline{\mathrm{grad}}\,(p) \cdot \mathrm{dv} \qquad (6.1)$$

$$\iiint_{\Omega_a} \mathrm{div}\left(-\frac{\overline{\mathrm{grad}}\,(p)}{\rho} \right) \cdot \mathrm{dv} = 0 \qquad (6.2)$$

$$\oiint_{\partial\Omega_a} -\frac{1}{\rho}\overline{\mathrm{grad}}\,(p) \cdot \mathbf{n^a} \cdot \mathrm{ds} = 0 \qquad (6.3)$$

Terms are discretized as the same way than the pressure term in the Navier-Stokes equation [Queutey and Visonneau, 2007], discretization that naturally take into account the free surface discontinuity without extra equation. Boundary conditions are also the same that the one used for pressure, except at the considered body where unit acceleration are used for each DOF (Eq. (6.1)) [Söding, 2001]. It can be noticed that the resolution is discretized on the same mesh used for the flow computation.

Added mass coefficients obtained are compared to analytical solutions, bibliographical data [Blevins, 2001] on simple geometries and potential codes results for a full scale boat Cargo Series 60. Numerical experiments show good agreements with reference solutions and show that only one iteration can be enough to correctly estimate the added mass effect for one DOF even if several iterations have to be done to accurately compute the explicit terms due to the mesh non-orthogonalities. Thus, the relaxation operator can be dynamically evaluated during the simulation without penalising the simulation time.

7 Application

The present application consists to study a 2D barge with one DOF in heave. Dimensions and important physical data are given at Fig. 2. At the initial time, the barge is not at its equilibrium position ($T_0 = 0.5$ m). Dimensions of the barge are chosen in order that the added mass coefficient at rest ($C_a = m_a/m$) is large. A potential solver and the previous method exposed give $C_a \approx 9.0$. Vertical acceleration of the barge is presented at the Fig. 3 for several time-steps.

Figure 2: A barge in heave : Geometry
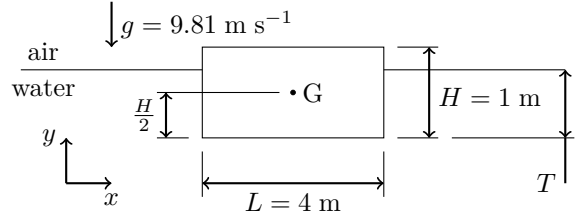
$$\rho_{water} = 1000 \text{ kg m}^{-3} \quad \rho_{barge} = 200 \text{ kg m}^{-3}$$
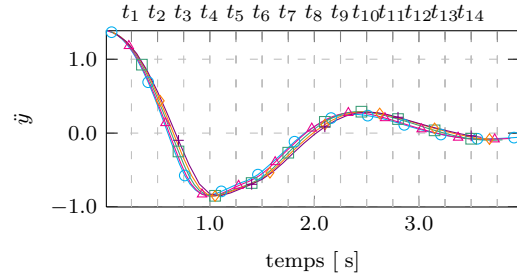
Figure 3: A barge in heave : Acceleration
○ $\Delta t = 0.010$ s, △ $\Delta t = 0.025$ s, □ $\Delta t = 0.050$ s,
◇ $\Delta t = 0.075$ s and $+$ $\Delta t = 0.100$ s

In order to analyse convergence properties of algorithms, 50 iterations by time-step are performed and the artificial added-mass coefficient is nor dynamically evaluated. The resolution of equations (5.4), (5.7) and (5.8) are respectively noticed as algorithm 1, 2 and 3. The obtained results are compared to two imposed motion simulations which are respectively noticed as algorithm a and b. The first one consist in apply the results of algorithm 1 at the first coupling iteration. For the second imposed motion simulation, a prediction with constant acceleration is used at the first coupling iteration and then the results of the algorithm 1.

Here, the time-step used is $\Delta t = 0.05$ s but same conclusions have been done for different time-step. When it is not specified, an artificial added mass close to the physical added mass is used ($\overline{C_a} = 9$). Depending on the algorithm used, kinematics or forces can be modified by the relaxation operator. If no subscript is used, this means that quantities are not modified by this operator and are directly the results of fluid or structure solvers. In the other case, the algorithm identifier is used.

Firstly, numerical simulations show that the different algorithms produce the same result when convergence is reached (Fig. 4 to 6). More precisely, the stability domain is a little larger for the algorithm 1 because no approximation is used in the artificial added mass method. Nevertheless, the observed differences are only for large time-step with small artificial added mass coefficients ($\overline{C_a} \le 2$) and much better convergence properties are observed if the relaxation operator is calculated with data that are closed to the physical added mass Fig. 8. More-

over, the comparison between solved and imposed motion simulations (Fig. 7) shows that, in this case, convergence can be reach sooner if appropriate relaxation factors are used. This means that the convergence properties of the proposed algorithm is very good because imposed motion simulations can be seen as the optimum since the result of the FSI coupling is directly imposed.
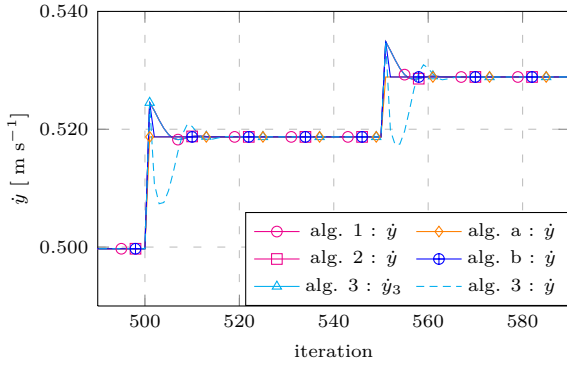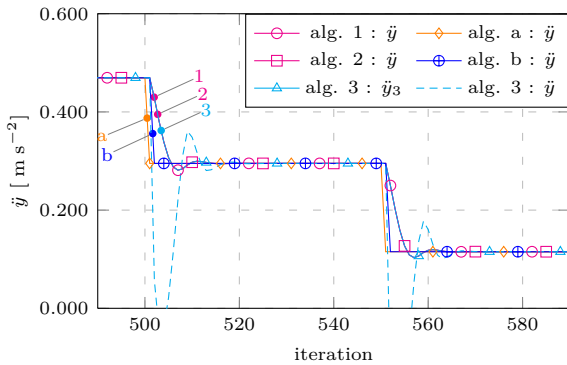

Figure 4: A barge in heave : Velocity

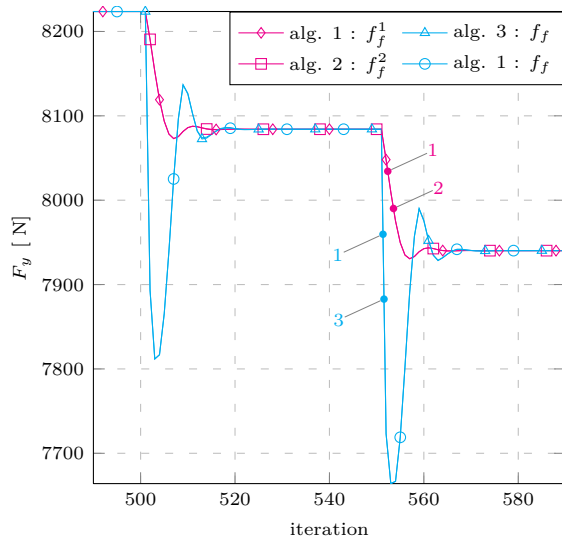Figure 5: A barge in heave : Acceleration

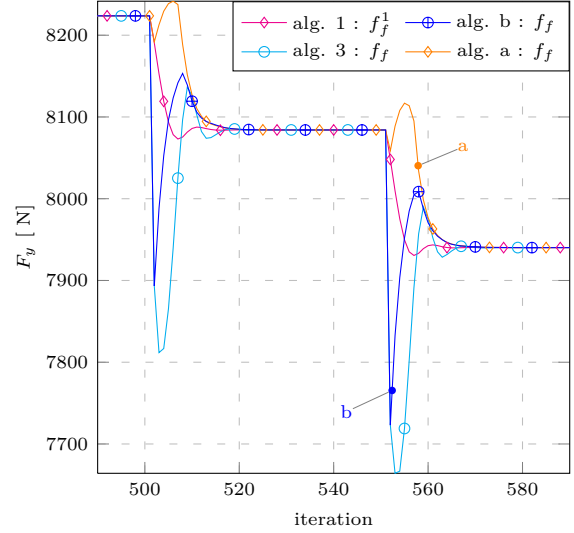Figure 6: A barge in heave : Fluid forces for solved motions

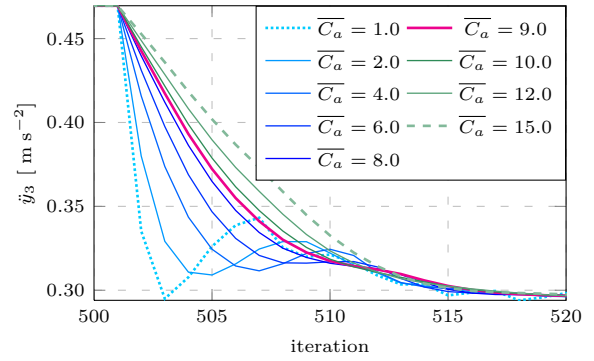Figure 7: A barge in heave : Fluid forces for solved and imposed motions

Figure 8: A barge in heave : Acceleration in function of $\overline{C_a}$

8   Conclusion

In this paper, an efficient coupling algorithm for fluid structure problems with large added mass effect is presented. The key-points of this coupling algorithm are the replacement of the Steklov-Poincaré operator by an linearised one and the resolution of an added-mass equation to correctly evaluate the relaxation operator. Comparison between solved and imposed motion simulation on a simple example show excellent convergence properties.

9   References

R. Blevins. *Formulas for Natural Frequency and Mode Shape.* Krieger, 2001.

M. Cervera, R. Codina, and M. Galindo. On the computational efficiency and implementation of block-iterative algorithms for nonlinear coupled problems. *Engineering Computations*, 13(6):4–30, 1996.

Joris Degroote, Klaus-Jürgen Bathe, and Jan Vierendeels. Performance of a new partitioned procedure versus a monolithic procedure in fluid–structure interaction. *Computers & Structures*, 87(11–12):793 – 801, 2009.

Simone Deparis, Marco Discacciati, Gilles Fourestey, and Alfio Quarteroni. Fluid–structure algorithms based on steklov–poincaré operators. *Computer Methods in Applied Mechanics and Engineering*, 195(41–43):5797 – 5812, 2006.

WulfG. Dettmer and Djordje Perić. On the coupling between fluid flow and mesh motion in the modelling of fluid–structure interaction. *Computational Mechanics*, 43:81–90, 2008.

Thomas Dunne and Rolf Rannacher. Adaptive Finite Element Approximation of Fluid-Structure Interaction Based on an Eulerian Variational Formulation. In Hans-Joachim Bungartz and Michael Schäfer, editors, *Fluid-Structure Interaction*, volume 53 of *Lecture Notes in Computational Science and Engineering*, chapter 6, pages 110–145. Springer Berlin Heidelberg, Berlin, Heidelberg, 2006.

Christiane Förster, Wolfgang A. Wall, and Ekkehard Ramm. Artificial added mass instabilities in sequential staggered coupling of nonlinear structures and incompressible viscous flows. *Computer Methods in Applied Mechanics and Engineering*, 196(7):1278 – 1293, 2007.

G.L. Ghiringhelli, P. Masarati, P. Mantegazza, and M.W. Nixon. Multi-body analysis of a tiltrotor configuration. *Nonlinear Dynamics*, 19(4):333–357, 1999.

Matthias Heil. An efficient solver for the fully-coupled solution of large-displacement fluid-structure interaction problems. *Computer Methods in Applied Mechanics and Engineering*, 193:1–23, 2004.

G. Hou, J. Wang, and A. Layton. Numerical methods for fluid-structure interaction a review. *Communications in Computational Physics*, 12(2):337–377, 2012.

Björn Hübner, Elmar Walhorn, and Dieter Dinkler. A monolithic approach to fluid–structure interaction using space–time finite elements. *Computer Methods in Applied Mechanics and Engineering*, 193(23–26):2087 – 2104, 2004.

Dominik Jürgens. Survey on software engineering for scientific applications: Reuseable software, grid computing and application. Technical report, Informatik-Bericht, 2009.

C. Kassiotis. *Nonlinear fluid-structure interaction : a partitioned approach and its application through component technology*. PhD thesis, Université Paris-Est, Êcole Doctorale MODES, 2009.

Ulrich Küttler and Wolfgang A. Wall. Fixed-point fluid–structure interaction solvers with dynamic relaxation. *Computational Mechanics*, 43:61–72, 2008.

A. Leroyer and M. Visonneau. Numerical methods for RANSE simulations of a self-propelled fish-like body. *Journal of Fluids and Structures*, 20(7):975–991, 2005.

E. Longatte, V. Verreman, and M. Souli. Time marching for simulation of fluid–structure interaction problems. *Journal of Fluids and Structures*, 25(1):95 – 111, 2009.

Pierangelo Masarati. *Comprehensive Multibody AeroServoElastic Analysis of Integrated Rotorcraft Active Controls*. PhD thesis, Dipartimento Di Ingegneria Aerospaziale, Politecnico Di Milano, 1999.

P. Queutey, G.B. Deng, J. Wackers, E. Guilmineau, A. Leroyer, and M. Visonneau. Sliding grids and adaptive grid refinement for rans simulation of ship-propeller interaction. *Ship Technology Research*, 59(2):44–58, April 2012.

Patrick Queutey and Michel Visonneau. An interface capturing method for free-surface hydrodynamic flows. *Computers & Fluids*, 36(9):1481–1510, 2007.

H. Söding. How to integrate free motions if solids in fluids. In *4ᵗʰ Numerical Towing Tank Symposium*, Hamburg, Germany, 2001.

Jeroen Wackers, Ganbo Deng, Alban Leroyer, Patrick Queutey, and Michel Visonneau. Adaptive grid refinement for hydrodynamic flows. *Computers & Fluids*, 55(0):85 – 100, 2012.

Wolfgang A. Wall, C. Förster, Malte Neumann, and Ekkehard Ramm. Advances in fluid-structure interaction. In *17th International Conference on the Application of Computer Science and Mathematics in Architecture and Civil Engineering*, Weimar, Allemagne, Juillet 2006.

Thomas Wick. Fluid-structure interactions using different mesh motion techniques. *Computers & Structures*, 89(13–14):1456 – 1467, 2011.

Investigation of Stability Failure of an Inland Tanker

Tobias Zorn, Vladimir Shigunov, FutureShip, Hamburg/Germany,
{tobias.zorn,vladimir.shigunov}@GL-group.com

Introduction

On January 13, 2011, an inland tanker *Waldhof*, loaded with sulphur acid, capsized in Rhine; this resulted in two fatalities. The investigation showed that the likely reason of the accident was wrong loading condition: the vessel was overloaded; besides, all tanks were partially filled, which led to large free surfaces in all load tanks. As a result of this loading, the initial metacentric height of the tanker was only about 0.26 m, against existing regulations. Because of exceptional flow conditions and bottom topography, the accident location is known as a hazardous location for ships. Previous to this study, multiple simulations of vessel dynamics were carried out by the Federal Waterways Engineering and Research Institute (BAW) in Karlsruhe with simplified motion simulators, to explain the capsizing process. FutureShip was commissioned to apply a more advanced simulation method, which can take into account all relevant physical phenomena in the most accurate way. Simulations based on numerical solution of Reynolds-averaged Navier-Stockes (RANS) equations, in order to investigate the influence of all factors on ship dynamics during the capsize.

Method

The aim of the study was to investigate the influence of different factors on capsize scenario. Because of nonlinear coupling between ship motions, sloshing of sulphur acid in partially filled tanks and external flow in Rhine, it is impossible to quantify the influence of different factors separately; the weighting of the different factors is nevertheless possible, if the numerical model is extended in steps. In each step, the next factor is added, and its contribution to ship dynamics is evaluated by the comparison of the results with the previous step. In all these steps, the motions of sulphur acid in the partially loaded tanks and the resulting forces and moments on the vessel were modelled with field methods; four steps of increasing complexity were used to model the external forces and moments. These steps are described below.

Influence of Sloshing in Tanks

To assess the influence of sloshing of sulphur acid in tanks on forces and moments acting on the vessel, in the first step the vessel was towed along ist trajectory following prescribed horizontal translations and heading from the BAW simulation that matched most accurately the available radar images, Fig. 1. This step of investigation considered therefore only the forces and moments on the ship, induced by sloshing in tanks, which in turn were caused by the longitudinal, transversal and yaw accelerations of the vessel. However, this step cannot quantify the influence of these forces and moments on the resulting roll motions of the vessel.
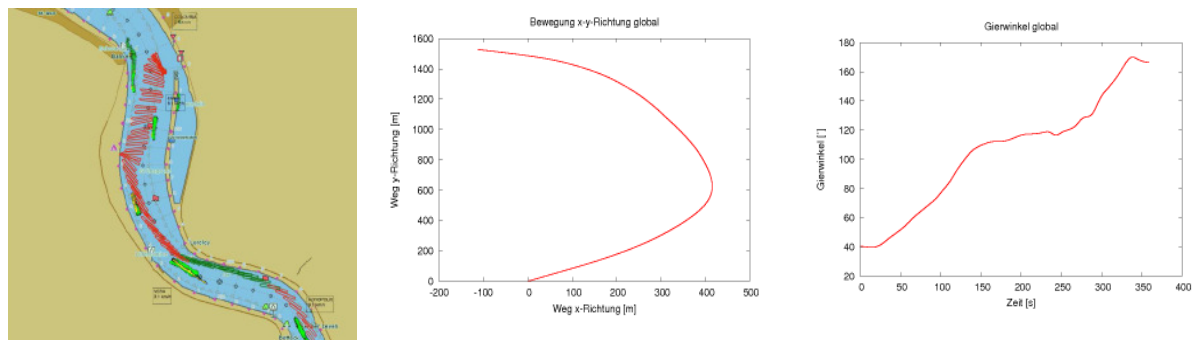

Fig. 1: Results of BAW simulation (left), used as input for ship trajectory (middle) and heading time history (right)

The computed heeling moment due to motions of the sulphur acid is shown in Fig. 2. The maximum values of the heeling moment to port and starboard are marked with circles. These results show that the resulting heeling moments from these simulations are not sufficient to cause tanker capsizing.
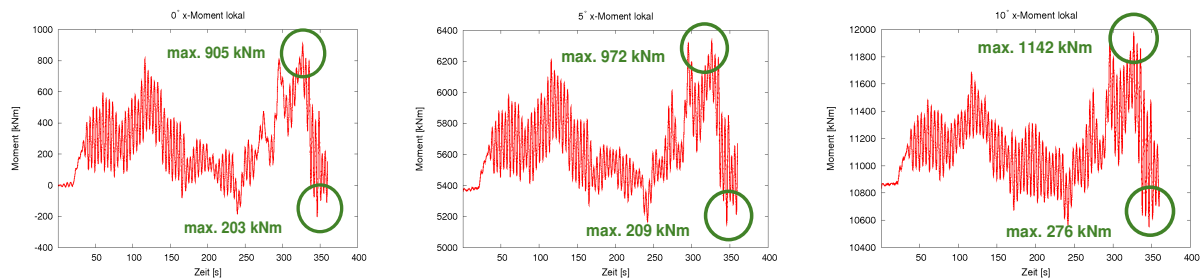

Fig. 2: Heeling moment due to motions of sulphur acid in tanks from simulations with restrained roll motion with three constant heel angles of 0° (left), 5° (middle) and 10° (right)

Influence of Free Roll

To assess the influence of forces and moments due to sloshing on roll motion of the vessel, the model on the next step of the study was extended with free roll motion. As in the first step, the time histories of the translatory horizontal motions and yaw motion were prescribed following BAW simulations.

The roll motion was integrated in time. The roll moment caused by drift forces was estimated, so that the horizontal lateral force, following from the prescribed lateral acceleration, was assumed to act at half draught. The restoring moment was calculated from the righting moment curve without free-surface correction. Fig. 3 shows the resulting time history of the roll angle. The maximum roll angle in this simulation appears sufficiently large to lead to capsize if the effects of the external flow were modelled more accurately.
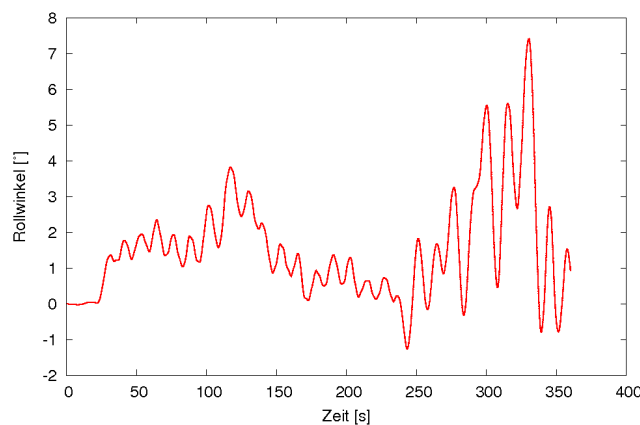

Fig. 3: Roll motion due to sloshing in tanks

Influence of External Flow

In the next step, the heeling moment due to drift forces and the restoring moment were computed directly by the integration of pressures and shear stresses over the hull surface. However, the external flow was modelled in a simplified way, neglecting the current in the river, so that the ship speed through water is equal to the ship speed over ground. The results of this simulation in Fig. 4 show that external forces have a significant influence on the roll motion of the vessel and can indeed be sufficient to cause capsizing. However, because the ship was sailing down the river, the disregard of the current in this case led to too large relative speed through water: the speed over ground was at the instant of accident about 1.7 times larger than the speed through water, i.e. the drift forces and moments were overestimated about 2.8 times.
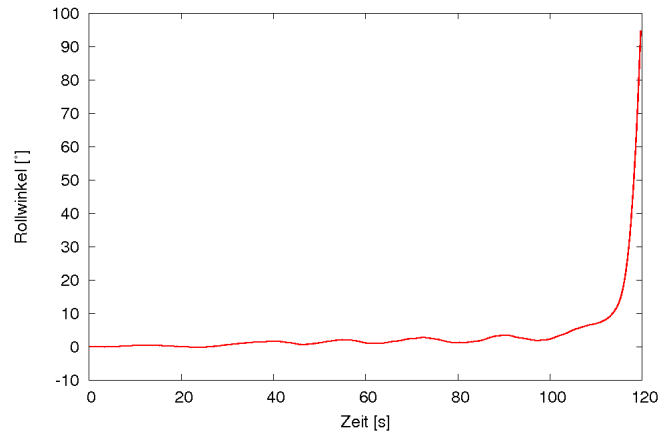
Fig. 4: Roll motion in simulation without taking into account current in the river

Simulation of Free Sailing Vessel in the River

On this step, the vessel was simulated as free in all degrees of freedom. The current in the river was computed in a preliminary simulation; the bottom topography was provided by BAW. Fig. 5 shows the stream lines from this simulation.
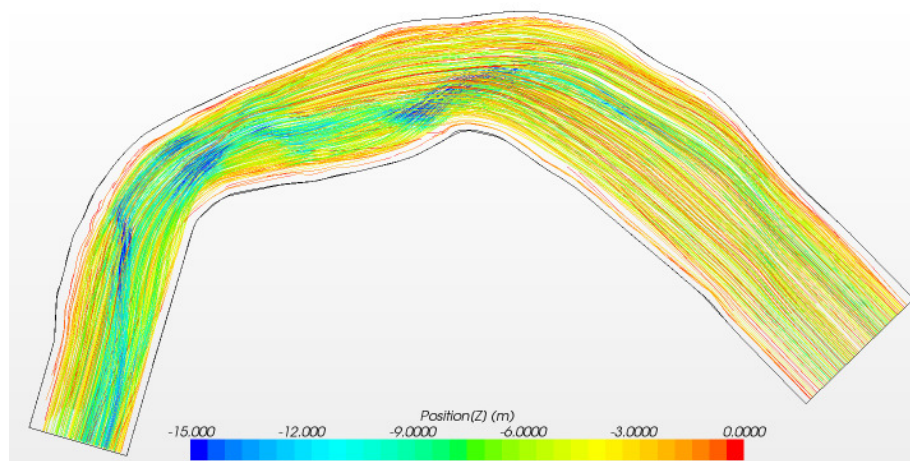

Fig. 5: Streamlines from the numerical simulation of the current in Rhine without vessel

As a starting point for the free sailing simulation, a time instant shortly before the abrupt reduction of the radar signal of the vessel was taken. The initial conditions for the free sailing simulation (vessel position, horizontal velocities, heading and yaw rate) at this time instant were taken from the BAW simulation, which best matched the radar images. Because motions and velocities in the remaining degrees of freedom at this time instant were unknown, as well as the position and distribution of velocities of the sulphur acid in tanks and external water in the river, a free simulation from this selected time instant with partly arbitrary initial conditions would have led to large disturbances in the simulation. Therefore, the ship was put into the flow at some distance up the flow and was unrestrained stepwise in all degrees of freedom: first, the ship was towed with prescribed motions in all degrees of freedom for some time after putting it into the flow, so that the disturbances in the current due to the introduction of the ship are flushed downstream from the solution domain. After that, the vessel was towed along a smooth trajectory with smoothly varied horizontal velocity and yaw angle, to the starting point of the free sailing phase, where ship position and velocities matched the data from the BAW simulation. Finally, the ship was unrestrained in all degrees of freedom. Fig. 6 shows the free surface heights in the river shortly after the start of the free sailing phase.
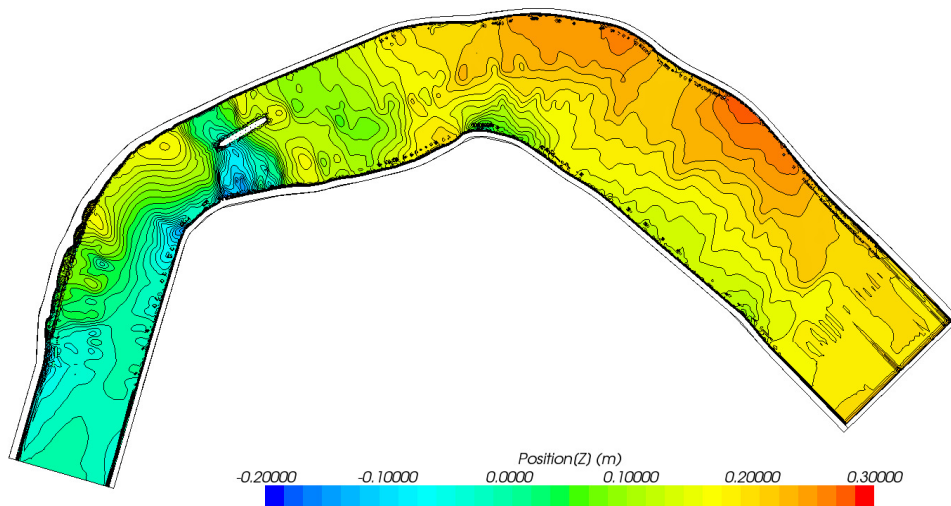
Fig. 6: Free surface height in the river during the free motion of the vessel

The relative motions between the vessel and the bottom of the river were treated in this simulation using overlapping grids; Fig. 7 shows the total simulation domain and the numerical grid, as well as details of refined grid around the vessel, including overlapping grid areas.
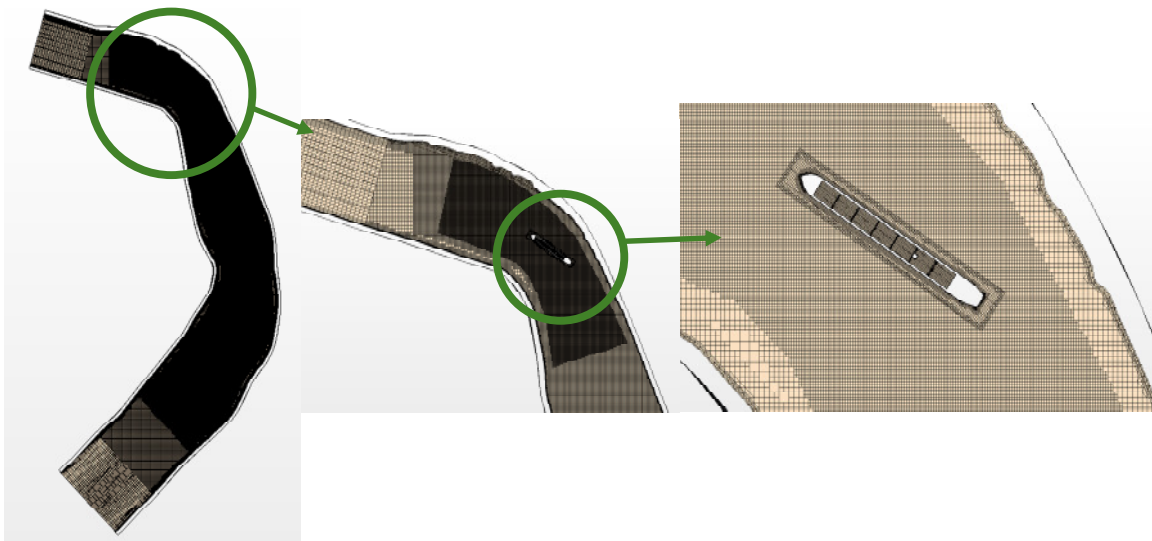

Fig. 7: Plan view of the computational domain and numerical grid

To investigate the influence of the initial *GM* on dynamic stability of the vessel, a sensitivity study with respect to the varied initial *GM* was carried out; *GM* was varied by changing the height of the centre of gravity of the lightship. Fig. 8 shows time histories of the roll angle from the simulations with the initial *GM* values from 0.297 m („reference" case, corresponding to the data from BAW) to 0.4, 0.45, 0.475 and 0.526 m.

These results show that capsize happens in the "reference" case, as well as at *GM* of 0.4 and 0,45 m; at higher initial *GM* values of 0.475 and 0.526 m, capsize does not happen for the considered scenario. Note that the *GM*-boundary between capsizing and not capsizing agrees well with regulations.
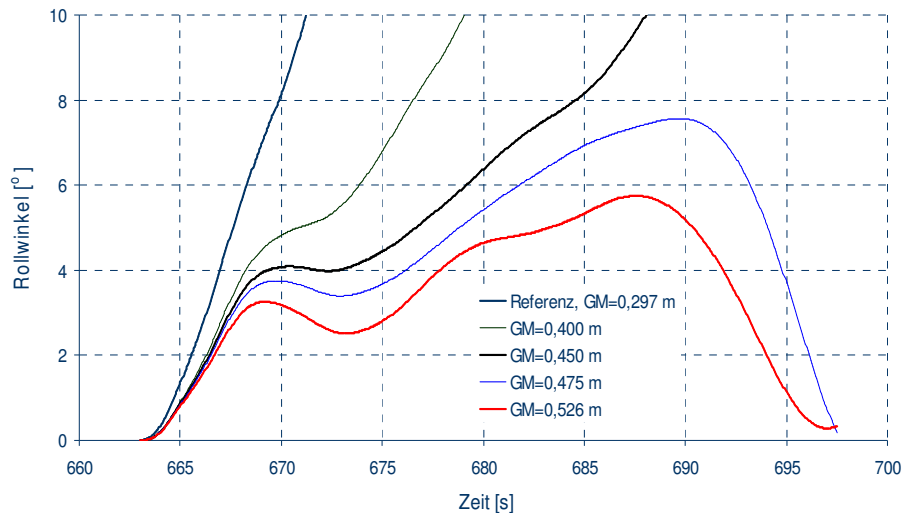
Fig. 8: Time histories of roll angle from simulations of free sailing vessel with five initial GM variations

These results also show that a roll angle of about 7.5° at the time instant 690.0 s can in principle lead to capsizing. Although such roll angle was achieved in the simulation with free roll motion without accurate consideration of the external flow, it did not lead to a capsize. To investigate the reasons of this, several simulations of the flow with the free surface around a restrained vessel with prescribed constant flow velocity, drift angle and heel were conducted. The flow velocity and the drift angle for these computations were estimated by averaging relative velocity through water and the local drift angle, respectively, at the start of free sailing simulation. To quantify the sensitivity of the forces and moments on the vessel to drift angle, the simulations were repeated with various flow directions, corresponding to drift angles from 50 to 0°. In addition, two representative heel angles, 0 und 5°, were considered.

Fig. 9 shows distributions of pressure and flow velocity for a drift angle of 20° at a heel of 10°. The pressure distribution indicates a domain with reduced pressure along the bilge, which generates a large vertical force, acting downwards, and a corresponding a large heeling moment to starboard. The results of these simulations also show that the additional heeling moment increases strongly with increasing drift angle and increasing heel angle. The estimated average relative velocity through water of 3.3 m/s and drift angle of 22° are sufficient to cause a sufficient additional heeling moment for capsizing.
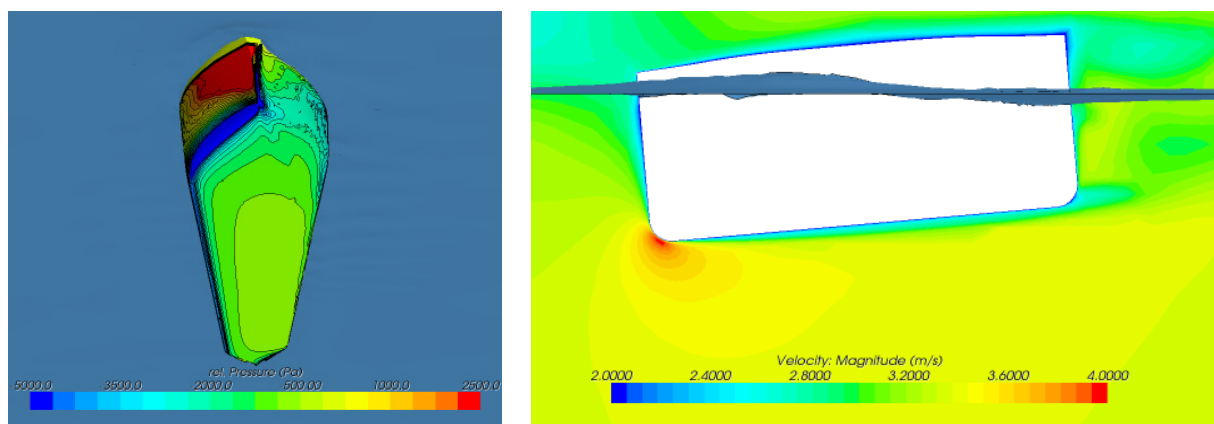

Fig. 9: Vessel kept in a steady flow with free surface at a constant drift angle of 20°, flow velocity of 3.3 m/s and heel angle of 10° to starboard: pressure distribution on the bottom of the vessel (left) and velocity magnitude in the cross section midships (right)

Summary

FutureShip was commissioned by the Federal Waterways Engineering and Research Institute to investigate the capsize dynamics of the inland tanker *Waldhof* during the accident on January 13, 2011. To quantify the influence of different physical factors on the ship dynamics, roll behaviour of the vessel was studied during the prescribed manoeuvre. As input for this investigation, the loading condition and the ship trajectory were provided by BAW; the ship trajectory was selected on the basis of multiple simulations by BAW as the trajectory describing best the available radar images of the accident. The influence of the following physical factors was investigated here: motions of sulphur acid in the partially loaded tanks, the lateral acceleration of the vessel during manoeuvre and current in the river. The investigation showed that capsizing of the vessel „*Waldhof*" is indeed possible taking into account the investigated loading and operative assumptions, and that the following factors are crucial for the capsizing: (1) vessel motions and accelerations in the horizontal plane, i.e. the trajectory and yaw motion of the vessel, (2) motions of the sulphur acid in the partially loaded tanks and (3) heeling moment due to lateral and, especially, vertical drift forces.

CALL FOR PAPERS

17th Numerical Towing Tank Symposium (NuTTS'14)

Marstrand, Sweden, 28-30 September 2014

Topics:

- Nonlinear flows around marine structures (LES, RANSE, Euler with or w/o free surface)
- Free-surface flows around marine structures (3-d ship seakeeping, free-surface viscous flows)
- Related topics (validation experiments, numerical techniques, grid generation, etc)

Deadlines: Early feedback (optional):   15 March 2014
Extended Abstracts received: 30 June 2014

You are invited to participate in the above event. The objective of the event is to provide a forum for informal discussions among experts in the field and to disseminate latest results. Younger workers and Ph.D. students are especially encouraged to participate. The event will be held at Villa Maritime in Marsstrand. All participants stay and have meals together to maximize interaction and discussion.

The extended abstracts of the proposed talk will be directly reproduced in pdf proceedings. Work in progress, encountered problems, etc. should be discussed in an open, informal atmosphere (no ties!) among colleagues. The first page of the extended abstract should be headed with the title and authors' names, affiliation and email address in a compact form to economize on space. Academic titles and page numbers shall be omitted. The extended abstract shall neither contain an abstract of the abstract, nor keywords, nor further headers. Font size shall not be less than 10pt Times New Roman. Extended abstracts should be limited to 6 pages in A4 format with 2.5 cm margin. An early reply will help us in organizing the event better. For the early feedback, a tentative title or topic will suffice.

Following the tradition of previous NuTTS events, the fees will be kept low to allow a maximum number of scientists to attend. The fees including accommodation (2 nights) and all meals during the symposium will be:

350 Euro PhD candidates and students
400 Euro authors
450 Euro other participants

Contact: Rickard Bensow
rickard.bensow@chalmers.se

Sponsors: to be announced